Numerical investigation of Taylor bubble and development of phase change model

Longkai Guo

▶ **To cite this version:**

Longkai Guo. Numerical investigation of Taylor bubble and development of phase change model. Fluids mechanics [physics.class-ph]. Université de Lyon, 2020. English. NNT : 2020LYSEI095 . tel-03177304

HAL Id: tel-03177304
https://theses.hal.science/tel-03177304

Submitted on 23 Mar 2021

HAL is a multi-disciplinary open access archive for the deposit and dissemination of scientific research documents, whether they are published or not. The documents may come from teaching and research institutions in France or abroad, or from public or private research centers.

L'archive ouverte pluridisciplinaire **HAL**, est destinée au dépôt et à la diffusion de documents scientifiques de niveau recherche, publiés ou non, émanant des établissements d'enseignement et de recherche français ou étrangers, des laboratoires publics ou privés.

N°d'ordre NNT : 2020LYSEI095

THESE de DOCTORAT DE L'UNIVERSITE DE LYON
opérée au sein de
l'INSA LYON

Ecole Doctorale N° EDA162
Mécanique, Energétique, Génie Civil, Acoustique

Spécialité/ discipline de doctorat : Mécanique des Fluides

Soutenue publiquement/à huis clos le 28/10/2020, par :
Longkai GUO

Numerical investigation of Taylor bubble and development of a phase change model

---

Devant le jury composé de :

DARU, Virginie	Maître de conférences	Arts et Métiers ParisTech - ENSAM	Rapporteur
JOSSERAND, Christophe	Directeur de Recherche	École Polytechnique	Rapporteur
NASO, Aurore	Chargée de Recherche	École Centrale de Lyon	Examinatrice
RUYER-QUIL, Christian	Professeur	Université Savoie Mont Blanc	Examinateur
XIN, Shihe	Professeur des Universités	INSA-LYON	Directeur de thèse
KNIKKER, Ronnie	Maître de conférences	INSA-LYON	Co-directeur de thèse
ALBIN, Eric	Maître de conférences	INSA-LYON	Invité

Cette thèse est accessible à l'adresse : http://theses.insa-lyon.fr/publication/2020LYSEI095/these.pdf
© [L. Guo], [2020], INSA Lyon, tous droits réservés

Cette thèse est accessible à l'adresse : http://theses.insa-lyon.fr/publication/2020LYSEI095/these.pdf
© [L. Guo], [2020], INSA Lyon, tous droits réservés

Département FEDORA – INSA Lyon - Ecoles Doctorales – Quinquennal 2016-2020

SIGLE	ECOLE DOCTORALE	NOM ET COORDONNEES DU RESPONSABLE
CHIMIE	**CHIMIE DE LYON** **http://www.edchimie-lyon.fr** Sec. : Renée EL MELHEM Bât. Blaise PASCAL, 3e étage **secretariat@edchimie-lyon.fr** INSA : R. GOURDON	**M. Stéphane DANIELE** Institut de recherches sur la catalyse et l'environnement de Lyon IRCELYON-UMR 5256 Équipe CDFA 2 Avenue Albert EINSTEIN 69 626 Villeurbanne CEDEX **directeur@edchimie-lyon.fr**
E.E.A.	**ÉLECTRONIQUE, ÉLECTROTECHNIQUE, AUTOMATIQUE** **http://edeea.ec-lyon.fr** Sec. : M.C. HAVGOUDOUKIAN **ecole-doctorale.eea@ec-lyon.fr**	**M. Gérard SCORLETTI** École Centrale de Lyon 36 Avenue Guy DE COLLONGUE 69 134 Écully Tél : 04.72.18.60.97 Fax 04.78.43.37.17 **gerard.scorletti@ec-lyon.fr**
E2M2	**ÉVOLUTION, ÉCOSYSTÈME, MICROBIOLOGIE, MODÉLISATION** **http://e2m2.universite-lyon.fr** Sec. : Sylvie ROBERJOT Bât. Atrium, UCB Lyon 1 Tél : 04.72.44.83.62 INSA : H. CHARLES **secretariat.e2m2@univ-lyon1.fr**	**M. Philippe NORMAND** UMR 5557 Lab. d'Ecologie Microbienne Université Claude Bernard Lyon 1 Bâtiment Mendel 43, boulevard du 11 Novembre 1918 69 622 Villeurbanne CEDEX **philippe.normand@univ-lyon1.fr**
EDISS	**INTERDISCIPLINAIRE SCIENCES-SANTÉ** **http://www.ediss-lyon.fr** Sec. : Sylvie ROBERJOT Bât. Atrium, UCB Lyon 1 Tél : 04.72.44.83.62 INSA : M. LAGARDE **secretariat.ediss@univ-lyon1.fr**	**Mme Sylvie RICARD-BLUM** Institut de Chimie et Biochimie Moléculaires et Supramoléculaires (ICBMS) - UMR 5246 CNRS - Université Lyon 1 Bâtiment Curien - 3ème étage Nord 43 Boulevard du 11 novembre 1918 69622 Villeurbanne Cedex Tel : +33(0)4 72 44 82 32 **sylvie.ricard-blum@univ-lyon1.fr**
INFOMATHS	**INFORMATIQUE ET MATHÉMATIQUES** **http://edinfomaths.universite-lyon.fr** Sec. : Renée EL MELHEM Bât. Blaise PASCAL, 3e étage Tél : 04.72.43.80.46 **infomaths@univ-lyon1.fr**	**M. Hamamache KHEDDOUCI** Bât. Nautibus 43, Boulevard du 11 novembre 1918 69 622 Villeurbanne Cedex France Tel : 04.72.44.83.69 **hamamache.kheddouci@univ-lyon1.fr**
Matériaux	**MATÉRIAUX DE LYON** **http://ed34.universite-lyon.fr** Sec. : Stéphanie CAUVIN Tél : 04.72.43.71.70 Bât. Direction **ed.materiaux@insa-lyon.fr**	**M. Jean-Yves BUFFIÈRE** INSA de Lyon MATEIS - Bât. Saint-Exupéry 7 Avenue Jean CAPELLE 69 621 Villeurbanne CEDEX Tél : 04.72.43.71.70 Fax : 04.72.43.85.28 **jean-yves.buffiere@insa-lyon.fr**
MEGA	**MÉCANIQUE, ÉNERGÉTIQUE, GÉNIE CIVIL, ACOUSTIQUE** **http://edmega.universite-lyon.fr** Sec. : Stéphanie CAUVIN Tél : 04.72.43.71.70 Bât. Direction **mega@insa-lyon.fr**	**M. Jocelyn BONJOUR** INSA de Lyon Laboratoire CETHIL Bâtiment Sadi-Carnot 9, rue de la Physique 69 621 Villeurbanne CEDEX **jocelyn.bonjour@insa-lyon.fr**
ScSo	**ScSo*** **http://ed483.univ-lyon2.fr** Sec. : Véronique GUICHARD INSA : J.Y. TOUSSAINT Tél : 04.78.69.72.76 **veronique.cervantes@univ-lyon2.fr**	**M. Christian MONTES** Université Lyon 2 86 Rue Pasteur 69 365 Lyon CEDEX 07 **christian.montes@univ-lyon2.fr**

*ScSo : Histoire, Géographie, Aménagement, Urbanisme, Archéologie, Science politique, Sociologie, Anthropologie

Cette thèse est accessible à l'adresse : http://theses.insa-lyon.fr/publication/2020LYSEI095/these.pdf
© [L. Guo], [2020], INSA Lyon, tous droits réservés

Cette thèse est accessible à l'adresse : http://theses.insa-lyon.fr/publication/2020LYSEI095/these.pdf
© [L. Guo], [2020], INSA Lyon, tous droits réservés

Acknowledgements

This work has been carried out at the Centre de Énergetique et de Thermique de Lyon (CETHIL UMR-5008), National Institute of Applied Sciences (INSA de lyon), and was made possible with the financial support of the china scholarship council (CSC), which are first gratefully acknowledged.

Sincere appreciation to my thesis advisors Prof. Shihe Xin and Prof. Ronnie KNIKKER. This thesis could not be finished without their direction and continuous support. Especially, Ronnie helps me to understand the research and gives me a lot inspiration when studying the numerical methods. I also want to thank Prof. Eric ALBIN for encouraging me a lot. Besides, I am very grateful to Dr. Chengsi ZHOU for providing experimental data.

I want to thank Prof. Virginie DARU of Arts et Métiers ParisTech - ENSAM, Prof. Christrophe JOSSERAND of Ecole Polytechnique, Prof. Aurore NASO of Ecole Centrale de Lyon and Prof. Christian RUYER-QUIL for being the examiners of this thesis.

I also want to express my thanks to my friends in the lab namely Naveed AHMAD, Karolina WOJTASIK, Fouad HAGANI, Axel PIC, Larysa Okhrimenko, Hazem BEN AISSIA, Pouya Jafari Fesharaki, Bao CHEN, Xin ZHENG, Xiaorui WANG, Cong YOU, Lan ZHANG and Feng WANG. Thanks for all your encouragement!

Last but not the least, I would like to thank my wife, my parents and my brother for their grand support.

Cette thèse est accessible à l'adresse : http://theses.insa-lyon.fr/publication/2020LYSEI095/these.pdf
© [L. Guo], [2020], INSA Lyon, tous droits réservés

The way ahead is long, I shall search high and low.

–Yuan QU

Cette thèse est accessible à l'adresse : http://theses.insa-lyon.fr/publication/2020LYSEI095/these.pdf
© [L. Guo], [2020], INSA Lyon, tous droits réservés

Abstract

English: The motion of a nitrogen Taylor bubble in glycerol-water mixed solutions rising through different types of expansions and contractions is investigated by a numerical approach. The CFD procedure is based on an open-source solver Basilisk, which adopts the volume-of-fluid (VOF) method to capture the gas-liquid interface. The results of sudden expansions/contractions are compared with experimental results. The results show that the simulations are in good agreement with experiments. The bubble velocity increases in sudden expansions and decreases in sudden contractions. The bubble break-up pattern is observed in sudden expansions with large expansion ratios, and a bubble blocking pattern is found in sudden contractions with small contraction ratios. In addition, the wall shear stress, the liquid film thickness, and pressure in the simulations are studied to understand the hydrodynamics of the Taylor bubble rising through expansions/contractions. The transient process of the Taylor bubble passing through sudden expansion/contraction is further analyzed for three different singularities: gradual, parabolic convex and parabolic concave. A unique feature in parabolic concave contraction is that the Taylor bubble passes through the contraction even for small contraction ratios. Moreover, a phase change model is developed in the Basilisk solver. In order to use the existed geometric VOF method in Basilisk, a general two-step geometric VOF method is implemented. Mass flux is calculated not in the interfacial cells but transferred to the neighboring cells around the interface. The saturated temperature boundary condition is imposed at the interface by a ghost cell method. The phase change model is validated by droplet evaporation with a constant mass transfer rate, the one-dimensional Stefan problem, the sucking interface problem, and a planar film boiling case. The results show good agreement with analytical solutions or correlations.

Key words: Two-phase flow, Taylor bubble, expansion, contraction, VOF, phase change

Cette thèse est accessible à l'adresse : http://theses.insa-lyon.fr/publication/2020LYSEI095/these.pdf
© [L. Guo], [2020], INSA Lyon, tous droits réservés

Cette thèse est accessible à l'adresse : http://theses.insa-lyon.fr/publication/2020LYSEI095/these.pdf
© [L. Guo], [2020], INSA Lyon, tous droits réservés

Résumé

Le mouvement d'une bulle d'azote de Taylor dans des solutions mixtes glycérol-eau s'élevant à travers différents types d'expansions et de contractions est étudié par une approche numérique. La procédure CFD est basée sur un solveur open-source Basilisk, qui adopte la méthode du volume de fluide (VOF) pour capturer l'interface gaz-liquide. Les résultats des expansions/contractions soudaines sont comparés aux résultats expérimentaux. Les résultats montrent que les simulations sont en bon accord avec les expériences. La vitesse de la bulle augmente dans les expansions soudaines et diminue dans les contractions soudaines. Le modèle de rupture des bulles est observé dans les expansions soudaines avec de grands taux d'expansion, et un modèle de blocage des bulles est observé dans les contractions soudaines avec de petits rapports de contraction. De plus, la contrainte de cisaillement de la paroi, l'épaisseur du film liquide et la pression dans les simulations sont étudiées pour comprendre l'hydrodynamique de la bulle de Taylor montant par expansions/contractions. Le processus transitoire de la bulle de Taylor passant par une expansion/contraction soudaine est ensuite analysé pour trois singularités différentes: graduelle, parabolique convexe et parabolique concave. Une caractéristique unique de la contraction concave parabolique est que la bulle de Taylor passe par la contraction même pour de petits rapports de contraction. De plus, un modèle de changement de phase est développé dans le solveur Basilisk. Afin d'utiliser la méthode VOF géométrique existante dans Basilisk, une méthode VOF géométrique générale en deux étapes est implémentée. Le flux de masse n'est pas calculé dans les cellules interfaciales mais transféré aux cellules voisines autour de l'interface. La condition aux limites de température saturée est imposée à l'interface par une méthode de cellule fantôme. Le modèle de changement de phase est validé par évaporation de gouttelettes avec un taux de transfert de masse constant, le problème de Stefan unidimensionnel, le problème d'aspiration de l'interface et un cas d'ébullition à film plan. Les résultats montrent un bon accord avec les solutions analytiques ou les corrélations.

Mots clés: écoulement diphasique, bulle de Taylor, expansion, contraction, VOF, phase change

Cette thèse est accessible à l'adresse : http://theses.insa-lyon.fr/publication/2020LYSEI095/these.pdf
© [L. Guo], [2020], INSA Lyon, tous droits réservés

Cette thèse est accessible à l'adresse : http://theses.insa-lyon.fr/publication/2020LYSEI095/these.pdf
© [L. Guo], [2020], INSA Lyon, tous droits réservés

Contents

Cette thèse est accessible à l'adresse : http://theses.insa-lyon.fr/publication/2020LYSEI095/these.pdf
© [L. Guo], [2020], INSA Lyon, tous droits réservés

Cette thèse est accessible à l'adresse : http://theses.insa-lyon.fr/publication/2020LYSEI095/these.pdf
© [L. Guo], [2020], INSA Lyon, tous droits réservés

Cette thèse est accessible à l'adresse : http://theses.insa-lyon.fr/publication/2020LYSEI095/these.pdf
© [L. Guo], [2020], INSA Lyon, tous droits réservés

Cette thèse est accessible à l'adresse : http://theses.insa-lyon.fr/publication/2020LYSEI095/these.pdf
© [L. Guo], [2020], INSA Lyon, tous droits réservés

List of Figures

Cette thèse est accessible à l'adresse : http://theses.insa-lyon.fr/publication/2020LYSEI095/these.pdf
© [L. Guo], [2020], INSA Lyon, tous droits réservés

Cette thèse est accessible à l'adresse : http://theses.insa-lyon.fr/publication/2020LYSEI095/these.pdf
© [L. Guo], [2020], INSA Lyon, tous droits réservés

Cette thèse est accessible à l'adresse : http://theses.insa-lyon.fr/publication/2020LYSEI095/these.pdf
© [L. Guo], [2020], INSA Lyon, tous droits réservés

Cette thèse est accessible à l'adresse : http://theses.insa-lyon.fr/publication/2020LYSEI095/these.pdf
© [L. Guo], [2020], INSA Lyon, tous droits réservés

Cette thèse est accessible à l'adresse : http://theses.insa-lyon.fr/publication/2020LYSEI095/these.pdf
© [L. Guo], [2020], INSA Lyon, tous droits réservés

Cette thèse est accessible à l'adresse : http://theses.insa-lyon.fr/publication/2020LYSEI095/these.pdf
© [L. Guo], [2020], INSA Lyon, tous droits réservés

List of Tables

Cette thèse est accessible à l'adresse : http://theses.insa-lyon.fr/publication/2020LYSEI095/these.pdf
© [L. Guo], [2020], INSA Lyon, tous droits réservés

Cette thèse est accessible à l'adresse : http://theses.insa-lyon.fr/publication/2020LYSEI095/these.pdf
© [L. Guo], [2020], INSA Lyon, tous droits réservés

Chapter 1

Introduction

Two-phase flow composed of gas and liquid is ubiquitous in nature and common in industrial processes. The two-phase flow, especially for gas-liquid flow, extensively affects and changes human life. In the following chapters, we will separately introduce two-phase flow without and with phase change. The Taylor bubble is firstly investigated and a phase-change model is later developed.

Taylor bubble

The injection of gas at the bottom of a liquid-filled pipe leads to a configuration where gaseous and liquid phases coexist. When the gas flow rate is large enough, the gas portion becomes *bullet-like* shape and occupies most of the pipe cross-section (see Fig. 1.1), which is often called Taylor bubbles after Geoffrey Taylor (Davies and Taylor, 1950). The Taylor bubble is an important part of the gas-liquid flow patterns, the details of flow patterns will be introduced in Chapter 2. The Taylor bubble has a large number of applications from chemical reactions with micro-scale systems to volcano eruption with a large scale (Ambrose et al., 2017). The Taylor bubble can be found in the transportation of hydrocarbons of oil and gas in industry, and the boiling, condensing processes in the thermal power plants. Due to a huge usage in industries, it is of great significance to study the Taylor bubble rising phenomenon. However, most studies related to Taylor bubbles focus on the bubble rising in straight pipes. There are few works considering expansions and contractions, which are called singularities. The Taylor bubble rising through expansions and contractions is also widely used in industrial and natural processes (James et al., 2006). The lack of the Taylor bubble rising through singularities motivates the present study. Moreover, several types of expansions and contractions are performed to further investigate the Taylor bubble motion through different types of singularities. The literature review of Taylor bubble is presented in Chapter 2. Moreover, some physical parameters are investigated, such as bubble terminal velocity, liquid falling film and wall shear stress. In Chapter 4, an individual Taylor bubble rising in a vertical pipe through sudden expansions and contractions is numerically studied. The simulation results are compared with the experimental results of a previous P.hD work (Zhou, 2017) in the CETHIL lab. In Chapter 5, the Taylor bubble rises through expansions and

Cette thèse est accessible à l'adresse : http://theses.insa-lyon.fr/publication/2020LYSEI095/these.pdf
© [L. Guo], [2020], INSA Lyon, tous droits réservés

contractions are further investigated by modeling three different singularities, which are gradual, parabolic convex and parabolic concave expansions and contractions, respectively.

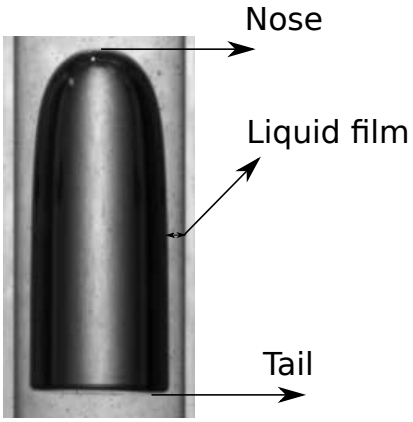

FIGURE 1.1: The experimental photo of Nitrogen Taylor bubble rising through glycerol-water mixed liquid, highlighting the bubble nose, liquid film and bubble tail.

Phase change

After exploring a two-phase flow problem without phase change, we focus our attention on two-phase flow with phase change. Two-phase flow with heat and mass transfer is essential in many industrial processes, such as chemical reactions, petroleum refining, and cooling systems. Accurate prediction of phase change characteristics is necessary for the above applications (Akhtar and Kleis, 2013). Two-phase Flows with phase change have been studied for many years. Some pioneer investigators studied the phase change phenomena primarily through experiments (Kharangate and Mudawar, 2017). After decades of research, there are many experimental results to analyze the phase change phenomena. However, most of the experiments adopt visualization methods to observe flow dynamics. This creates considerable difficulties in measuring transient data, such as temperature field, flow velocity, and so on. Besides, the cost of the experiments is high. With the development of computer science, considerable attention has been paid to use numerical simulation methods to study physical problems. To study phase change problems, an accurate phase change model is required. In Chapter 2, we review several phase-change models. In addition, the interface capturing method (VOF) with phase change is reviewed. The details of the development of a phase change model are introduced in Chapter 6. The geometric VOF method is used to capture the interface. The phase change model is implemented by calculating the mass flux in the cells which are close to the interface and imposing saturated boundary condition on the interface.

Cette thèse est accessible à l'adresse : http://theses.insa-lyon.fr/publication/2020LYSEI095/these.pdf
© [L. Guo], [2020], INSA Lyon, tous droits réservés

1.1 Objective and contributions of the thesis

An open-source solver, named Basilisk Popinet (2013a), is adopted in this thesis for establishing the model to investigate the Taylor bubble and two-phase flow with phase change. We compare the experimental results and simulation results of the Taylor bubble to verify the accuracy of the solver.

This thesis can be divided into two main parts. The first one is to study the Taylor bubble rising motion, which is considered by numerical approaches and to compare the simulation results with experimental results. Inspired by the Taylor bubble rising in straight pipes, different types of expansions and contractions have been considered.

This thesis contributes to investigate numerically the behavior of rising bubbles in 3 different expansions and contractions, including sudden, gradual, parabolic convex, parabolic concave types, respectively. The experimental and numerical results are compared for Taylor bubble cases. The second part considers phase change in two-phase flow. In particular, a phase-change model is developed within the incompressible Navier-Stokes solver. Its main feature is that a two-step geometric VOF method is used (Malan et al., 2020; Scapin et al., 2020). Several benchmark test cases are used to validate the phase change model.

1.2 Outline of the thesis

The thesis contains seven chapters, which is organized as follows:

- Chapter 1: Background and objective of the thesis.
- Chapter 2: Brief literature review of the Taylor bubble and two-phase flow with phase change.
- Chapter 3: Presentation of the Navier-Stokes equations, and the geometric VOF method in the Basilisk solver.
- Chapter 4: Numerical study of the Taylor bubble rising in a vertical pipe through sudden expansions and contractions by comparing with experiments.
- Chapter 5: Numerical investigation of the Taylor bubble rising in a vertical pipe through various expansions and contractions types.
- Chapter 6: Development of a phase change model.
- Chapter 7: General conclusions and perspectives.

Cette thèse est accessible à l'adresse : http://theses.insa-lyon.fr/publication/2020LYSEI095/these.pdf
© [L. Guo], [2020], INSA Lyon, tous droits réservés

Cette thèse est accessible à l'adresse : http://theses.insa-lyon.fr/publication/2020LYSEI095/these.pdf
© [L. Guo], [2020], INSA Lyon, tous droits réservés

Chapter 2

Literature review

In this chapter, gas-liquid flow without and with phase change are reviewed. The first section contains the classification of two-phase flow patterns and the introduction of a single spherical bubble rising in vertical pipes. In the second part, we review the development of experiments and simulations of the Taylor bubble rising in vertical pipes. Moreover, the motion of the Taylor bubble with expansions and contractions are analyzed. Last, we introduce different mass transfer models and the two-phase geometric VOF method with phase change.

2.1 General introduction of two-phase flows

2.1.1 The definition of flow pattern

When gas and liquid flow simultaneously exist in a vertical pipe, different flow patterns need to be characterized according to the gas flow rates, pressure drop, heat and mass transfer. The flow pattern is crucially important in the study of flow dynamics and heat transfer of two-phase flow. A large amount of research has been dedicated to classifications for gas-liquid flow in vertical pipes (Barnea, 1987). Generally, five main types of gas-liquid flow patterns are categorized: bubbly, slug, churn, annular and wispy annular flow (Ghajar, 2005) (see Fig. 2.1).

- Bubbly flow:
  The gas phase is in the form of discrete small bubbles in the liquid portion. The typical feature of this flow pattern is that the diameter of the bubbles is much smaller than that of the pipe. The bubble interfaces are moving and deformable with the evolution of time, and complex interactions exist between interfaces.

- Slug flow:
  Increasing the gas flow rate, the density of small bubbles in the bubbly flow pattern consequently increases and promotes the coalescence of bubbles. This leads to large, bullet-shaped slug bubbles (often called Taylor bubbles) which nearly occupies the entire cross-sectional area of the liquid-filled pipe. There is a thin liquid film layer between the pipe wall and the bubble interface.

Cette thèse est accessible à l'adresse : http://theses.insa-lyon.fr/publication/2020LYSEI095/these.pdf
© [L. Guo], [2020], INSA Lyon, tous droits réservés

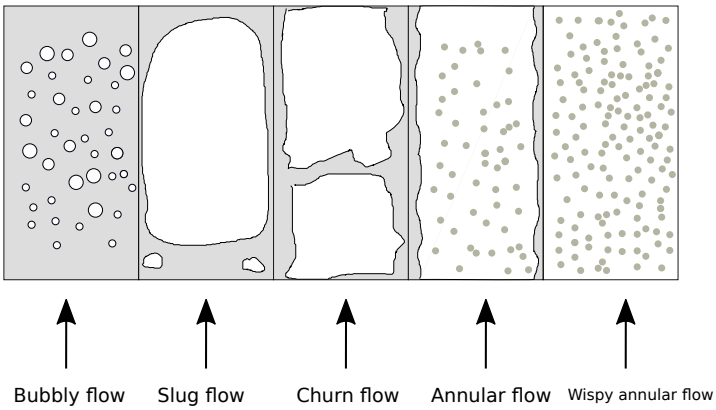

FIGURE 2.1: Schematic representation of two-phase flow patterns in vertical pipes.

- Churn flow:
  When the gas flow rate is continually increasing, the slugs break into highly turbulent and unstable regimes, often characterized by pulsing oscillations. This pattern is a transient flow regime between the slug and the annular flow.

- Annular flow:
  With a tremendous gas flow rate, the domain is characterized by a central core of gas. The liquid acts as an annular liquid film close to the pipe wall. The gas-liquid interface has wavy shapes, and small liquid droplets are entrained in the gas phase.

- Wispy annular flow:
  The flow regime occurs when the gas flow rate is remarkably higher than the liquid flow rate. The liquid droplets appear in the continuous gas, which is an inversed pattern of bubbly flow.

2.1.2 The determination of flow pattern

The Hewitt & Roberts map (Hewitt and Roberts, 1969) of gas-liquid flow pattern is presented in Fig. 2.2. When the gas flux is small, the flow pattern is the slug flow. As the gas flux increases, the flow pattern tends to the churn bubble regime. The two-phase flow pattern map is usually used to predict local flow patterns.

Cette thèse est accessible à l'adresse : http://theses.insa-lyon.fr/publication/2020LYSEI095/these.pdf
© [L. Guo], [2020], INSA Lyon, tous droits réservés

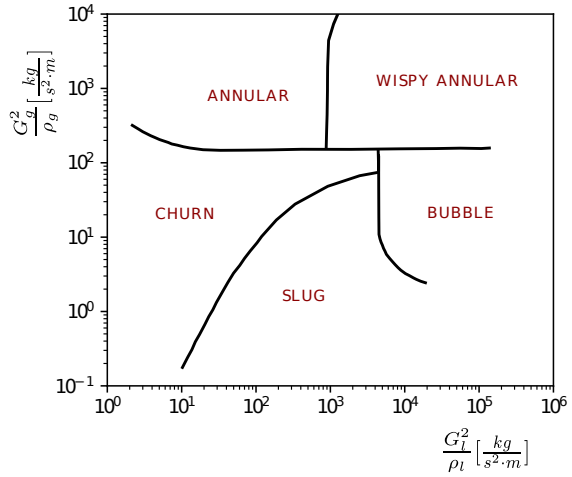

FIGURE 2.2: Hewitt & Roberts flow pattern map (Hewitt and Roberts, 1969), where G is the mass flux and the subscript l and g indicates the liquid and gas, respectively.

2.2 Basic literature review on two-phase flows without phase-change

The objective of this part is to review the development of Taylor bubbles rising in vertical pipes. Before introducing the Taylor bubble, a freely single rising bubble is introduced to describe the basic principles of single bubble rising in vertical pipes.

2.2.1 Non-dimensional groups

From the physical point of view, the gas bubble is affected by forces acting on it, such as buoyancy, gravitational, viscous, inertial, and surface tension forces. The combined effect of these forces leads to the evolution of bubble shape, velocity, and pressure. Several dimensionless numbers can be defined according to the interactions of different forces:

- Eötvös number, $Eo = \dfrac{(\rho_l - \rho_g) g D^2}{\sigma}$, which is a ratio of the gravitational force to the surface tension force and also called Bond number (Bo).
- Froude number, $Fr = \dfrac{U}{\sqrt{gD}}$, which is a ratio of the inertial force to the gravitational force.
- Reynolds number, $Re = \dfrac{\rho_l U D}{\mu_l}$, which is a ratio of the inertial force to the viscous force.
- Galilei number, $Ga = \dfrac{g D^3}{\mu_l^2}$, which is a ratio of the gravitational force to the viscous force.

Cette thèse est accessible à l'adresse : http://theses.insa-lyon.fr/publication/2020LYSEI095/these.pdf
© [L. Guo], [2020], INSA Lyon, tous droits réservés

- Inverse viscosity number, $N_f = \frac{\rho_l \sqrt{gD^3}}{\mu_l}$, which is a ratio of the gravitational force to the viscous force.
- Archimedes number, $Ar = N_f^2$.
- Morton number, $Mo = \frac{g\mu_l^4}{\rho_l \sigma^3}$, also called the property group since it only contains the properties of the fluid.
- Density ratio, $\rho_r = \frac{\rho_l}{\rho_g}$.
- Viscosity ratio, $\mu_r = \frac{\mu_l}{\mu_g}$.

where σ is the surface tension coefficient. g is gravity acceleration. D is the characteristic length, which depends on the specific physical problem, i.e. in a single spherical bubble rising, D is the initial bubble diameter. However, for the Taylor bubble rising problem, D is the diameter of the pipe. U is the bubble velocity. In non-dimensional groups, only four dimensionless groups are independent, e.g. Mo, ρ_r, μ_r and Re. It should be noted for different physical problems, Re can be replaced by N_f, Ar or Ga.

2.2.2 Freely rising single bubble

Experiments review

The motion of a single bubble rising in a quiescent liquid driven by buoyancy force has been extensively studied for many decades. It is still a widespread problem of great interest today (Tripathi et al., 2015). Bubble dynamics are of enormous significance in many applications, including some phenomena involving heat and mass transfer, such as volcano eruption and nuclear plant. Significant achievements have been obtained in studying bubble dynamics. However, the nonlinearity of convection term in Navier-Stokes equations and the full three-dimensional nature of the problem still makes it vast and daunting (Tripathi et al., 2015).

For a single bubble rising in viscous or inviscous fluid, some pioneering experiments were reported (Haberman and Morton, 1953; Hartunian and Sears, 1957; Walters and Davidson, 1962, 1963; Clift et al., 1978; Bhaga and Weber, 1981; Tomiyama et al., 2002; Wu and Gharib, 2002; Veldhuis et al., 2008; Tagawa et al., 2014; Aoyama et al., 2016; Sharaf et al., 2017)). In the work of Bhaga and Weber (1981), experiments on a wide range of Eo and Re numbers have been carried out. Based on the analysis of the experimental data, they presented bubble shape regimes and classified the bubble shapes into 7 groups (see Fig. 2.3): spherical (s); oblate ellipsoid (oe); oblate ellipsoidal (oed) (disk-like and wobbling) ; oblate ellipsoidal cap (oec); spherical cap with closed (scc), steady wake; spherical cap with open (sco), unsteady wake; skirted with smooth (sks), steady skirt; skirted with wavy (skw), unsteady skirt.

Cette thèse est accessible à l'adresse : http://theses.insa-lyon.fr/publication/2020LYSEI095/these.pdf
© [L. Guo], [2020], INSA Lyon, tous droits réservés

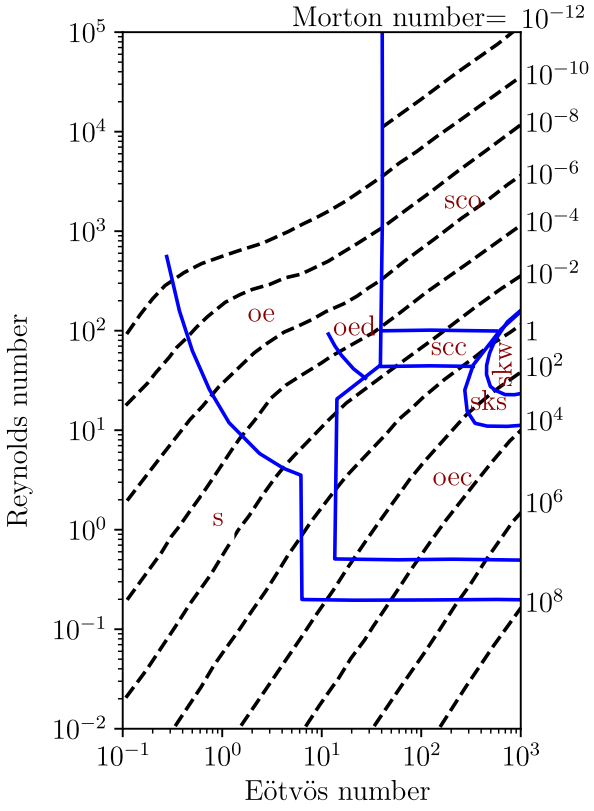

FIGURE 2.3: Single rising bubble shape regime map in stagnant liquids with various properties (Bhaga and Weber, 1981).

From the experimental point of view, it is challenging to measure physical properties such as velocity, temperature, and pressure inside the bubbles. Though the experiments have merits to observe the superficial phenomenon, it is still difficult to study the details of the event. In order to solve this kind of problem, numerical simulation has been increasingly used in recent years to analyze the flow structure and stability, providing more detailed fluid information.

Numerical simulation review

For numerical simulation of a single bubble rising, most studies have been focused on axisymmetric or two-dimensional (2D) cases to save computational time. Tomiyama et al. (1993) and Ohta et al. (2005) studied a single bubble rising in stagnant and linear shear flow, and found the bubble motion is affected by Mo and Eo numbers. Hua and Lou (2007) simulated a rising bubble with a wide range of Re, Eo numbers, ρ_r and μ_r. The results showed that Re and Eo numbers have a great influence on bubble shapes and motions, and ρ_r and μ_r only affect the bubble motion under low ratios.

With the development of computer techniques, more and more interest is attracted by three-dimensional (3D) simulations (Bunner and Tryggvason, 1999; Sussman and

Cette thèse est accessible à l'adresse : http://theses.insa-lyon.fr/publication/2020LYSEI095/these.pdf
© [L. Guo], [2020], INSA Lyon, tous droits réservés

Puckett, 2000; Shin and Juric, 2002; Hua et al., 2008; Pivello et al., 2014). Tripathi et al. (2015) conducted 3D bubble rising by changing Ga and Eo numbers in liquid with $\rho_r = 1000$ and $\mu_r = 100$. Five different regions for bubble behaviors are identified (see Fig. 2.4 (A)). With different dimensionless numbers, the single bubble presents different bubble shapes. The researchers can predict bubble shapes with Eo and Ga numbers by this map. Sharaf et al. (2017) subsequently conducted extensive experiments according to the numerical results of Tripathi et al. (2015). An experimental map is obtained in Fig. 2.4 (B) to show the bubble terminal shapes in quiescent liquid as a function of the Ga and Eo numbers (see Fig. 2.4). The region V in simulation (Tripathi et al., 2015) did not appear in the experiments of Sharaf et al. (2017). Some other researchers investigated multiple bubbles rising (including co-axial and lateral bubbles). They studied the interaction between bubbles and the different dynamic behavior (van Sint Annaland et al., 2006; Lu and Tryggvason, 2008; Roghair et al., 2011).

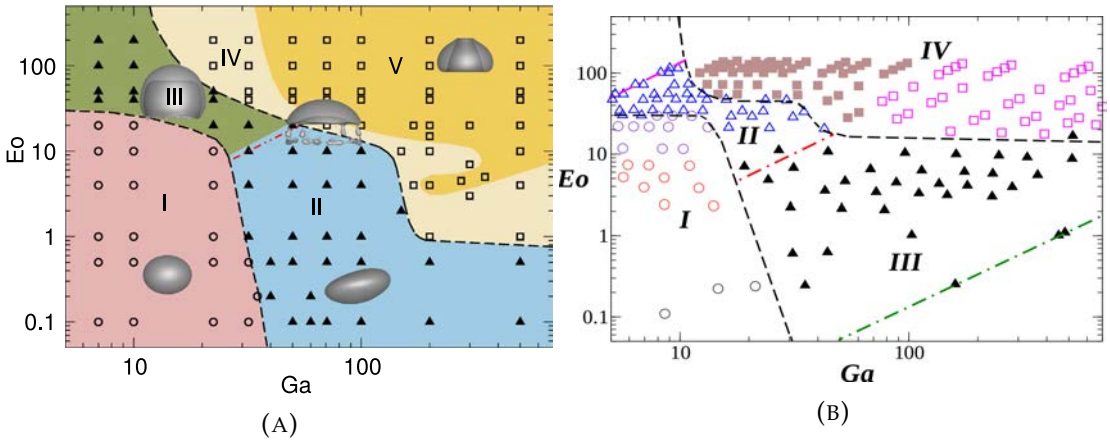

FIGURE 2.4: (A). Numerical simulation of 3D bubble shapes and behaviour in different liquids (Tripathi et al., 2015). (B). Different regions of bubble shape and behavior obtained from experiments implemented by Sharaf et al. (2017).

From the literature review on the single rising bubble, some remarks can be concluded,

- The experimental study on bubble motion focuses on the evolution of bubble shapes due to the technique of measurement.
- The bubble shapes are affected by several dimensionless numbers, the numerical analysis of wide range dimensionless numbers provide more detailed information on bubble motion.

2.2.3 Taylor bubble: a state of the art review

The literature review on the Taylor bubble focuses on several aspects, such as terminal velocity, liquid falling film, stabilization length, etc. The schematic diagram

Cette thèse est accessible à l'adresse : http://theses.insa-lyon.fr/publication/2020LYSEI095/these.pdf
© [L. Guo], [2020], INSA Lyon, tous droits réservés

of the Taylor bubble in a stagnant liquid inside a vertical pipe with a radius of R is displayed in Fig. 2.5.

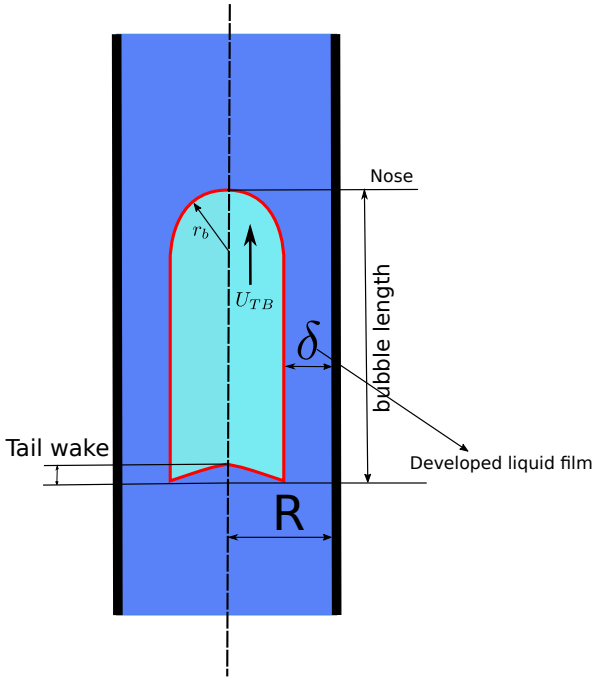

FIGURE 2.5: Schematic of a Taylor bubble rising in a stagnant liquid inside a vertical pipe.

Applications

The Strombolian volcano is a relatively small-scale explosive eruption. The Taylor bubbles are formed by bubble coalescence in conduit before bursting at the surface, as shown in Fig. 2.6. After the bubble leaving the conduit, it undergoes a large expansion. Bouche et al. (2010) pointed out the Taylor bubble may bring hot magma from the depth, which affects the bubble wake region and drive convection currents in the conduit. Harris and Ripepe (2007) showed the Strombolian explosion could be recorded by seismo-acoustic signals, which are thought to be generated from phenomena associated with slug dynamics. This deduction was further corroborated by James et al. (2006).

Cette thèse est accessible à l'adresse : http://theses.insa-lyon.fr/publication/2020LYSEI095/these.pdf
© [L. Guo], [2020], INSA Lyon, tous droits réservés

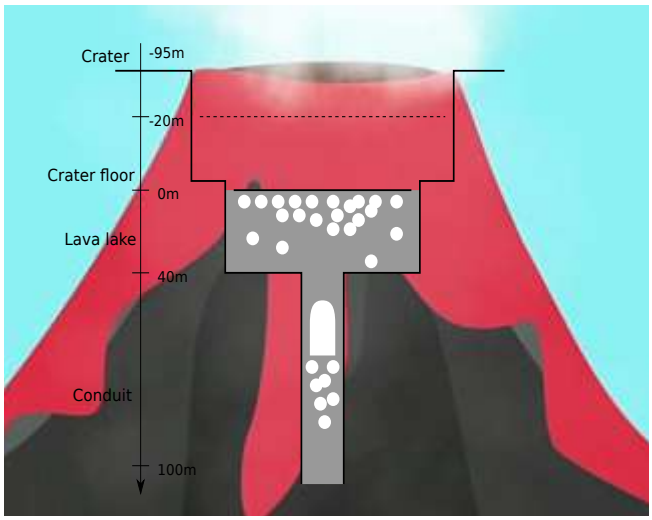

FIGURE 2.6: Taylor bubble in lava conduit and its rising in Strombolian type volcano eruption (Bouche et al., 2010).

Another application is related to the biological field. For example, in smaller blood vessels (see Fig 2.7), the red blood cells are separated by blood plasma under stresses. The red blood cells behave like Taylor bubbles (Taha and Cui, 2004). Prothero and Burton (1961) pointed out that strong circulation ahead of the red cells was found very useful in nutrient distribution. The blood vessels have many branches when red blood cells are transported through these branches, which would cause expansion or contractions.

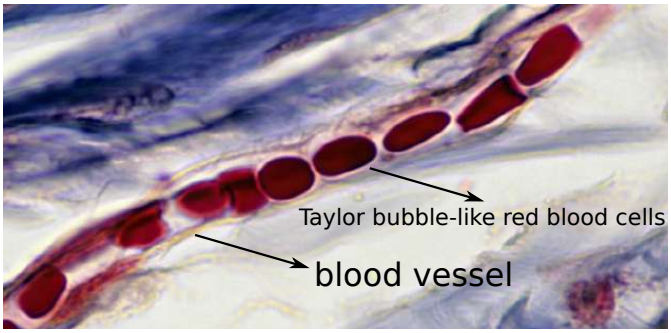

FIGURE 2.7: Taylor bubble-like red blood cells transport in blood vessels.

Investigations on the Taylor bubble

The approaches used to study Taylor bubbles include analytical, experimental, and numerical simulation. Since the 1940s, many studies on the Taylor bubble have been devoted to understanding this physical problem. Some researchers use experimental and/or analytical approaches to develop correlations to describe Taylor bubble motions (Kang et al., 2010).

White and Beardmore (1962) firstly performed a comprehensive experimental study on Taylor bubbles and proposed a general graphical correlation involving Fr, Eo, and Mo numbers. Zukoski (1966) experimentally studied the influence of surface

Cette thèse est accessible à l'adresse : http://theses.insa-lyon.fr/publication/2020LYSEI095/these.pdf
© [L. Guo], [2020], INSA Lyon, tous droits réservés

tension, liquid viscosity, and inclination angle of pipes on the motion of bubbles. A correlation was also proposed to calculate bubble velocity. Later, this subject was addressed by Spedding and Nguyen (1978), Hasan et al. (1988), Bendiksen (1984), Shosho and Ryan (2001), Moreiras et al. (2014). It is challenging and difficult to determine the wake flow patterns in the Taylor bubble flow. Campos and De Carvalho (1988) performed an exclusive photographic study to investigate the details of the wake structures of the Taylor bubble rising in stagnant liquids, which covers a wide range of viscosities, inside vertical pipes with diameters from 19 mm to 52 mm. They concluded that the wake structures are affected by N_f numbers, and the flow regimes can be categorized into three main parts depending on the value of N_f. For $N_f < 500$, a closed axisymmetric laminar wake is observed, while for $500 < N_f < 1500$, the wake tends to be asymmetric with a periodic undulation. For N_f higher than 1500, the wake is turbulent with the recirculatory flow. Other experimental achievements have been obtained by researchers related to flow patterns on Taylor bubbles (Mao and Dukler, 1991; Nogueira et al., 2003; Pinto et al., 1998). In recent years, with the development of non-intrusive optical experimental techniques, investigators made a further understanding of hydrodynamics features of Taylor bubbles and surrounding liquid (Bugg and Saad, 2002; Van Hout et al., 2002). Many correlations $Fr = f(Eo, Mo)$ on Taylor bubble rising in vertical pipes have been proposed based on experimental results (Wallis, 1969; Viana et al., 2003).

Clarke and Issa (1997) numerically investigated a Taylor bubble rising through a stagnant liquid in a vertical pipe and used the volume-of-fluid (VOF) method to capture the bubble interface. Bugg et al. (1998) used the finite difference method to predict the Taylor bubble velocity for $10 < Eo < 100$ and $10^{-12} < Mo < 10^{-1}$. They also compared the film thickness and the average velocity in the liquid film with experiments. Similar studies can be found in the work of Taha and Cui (2006) and Ndinisa et al. (2005). Lu and Prosperetti (2008) used the finite volume method combined with the interface tracking method to study the Taylor bubble rising through stagnant co-current and counter-current flowing liquid in vertical pipes. Kang et al. (2010) adopted a front tracking methodology to simulate the effects of ρ_r, μ_r, Eo and Ar on the dynamics of Taylor bubbles . They developed correlations of the dimensionless liquid film and non-dimensional wall shear stress as a function of Ar number. Gutiérrez et al. (2017) used an arbitrary Lagrangian-Eulerian approach to optimize the computational domain and found the efficiency of the simulation can be notably improved. Further numerical investigations are on the two-consecutive bubble and non-circular pipes. Araújo et al. (2013a,b, 2015) analyzed the hydrodynamics coalescence of pairs of consecutive Taylor bubbles in a stagnant liquid. In terms of non-circular pipes, several studies (Liao and Zhao, 2003; Liu and Wang, 2008) performed Taylor bubble rising in mini non-circular channels and capillaries.

Cette thèse est accessible à l'adresse : http://theses.insa-lyon.fr/publication/2020LYSEI095/these.pdf
© [L. Guo], [2020], INSA Lyon, tous droits réservés

Terminal velocity

To investigate the motion of Taylor bubbles, the terminal velocity (U_{TB}) is one obvious but significant parameter. Through U_{TB}, the researchers can obtain the underlying state of motion and the principles of bubble behavior combined with bubble shapes.

The pioneer investigation was performed by Dumitrescu (1943), who investigated the rise of Taylor bubbles in the stagnant liquid and pointed out the correlation of U_{TB} based on potential flow theory. The U_{TB} can be expressed as: $U_{TB} = C\sqrt{gD}$ in this work, where C is 0.351.

Afterward, Davies and Taylor (1950) experimentally studied the Taylor bubble rising in mixed nitrobenzene and water. They obtained a series of experimental data of bubble shape and bubble velocity. They analyzed the data theoretically by considering potential flow around the bubble and assuming the pressure above the Taylor bubble ideal state. Finally, they modified C in Dumitrescu (1943) and gave a small value of 0.328.

A watershed work for the Taylor bubble rising was accomplished by White and Beardmore (1962). They considered gas expansion occurring on the bubble velocity when it rises towards a lower pressure region. After a wide range of experiments, they proposed a general graphical correlation describing the Taylor bubble velocity using N_f and Eo numbers. As Fig. 2.8 shows, by ignoring the density and viscosity of the gas phase, the basic behavior of the Taylor bubble can be summarized in Tab. 2.1. Some results are from the analysis of the work of White and Beardmore (1962) as follows:

- $Eo < 4$: The Taylor bubble does not rise due to high surface tension.
- $Eo > 70$: Surface tension effects are negligible.
- $Fr < 2.5 \times 10^{-4}$: Inertial effects are negligible.
- $Mo < 10^{-8}$: Viscosity effects are negligible, and $N_f > \sqrt{3 \times 10^5}$.

Based on the experimental data, White and Beardmore (1962) proposed a polynomial fit correction for Taylor bubble velocity.

$$U_{TB} = \left(\frac{a_1 a_2 e^{a_3 b}}{a_1 + a_2(e^{a_3 b} - 1)} - a_4 \right) \sqrt{gD} \tag{2.1}$$

where

$$b = \lg(Eo) \tag{2.2}$$

Cette thèse est accessible à l'adresse : http://theses.insa-lyon.fr/publication/2020LYSEI095/these.pdf
© [L. Guo], [2020], INSA Lyon, tous droits réservés

The parameters a_i in Eq. (2.1) are seventh-degree polynomials:

$$a_i = \sum_{j=1}^{8} c_{ij} x^{j-1} \quad (i = 1, ..., 4)$$
$$x = \lg(\mathrm{Mo})$$

the coefficients c_{ij} are given by the matrix:

$$\begin{bmatrix} 3.5603852\times10^{-1} & 2.6717658\times10^{-3} & -2.7121907\times10^{-3} & -2.0001955\times10^{-3} \\ 1.5642441\times10^{-3} & 2.8532721\times10^{-4} & 4.7831508\times10^{-5} & 3.605927\times10^{-5} \\ 3.059819 & -5.2353564\times10^{-1} & 3.3906415\times10^{-2} & 2.1368428\times10^{-2} \\ 2.3221312\times10^{-2} & -1.809746\times10^{-3} & 9.3468732\times10^{-5} & -2.3440168\times10^{-4} \end{bmatrix}$$

$$\begin{bmatrix} 8.622533\times10^{-5} & 5.7198751\times10^{-5} & -2.4316663\times10^{-6} & -6.7582431\times10^{-7} \\ 7.6382727\times10^{-6} & 1.1736259\times10^{-6} & -1.5186036\times10^{-7} & 1.9756221\times10^{-8} \\ -3.2676237\times10^{-3} & -7.302379\times10^{-4} & 7.2215493\times10^{-5} & 1.1273658\times10^{-5} \\ 5.9716008\times10^{-5} & 9.7852173\times10^{-6} & -1.3514105\times10^{-6} & -1.74642\times10^{-7} \end{bmatrix}$$

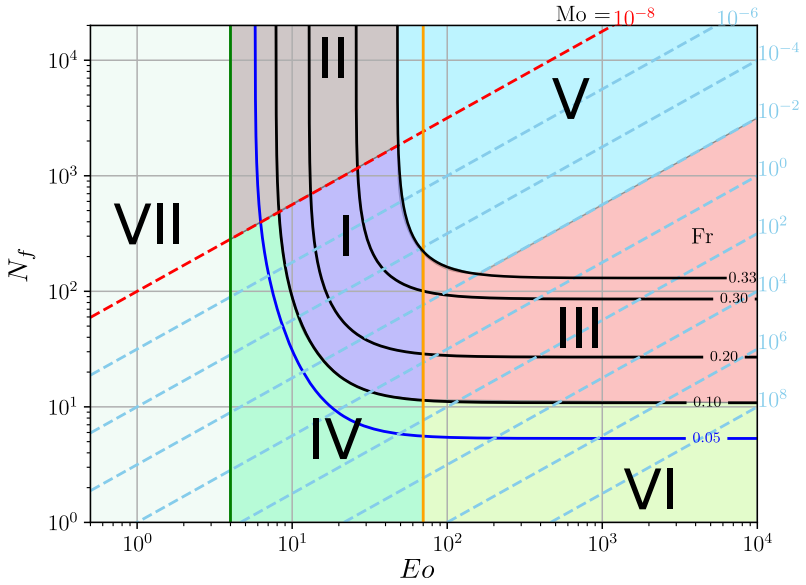

FIGURE 2.8: Crossplot of dimensionless numbers showing different flow regimes (replotted from White and Beardmore (1962)).

Cette thèse est accessible à l'adresse : http://theses.insa-lyon.fr/publication/2020LYSEI095/these.pdf
© [L. Guo], [2020], INSA Lyon, tous droits réservés

TABLE 2.1: The Taylor bubble velocity and bubble behavior proposed by White and Beardmore (1962).

Region	Bubble velocity	Independent of forces	Limits of Dimensionless numbers
I	Graphical	none	$3 < Eo < 400, 10^{-12} < Mo < 10^{8}$
II	Graphical	viscous forces	$N_f > \sqrt{3 \times 10^5}$
III	Graphical	interfacial forces	$Eo > 70$
IV	Graphical	inertial forces	$Fr < 0.05^2$
V	$U_{TB} = 0.345\sqrt{gD}$	viscous and interfacial forces	$Eo > 70, N_f > \sqrt{3 \times 10^5}$
VI	$U_{TB} = 0.0096\rho_l g D^2/\mu_l$	inertial and interfacial	$Eo > 70, Fr < 2.5 \times 10^{-4}$
VII	$U_{TB} \approx 0$	inertial and viscous	$Eo < 4$

Brown (1965) made both experimental and theoretical studies on U_{TB} for the Taylor bubble rising in liquid with different viscosities. He stated that U_{TB} in Davies and Taylor (1950) is applicable for low viscosity but not for high viscosity liquid. He also proposed a more general correlation for U_{TB} regarding the liquid viscosity.

$$U_{TB} = 0.351\sqrt{gD}\sqrt{1 - 2\left(\frac{\sqrt{1+ND}-1}{ND}\right)} \tag{2.3}$$

where

$$N = \sqrt[3]{14.5\frac{\rho_l^2 g}{\mu_l^2}} \tag{2.4}$$

The limits of applicability of Eq. (2.3) were established empirically as:

surface tension:

$$\frac{Eo}{4}\left(1 - 2\left(\frac{\sqrt{1+ND}-1}{ND}\right)\right) > 5.0 \tag{2.5}$$

viscosity:

$$ND > 60 \tag{2.6}$$

where ND is dimensionless and $ND \propto N_f$.

Wallis (1969) came up with a correlation based on extensive experimental data for U_{TB}. The correlation can be presented in terms of all the relevant variables:

$$U_{TB} = 0.345\left(1 - e^{-0.01\,\mathrm{Re}/0.345}\right)\left(1 - e^{(3.37\,-\,\mathrm{Eo})/m}\right)\sqrt{\frac{(\rho_l - \rho_g)gD}{\rho_l}} \tag{2.7}$$

The parameter m is a function of Re numbers and takes on the following values:

$$m = \begin{cases} 10 & : \mathrm{Re} > 250 \\ 69\,\mathrm{Re}^{-0.35} & : 18 < \mathrm{Re} < 250 \\ 25 & : \mathrm{Re} < 18 \end{cases}$$

Cette thèse est accessible à l'adresse : http://theses.insa-lyon.fr/publication/2020LYSEI095/these.pdf
© [L. Guo], [2020], INSA Lyon, tous droits réservés

Tung and Parlange (1976) studied long gas bubbles rising in closed cylindrical tubes. In these cases, $Re > 50$ and the surface tension effect was neglected. An analytical correlation for Taylor bubble velocity was proposed as a function of surface tension, gravity, pipe diameter, and liquid density as follows:

$$U_{TB} = \left(0.136 - 0.944\frac{1}{Eo}\right)^{1/2}\sqrt{gD} \tag{2.8}$$

If ignoring the surface tension effect, the Eq. (2.8) can be rewritten as:

$$U_{TB} = 0.369\sqrt{gD} \tag{2.9}$$

Viana et al. (2003) assembled previously published papers and performed new experimental data. They proposed a correlation for Taylor bubble velocity according to a different range of Re numbers. Three separate equations are obtained for different Re numbers. For large Re (> 200) they found:

$$U_{TB} = \frac{0.34}{(1 + 3805/Eo^{3.06})^{0.58}}\sqrt{gD} \tag{2.10}$$

For small Re (< 10), they found:

$$U_{TB} = \frac{9.494 \times 10^{-3}}{(1 + 6197/Eo^{2.561})^{0.5793}}Re^{1.026}\sqrt{gD} \tag{2.11}$$

The author described the transition region ($10 < Re < 200$) by fitting experimental data to a logistic curve. A universal correlation was carried out as follows:

$$U_{TB} = L[\mathrm{Re}; A, B, G, H] \approx \frac{A}{(1 + (\frac{\mathrm{Re}}{B})^G)^H}\sqrt{gD} \tag{2.12}$$

where

$$A = L[\mathrm{Eo}; a, b, c, d], \quad B = L[\mathrm{Eo}; e, f, g, h],$$
$$G = L[\mathrm{Eo}; i, j, k, l], \quad H = m/G,$$

and the parameters (a,b,...,l) are:

$$a = 0.34; \quad b = 14.793; \quad c = -3.06; \quad d = 0.58;$$
$$e = 31.08; \quad f = 29.868; \quad g = -1.96; \quad h = -0.49;$$
$$i = -1.45; \quad j = 24.867; \quad k = -9.93; \quad l = -0.094;$$
$$m = -1.0295$$

Hayashi et al. (2010) proposed a general correlation for Taylor drops. Comparison with simulation and experimental results show that the proposed correlation is valid for Taylor drops under a wide range conditions, i.e. $0.002 < Re < 4960$, $4.8 < Eo <$

Cette thèse est accessible à l'adresse : http://theses.insa-lyon.fr/publication/2020LYSEI095/these.pdf
© [L. Guo], [2020], INSA Lyon, tous droits réservés

228, $1 < N_f < 14700$, $-12 < lg(Mo) < 4$, and $d/D < 16$, where d is the sphere-volume equivalent drop diameter and D the pipe diameter.

$$U_{TB} = \sqrt{\frac{0.0089\left(1+\frac{41}{Eo^{1.96}}\right)^{-4.63}}{0.0725+\frac{1}{Re}\left(\frac{1+1.9\mu_r}{1+0.31\mu_r}\right)(1-0.11Re^{0.33})}gD} \tag{2.13}$$

In Eq. (2.13), if we ignore the effect of density and viscosity, the simplified equation can be written as:

$$U_{TB} = \sqrt{\frac{0.01\left(1+\frac{41}{Eo^{1.96}}\right)^{-4.63}}{0.0816+Re^{-1}}gD} \tag{2.14}$$

Araújo et al. (2012) analyzed a detailed study on the rising of individual Taylor bubbles including a wide range of Eo and Mo numbers ($Eo \in [6, 900], Mo \in [4.72 \times 10^{-5}], N_f \in [3.5, 517]$). Massoud et al. (2018) performed a complete dimensionless analysis of individual Taylor bubbles rising in stagnant Newtonian liquid and concluded that the Fr is a function of Eo, Re, ρ_r, μ_r and bubble length (L_{TB}/D) which can be expressed as $Fr = f[Eo, Re, \rho_r, \mu_r, L_{TB}/D]$.

Kurimoto et al. (2013) experimentally and numerically investigated the Taylor bubble terminal velocity in vertical pipes. A general correlation was proposed based on experiments and simulation data.

$$U_{TB} = \sqrt{\frac{AB}{\frac{B}{0.35^2}}+G\sqrt{gD}} \tag{2.15}$$

where $A = (1+\frac{3.87}{Eo^{1.68}})^{-18.4}$, $B = 0.0025 \times (3+A)$ and $G = \frac{1}{Re}(1-0.05\sqrt{Re})$.

Liquid film thickness around Taylor bubble

The stability of liquid film directly affects the Taylor bubble behavior in pipes. The thin falling films are usually characterized by the film Reynolds numbers Re_f, which is proposed by Dukler (1952). Re_f is often defined by $Re_f = 4\frac{\rho_l \delta U_f}{\mu_l}$, where δ is the film thickness and U_f is the average velocity in the film.

Nusselt (1916) presented a representative theoretical analysis on the liquid film of a viscous liquid. He derived a solution for the film thickness:

$$\delta = \left(\frac{3\mu_l^2}{4\rho_l^2 g}Re_f\right)^{1/3} \tag{2.16}$$

It should be noted that the liquid is laminar flow, which underpredicts film thickness for flow with high Reynolds number. Based on the work of Nusselt (1916), Dukler (1952) performed experiments for flow with high Re numbers. They concluded the model Eq. (2.16) is not capable of transition turbulent flow. A new theoretical

Cette thèse est accessible à l'adresse : http://theses.insa-lyon.fr/publication/2020LYSEI095/these.pdf
© [L. Guo], [2020], INSA Lyon, tous droits réservés

model for liquid film thickness over the transition flow was developed in their work.

$$Re_f = 4\eta(3 + 2.5\ln\eta) - 256 \tag{2.17}$$

where η can be rewritten in terms of the inverse viscosity and the dimensionless film thickness (i.e., $\eta = N_f(0.5\delta)^{1.5}$). To validate the theoretical model, Dukler (1952) performed experiments limited the film Reynolds number in the range of $500 < Re_f < 3000$. The film thickness presented waves form in the falling film, and the mean film thickness is in good agreement with Eq. (2.17). Fulford (1964) found the transition to turbulence has a wider range of Re_f than the pipe flow because the boundary layer occupies a considerable fraction of the film thickness.

Because of the limited practicality of the model Eq. (2.17), several more general empirical correlations for film thickness as a function of Re_f were developed by the work of Karapantsios et al. (1989), Lel et al. (2005) and Zhou et al. (2009). For $Re_f < 3000$, the model of Lel et al. (2005) successfully predicted the liquid film thickness,

$$\delta\sqrt[3]{\frac{\rho_l^2 g}{\mu_l^2}} = 1 + 0.321Re_f^{0.47} \tag{2.18}$$

while for the range of $Re_f > 3000$, the other one model of Karapantsios et al. (1989) is better to determine the film thickness,

$$\delta\sqrt[3]{\frac{\rho_l^2 g}{\mu_l^2}} = 0.214Re_f^{0.538} \tag{2.19}$$

For now, we have already introduced several models to predict film thickness. Still, it should be noted that the models are valid when the film is thin enough such that the local curvature of the free surface can be neglected. For the circumstance that directly addresses the Taylor bubble's liquid film thickness, the models below have differences.

Brown (1965) proposed an expression based on the work of Goldsmith and Mason (1962) for U_{TB} in their work. They obtained the relationship between U_{TB} and δ.

$$U_{TB} = \frac{2\rho_l g\delta^3}{3\mu_l(R-\delta)} \tag{2.20}$$

where R indicates the pipe radius. Under the assumption of a thin liquid film (i.e. $\delta << R_b$), the denominator in Eq. (2.20) is reduced to $3\mu_l R$. Brown (1965) further changed the definition of Froude number by using the Taylor bubble radius (R_b) to instead pipe radius (R). The Taylor bubble Froude number Fr_b can be written by

$$Fr_b = \frac{U_{TB}}{\sqrt{gD_b}} \tag{2.21}$$

Cette thèse est accessible à l'adresse : http://theses.insa-lyon.fr/publication/2020LYSEI095/these.pdf
© [L. Guo], [2020], INSA Lyon, tous droits réservés

by substituting Fr_b into Eq. (2.20), Brown got a more general quadratic solution for film thickness as follows

$$\delta = \frac{\sqrt{1+2NR}-1}{N} \tag{2.22}$$

Llewellin et al. (2011) summarized the models for predicting liquid film thickness and proposed a model that can avoid the thin-film limit and also for the drawback of Eq. (2.22) which needs to assume a constant Froude number. They named the model 'Cubic Brown'.

$$\delta'^3 + a\delta' - a = 0 \tag{2.23}$$

where δ' is the dimensionless liquid film thickness which is expressed by $\delta' = \delta/R$ and $a = 6Fr/N_f$. The Eq. (2.23) is valid for $N_f < 3000$.

Other approaches, such as numerical simulation, also attract some researchers to study the Taylor bubble's liquid film thickness. For example, Kang et al. (2010) found the relationship between the film thickness and N_f and performed simulations at $Eo = 200$ using the data to derive an empirical correlation:

$$\frac{\delta}{D} = 0.32N_f^{-0.2} \tag{2.24}$$

The empirical correlations proposed based on experiments or simulations for liquid film thickness are summarized in Tab. 2.2.

TABLE 2.2: Summary of the models for liquid film thickness of the Taylor bubble presented in literatures. Llewellin et al. (2011)

Source	Equation	Validity
Nusselt (1916)	(2.16)	$Re_f < 1000$
Dukler (1952)	(2.17)	$500 < Re_f < 3000$
Lel et al. (2005)	(2.18)	$10 < Re_f < 3000$
Karapantsios et al. (1989)	(2.19)	$3000 < Re_f < 15000$
Brown (1965)	(2.22)	$Re_f > 40$
Llewellin et al. (2011)	(2.23)	laminar
Kang et al. (2010)	(2.24)	$3 < Re_f < 150$

The dimensionless liquid film thickness δ' can be expressed as $\delta'(N_f)$. The relationship between δ' and N_f is shown in Fig. 2.9 by Morgado et al. (2016). The results show that when $N_f < 200$, δ' is strongly influenced by the Morton numbers (indicated by M in Fig. 2.9 taken from Araújo et al. (2012)). Higher Morton numbers correspond to higher maximum value of δ'. Under the condition of $N_f > 200$, the δ' is independent of Morton numbers, the curves for different Morton numbers assembled overlapping and decreases as N_f increases. The simulations in Araújo et al. (2012) are in agreement with the experiments data from Brown (1965), Mao and Dukler (1991), Nogueira et al. (2006a,b), Kang et al. (2010) and Llewellin et al. (2011). It should be noted that the experimental results on δ' are plotted only when $N_f > 100$.

Cette thèse est accessible à l'adresse : http://theses.insa-lyon.fr/publication/2020LYSEI095/these.pdf
© [L. Guo], [2020], INSA Lyon, tous droits réservés

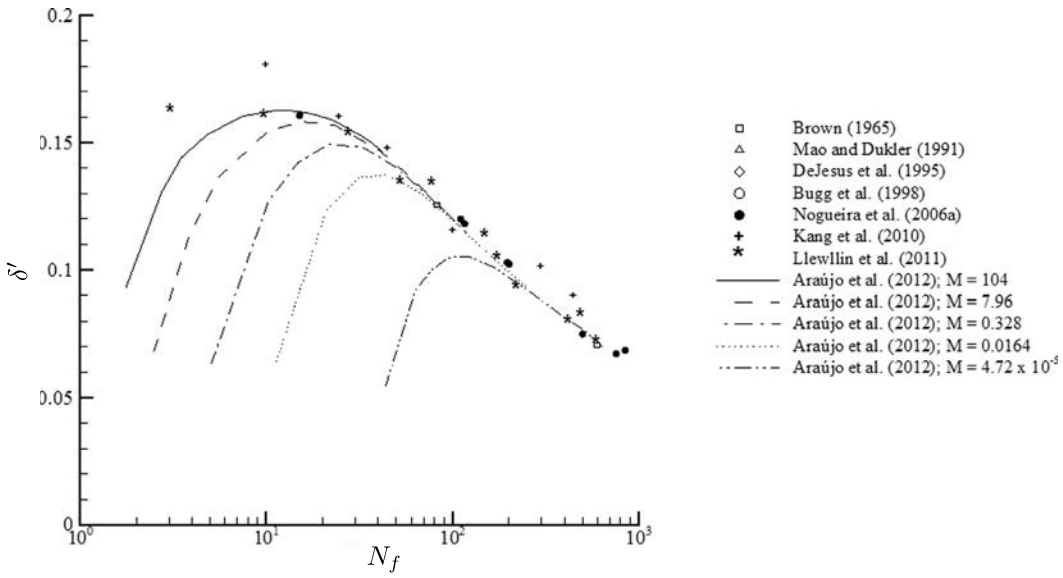

FIGURE 2.9: The relationship of dimensionless liquid film thickness and the inverse viscosity number (from Morgado et al. (2016)).

Wall shear stress

The wall shear stress is a significant physical parameter if the slug flow co-occurs with heat or mass transfer, in phenomena like membrane separations (Taha and Cui, 2006) or flow-induced corrosion in pipe wells (Villarreal et al., 2006). The wall shear stress can be expressed as follows:

$$\tau = \mu_l \frac{du_z}{dr} \tag{2.25}$$

Brown (1965) predicted the velocity gradient in Eq. (2.25) in his work.

$$\frac{du_z}{dr} = \frac{g}{\mu_l}\left(\frac{r}{2} - \frac{(R-\delta)^2}{2r}\right) \tag{2.26}$$

we substitute Eq. (2.26) into Eq. (2.25) and using radial coordinate R to get the simplified expression for the wall shear stress:

$$\tau_w = \rho_l g \frac{\delta(2R-\delta)}{2R} \tag{2.27}$$

It is difficult to perform experiments to measure the wall shear stress in the liquid film region. Therefore, several researchers studied numerical used to understand the evolution of the wall shear stress. The work of Kang et al. (2010), Araújo et al. (2012), Massoud et al. (2018) shows that the wall shear stress starts to increase near the bubble nose and reaches a kind of plateau further down from the tip of the bubble. The τ_w decreases near the bubble trailing edge due to the sudden widening of the separation between the wall and the bubble interface. Araújo et al. (2012) concluded

Cette thèse est accessible à l'adresse : http://theses.insa-lyon.fr/publication/2020LYSEI095/these.pdf
© [L. Guo], [2020], INSA Lyon, tous droits réservés

that lower Eo has higher refereed peaks since the liquid film is smaller under this condition and has a significant influence on the variation of τ_w.

2.2.4 Tayor bubble motion through expansions and contractions

In many natural and industrial processes involving slug flow, the pipes' size and geometry are variable. For example, the Strombolian volcanoes are affected by large gas bubbles rising in vents of continuously varying sizes. Despite the Taylor bubbles have been studied, there is few published experimental or numerical work on the Taylor bubble rising through expansions and contractions. In this section, we will review Taylor bubbles (or slug flow) rising in a vertical pipe with expansions/contractions.

Expansions

Rinne and Loth (1996) measured vertical air-water bubbly flow by fiber-optic sensors in a pipe with sudden expansion (40 mm to 90 mm). The experimental results show that the sudden pipe expansion produced a flow disturbance that led to a transient redistribution of the local two-phase flow parameters. A region with no bubbles is detached can be found downstream.

Kondo et al. (2002) experimentally studied air-water slug flow at near atmospheric conditions through the vertical round tube. The tube's geometry is composed of a sudden axisymmetric expansion with a diameter from 0.02 m to 0.05 m. Fig. 2.10 (A) shows that the Taylor bubble rises through sudden expansion in the experiments. After the bubble leaving expansion, Fig. 2.10 (B) shows that the rear of the bubble moves towards the bubble nose and burst up.

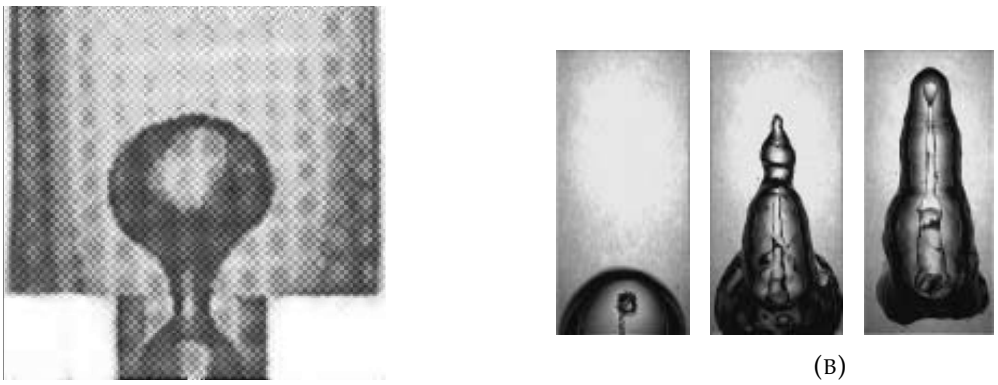

(A) (B)

FIGURE 2.10: (A). Video image snapshot extracted from Kondo et al. (2002) which shows the moment that Taylor bubble passing through the sudden expansions. (B). Taylor bubble penetration and bursts after leaving sudden expansion (from Kondo et al. (2002)).

James et al. (2006) reported an experimental investigation on the Taylor bubble passing through a variety of pipe expansions and contractions. The objective is to accurately describe the processes that the bubble rising through the expansions. The

Cette thèse est accessible à l'adresse : http://theses.insa-lyon.fr/publication/2020LYSEI095/these.pdf
© [L. Guo], [2020], INSA Lyon, tous droits réservés

pressure in the experiments is compared with the seismic data, which is recorded at volcanic sites. They concluded that the pressure oscillation in the seismic data was caused by gas slug passing through the sudden expansion section. The working fluids are sugar syrup solutions with viscosities of 0.001, 0.1, and 30 pa·s to compare different behavior in a range of Fr numbers. They observed that the gas slugs undergoes an abrupt flow pattern change and expanded laterally. For sufficient long bubbles, the bubble will split into two or more daughter bubbles, as shown in Fig. 2.11 when passing through expansions, causing pressure oscillation.

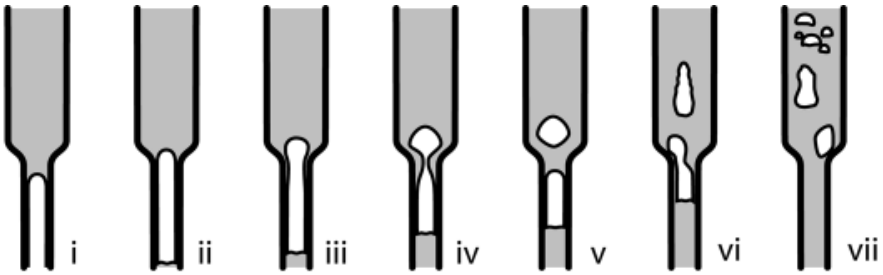

FIGURE 2.11: Skematic diagrame of Taylor bubble splitting into several daughter bubble (from James et al. (2006)).

Danabalan (2012) designed an experimental setup for the Taylor bubble rising from a vertical pipe into a rounded glass bowl or a cubic box, which is an analog of the volcano expanding into a lava lake. The author found that the Taylor bubble passes through the expansion without breakup. The critical volume of the Taylor bubble rising through expansion relies on the liquid viscosity and the expansion structures. For example, the rounded glass bowl makes it easier for the Taylor bubble to pass through intact. This finding was further corroborated by Soldati et al. (2013). Moreover, Soldati et al. (2013) studied the angle of expansion and obtained the critical bubble length increases as the angle of expansion (θ), see Fig. 2.12. The results are consistent with Danabalan (2012), who showed that sudden expansion ($\theta = 90°$) has a smaller critical bubble length than any gradual expansions.

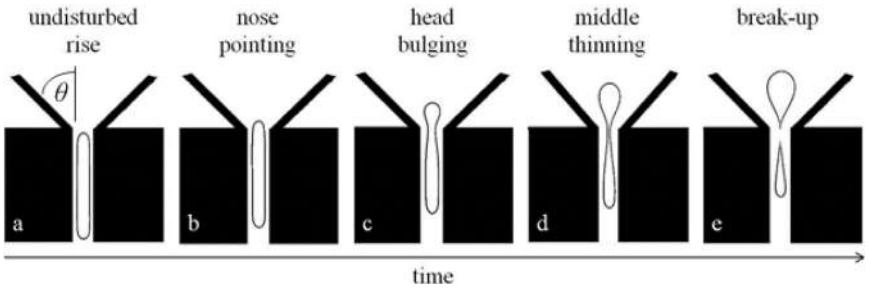

FIGURE 2.12: Images taken from high speed video of Taylor bubble rising from a smaller tube into a wider tube (from Carter et al. (2016)).

Carter et al. (2016) measured the acoustic signals produced by Taylor bubble breakup when rising through expansions. This study's experimental apparatus consists of two tubes, a smaller tube of 0.01 m diameter emerging inside a larger tube of 0.025

Cette thèse est accessible à l'adresse : http://theses.insa-lyon.fr/publication/2020LYSEI095/these.pdf
© [L. Guo], [2020], INSA Lyon, tous droits réservés

m diameter. The Taylor bubble reaching the expansion section is split into two parts (See Fig. 2.13). They used high sensitivity microphone above the expansion to record the acoustic signals during bubble breakup.

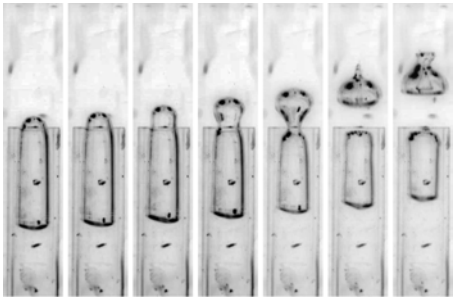

FIGURE 2.13: Images taken from high speed video of Taylor bubble rising from a smaller tube into a wider tube (from Carter et al. (2016)).

In the work of Ambrose et al. (2017), they numerically studied the qualitative and quantitative behavior of a Taylor bubble rising through an expansion pipe. They studied the gradual expansion structures by changing the expansion degree (θ) from $15°$ to $90°$. The expansion ratio is 2.1, and the initial bubble length is 4.4D, D is the lower pipe diameter. The results show that the gradual expansion could pass a much longer bubble without breakup by comparing it with sudden expansion. For a fixed θ, a critical bubble length can be defined for bubble breakup. When they changed the expansion ratio more prominent than 2.6, they found the critical bubble length is not changing anymore.

Recently, Amani et al. (2019) numerically studied the Taylor bubble through sudden/gradual expansions and analyzed the Taylor bubble behavior between Newtonian and shear-thinning liquids. When bubble rising through expansion, the bubble is split into two parts: the upper daughter and lower daughter bubbles. The results show that the upper daughter bubble diameter is decreased by increasing the shear-thinning liquid concentration and the expansion angle. The shear-thinning liquid significantly reduces the pressure drop when the Taylor bubble rising through expansions.

From the literature review about expansions, we can conclude that:

- Experimental study mainly focused on the Taylor bubble breakup and penetration phenomena in the expansion region. The evolution of bubble shapes in experiments attracts researchers on this point.
- Taylor bubble in different viscous liquids with expansions also interests people to do experiments or simulations. The objective is to pursue the Taylor bubble hydrodynamic behavior in various liquids with different N_f, Eo numbers.
- The critical length for bubble breakup: investigators experimentally or numerically studied different conditions of the Taylor bubble rising through expansions to explore the critical state of bubble length, bubble shapes, bubble velocity, etc.

Cette thèse est accessible à l'adresse : http://theses.insa-lyon.fr/publication/2020LYSEI095/these.pdf
© [L. Guo], [2020], INSA Lyon, tous droits réservés

- Other studies focus on the pressure drop, the expansion structures (or gradual expansion with different degrees), and flow patterns related to the real applications, such as photobioreactors (Singh and Sharma, 2012) or volcanology (Bouche et al., 2010).

Contractions

When the upper tube's diameter is smaller than the lower one, the singularity is a contraction. To our knowledge, the study of the Taylor bubble or slug flow rising through contractions is scarce, especially in vertical pipes.

Abdelall et al. (2005) used air and water at room temperature and near-atmospheric pressure to experimentally investigate the pressure drop caused by contractions in small circular channels. The largest tube diameter is 1.6 mm, and the smallest one is 0.84 mm. They proposed a correlation for pressure drop with contractions.

Chen et al. (2009b) investigated the pressure change and flow pattern subject to sudden contractions in the horizontal direction. In their work, the working fluids are air and water mixed in small rectangular channels with a size of 3×9 mm and 3×6 mm into a 3 mm diameter round tube. Similar to the work of Abdelall et al. (2005), they also established a pressure drop correlation for sudden contractions.

Kourakos et al. (2009) experimentally studied three types of singularities for single and two-phase (air-water) horizontal flow in the presence of expansion and contraction. A modified correlation of (Janssen and Kervinen, 1964) is suggested for progressive diminution. The results show that the pressure is decreased before contraction, and the contraction creates a high-pressure drop step.

Balakhrisna et al. (2010) experimentally studied the sudden expansion and contraction in a horizontal pipe for oil-water flows. They observed that sudden changes have a significant influence on the downstream phase distribution of liquid-liquid flows for different flow patterns.

Kaushik et al. (2012) performed a numerical study on the core annular flow through sudden expansion and contraction using the VOF method to capture the interface. They provided detailed information about the profiles of velocity, pressure, and volume fraction over a wide range of oil and water velocities sudden expansion and contraction. The numerical method is validated by experimental results from Balakhrisna et al. (2010).

Padilla et al. (2013) visualized the two-phase flow of HFO-1234yf, R-134a, and R-410A in a 10 mm glass tube with a sudden contraction (contraction ratio is 0.49). The perturbation lengths in upstream and downstream were studied, and the contribution of the perturbation to the pressure drop was identified. After comparing with other pressure drop correlations, a new method for predicting pressure drop was proposed. The correlation has better accuracy compared with other methods.

Cette thèse est accessible à l'adresse : http://theses.insa-lyon.fr/publication/2020LYSEI095/these.pdf
© [L. Guo], [2020], INSA Lyon, tous droits réservés

TABLE 2.3: Summary of the experimental/numerical studies of the Taylor bubble rising through expansions.

Published articles	Approach	Expansion ratio	Pipe direction	Liquid	Comments
Rinne and Loth (1996)	Experiment	2.25	Vertical round tube	water	A method is proposed for determining the interfacial area concentration.
Kondo et al. (2002)	Experiment	2.5	Vertical round tube	water	Bubble break-up, deformation, liquid micro jet penetration were observed.
Abdelall et al. (2005)	Experiment	1.9	Horizontal round tube	water	Pressure drop empirical correlation was proposed.
James et al. (2006)	Experiment	2.1, 1.6, 1.3	vertical round tube	white cane sugar diluted commercial sugar	Downward forces result from rapid deceleration of downward-moving liquid.
Ahmed et al. (2008)	Experiment	4.0, 2.0	Horizontal round tube	oil	Void fraction increases across the expansion, then constant. Liquid turbulence intensity is higher in the expansion.
Bhusan et al. (2009)	Experiment	2.0	Inclined rectangular channels	water	Bubble velocity in vertical pipes could not be predicted by correlations proposed for non-circular channels.
Danabalan (2012)	Experiment	1.53, 1.25	Vertical bowl cubic box	water	Rounded bowl is easier for Taylor bubble passing through the expansion.
Sadatomil et al. (2013)	Experiment	2.0	Horizontal rectangular channel	water	Local pressures upstream and downstream from the singularity were measured.
Carter et al. (2016)	Experiment	2.5	Vertical jointed tubes	water	High sensitivity method used to record the acoustic signals when bubble breakup.
Zhou (2017)	Experiment Simulation	1.72, 1.45, 1.33, 1.24, 1.12	Vertical round tubes	Glycerol-water	Bubble breakup pattern was studied.
Ambrose et al. (2017)	Simulation	2.1	vertical round tubes	water	Critical length for bubble splitting is found.
Amani et al. (2019)	Simulation	2.1	Vertical round tubes	water CarboxyMethyl Cellulose (CMC)	Flow field and bubble length are affected by the CMC content of the aquatic solution and the strength of non-Newtonian fluid rheology.

Cette thèse est accessible à l'adresse : http://theses.insa-lyon.fr/publication/2020LYSEI095/these.pdf
© [L. Guo], [2020], INSA Lyon, tous droits réservés

TABLE 2.4: Summary of the experimental/numerical studies of the Taylor bubble rising through contractions.

Published articles	Approach	Contraction ratio	Pipe direction	Liquid	Comments
Abdelall et al. (2005)	Experiment	0.53	Vertical round tube	water	Empirical correlation was developed for contraction two-phase multiplier.
Chen et al. (2009b)	Experiment	0.5, 0.33	Horizontal rectangular channels to a tube	water	A modified homogeneous correlation is proposed.
Kourakos et al. (2009)	Experiment	0.8	Horizontal round tube	water	Contractions create a high pressure drop.
Balakhrisna et al. (2010)	Experiment	0.5	Horizontal round tube	oil-water	Contraction reduces oil thickness core and decreases chances of wall fouling.
Kaushik et al. (2012)	Simulation	0.48	Horizontal round tube	oil	Asymmetric nature of velocity across the radial plane is observed in contraction.
Padilla et al. (2013)	Experiment	0.7	Horizontal round tube	HFO-1234yf, R-134a, R-410A	A method is proposed for predicting the pressure drop.
Sadatomil et al. (2013)	Experiment	0.5	Horizontal rectangular mini-channels	water	Different gas flow rate produces different behavior passing through contractions.
Kawahara et al. (2015)	Experiment Numerical	0.51, 0.35	Horizontal rectangular microchannels	water, Ethanol, HFE7200	HFE-7200 and distilled water showed higher pressure drop across sudden contraction.
Zhou (2017)	Experiment Simulation	0.93, 0.81, 0.69	Vertical round tubes	Glycerol-water	Bubble blocking pattern was studied
Sudhakar and Das (2018)	Simulation	a wide range values	rectangular channel	kerosene–water	The contraction ratio resists the Taylor droplet passing through contraction.
Qin et al. (2018)	Simulation	a wide range values	vertical round tubes	Golden syrup	Bubble in contractions is less prone to break up and with entire body rising.

Cette thèse est accessible à l'adresse : http://theses.insa-lyon.fr/publication/2020LYSEI095/these.pdf
© [L. Guo], [2020], INSA Lyon, tous droits réservés

Sadatomil et al. (2013) have studied the flow pattern for air-water two-phase flow through U-bend, sudden expansion, and sudden contraction in horizontal rectangular mini-channels. Some results of the experiments are shown in Fig. 2.14. For different gas flow rates, the gas phase presents discrepancy behavior when rising through the same contraction.

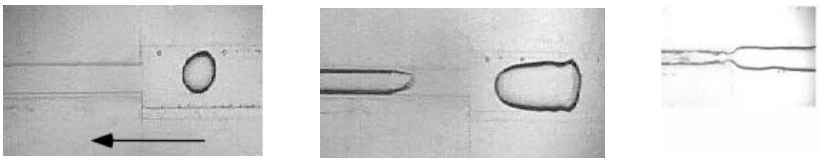

(a) j_G = 0.08 m/s (b) j_G = 0.5 m/s (c) j_G = 10 m/s

FIGURE 2.14: Typical flows in contraction channel at $J_L = 0.5$ m/s (J_L indicates the liquid velocity and J_G is gas velocity (from Sadatomil et al. (2013)).

Kawahara et al. (2015) have conducted a series of experiments to study the effect of the contraction ratios with different liquids on gas-liquid horizontal flow through a sudden contraction in micro-channel. They compared the numerical results with experiments (as shown in Fig. 2.15). The results show that the bubble is compressed by contraction and stretched into a longer bubble after contraction.

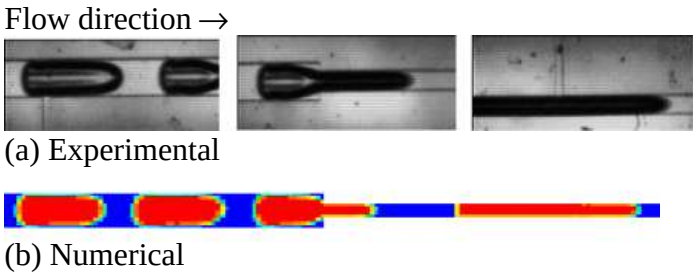

(a) Experimental

(b) Numerical

FIGURE 2.15: The comparison of experimental and numerical results for pure ethanol two-phase flow through contraction (contraction ratio is 0.51) from Kawahara et al. (2015).

Sudhakar and Das (2018) numerically studied Taylor droplets rising through sudden contractions in a rectangular channel using the lattice Boltzmann method. The interfacial droplet evolution is established using streamlines and velocity vector fields.

Qin et al. (2018) studied lava lakes with contraction geometries. In Fig. 2.16, the bubble in contractions are less prone to break up.

Cette thèse est accessible à l'adresse : http://theses.insa-lyon.fr/publication/2020LYSEI095/these.pdf
© [L. Guo], [2020], INSA Lyon, tous droits réservés

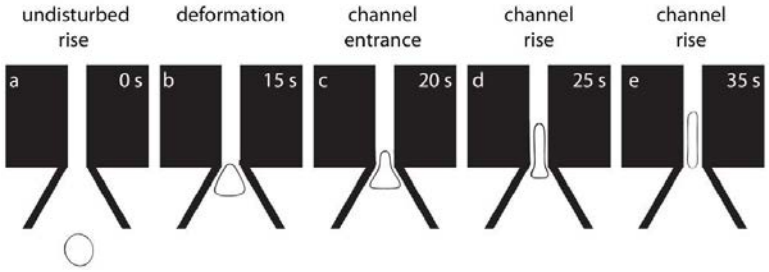

FIGURE 2.16: Video recording experiment to describe bubble rise and deformation through an inverted shallow flaring geometry (from Qin et al. (2018)).

From this literature review, we can summarize several topics about contractions.

- The experimental contraction, including horizontal or vertical all obtain the conclusion that the Taylor bubble (or slug flow) is stretched by contractions and a sudden increased pressure at contraction.
- Compared with expansions, researchers have focused more on pressure drop in contractions, which has led to a series of correlations to describe the pressure change after contraction.

2.3 Literature review for two-phase flow simulation with phase-change

When phase change occurs, mass and heat transfer across the interface needs to be considered. Phase change models usually impose additional source terms in the governing equations to balance mass, momentum, and energy at the interface. Because of the presence of interfacial mass transfer term, interface topology tends to be unstable. Therefore, mass transfer models are required to estimate the mass transfer at the interface accurately.

2.3.1 Model based on thermal equilibrium

A general phase change model is based on thermal equilibrium at the interface, leading to a set of Rankine-Hugoniot jump conditions for mass, momentum, and energy conservation. This model is widely used by many investigators to calculate the interfacial phase change (Gibou et al., 2007). In this model, heat transfer at the interface is assumed to be consumed by the latent heat of the fluid. The heat flux at the interface is estimated by Fourier's law as:

$$\dot{q} = (\lambda_l \nabla T_l - \lambda_g \nabla T_g) \cdot \mathbf{n} = \dot{m} h_{lg} \tag{2.28}$$

where $\mathbf{n}$ is the normal vector of the interface towards the opposite liquid side by convention, λ is the conductivity of fluids, $\dot{m}$ [kg/(m^2 s)] is the mass flux (counted

Cette thèse est accessible à l'adresse : http://theses.insa-lyon.fr/publication/2020LYSEI095/these.pdf
© [L. Guo], [2020], INSA Lyon, tous droits réservés

positive for evaporation) due to the phase change across the interface, h_{lg} is the latent heat. The subscript g and l denote the vapor and liquid phase, respectively.

The mass flux $\dot{m}$ is derived for the interface surface area, which is not always explicitly known. In finite volume based methods, such as the VOF method, it is more convenient to use a volumetric mass source term. The volumetric mass source term S [kg/(m^3 s)] is defined by $S_g = -S_l = \dot{m}|\nabla\alpha_l|$. α_l indicates the volume fraction of liquid. In a computational cell, with pure liquid or gas, $|\nabla\alpha|$ is zero. In a cell contains interface, this term is directly related to the interface surface,

$$\frac{1}{V}\int_{\Gamma}|\nabla\alpha_l|dA = \frac{A_\Gamma}{V}$$

where A_Γ is the interfacial area and V the cell volume.

Juric and Tryggvason (1998) simulated film boiling flow phenomenon. The mass flux is added as a delta function that is non-zero only at the interface. The equations are discretized by a finite difference method on a regular grid, and the interface is explicitly tracked by a front moving method. Welch and Wilson (2000) constructed the interface geometry associated with Young's method (Youngs, 1982), aiming to derive mass flux through calculating the discontinuous normal component of the normal vector of the heat flux vector. Esmaeeli and Tryggvason (2004a,b) used the method of Udaykumar et al. (1996) to calculate the heat source using a first-order finite difference approximation. They added mass source and heat source in governing equations to investigate the behavior of film boiling. Gibou et al. (2007) proposed a new algorithm for multiphase flows with phase change based on the sharp interface method. This algorithm uses the ghost fluid method to impose the interface boundary conditions. Akhtar and Kleis (2013) studied boiling flow simulations using adaptive octree grids. A phase change model based on the sharp interface model associated with the mixture formulation was developed.

Son et al. (1999) simplified Eq. (2.28) by assuming saturation temperature at vapor side. Therefore, they considered only the temperature gradient on the liquid side. Using $\mathbf{n} \approx \frac{\nabla\alpha}{|\nabla\alpha|}$, the volumetric mass source term then can be rewritten as

$$S_g = -S_l = \frac{\lambda_{eff}(\nabla T \cdot \nabla\alpha_l)}{h_{lg}} \tag{2.29}$$

where λ_{eff} is effective thermal conductivity and calculated as the average of the liquid and vapor phases, weighted by their respective volume fractions. Nichita and Thome (2010) and Ganapathy et al. (2013) used a similar formulation for the source term. This simplification is also used by Luo et al. (2005) to simulate multiphase incompressible flow with phase change.

However, this simplification is less accurate. For example, in film boiling, the liquid is saturated, and vapor is superheated. The bubble growth rate is not relevant to the liquid thermal conductivity λ_l in the growing process of a vapor bubble.

Cette thèse est accessible à l'adresse : http://theses.insa-lyon.fr/publication/2020LYSEI095/these.pdf
© [L. Guo], [2020], INSA Lyon, tous droits réservés

However, in Eq. (2.30), λ_{eff} contains the effect of λ_l, which not matching the physical phenomena. To overcome this problem, Sun et al. (2012) proposed an alternative simplified from based on neglect of heat conduction in the saturated phase, and linear temperature profile is in unsaturated phase, namely

$$S_g = -S_l = \frac{2\lambda_l(\nabla T \cdot \nabla \alpha_l)}{h_{lg}} \tag{2.30}$$

2.3.2 Non-equilibrium phase change models

Based on the Hertz-Knudsen equations (Knudsen and Partington, 1935), Schrage (1953) was the first to develop a mass transfer model. This model assumes vapor and liquid are saturated but allows jump conditions to occur at the interface. According to the gaseous kinetic theory, high dynamic molecules cross the interface due to the temperature deviation at the interface. A ratio of γ between numbers of molecules changing phase and transferring across the interface is defined as evaporation and condensation processes as follows:

$$\gamma_e = \frac{\text{number of molecules obtained by vapor phase}}{\text{number of molecules from liquid to vapor}} \quad \text{for evaporation} \tag{2.31}$$

$$\gamma_c = \frac{\text{number of molecules absorbed by liquid phase}}{\text{number of molecules from vapor to liquid}} \quad \text{for condensation} \tag{2.32}$$

The mass flux is determined by the deviation between vapor-liquid or liquid-vapor mass flux.

$$\dot{m} = \frac{2\gamma}{2-\gamma}\sqrt{\frac{M}{2\pi R}}\left[\frac{p_g}{\sqrt{T_{g,sat}}} - \frac{p_l}{\sqrt{T_{l,sat}}}\right] \tag{2.33}$$

where M is molecular weight, R the universal gas constant (8.314 J/(mol K)) and γ the evaporation or condensation coefficients. The coefficient γ is estimated from experimental data. Marek and Straub (2001) adopted $\gamma = 0.1$ and 1, respectively, in simulation of jets and moving films. Hardt and Wondra (2008), Kunkelmann and Stephan (2009) and Magnini and Pulvirenti (2011) recommended $\gamma = 1$ for film boiling. Kharangate et al. (2015) recommended $\gamma = 0.1$ and concluded larger γ affects numerical stability. Kartuzova and Kassemi (2011) suggested a low value of $\gamma = 0.01$ for turbulent phase change flow.

Furthermore, some researchers developed several simplified forms of this phase-change model. For example, Tanasawa (1991) assumes for a small deviation of interfacial temperature, mass flux has a linear property with temperature jump between the interface and vapor phase. This model can be written as:

$$\dot{m} = \frac{2\gamma}{2-\gamma}\sqrt{\frac{M}{2\pi R}}\frac{\rho_g h_{lg}(T - T_{sat})}{T_{sat}^{3/2}} \tag{2.34}$$

Samkhaniani and Ansari (2017) implemented this model to simulate bubble condensation in OpenFOAM. This simplified model is available for most phase-change

Cette thèse est accessible à l'adresse : http://theses.insa-lyon.fr/publication/2020LYSEI095/these.pdf
© [L. Guo], [2020], INSA Lyon, tous droits réservés

problems except for micro scales, where interfacial jump conditions need to be specially considered. Silvi et al. (2020) used Eq. (2.34) to model two-phase annular flow boiling inside a tube.

2.3.3 The Lee model

Lee (1980) proposed a simple phase-change model for studying evaporation and condensation processes. In this model, the phase change is driven by the deviation of temperature from the saturated temperature T_{sat} and the local temperature. The volumetric mass source term is given by:

$$S_g = -S_l = R_i \alpha_l \rho_l \frac{T - T_{sat}}{T_{sat}} \quad \text{for evaporation: } T > T_{sat} \tag{2.35}$$

$$S_l = -S_g = R_i \alpha_g \rho_g \frac{T - T_{sat}}{T_{sat}} \quad \text{for condensation: } T < T_{sat} \tag{2.36}$$

where R_i is an empirical value called mass transfer intensity factor with unit s^{-1}, which has different values for different phase change problems. Extremely large values of R_i result in a numerical instability, while excessively small values of R_i cause a significant deviation between interfacial temperature and saturation temperature. An optimum of R_i depends on many factors, such as mesh size, and computational time step. A wide range of R_i from 0.1 to 10^8 s^{-1} has been reported in literature. For instance, R_i is defined as 0.1 s^{-1} by some authors (Lee and Nydahl, 1989; Wu et al., 2007; De Schepper et al., 2009; Alizadehdakhel et al., 2010). However, R_i is specified as 100 s^{-1} in the work of Yang et al. (2008) and Goodson et al. (2010). Gorlé et al. (2015) gave large R_i as 5000 s^{-1} in their simulation. In turbulent flow, R_i has larger value. Da Riva et al. (2012) used R_i value from 7.5×10^5 to $5{\times}10^6$ in their study on the condensation of turbulent flow in a horizontal circular minichannel. In addition, Chen et al. (2014) eliminated T_{sat} from numerator of the source term to simplify the expression, which can be regarded as introducing a similar factor $r_i = \frac{R_i}{T_{sat}}$ in the calculation. Chen et al. (2020) proposed an expression (see Eq. (2.37)) to approximately compute the value of R_i. Using this expression, the initial guess of R_i is not needed anymore.

$$S_g = -S_l = \frac{T_{sat}}{h_{lg}(0.5 + 0.5\alpha_l)\Delta x \cdot \alpha_l \rho_l / \lambda_l} \frac{A_\Gamma}{V} \cdot \frac{\alpha_l \rho_l (T - T_{sat})}{T_{sat}} \tag{2.37}$$

By comparing with the Lee model, R_i in Eq. (2.37) can be expressed as

$$R_i = \frac{1}{\frac{(0.5+0.5\alpha_l)\Delta_x}{\lambda_l/(\rho_l cp_l \alpha_l)} \cdot \frac{h_{lg}}{cp_l T_{sat}}} \frac{A_\Gamma}{V} \tag{2.38}$$

To overcome the dependency on R_i, Rattner and Garimella (2014) proposed a phase change model that includes the computing time interval for predicting the

Cette thèse est accessible à l'adresse : http://theses.insa-lyon.fr/publication/2020LYSEI095/these.pdf
© [L. Guo], [2020], INSA Lyon, tous droits réservés

phase change amount. The volumetric heat source (Q) can be calculated using three different parts:

$$Q = \begin{cases} -\min(Q_1, Q_2, Q_3) & \text{for evaporation} \\ \min(Q_1, Q_2, Q_3) & \text{for condensation} \end{cases} \tag{2.39}$$

In Eq. (2.39), Q_1, Q_2, Q_3 are expressed by:

$$Q_1 = \frac{(\rho c_p)_{eff}(T - T_{sat})}{\Delta t}$$

$$Q_2 = \begin{cases} \dfrac{\alpha_l \rho_l h_{lg}}{\Delta t} & \text{for evaporation} \\ \dfrac{\alpha_g \rho_g h_{lg}}{\Delta t} & \text{for condensation} \end{cases}$$

$$Q_3 = \frac{h_{lg}}{\Delta t}\left(\frac{1}{\rho_g} - \frac{1}{\rho_l}\right)^{-1}$$

where c_p is the specific heat under a constant pressure condition, $(\rho c_p)_{eff}$ is an effective coefficient calculated as the average of the liquid and vapor phases, weighted by their respective volume fractions. Q_1 is defined to force the interface to the saturation temperature at every time step Δt, recovering the physical equilibrium condition. To ensure the physical results, Q_2 limits the mass flux in each time step to the mass of vapor present in that cell. Q_3 guarantees the phase change model satisfies the Courant-Friedrichs-Lewy (CFL) condition.

The mass flux can be calculated using the following equation:

$$\dot{m}_g = -\dot{m}_l = \frac{\dot{q}}{h_{lg}} \tag{2.40}$$

Pan et al. (2016) used a similar model to simulate flow boiling. However, they only considered Q_1 and neglected the other two volumetric heat sources. Kim et al. (2017) used the model (Eq. (2.39)) to compare with different phase change models and validated the models using the one-dimensional Stefan problem. Luo et al. (2020) used this model to investigate annular flow boiling in a rectangular microchannel.

Overall, the Lee model's advantages are its simplicity, and the source term field is relatively smooth. However, this model depends on the value of mass transfer intensity. It is necessary to choose the optimum amount for different studies and meshes. There is also no exact physical explanation on the mechanism of this phase change model. Unlike the models Eqs (2.28 and 2.34), which only allow mass transfer along with the interface, the Lee models allow for phase change both along with the interface and within the saturated phase (Kharangate and Mudawar, 2017). The Lee models can be widely used to simulate full-scale flow boiling and flow condensation processes, but with reduced accuracy.

Cette thèse est accessible à l'adresse : http://theses.insa-lyon.fr/publication/2020LYSEI095/these.pdf
© [L. Guo], [2020], INSA Lyon, tous droits réservés

2.3.4 Other methods to calculate mass transfer

Other methods have been used to simulate phase change. Krepper et al. (2007) proposed one simple method to compute mass flux in order to simulate subcooled boiling, as follows:

$$\begin{cases} \dot{m}_l = max\left(\dfrac{h_i(T_{sat}-T)A_\Gamma}{h_{lg}}, 0\right) & \text{for subcooled liquid} \\ \dot{m}_g = max\left(\dfrac{h_i(T-T_{sat})A_\Gamma}{h_{lg}}, 0\right) & \text{for superheated liquid} \end{cases} \tag{2.41}$$

where h_i is the heat transfer coefficient, which is calculated according to Ranz et al. (1952). Jeon et al. (2011) used the same method to study bubble condensation in subcooled boiling flow. It was found that the condensing bubble has many different aspects compared with the adiabatic bubble. In the work of Chen et al. (2009a), they applied a similar model but different in calculating mass flux, the cell temperatures near interface are used for vapor and liquid, namely $\dot{m} = \frac{h_i(T_g - T_l)A_\Gamma}{h_{lg}}$. Sun et al. (2014) computed the mass flux at the interface through the heat exported from interface and neighboring cell for the condensation process, or the heat imported in the interface and neighboring unsaturated cell for the evaporation process. Zhang et al. (2001) added a large artificial source term to the enthalpy equation to force interface temperature saturated, the heat and mass source terms are computed using the updated temperature filed.

2.3.5 Two-phase VOF method with phase change

Welch and Wilson (2000) firstly used the VOF method to simulate film boiling flow. They compared the results with Son and Dhir (1998) and Juric and Tryggvason (1998) who used different interface capturing methods, and found the results matching well. For a lower heat flux with smaller superheated temperature (T_{sup}, the difference between heated wall and saturated temperatures), the vapor bubble showed quasi-steady releasing behavior. However, when increasing the heat flux, the vapor bubble did not detach from the vapor film. Similar behavior was observed in the work of Juric and Tryggvason (1998).

Some researchers used smoothing techniques to smear mass sources to improve numerical stability. Yuan et al. (2008) used the VOF method to track the liquid-vapor interface on non-orthogonal body-fitted coordinates. Due to mass transfer at the interface, the volume expansion or contraction is moved from a mixture cell to the nearest vapor cell to overcome the discontinuous velocity field. Hardt and Wondra (2008) developed an evaporation model compatible for vapor-liquid flow. They performed numerical simulations of film boiling and droplet evaporation using the VOF method. In their method, the evaporating mass flux is calculated from Eq. (2.33). The mass source term is smeared, redistributed in some finite region around the interface,

Cette thèse est accessible à l'adresse : http://theses.insa-lyon.fr/publication/2020LYSEI095/these.pdf
© [L. Guo], [2020], INSA Lyon, tous droits réservés

smoothing out the sharp discontinuity in velocity at the interface. The most notable feature of the model is that almost any evaporation law can be implemented, the mass source terms are compatible with the VOF and the level-set method. Based on this evaporation model, Kunkelmann and Stephan (2010) developed a phase-change model combined with the algebraic VOF method in OpenFOAM and introduced a microlayer and contact angle model to simulate nucleate boiling on unstructured meshes. Magnini and Pulvirenti (2011) used a similar method to smear the mass source term into the neighbor cells, and the numerical study of vapor bubbles growing in the quiescent superheated liquid was investigated.

Sun et al. (2014) developed a phase-change model based on the VOF method in the FLUENT code. The model is suitable for the case in which one phase is unsaturated, and the other is saturated. Tsui and Lin (2013) proposed a simple interface-reconstruction scheme (CISIT) based on the VOF method. Later, they (Tsui et al., 2014) extended the method to calculate two-phase flow, including heat and mass transfer, due to phase change. They proposed an implicit way to solve the energy equation.

In the work of Fleckenstein and Bothe (2015), a numerical method is developed for multi-component mass transfer with volume effects at a moving interface. The central thought of this method is spatial averaging techniques to solve Navier-Stokes equations combined with the VOF method accounting for volume effects. The simulations proved the way could capture volume effects with the multi-components transfer. Strotos et al. (2016) studied the evaporation of suspended single or multi-component droplets using the VOF method. They estimated the local evaporation rate using Fick's law and compared the simulation results with experimental data. It was concluded the prediction of the overall evaporation rate for a wide range of cases was satisfactory. Georgoulas et al. (2017) used a VOF method to study heat transfer and phase change of bubble detachment in saturated pool boiling in OpenFOAM. The simulation results showed that the initial thermal boundary layer plays an important role in the bubble growth and detachment process. The contact angle equals 45° has a significant effect on bubble detachment behavior. Samkhaniani and Ansari (2017) implemented a method in OpenFOAM to simulate boiling and condensation based on the VOF method. He compared the models by Lee (1980), and Tanasawa (1991) and found they produced significantly different results in film boiling simulations. Moreover, the slight variation of saturation temperature was considered with the simplified Clausius-Clapeyron relation. Based on the Gerris solver (Popinet, 2013b), an open-source solver similar to Basilisk solver, Zhang and Ni (2018) developed a phase change model using the VOF method. A smoothed mass transfer rate within a narrow region surrounding the interface is adapted to decrease the pressure oscillations for large density ratios. The saturated temperature is imposed at the interface using a ghost-cell approach. Reutzsch et al. (2020) proposed a phase change model to investigate various phenomena with evaporation.

Cette thèse est accessible à l'adresse : http://theses.insa-lyon.fr/publication/2020LYSEI095/these.pdf
© [L. Guo], [2020], INSA Lyon, tous droits réservés

Malan et al. (2020) developed a phase-change model in open-source solver PARIS (Aniszewski et al., 2019). The numerical methods adopted in PARIS are similar to the Basilisk solver (Popinet, 2013a). The PLIC-VOF method is used to capture the motion of the gas-liquid interface. However, these VOF methods are developed for incompressible flows and can not, in theory, consider volume expansion/contraction due to phase change. To solve this problem, he proposed splitting the VOF advection equation into two steps using the time-fractional method. The first one is to construct an extended, divergence-free liquid velocity domain; subsequently, the interface is shifted to account for phase change. This method keeps the conservation of mass. Using this similar extended domain method, Scapin et al. (2020) investigated simulations of evaporating two-fluid flows. Unlike the method of Malan et al. (2020), they did not construct a sub-domain but constructed a divergence-free extension of the liquid velocity field onto the entire domain. In the study of Malan et al. (2020), they calculated the mass transfer rate from the temperature field. However, Scapin et al. (2020) computed mass transfer rate using diffusion of vapor mass fraction, which would be solved by a standard convection-diffusion transport equation.

Sussman and Puckett (2000) first proposed a coupled level-set and volume-of-fluid method (CLSVOF), taking advantage of both the VOF the LS methods. The basic idea of this method is using the smooth LS function to estimate curvature and surface tension while the VOF method ensures exact mass conservation. The CLSVOF method has also been applied in two-phase flow with phase change. For example, Tomar et al. (2005) used the coupled CLSVOF method to model film boiling at critical pressure for different excess temperatures in water and R134a liquid. The results showed that the bubble release frequency is higher in R134a near critical condition but reduced considerably in far critical conditions. However, they did not provide a validation case for the phase-change model. Zeng et al. (2015) simulated single bubble condensation in subcooled flow using OpenFOAM based on the CLSVOF method. The results showed that the initial bubble size, subcooling of liquid, and system pressure affect the bubble behavior. The bubble will be pierced when the subcooling and initial diameter reach a specific value at the later condensing stage. As noted in Ningegowda and Premachandran (2014), all the CLSVOF methods adopted operator split advection except Yang et al. (2006) who used a Lagrangian−Eulerian method for the advection of VOF function. Therefore, the CLSVOF is restricted to structured grids, which will require more computational time for interface reconstruction and re-initialization. Ningegowda and Premachandran (2014) developed a new CLSVOF method with multi-directional advection algorithms for the phase change problems.

Sun and Tao (2010) proposed a new coupled volume-of-fluid and level set (VOSET) method. Unlike the CLSVOF method, this method is much easier to implement because it does not need to solve the volume fraction and level set advection equations. Only the volume fraction advection equation needs to be addressed, and the level set

Cette thèse est accessible à l'adresse : http://theses.insa-lyon.fr/publication/2020LYSEI095/these.pdf
© [L. Guo], [2020], INSA Lyon, tous droits réservés

function is calculated by a simple iterative geometric operation. Ansari et al. (2016) used the VOSET method to study the bubble topology rising in a quiescent liquid for different Mo and Eo numbers. Guo et al. (2011) investigated vapor bubbles arising from a vapor film by the VOSET method. The relationship between gas/liquid velocity in interfacial cell and volume change is obtained. The discontinuity of velocity due to the difference between mass-weighted velocity and volume-weighted velocity caused by phase change is solved using this special treatment. Ling et al. (2014) performed a simulation of 2D nucleate boiling using the VOSET method. A temperature interpolation method is presented to compute the temperature field in interface cells.

TABLE 2.5: Summary of numerical simulation on film boiling flow with different interface capturing methods.

Source	Interface methods
Son and Dhir (1997)	Level-Set (LS)
Juric and Tryggvason (1998)	Front Tracking (FT)
Welch and Wilson (2000)	Volume of Fluid (VOF)
Tomar et al. (2005)	Coupled LS and VOF (CLSVOF)
Gibou et al. (2007)	LS and Ghost Fluid (GF)
Guo et al. (2011)	Volume of Fluid Level Set (VOSET)
Dong et al. (2018)	Lattice Boltzmann (LB)

2.4 Chapter conclusion

In this chapter, we have reviewed two-phase flow with a single bubble rising and Taylor bubble rising in the vertical pipe and through expansions/contractions without phase change. In addition, phase change models with interface capturing methods are reviewed. Some conclusions can be obtained from the literature review as follows:

- The single bubble rising in stagnant liquid can be investigated by experimental and numerical approaches. In experiments, the bubble shapes and velocity can be measured. In numerical simulations, several dimensionless numbers, i.e., Re, Mo, ρ_r, and μ_r, are related to describe bubble motion.

- Main features of a single Taylor bubble rising in vertical pipes are bubble velocity, bubble shape, liquid film thickness, and wall shear stress. A detailed review of these features is introduced. Taylor bubble terminal velocity is a significant parameter to describe the Taylor bubble motion in experiments and simulations. Like a single spherical bubble rising, the Taylor bubble shapes are affected by several dimensionless numbers, i.e., N_f, Eo, ρ_r, and μ_r. The influence of these dimensionless numbers will be discussed in Chapter. 4.

Cette thèse est accessible à l'adresse : http://theses.insa-lyon.fr/publication/2020LYSEI095/these.pdf
© [L. Guo], [2020], INSA Lyon, tous droits réservés

- Taylor bubble rises faster in the expansion region, and the pressure has a large change at expansion. Also, the Taylor bubble shows the breakup phenomenon at expansion, depending on the value of N_f, Eo, the expansion ratios and initial bubble length. Shear-thinning liquid decreases the pressure drop at expansion. For contractions, the pressure is decreased before the singularity. Contractions compress bubble, and the bubble length is longer after contractions. In summary, the Taylor bubble motion in expansion and contraction shows different behavior; more information will be introduced in Chapter. 4. Moreover, several different singularities will be modeled in Chapter. 5.

- Models for two-phase flow with phase change are reviewed. Three mass transfer models are identified. In this thesis, we use the VOF method to capture the interface. Therefore, we have reviewed in particular those works on two-phase flow with phase change related to the VOF method.

Cette thèse est accessible à l'adresse : http://theses.insa-lyon.fr/publication/2020LYSEI095/these.pdf
© [L. Guo], [2020], INSA Lyon, tous droits réservés

Chapter 3

Numerical methods

In this chapter, we mainly introduce the numerical methods described in the Basilisk solver to solve physical two-phase flow problems. The chapter is organized as follows. First, the VOF method is presented for capturing the gas-liquid interface. Combining with the VOF method, the implementation of the Navier-Stokes equations is then explained. In the last part, the grid structures in the Basilisk solver is introduced.

3.1 General structure of Navier-Stokes equations

3.1.1 Governing equations

The Navier-Stokes equations are used to govern the two-phase flow dynamics. The general constant temperature governing equations are based on two conservation laws: the conservation of mass and momentum. For an incompressible fluid, the Navier-Stokes equations read,

$$\nabla \cdot \mathbf{u} = 0 \tag{3.1}$$

$$\rho \left(\frac{\partial \mathbf{u}}{\partial t} + \mathbf{A} \right) = -\nabla p + \nabla \cdot (2\mu \mathbf{D}) + \mathbf{f} \tag{3.2}$$

where p is the dynamic pressure, $\mathbf{u} = (u, v, w)$ the fluid velocity, $\rho = \rho(\mathbf{x}, t)$ and $\mu = \mu(\mathbf{x}, t)$ the fluid density and dynamic viscosity, respectively. $\mathbf{A} = \mathbf{u} \cdot \nabla \mathbf{u}$ is the convection term, $\mathbf{D} = \frac{1}{2}(\nabla \mathbf{u} + \nabla \mathbf{u}^T)$ is the velocity deformation tensor and $\mathbf{f}$ denotes additional forces, such as gravity and surface tension.

3.1.2 Computational grid

When doing spatial discretization, there are three types of fields in the Basilisk solver to store variables. They can be seen as a generalization of the C programming arrays: scalars, vectors, and tensors. Scalar fields are used to store scalars in cell centers. Vector fields are a collection of D scalar fields (where D is the dimension of the spatial discretization), and tensor fields are a collection of D vector fields. When decoupling pressure and velocity in order to solve the Navier-Stokes equations, the cell face velocity needs to be used in a staggered grid system (also called MAC grid).

Cette thèse est accessible à l'adresse : http://theses.insa-lyon.fr/publication/2020LYSEI095/these.pdf
© [L. Guo], [2020], INSA Lyon, tous droits réservés

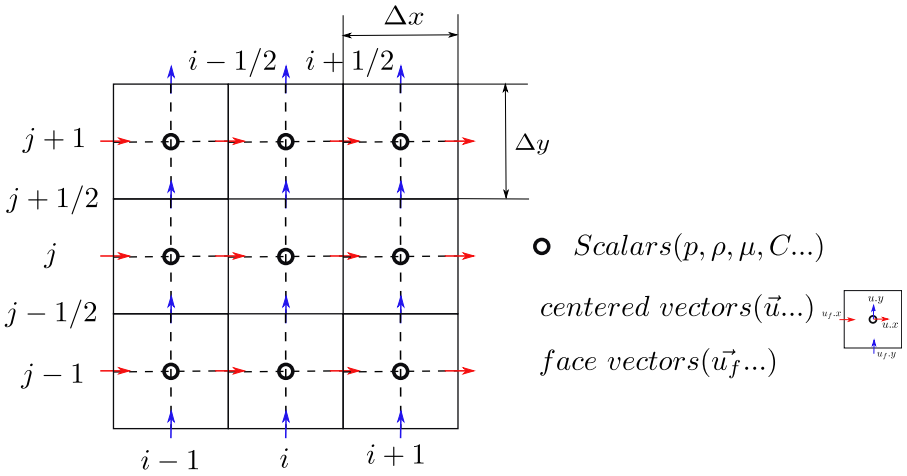

FIGURE 3.1: Staggered grid for discretized equations.

Basilisk provides support for the three most common types of staggering: centered (the default in Basilisk), face and vertex staggering. In this work, we mainly consider centered and face variables. The centered variables include scalars, centered vectors, and face variables include face vectors (see Fig. 3.1). For a random computational grid, e.g. the cell (i, j) is defined by the region composited with $[x_{i-1/2}, x_{i+1/2}]$ and $[y_{j-1/2}, y_{j+1/2}]$. The grid sizes for x-direction and y-direction are equal, which are indicated by $\Delta x = x_{i+1/2} - x_{i-1/2}$ and $\Delta y = y_{j+1/2} - y_{j-1/2}$, respectively.

3.1.3 Fluid properties

In the VOF-based methods, a general fluid property ϕ (e.g. density, viscosity) is defined by using the volume-fraction weighted average method (Puckett et al., 1997; Popinet, 2003):

$$\phi = C\phi_l + (1 - C)\phi_g \tag{3.3}$$

where ϕ_l, ϕ_g represent the physical properties for liquid and gas, respectively. C is the volume fraction of liquid in each computational grid, the details of the VOF method are introduced in Sec. 3.2.2.

3.1.4 Surface tension model

In the context of VOF method, Brackbill et al. (1992) proposed a continuum surface force (CSF) model to transfer the surface tension force throughout the fluid rather than just on the surface. The origin expression is written in the following approximation:

$$\mathbf{f}_\sigma = \sigma\kappa\delta_s\mathbf{n} \approx \sigma\kappa\nabla C \tag{3.4}$$

where the delta function indicates the surface tension force exists at the interface and zero elsewhere. $\kappa = \nabla \cdot \mathbf{n}$ is the interface curvature and the interface normal vector $\mathbf{n}$ can be expressed as $\mathbf{n} = \frac{\nabla C}{|\nabla C|}$.

Cette thèse est accessible à l'adresse : http://theses.insa-lyon.fr/publication/2020LYSEI095/these.pdf
© [L. Guo], [2020], INSA Lyon, tous droits réservés

The CSF model is extensively used in interfacial flows, particularly combined with the VOF method (Kothe et al., 1996; Lörstad et al., 2004; Renardy and Renardy, 2002) and the level-set (Kang et al., 2000; Sussman, 2003). In this work, we keep the surface tension constant.

Height function

An accurate estimation of interface curvature is essential for calculating deformable interface. The interface curvature is estimated by using the height function method in the Basilisk solver. The standard height function method described in Sussman and Ohta (2007) can be summarized as:

1). The height function orientation is determined by the optimal interface normal.

2). Sum the volume fractions in each column of the stencil to calculate the interface height, $y = h(x)$ or $x = h(y)$.

3). The finite-difference method is used to differentiate the interface normal vector to compute the interface curvature, the final formation of curvature is written as follows:

$$\begin{aligned} \mathbf{n} &= \left.\frac{1}{(1+h')^{1/2}}\right|_{x=0} \\ \kappa = \nabla \cdot \mathbf{n} &= \frac{h''}{(1+h'^2)^{3/2}} \end{aligned} \tag{3.5}$$

3.1.5 General Chorin's projection method

The pressure and velocity are coupled in Eq. (3.2). It is difficult to solve the pressure and velocity simultaneously in a non-linear equation. However, for an incompressible flow, during one timestep, the pressure must be adjusted to form a divergence-free velocity field. In order to solve this problem, some investigators solve the governing equations by a so-called projection method (Chorin, 1968, 1969). The main idea of this method is to decouple the velocity and pressure by the Helmholtz decomposition, which splits the velocity field into solenoidal and irrotational components.

The Chorin's projection method consists of two main stages. In the first stage, an intermediate velocity ($\mathbf{u}^*$) is calculated, which does not satisfy the incompressible assumption. In the second stage, the pressure field at the next time step (p^{n+1}) is solved based on the fluid incompressibility, and the intermediate velocity is projected onto a divergence-free field to calculate the updated velocity ($\mathbf{u}^{n+1}$). To clarify the description, the Navier-Stokes equation (3.1) and (3.2) are simplified as follows:

$$\nabla \cdot \mathbf{u} = 0 \tag{3.6}$$

Cette thèse est accessible à l'adresse : http://theses.insa-lyon.fr/publication/2020LYSEI095/these.pdf
© [L. Guo], [2020], INSA Lyon, tous droits réservés

$$\frac{\partial \mathbf{u}}{\partial t} + \mathbf{A} = -\frac{1}{\rho}\nabla p + \epsilon \nabla^2 \mathbf{u} + \mathbf{f} \tag{3.7}$$

where $\epsilon = \mu/\rho$.

The mathematical procedure of projection method is illustrated below. First, the pressure term is dropped from Eq. (3.7) to predict the intermediate velocity $\mathbf{u}^*$.

$$\frac{\mathbf{u}^* - \mathbf{u}^n}{\Delta t} + A^n = \epsilon \nabla^2 \mathbf{u}^n \tag{3.8}$$

The next step uses $\mathbf{u}^*$ to obtain a new pressure. Using the divergence-free property of new velocity, the Poisson equation provides an available route to solve the updated pressure. Then, the new velocity filed $\mathbf{u}^{n+1}$ can be obtained by back-substituting p^{n+1} and $\mathbf{u}^*$ in Eq. (3.9).

$$\begin{aligned} \mathbf{u}^{n+1} &= \mathbf{u}^* - \frac{\Delta t}{\rho}\nabla p^{n+1} \\ \nabla \cdot \mathbf{u}^{n+1} &= 0 \\ \nabla^2 p^{n+1} &= \frac{\rho}{\Delta t}\nabla \cdot \mathbf{u}^* \end{aligned} \tag{3.9}$$

3.2 The interface tracking method

Considering the properties of immiscible two-phase flows, an import issue is how to capture the interface accurately. In this section, we briefly introduce some numerical methods to describe and track the interface. Moreover, the VOF method is illustrated in detail, in particular the interface reconstruction and interface advection.

3.2.1 Interface tracking and capturing methods – a brief introduction

Investigators have proposed some related moving interface methods. These methods can be classified into three main groups: the marker particle method (MPM), the front tracking method (FTM), and the interface capturing method (ICM).

The MPM has been studied in two-phase flow by (Welch, 1968; Rider and Kothe, 1995). The idea of this method is to view the instantaneous positions of the marker particles, and track the fluid properties related to solve the Navier-Stokes equations. The MPM is an accurate and robust method to predict the moving interface. However, due to a large number of particles, this method is costly for computation, especially for 3D cases. Moreover, The MPM has difficulties in simulating complex interface changing, such as interface stretches, shrinks, or break up (van Sint Annaland et al. (2005)).

The most famous FTM is developed by Unverdi and Tryggvason (1992). The basic idea of this method is using massless marker particles moving with liquid velocity to describe the interface. The marker particles are connected to a set of interface points (see Fig. 3.2) and these particles are advected in a Lagrangian manner. The method

Cette thèse est accessible à l'adresse : http://theses.insa-lyon.fr/publication/2020LYSEI095/these.pdf
© [L. Guo], [2020], INSA Lyon, tous droits réservés

depends on the distance between particles, i.e., the interface is not accurate if the distance is far or close. Therefore, it is a challenge to specify the particles automatically. Moreover, for the coalescence or breakup of the interface, the FTM requires a proper sub-grid model (Tryggvason et al., 2001).

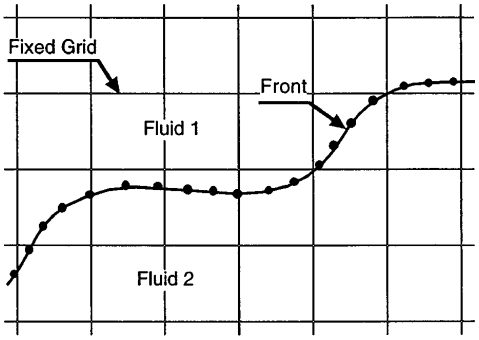

FIGURE 3.2: The schematic diagram of interface indicated by FTM, the governing equations are solved on fixed grid but the interface tracked by moving marker points (adopted from Tryggvason et al. (2001)).

The ICM are based on Eulerian approaches. The most popular ICM is the level-set method and the volume of fluid method (VOF). The level-set method is first introduced by Osher and Sethian (1988) and utilizes a smooth function $\phi(\mathbf{x}, t)$ to define a set of points with the same constant distance value. Therefore, a signed function is generated to indicate the minimum distance point from $\mathbf{x}$ to the interface. The liquid-gas interface is always set to be zero. For example, as shown in Fig. 3.3, the interface is represented by $\phi = 0$. The region for gas or liquid is dependent on the value of ϕ. The following equation governs the evolution of the level-set function:

$$\frac{\partial \phi}{\partial t} + \mathbf{u} \cdot \nabla \phi = 0 \tag{3.10}$$

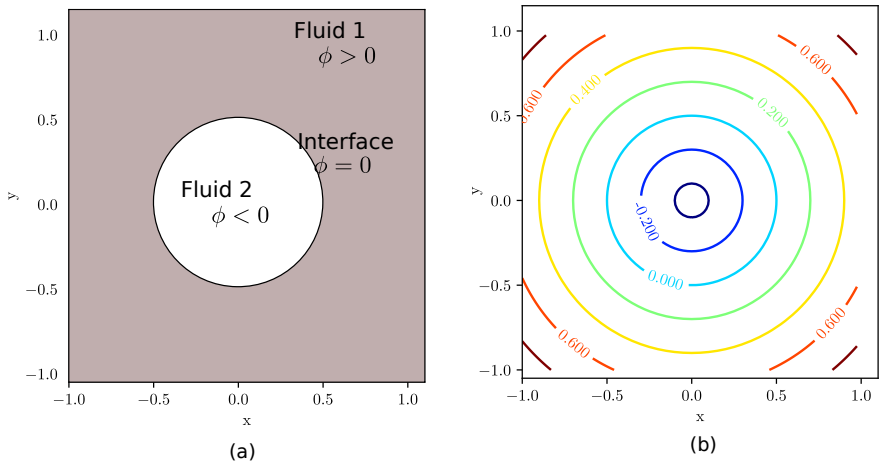

FIGURE 3.3: Level-set method; (a) interface representation; (b) level-set contours for a circular bubble initialized at $(x = 0.5, y = 0.5)$ with 0.5 radius.

Cette thèse est accessible à l'adresse : http://theses.insa-lyon.fr/publication/2020LYSEI095/these.pdf
© [L. Guo], [2020], INSA Lyon, tous droits réservés

The geometrical properties are easily obtained from the level-set function. A smoothing method for large density and viscosity ratios was proposed by Sussman et al. (1998). However, one drawback of the level-set method is the numerical solution in Eq. (3.10) can not guarantee the mass conservation.

3.2.2 The VOF method

The VOF method was initially proposed by Hirt and Nichols (1981), and was designed for two or more immiscible fluids where the interface exists and deforms. In the VOF method, an indicator function, representing the volume fraction of the reference fluid in each computational cell, is employed to capture the interface. The equation for transporting the indicator function is similar to the level-set function. The VOF method is flexible, robust, and has good advantages to handle fragmentation and coalescence without special treatment. For physical problems with deforming geometrical interface, the VOF method is well suited to capture the interface.

The VOF method is based on the Eulerian method which needs to define a function $C(\mathbf{x}, t)$ to indicate the volume fraction value from 0 to 1. $C = 1$ means the computational cell is filled with reference fluid, and $C = 0$ for the other fluid. When C is between 0 and 1, it shows the presence of the interface in the cell. In the two-phase flow model, we assume the computational domain is Ω, and Ω_1 is the reference fluid, Ω_2 is the other fluid. The diagram of the computational domain is shown in Fig. 3.4. $C(\mathbf{x}, t)$ is expressed as:

$$C(\mathbf{x}, t) = \begin{cases} 1 & \text{for } \mathbf{x} \in \Omega_1 \\ (0, 1) & \text{for interfacial region} \\ 0 & \text{for } \mathbf{x} \in \Omega_2 \end{cases} \tag{3.11}$$

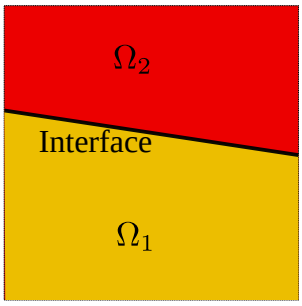

FIGURE 3.4: The schematic diagram of the computational domain.

For immiscible two-phase flow without phase-change, C should satisfy the characteristic of fluid in Lagrangian reference system, therefore we can write the transport equation for C:

$$\frac{\partial C}{\partial t} + \mathbf{u} \cdot \nabla C = 0 \tag{3.12}$$

Cette thèse est accessible à l'adresse : http://theses.insa-lyon.fr/publication/2020LYSEI095/these.pdf
© [L. Guo], [2020], INSA Lyon, tous droits réservés

With the incompressible flow property $\nabla \cdot \mathbf{u} = 0$, further equation form is written:

$$\frac{\partial C}{\partial t} + \nabla \cdot (\mathbf{u}C) = 0 \tag{3.13}$$

There are two different approaches to compute the evolution of C. The first one uses so-called compressive schemes to solve the Eq. (3.13), which does not need to reconstruct the interface. The approach is based on the donor-acceptor scheme by Hirt and Nichols (1981). The second is the geometric VOF method, which reconstructs the volume fraction in each computational cell and then solves the VOF equation to get the new volume fraction value. Basilisk solver utilizes the geometric VOF method, therefore, we mainly introduce this method in the following parts. The geometric VOF schemes classically contain two steps:

- Interface reconstruction
- Interface advection

Interface reconstruction

We consider a computational cell with Cartesian coordinates (x, y) in Fig. 3.5. The piecewise linear interface calculation (PLIC) method is used to approximate the interface line by a linear equation with local normal vector $\mathbf{m}$. The interface line can be defined by the Hesse normal form:

$$\mathbf{m} \cdot \mathbf{x} = \alpha \tag{3.14}$$

where the vector, $\mathbf{m} = (m_x, m_y)$, is normal to the interface and the direction is opposite to the reference fluid by convention. α is the line constant linked to the smallest distance from the interface line to the origin position of the cell (Scardovelli and Zaleski, 2000).

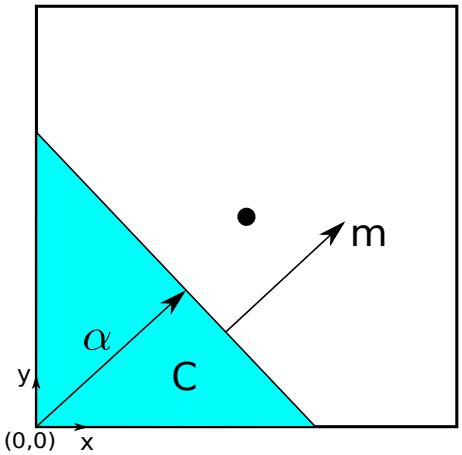

FIGURE 3.5: 3×3 stencil for calculating interface normal.

Cette thèse est accessible à l'adresse : http://theses.insa-lyon.fr/publication/2020LYSEI095/these.pdf
© [L. Guo], [2020], INSA Lyon, tous droits réservés

In general, the interface reconstruction problem is distinguished by the "forward" and "inverse" problem (Scardovelli and Zaleski, 2000). The "forward" problem is to calculate C with $\mathbf{m}$ and α, which can be expressed by a function $C = f(\mathbf{m}, \alpha)$. As stated above, the problem is geometric, which uses several extensively *if-elseif-endif* structures in the programming (Wu and Dhir, 2010). The "inverse" problem consists of finding α by giving $\mathbf{m}$ and C, which uses a function $\alpha = f(C, \mathbf{m})$. The details of "forward" and "inverse" problems can be found in the Appendix. A.

In order to investigate the problem in details, the determination of the constant parameters (m_x, m_y, α) can be implemented by a three-step procedure:

- Evaluation of the interface normal vector $\mathbf{m} = (m_x, m_y)$.
- Computation of volume fraction C based on the known $\mathbf{m}$ and α.
- Computation of constant distance α based on the known $\mathbf{m}$ and C.

Evaluation of the interface normal

From the above procedure, the first step for interface reconstruction is to determine the interface normal vector $\mathbf{m}$, which is necessary for both "forward" and "inverse" problem. Usually, in the VOF/PLIC reconstruction, $\mathbf{m}$ is determined by the gradient of volume fraction $\mathbf{m} = -\nabla C$ and several methods have been introduced in Rider and Kothe (1998) and Pilliod Jr and Puckett (2004). In what follows, we quickly introduce some classical schemes to compute interface normal vector. Before doing this, we assume the equilateral Cartesian grid, namely the grid size $\Delta x = \Delta y = h$.

Mixed Youngs-Centered (MYC) method

Basilisk adopts a method combining Youngs' scheme (Youngs, 1982) and the Centered Columns scheme. For a low grid resolution, it computes the interface normal vector with Youngs' method. It uses the Centered Columns scheme for high resolution because of its good behavior.

Youngs' scheme

Youngs (1982) proposed a method to evaluate the interface normal from the gradient of C, namely $\mathbf{m} = -\nabla C$ by means of finite-difference approximations. As shown in Fig. 3.6, ∇C in the cell center (i, j) is computed from the average of four cell-corner values in one cell.

Cette thèse est accessible à l'adresse : http://theses.insa-lyon.fr/publication/2020LYSEI095/these.pdf
© [L. Guo], [2020], INSA Lyon, tous droits réservés

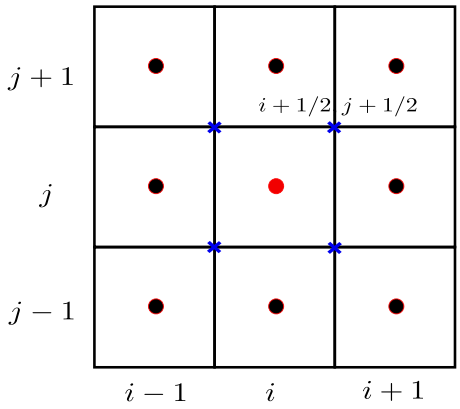

FIGURE 3.6: 3×3 stencil for calculating interface normal.

$$\mathbf{m}_{i,j} = \frac{1}{4}\left(\mathbf{m}_{i+1/2,j+1/2} + \mathbf{m}_{i-1/2,j+1/2} + \mathbf{m}_{i+1/2,j-1/2} + \mathbf{m}_{i-1/2,j-1/2}\right) \tag{3.15}$$

At the vertex $(i+1/2, j+1/2)$, $\mathbf{m}_{i+1/2,j+1/2}$ can be expressed by components of each coordinates, namely $\mathbf{m}_{i+1/2,j+1/2} = (m^x_{i+1/2,j+1/2}, m^y_{i+1/2,j+1/2})$. For the other three vertex points, we use a similar method.

$$m^x_{i+1/2,j+1/2} = \frac{\overline{C}_{i+1/2,j} - \overline{C}_{i+1/2,j+1}}{h} \tag{3.16}$$

$$m^y_{i+1/2,j+1/2} = \frac{\bar{C}_{i,j+1/2} - \bar{C}_{i+1,j+1/2}}{h} \tag{3.17}$$

where,

$$\begin{cases} \overline{C}_{i+1/2,j} = \frac{C_{i,j}+C_{i+1,j}}{2} \\ \overline{C}_{i+1/2,j+1} = \frac{C_{i,j+1}+C_{i+1,j+1}}{2} \\ \overline{C}_{i,j+1/2} = \frac{C_{i,j}+C_{i,j+1}}{2} \\ \overline{C}_{i+1,j+1/2} = \frac{C_{i+1,j}+C_{i+1,j+1}}{2} \end{cases} \tag{3.18}$$

Centered columns scheme

However, Young's method makes it difficult to obtain accurate linear interfaces. Based on Young's method, some investigators (Aulisa et al., 2007; Popinet, 2009) used a different method called *centered columns scheme*. In this approach, the volume fraction values in 3×3 stencil can be added along the vertical and horizontal direction. The interface is defined as local height function or local width function of the interface, $y = f(x)$ or $x = g(y)$ as schematically shown in Fig. 3.7.

In Fig. 3.7 (a), y_{i+1} is indicated by $y_{i+1} = h\sum_{k=-1}^{1} C_{i+1,j+k}$. The linear interface function $y = f(x)$ in the cell center of the stencil can be described as

$$sgn(m_y)y = m_x x + \alpha \tag{3.19}$$

Cette thèse est accessible à l'adresse : http://theses.insa-lyon.fr/publication/2020LYSEI095/these.pdf
© [L. Guo], [2020], INSA Lyon, tous droits réservés

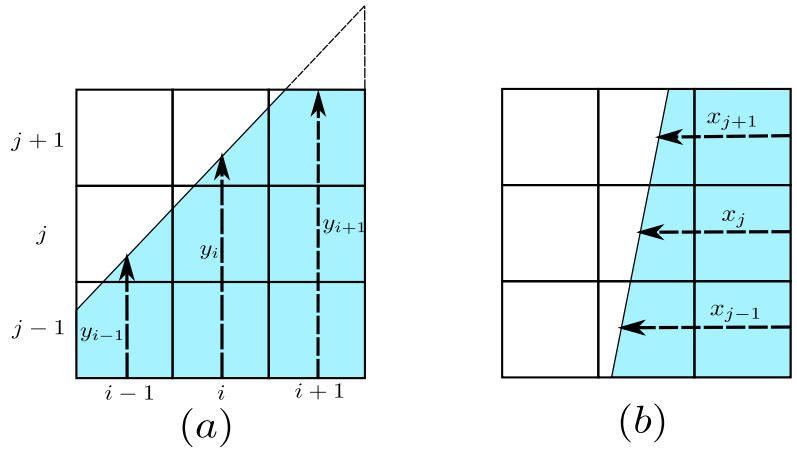

FIGURE 3.7: Calculating volume fraction from column-wise and row-wise to compute the slope of a linear interface (Wu and Young, 2013; Aulisa et al., 2007)

.

The sign and angular coefficient m_x is defined by three types of finite differences, which are backward (m_x^b), forward (m_x^f), and central (m_x^c) schemes, respectively. The demonstrations of these three finite-difference schemes are described as follows:

$$m_x^b = \frac{y_i - y_{i-1}}{h} \tag{3.20}$$

$$m_x^f = \frac{y_{i+1} - y_i}{h} \tag{3.21}$$

$$m_x^c = \frac{y_{i+1} - y_{i-1}}{2h} = \frac{1}{2h} \sum_{k=-1}^{1} (C_{i+1,j+k} - C_{i-1,j+k}) \tag{3.22}$$

It should be noted in Fig. 3.7 (a), the interface cuts the two neighboring sides of the column, where the two local heights y_{i-1} and y_i are on the interface with backward finite difference $m_x = m_x^b$. However, in column $(i+1)$, the interface intersects with an extended length of cell side. Therefore, the height is not on the interface, but outside the prospected area. It forms a small missing area outside of the block of the cell, and the forward and central finite-difference scheme would underestimate the coefficient m_x. Therefore, we need to select one of them as the slope of the linear interface by following simple criterion (Wu and Young, 2013).

$$|m_x| = \max(|m_x^b|, |m_x^c|, |m_x^f|) \tag{3.23}$$

where the absolute values are required to circumvent the negative values of the angular coefficients.

We use a similar approach to obtain the optimum value for the local width function of the linear interface on the slope of m_y. As shown in Fig. 3.7 (b), a little difference between height and width cases is for the latter one, there is no missing area

Cette thèse est accessible à l'adresse : http://theses.insa-lyon.fr/publication/2020LYSEI095/these.pdf
© [L. Guo], [2020], INSA Lyon, tous droits réservés

outside of the proper area, so we select one of normal values from 3 schemes for the case of $x = g(y)$.

$$|m_y| = \max(|m_y^f|, |m_y^c|, |m_y^b|) \tag{3.24}$$

In the case of Fig. 3.7 (b), we calculate the interface slope accurately. If not using $sgn(m_x)x = m_y y + \alpha$, but $sgn(m_y)y = m_x x + \alpha$, m_x would be larger than previous one and this value is not correct. So we should give a second criterion to distinguish the best interface line slope from the above two interface slope values.

$$|m^*| = \min(|m_x|, |m_y|) \tag{3.25}$$

In this way, if the interface orients as shown in Fig. 3.7 (a), we adopt m_x as the real slope of the interface and m_y for the interface orients in Fig. 3.7 (b). However, it should be noted that the above criteria optimization of reconstruction of the linear interface may not obtain the optimum value in the case of curved interface. For example, in Fig. 3.8, the interface $y = f(x)$ at (i, j) has the best approximation of $m_x^c = 0$. However, according to the Eq. (3.24), this would not be the optical value for m_x. Nevertheless, the two criteria can get the better guess of interface normal estimation (Wu and Young, 2013; Aulisa et al., 2007).

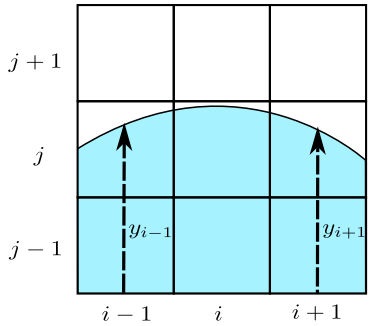

FIGURE 3.8: Special case for calculating the interface slope.

Interface advection

After interface reconstruction step, the interface is advected by Eq. (3.26) using a conservative, non-diffusive geometric VOF scheme.

$$\frac{\partial C}{\partial t} + \nabla \cdot (\mathbf{u}C) = C\nabla \cdot \mathbf{u} \tag{3.26}$$

In Eq. (3.26), the second term on the left-hand side represents the net reference phase flux through the interface (Aulisa et al., 2007), this term in the grid cell is expressed by the portion of the area of grid cut by the reconstructed interface and is computed by analytical expressions (Scardovelli and Zaleski, 2000). Although the Eq. (3.26) is conservative, it is not trivial to obtain the total volume of the reference

Cette thèse est accessible à l'adresse : http://theses.insa-lyon.fr/publication/2020LYSEI095/these.pdf
© [L. Guo], [2020], INSA Lyon, tous droits réservés

fluid. The primary problem resides in the fact that many finite-difference schemes would overestimate or underestimate C, which leads to loss of conservation properties. In order to update the volume fraction C at the next discrete time, either splitting methods (one-dimensional) (Puckett et al., 1997) or un-splitting methods (multi-dimensional) have been considered. Because of the complexity and non-trivial of un-splitting methods, Basilisk adopts splitting operator methods to capture the interface. Therefore, in the following sections, we mainly introduce a geometrical splitting method that are conservative and consistent to capture the interface ($0 < C < 1$).

General conservative split-direction advection

In this section, a conservative splitting method (Puckett et al., 1997) for solving Eq. (3.26) is implemented on a 2D Cartesian grid system by the following equations:

- For the x direction:

$$\frac{C^*_{i,j} - C^{n-1/2}_{i,j}}{\Delta t} = C^*_{i,j}\frac{u^n_{i+1/2,j} - u^n_{i-1/2,j}}{\Delta x} - \frac{F^n_{i+1/2,j} - F^n_{i-1/2,j}}{\Delta x} \tag{3.27}$$

- For the y direction:

$$\frac{C^{n+1/2}_{i,j} - C^*_{i,j}}{\Delta t} = C^*_{i,j}\frac{v^n_{i,j+1/2} - v^n_{i,j-1/2}}{\Delta y} - \frac{G^n_{i,j+1/2} - G^n_{i,j-1/2}}{\Delta y} \tag{3.28}$$

The combination of Eqs. (3.27) and (3.28) leads to:

$$C^*_{i,j} = \frac{C^{n-1/2}_{i,j} + \frac{\Delta t}{\Delta x}(F^n_{i-1/2,j} - F^n_{i+1/2,j})}{1 - \frac{\Delta t}{\Delta x}(u^n_{i+1/2,j} - u^n_{i-1/2,j})} \tag{3.29}$$

$$C^{n+1/2}_{i,j} = C^*_{i,j}\left(1 + \frac{\Delta t}{\Delta y}(v^n_{i,j+1/2} - v^n_{i,j-1/2})\right) - \frac{\Delta t}{\Delta y}(G^n_{i,j+1/2} - G^n_{i,j-1/2}) \tag{3.30}$$

where C^* denotes the temporary volume fraction after discretization of x direction. F and G are the volume fluxes across the cell faces in the x and y directions. n is time step. It should be noted this is a numerical approximation expression of Eq. (3.26).

The first term on the right-hand side named "compression" disappears for incompressible flow, while we keep it here because of doing a mass conservative method (Fuster et al., 2018). The operator splitting method is second-order accuracy in time by using Strang-splitting. Nevertheless, it is still possible to get non-physical values for the update volume fraction $C^{n+1}_{i,j}$. To solve the problem including arbitrary addition and removal of the mass, it is necessary to compute the geometric volume flux $F_{i+1/2,j}$ and $G_{i,j+1/2}$. The details of this part is refereed to Popinet (2009).

Cette thèse est accessible à l'adresse : http://theses.insa-lyon.fr/publication/2020LYSEI095/these.pdf
© [L. Guo], [2020], INSA Lyon, tous droits réservés

Weymouth and Yue advection

The Basilisk solver adopts the slightly different mass-conservative method proposed by Weymouth and Yue (2010). In this method, the conservative and consistent flux splitting equations are written as:

$$\frac{C^{*}_{i,j} - C^{n-1/2}_{i,j}}{\Delta t} + \frac{F^{n}_{i+1/2,j} - F^{n}_{i-1/2,j}}{\Delta x} = h^{n-1/2}_{i,j} \frac{u^{n}_{i+1/2,j} - u^{n}_{i-1/2,j}}{\Delta x} \tag{3.31}$$

$$\frac{C^{n+1/2}_{i,j} - C^{*}_{i,j}}{\Delta t} + \frac{G^{n}_{i,j+1/2} - G^{n}_{i,j-1/2}}{\Delta y} = h^{n-1/2}_{i,j} \frac{v^{n}_{i,j+1/2} - v^{n}_{i,j-1/2}}{\Delta y} \tag{3.32}$$

where $h^{n}_{i,j}$ is the characteristic function defined as

$$h^{n-1/2}_{i,j} = H(C^{n-1/2}_{i,j} - 1/2) \tag{3.33}$$

wherein H is Heaviside function, which means $h^{n-1/2}_{i,j} = 1$ if $C^{n-1/2}_{i,j} > 1/2$ and $h^{n-1/2}_{i,j} = 0$ if $C^{n-1/2}_{i,j} < 1/2$. Eq. (3.31) and Eq. (3.32) are explicit schemes for solving multi-dimensional direction of interface advection. It should be noted that there is no cell compression or expansion in this method. The update value of the volume fraction is performed as

$$C^{*}_{i,j} = C^{n-1/2}_{i,j} + (\Delta t/\Delta x)\left[F^{n}_{i-1/2,j} - F^{n}_{i+1/2,j} + h^{n-1/2}_{i,j}(u^{n}_{i+1/2,j} - u^{n}_{i-1/2,j})\right] \tag{3.34}$$

$$C^{n+1/2}_{i,j} = C^{*}_{i,j} + (\Delta t/\Delta y)\left[G^{n}_{i,j-1/2} - G^{n}_{i,j+1/2} + h^{n-1/2}_{i,j}(v^{n}_{i,j+1/2} - v^{n}_{i,j-1/2})\right] \tag{3.35}$$

3.3 Implementation of Navier-Stokes equations

Bell et al. (1989) introduced a projection method to solve the Navier-Stokes equations based on Chorin's projection method. The BCG scheme has a second-order temporal discretization, which is different from Chorin's projection method. The Basilisk solver uses the BCG scheme to solve incompressible Navier-Stokes equations. In this section, this method is introduced by solving the convection term, viscous term, and the fully time-marching scheme for the Navier-Stokes equations.

3.3.1 Advection scheme

Convection scheme

Under the condition of incompressibility assumption, the convection term can be expressed as $[\mathbf{u} \cdot \nabla \mathbf{u}]^{n+1/2}$. Bell et al. (1989) solved the convection term based on the

Cette thèse est accessible à l'adresse : http://theses.insa-lyon.fr/publication/2020LYSEI095/these.pdf
© [L. Guo], [2020], INSA Lyon, tous droits réservés

construction of unsplit, second-order Godunov methods proposed by Colella (1990) and Vanleer (1983). Unlike conventional upwind differencing methods, these methods propagate the information along with characteristics to couple the spatial and temporal discretization, leading to a robust higher-order discretization and better phase-error. This algorithm has three main steps, namely, data reconstruction, characteristic extrapolation, and flux computation.

- **Data reconstruction**: In this step, we compute the linear profile in each cell, as expressed in Eq. (3.36). Limiter methods based on Godunov methods are used to limit the centered slopes from introducing maxima and minima in the velocity field. For example, the velocities at right and left boundaries (see Fig. 3.9) of the cell are obtained in x direction by Eq. (3.37).

$$u_x \approx \frac{\Delta_x u}{\Delta x} \tag{3.36}$$

$$\begin{aligned} u^R_{i-1/2,j} &= u_{i,j} - \phi(r_{i,j})\frac{u_{i+1,j} - u_{i-1,j}}{2} \\ u^L_{i+1/2,j} &= u_{i,j} + \phi(r_{i,j})\frac{u_{i+1,j} - u_{i-1,j}}{2} \end{aligned} \tag{3.37}$$

where $\phi(r_{i,j})$ is the slope limiter and $r_{i,j}$ is expressed as $r_{i,j} = \frac{\Delta u_{i+1/2}}{\Delta u_{i-1/2}} = \frac{u_{i+1,j}-u_{i-1,j}}{2(u_{i,j}-u_{i-1,j})}$. Here to simplify the analysis, we use several simple symbols $a_1 = u_{i+1,j} - u_{i,j}, a_2 = \frac{u_{i+1,j}-u_{i-1,j}}{2}, a_3 = u_i - u_{i-1,j}$. With the constraint of cell edge velocity in maximum and minimum velocity field and also the self-constraint of slope limiter, the slope approximation $\Delta_x u$ as

$$\Delta_x u = \begin{cases} min(a_1, a_3), & \text{if } a_2 \leq a_3 \text{ and } u_{i-1,j} \leq u_{i,j} \leq u_{i+1,j} \\ max(a_1, a_3), & \text{if } a_2 \geq a_3 \text{ and } u_{i-1,j} \geq u_{i,j} \geq u_{i+1,j} \\ 0, & \text{otherwise} \end{cases} \tag{3.38}$$

We get minmod limiter when $\phi(r_{i,j}) = 1$, which is the most dissipative scheme. The least dissipative scheme called superbee limiter is derived when $\phi(r_{i,j}) = 2$.

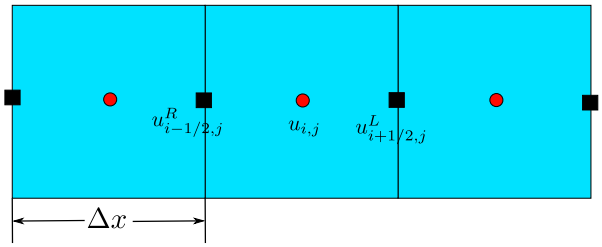

FIGURE 3.9: Control volume description in one dimension.

Cette thèse est accessible à l'adresse : http://theses.insa-lyon.fr/publication/2020LYSEI095/these.pdf
© [L. Guo], [2020], INSA Lyon, tous droits réservés

- **Characteristic extrapolation**: The boundary-extrapolated $\mathbf{u}^{n+1/2}$ is evaluated using simple Taylor series expansion to second order accuracy at $t^{n+1/2}$.

$$\mathbf{u}_{i-1/2,j}^{n+1/2,R} = \mathbf{u}_{i-1/2,j}^{n,R} + \frac{\Delta t}{2}(\mathbf{u}_t)_{i,j} \tag{3.39a}$$

$$\mathbf{u}_{i+1/2,j}^{n+1/2,L} = \mathbf{u}_{i+1/2,j}^{n,L} + \frac{\Delta t}{2}(\mathbf{u}_t)_{i,j} \tag{3.39b}$$

$$\mathbf{u}_{i,j+1/2}^{n+1/2,B} = \mathbf{u}_{i,j+1/2}^{n,B} + \frac{\Delta t}{2}(\mathbf{u}_t)_{i,j} \tag{3.39c}$$

$$\mathbf{u}_{i,j-1/2}^{n+1/2,T} = \mathbf{u}_{i,j-1/2}^{n,T} + \frac{\Delta t}{2}(\mathbf{u}_t)_{i,j} \tag{3.39d}$$

where $\mathbf{u}_{i-1/2,j}^{n,R} = \mathbf{u}_{i,j}^{n} - \frac{\Delta x}{2}(\mathbf{u}_x)_{i,j}$ other boundary velocity vectors can use similar formula. The cell boundary velocities like $\mathbf{u}_{i-1/2,j}^{n,R}$ are calculated using limited slopes performed in reconstruction step. While the expression for $\mathbf{u}_t$ uses differential equations to express the time derivatives in term of spatial derivatives using current pressure to estimate the projection influence; i.e.,

$$\mathbf{u}_t = \mathbf{P}\begin{pmatrix} \epsilon\nabla^2 u - uu_x - vu_y \\ \epsilon\nabla^2 v - uv_x - vv_y \end{pmatrix} \approx \begin{pmatrix} \epsilon\nabla^2 u - uu_x - vu_y \\ \epsilon\nabla^2 v - uv_x - vv_y \end{pmatrix} - \begin{pmatrix} p_x^{n-1/2} \\ p_y^{n-1/2} \end{pmatrix} \tag{3.40}$$

$\mathbf{P}$ is the orthogonal projection to project one vector onto the divergence-free field, which transfers the Eq. (3.7) into the incompressible Euler equation. The derivatives normal to the cell edge ($(u_x)_{i,j}$) are evaluated using limited slopes, whereas the transverse derivatives ($(u_y)_{i,j}$) are treated as upwind scheme due to the stability reasons (Colella, 1990).

$$(u_y)_{i,j} = \begin{cases} \dfrac{u_{i,j} - u_{i,j-1}}{\Delta y} + \dfrac{1}{2}\left(1 - \dfrac{\Delta t v_{i,j}}{\Delta y}\right)\dfrac{(\Delta_y u)_{i,j} - (\Delta_y u)_{i,j-1}}{\Delta y}, & \text{if } v_{i,j} \geq 0 \\ \dfrac{u_{i,j+1} - u_{i,j}}{\Delta y} + \dfrac{1}{2}\left(1 - \dfrac{\Delta t v_{i,j}}{\Delta y}\right)\dfrac{(\Delta_y u)_{i,j+1} - (\Delta_y u)_{i,j}}{\Delta y}, & \text{if } v_{i,j} < 0 \end{cases} \tag{3.41}$$

the two first order derivative in Eq. (3.40) corresponds to left-right and top-bottom cell edges, respectively.

- **Flux computation**: With the constraint of incompressibility, the convection term $\mathbf{A}^{n+1/2}$ in Eq. (3.2) can be rewritten as $\mathbf{u}\cdot\nabla\mathbf{u} = \nabla\cdot(\mathbf{u}\otimes\mathbf{u})$. However, this relationship is not available at $t^{n+1/2}$ due to the projection approximation in Eq. (3.40) using old pressure. The method in this study is using conservative form subtracts the required form to modify into convective form. Therefore, the final expression for $\mathbf{u}\cdot\nabla\mathbf{u}$ is given by Eq. (3.42).

Cette thèse est accessible à l'adresse : http://theses.insa-lyon.fr/publication/2020LYSEI095/these.pdf
© [L. Guo], [2020], INSA Lyon, tous droits réservés

$$\mathbf{u}\cdot\nabla\mathbf{u} = u\mathbf{u}_x + v\mathbf{u}_y \approx \frac{u_{i+1/2,j}+u_{i-1/2,j}}{2}\frac{\mathbf{u}_{i+1/2,j}-\mathbf{u}_{i-1/2,j}}{\Delta x} + \frac{v_{i,j+1/2}+v_{i,j-1/2}}{2}\frac{\mathbf{u}_{i,j+1/2}-\mathbf{u}_{i,j-1/2}}{\Delta y} \tag{3.42}$$

As described in the characteristic extrapolation step, there are two u for each cell edge. It is necessary to select optimal one from these two values, e.x, the computation of $u_{i+1/2,j}$ on the $(i+1/2,j)$ face comes from $u^R_{i+1/2,j}$ and $u^L_{i+1/2,j}$. In order to solve this ambiguity, we simplify the Eq. (3.7) by dropping out the diffusion term, the pressure gradient focuses on normal flux, which is a simple Riemann problem, namely,

$$\begin{aligned} u_t + uu_x &= 0 \\ u_t + uv_x &= 0 \end{aligned} \tag{3.43}$$

The Eq. (3.43) shows that u satisfies the quasilinear form of Burger's equation which upwinds u based on

$$u_{i+1/2,j} = \begin{cases} u^L, & \text{if } u^L \geq 0, u^L + u^R \geq 0 \\ 0, & \text{if } u^L < 0, u^R > 0 \\ u^L, & \text{otherwise} \end{cases} \tag{3.44}$$

It should be noted that the temporal and spatial indices are suppressed. v is passively advected by u, determined by the upwind direction of the flow as

$$v_{i+1/2,j} = \begin{cases} v^L, & \text{if } u_{i+1/2,j} > 0 \\ \dfrac{v^L + v^R}{2}, & \text{if } u_{i+1/2,j} = 0 \\ v^R, & \text{otherwise} \end{cases} \tag{3.45}$$

3.3.2 Time integration

We rewrite the incompressible Navier-Stokes equations with surface tension and gravity for the sake of convenience:

$$\begin{aligned} &\nabla\cdot\mathbf{u} = 0 \\ &\rho\left(\frac{\partial\mathbf{u}}{\partial t} + \mathbf{u}\cdot\nabla\mathbf{u}\right) = -\nabla p + \nabla\cdot(2\mu\mathbf{D}) + \rho\mathbf{g} + \sigma\delta_s\kappa\mathbf{n} \end{aligned} \tag{3.46}$$

Cette thèse est accessible à l'adresse : http://theses.insa-lyon.fr/publication/2020LYSEI095/these.pdf
© [L. Guo], [2020], INSA Lyon, tous droits réservés

An overall time discretization for Navier-Stokes equations with VOF transport equation in staggered grid leads to the following expressions,

$$\begin{aligned}
&\frac{C^{n+1/2}-C^{n-1/2}}{\Delta t}+\nabla\cdot(C^n\mathbf{u}^n)=0\\
&\nabla\cdot\mathbf{u}^{n+1}=0\\
&\rho^{n+1/2}\left(\frac{\mathbf{u}^{n+1}-\mathbf{u}^n}{\Delta t}+\mathbf{A}^{n+1/2}\right)=-\nabla p^{n+1/2}+\nabla\cdot[\mu^{n+1/2}(\mathbf{D}^n+\mathbf{D}^{n+1})]+\rho^{n+1/2}\mathbf{g}+(\sigma\kappa\delta_s\mathbf{n})^{n+1/2}
\end{aligned} \tag{3.47}$$

First, the new vof value $C^{n+1/2}$ is obtained from the VOF equation (Eq. (3.26)). Subsequently, the physical parameters such as density and viscosity at $t^{n+1/2}$ are determined by the weighted average method as similar in Eq. (3.3).

$$\phi^{n+1/2}=C^{n+1/2}\phi_l+(1-C^{n+1/2})\phi_g \tag{3.48}$$

The time-stepping projection method is used to decouple the pressure and velocity in Eq. (3.47).

$$\rho^{n+1/2}\left(\frac{\mathbf{u}^*-\mathbf{u}^n}{\Delta t}+\mathbf{A}^{n+1/2}\right)=\nabla\cdot[\mu^{n+1/2}(\mathbf{D}^n+\mathbf{D}^*)]+(\sigma\kappa\delta_s\mathbf{n})^{n+1/2} \tag{3.49}$$

$$\mathbf{u}^{n+1}=\mathbf{u}^*-\frac{\Delta t}{\rho^{n+1/2}}\nabla p^{n+1/2} \tag{3.50}$$

$$\nabla\cdot\mathbf{u}^{n+1}=0 \tag{3.51}$$

By solving the Poisson equations, the update pressure can be obtained.

$$\nabla\cdot\mathbf{u}^*=\nabla\cdot\left[\frac{\Delta t}{\rho^{n+1/2}}\nabla p^{n+1/2}\right] \tag{3.52}$$

If we rearrange the Eq. (3.47), an Helmholtz-Poisson type equation can be obtained:

$$\frac{\rho^{n+1/2}}{\Delta t}\mathbf{u}^*-\nabla\cdot(\mu^{n+1/2}\mathbf{D}^*)=\nabla\cdot(\mu^{n+1/2}\mathbf{D}^n)+(\sigma\kappa\delta_s\mathbf{n})^{n+1/2}+\rho^{n+1/2}\left[\frac{\mathbf{u}^n}{\Delta t}-\mathbf{A}^{n+1/2}\right] \tag{3.53}$$

where the RHS of Eq. (3.53) only depends on prior values or calculated value at $n+1/2$. In Basilisk, a multigrid Poisson solver is used to solve this equation. The viscous term is treated as semi-implicit Crank-Nicolson discretization, formally second-order accurate and unconditional stable. It should be noted that the criterion for convergence of the multigrid solver should be set as the difference relative error in each component of the velocity field. Otherwise, this threshold is set to a relatively

Cette thèse est accessible à l'adresse : http://theses.insa-lyon.fr/publication/2020LYSEI095/these.pdf
© [L. Guo], [2020], INSA Lyon, tous droits réservés

small value 10^{-6} by default. The algebraic process uses the Gauss-Seidel iterative method, and set the relaxations per level is four (Popinet, 2009).

The BCG algorithm procedure is summarized for the implementation of the full Navier-Stokes equations and the flow chart of the numerical methods is shown in Fig. 3.10.

1). Timestep (Δt) is followed by the CFL condition and constrain of surface tension stability.

$$\Delta t = \min\left(\left(\frac{|u_{i,j}|}{\Delta x} + \frac{|v_{i,j}|}{\Delta y}\right)^{-1}, \sqrt{\frac{(\rho_l + \rho_g) min(\Delta x^3, \Delta y^3)}{4\pi\sigma}}\right) \tag{3.54}$$

2). Using time stepping method to compute the contribution of advection term at half time step on velocity field ($\mathbf{u}^{adv,*}$) by dropping other terms in Eq. (3.46).

$$\mathbf{u}_c^{adv,*} = \mathbf{u}_c^n - \Delta t[\mathbf{u}\cdot\nabla\mathbf{u}]_c^{n+1/2} \tag{3.55}$$

where c indicates the cell centered value, $\mathbf{u}_c^{adv}$ indicates the advection temporal centered velocity. $[\mathbf{u}\cdot\nabla\mathbf{u}]_c^{n+1/2}$ is solved by the BCG scheme.

3). Use the pressure gradient and source acceleration terms ($\mathbf{a}$) at $t^{n-1/2}$ to correct the advection term.

$$\mathbf{u}_c^{adv} = \mathbf{u}_c^{adv,*} + \Delta t\left(\mathbf{a} - \frac{1}{\rho}\nabla p\right)_{f\to c}^{n-1/2} \tag{3.56}$$

where f is cell edge centered (staggered) value. $[\cdot]_{f\to c}$ denotes the transformation from cell face-centered to cell-centered. The additional vector $\mathbf{a}$ stands for the surface tension, gravity, or other acceleration terms.

4). By adding the viscous term and using the corrected advection velocity, the intermediate velocity ($\mathbf{u}^{vis}$) can be obtained.

$$\frac{\mathbf{u}_c^{vis} - \mathbf{u}_c^{adv}}{\Delta t} = \frac{1}{\rho_c^{n+1/2}}\nabla\cdot\mu^{n+1/2}(\mathbf{D}^{vis} + \mathbf{D}^n)_c \tag{3.57}$$

where $\mathbf{u}_c^{vis}$ is the centered viscous temporal centered velocity.

5). Remove the old pressure gradient and acceleration terms at $t^{n-1/2}$, which would be replaced by the updated values at time t^{n+1}.

$$\mathbf{u}_c^{*} = \mathbf{u}_c^{vis} - \Delta t\left(\mathbf{a} - \frac{1}{\rho}\nabla p\right)_{f\to c}^{n-1/2} \tag{3.58}$$

6). The provisional face velocity ($\mathbf{u}_f^{n+1,*}$) at t^{n+1} is obtained by interpolating the centered intermediate velocity ($\mathbf{u}_c^*$) in Eq. (3.58). Then use approximate projection

Cette thèse est accessible à l'adresse : http://theses.insa-lyon.fr/publication/2020LYSEI095/these.pdf
© [L. Guo], [2020], INSA Lyon, tous droits réservés

to compute $p^{n+1/2}$ and divergence-free face velocity ($\mathbf{u}_f^{n+1}$).

$$\begin{aligned} &\nabla \cdot \mathbf{u}_f^{n+1} = 0 \\ &\rho_c^{n+1/2} \frac{\mathbf{u}_f^{n+1} - \mathbf{u}_f^{n+1,*}}{\Delta t} = -\nabla p_c^{n+1/2} \end{aligned} \tag{3.59}$$

7). Use interpolation method to obtain $\mathbf{u}_c^{n+1,*}$ from $\mathbf{u}_f^{n+1}$.

8). Correct $\mathbf{u}_c^{n+1,*}$ using new pressure gradient and acceleration terms at $t + 1/2$.

$$\mathbf{u}_c^{n+1} = \mathbf{u}_c^{n+1,*} + \Delta t \left(\mathbf{a} - \frac{1}{\rho} \nabla p \right)_{f \to c}^{n+1/2} \tag{3.60}$$

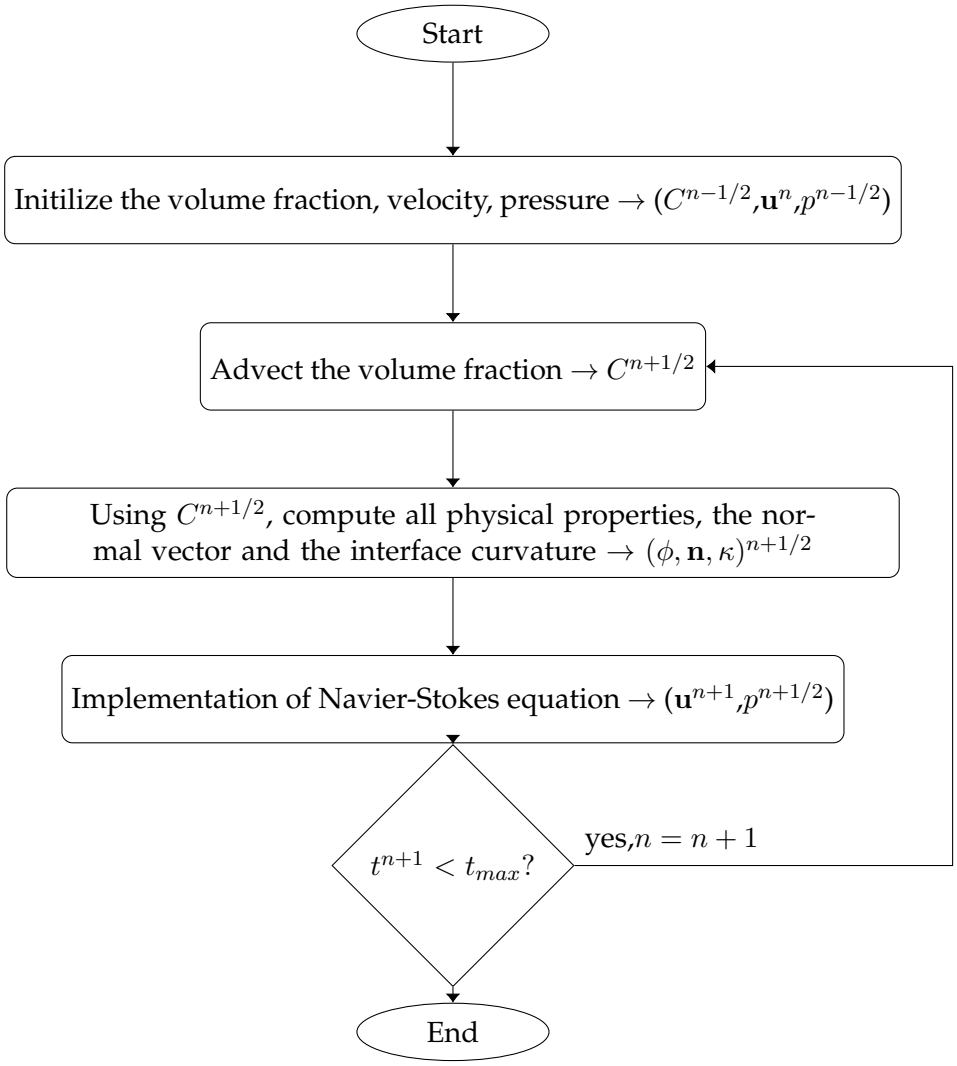

FIGURE 3.10: Diagram of the overall solution procedure. t^{n+1} is the physical corresponding to time-step $n+1$ and t_{max} is the maximum physical time in the simulation.

Cette thèse est accessible à l'adresse : http://theses.insa-lyon.fr/publication/2020LYSEI095/these.pdf
© [L. Guo], [2020], INSA Lyon, tous droits réservés

3.4 Grid structure in Basilisk solver

The Basilisk solver adopts a quadtree (2D) and octree (3D) grid for numerical simulations. This type of spatial discretization has been widely used in computer graphics and image processes (Popinet, 2003; Samet, 1990), which is also used to solve the Euler equations for compressible flows (Khokhlov, 1998). The schematic of spatial discretization and tree representation is given in Fig. 3.11. Before introducing the grid structure, some prime definitions are specified. For example, each computational grid is described as *cell*. The basic and root cell (as depicted by 0) is *parent* and each *parent* should have four *children* cells (eight in 3D). The *level* of a cell in the calculation is defined by starting from root cell, and adding one level corresponding to four children cells is added. In Fig. 3.12, each cell with tree structure has four vertices, the line segment between two neighboring vertices is called the cell side, while the line between adjacent nodes on the cell side is cell edge. If the cell side has one cell edge, we call this is the minimum cell edge. Otherwise, for one cell side with two cell edges, we call the two cells are neighboring. A solid boundary cuts the mixed cells.

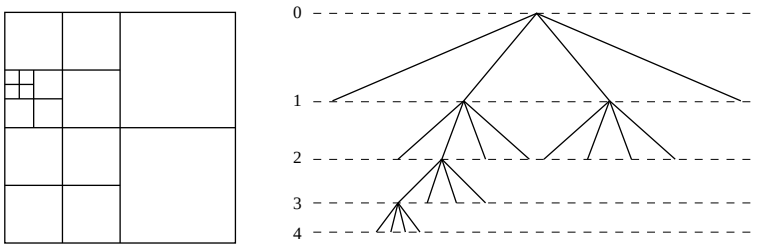

FIGURE 3.11: Schematic of quadtree adaptive grid and corresponding tree representation (Popinet, 2003).

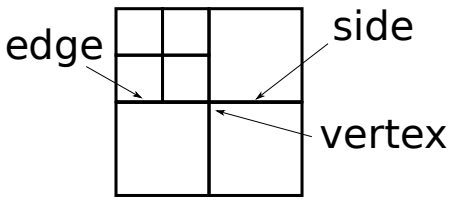

FIGURE 3.12: The definition of cell.

For value calculation on cell boundaries between different levels, Basilisk provides several constraints as shown in Fig. 3.13

- The difference of grid level is no more than 1 between the direct neighboring cells.
- The difference of grid level is no more than 1 between the diagonally neighboring cells.
- All the mixed cells must be at the same level.

Cette thèse est accessible à l'adresse : http://theses.insa-lyon.fr/publication/2020LYSEI095/these.pdf
© [L. Guo], [2020], INSA Lyon, tous droits réservés

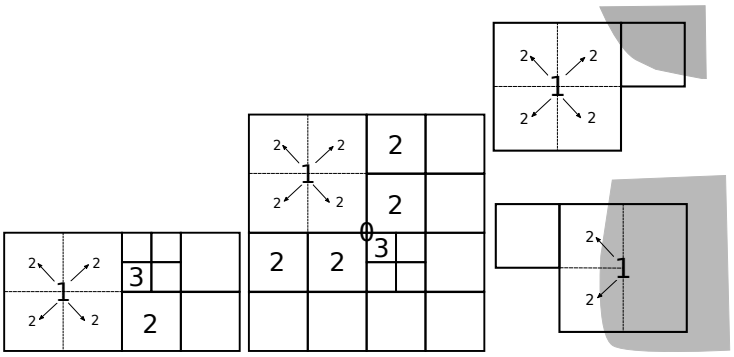

FIGURE 3.13: Several constraints for quadtree discretization.

The refinement procedure needs to interpolate values from the coarse grid to the fine grid. To illustrate the value refinement in detail, we introduce two functions: "prolongation" and "restriction" in Basilisk. The prior physical variables are collocated in the center of the cell, depicted by black dots named active points, as shown in Fig. 3.14. To calculate red pentagrams, one simple way to use a $prolongation$ function is a bilinear interpolation from the coarser grid (larger dots in the figure) (Popinet, 2015). It should be noted that the larger blue dot is not defined explicitly, so another function named $restriction$ is used to calculate the finer centered value from the coarser grid.

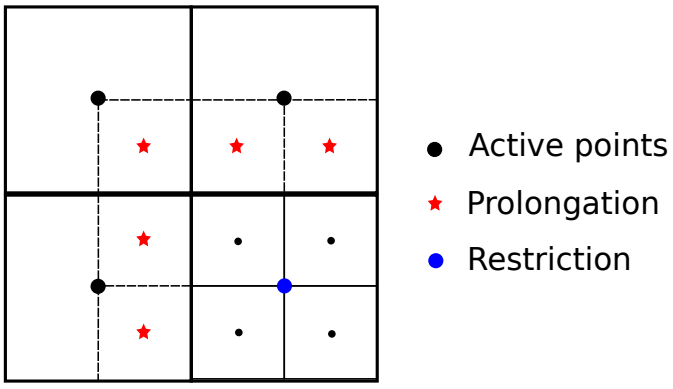

FIGURE 3.14: Schematic of local variable-resolution stencil on quadtree mesh.

In order to simplify discretization, the declaration of velocity and pressure utilizes a staggered-grid definition. The pressure is defined in the center of the leaf cells, and the velocity components are defined on the minimum cell side (as shown in Fig. 3.15). The cell side velocity can be interpolated by the minimum cell sides velocity components; for example, in Fig. 3.15 the right cell side velocity for the root cell could be interpolated by the leaf cells on the right cell side, namely $u_0 = 1/2u_2 + 1/4u_5 + 1/8(u_{11} + u_{12})$.

Cette thèse est accessible à l'adresse : http://theses.insa-lyon.fr/publication/2020LYSEI095/these.pdf
© [L. Guo], [2020], INSA Lyon, tous droits réservés

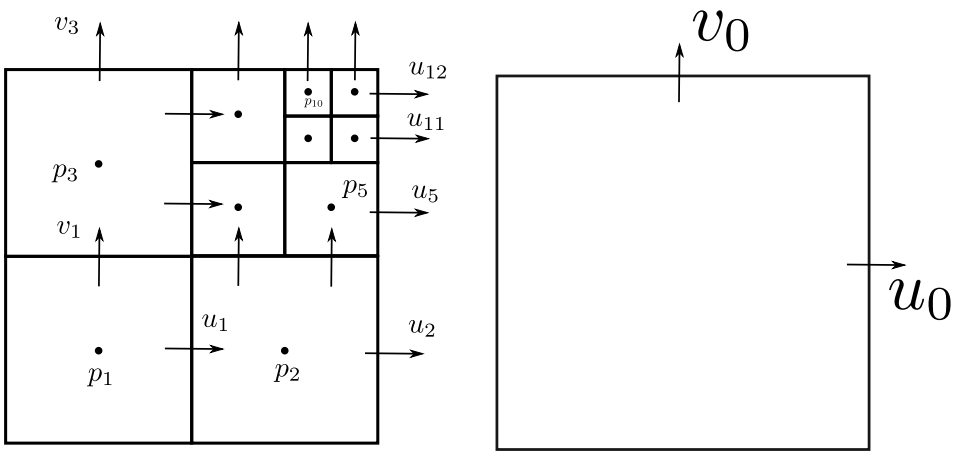

FIGURE 3.15: Definition of variables of a staggered quadtree mesh.

The quadtree/octree grid structure is of high applicability for adaptive mesh refinement (AMR). AMR's basic principle is to provide criteria that will determine if the grid is coarsened or refined. For instance, the scale of vorticity is usually chosen in CFD to judge the requirements. The grid will be refined if it satisfies the following formulation,

$$\frac{h\|\nabla \times \mathbf{u}\|}{\max\|\mathbf{u}\|} > \tau \tag{3.61}$$

where h is the grid size, $\mathbf{u}$ the fluid velocity, $0 < \tau < 1$ is constant value.

The mesh is refined when the velocity in one cell satisfies the above criteria and coarsened for the contrary side. One can apply these criteria at each timestep or after some timesteps in the calculation. In addition to the vortex, the gradient of any variable can be utilized as the criteria value for the AMR, and It also makes some interesting regions (such as coastline, islands) always refined. Fig. 3.16 displays the vorticity field simulation of Cook Strait tidal and the details of corresponding local adaptive quadtree mesh. It is observed that the AMR technique is used for the region close to the coastline, and the vorticity is the criteria value for the AMR. Furthermore, due to the square control volumes in quadtree meshes are the same as for the pure Cartesian meshes (Popinet, 2015), so that the schemes in Cartesian meshes can easily be implemented to quadtrees using interpolation methods.

Cette thèse est accessible à l'adresse : http://theses.insa-lyon.fr/publication/2020LYSEI095/these.pdf
© [L. Guo], [2020], INSA Lyon, tous droits réservés

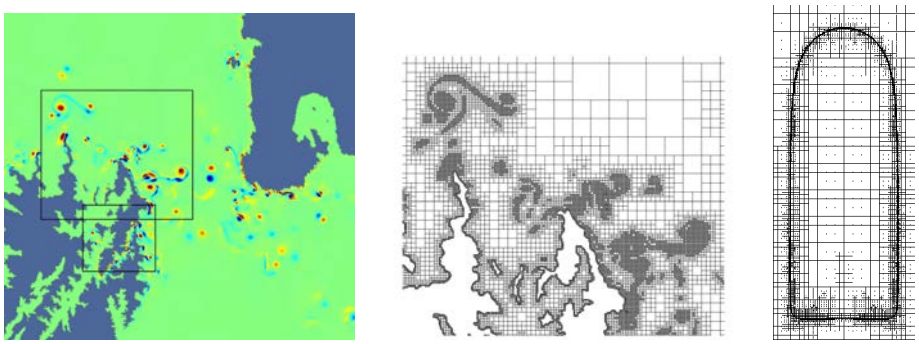

FIGURE 3.16: Details of vorticity field and adaptive quadtree tree of Cook Strait tidal (Popinet and Rickard, 2007) and AMR of Taylor bubble case in the present thesis.

3.5 Chapter conclusion

In this chapter, we introduced numerical methods in Basilisk solver, including the VOF method and the implementation of Navier-Stokes equations. Moreover, the grid structures in Basilisk is also introduced. In the following two chapters, we will analyze some results of Taylor bubbles with expansions and contractions structures. The numerical methods and results of two-phase flow with phase change will be performed in Chapter. 6.

Cette thèse est accessible à l'adresse : http://theses.insa-lyon.fr/publication/2020LYSEI095/these.pdf
© [L. Guo], [2020], INSA Lyon, tous droits réservés

Cette thèse est accessible à l'adresse : http://theses.insa-lyon.fr/publication/2020LYSEI095/these.pdf
© [L. Guo], [2020], INSA Lyon, tous droits réservés

Chapter 4

Numerical investigation on individual Taylor bubbles rising through sudden expansions/contractions in stagnant flow

In this chapter, we present the numerical results of individual Taylor bubbles rising in vertical pipes through expansions/contractions filled with glycerol-water solutions. The simulation results are compared with experimental data from a previous Ph.D. work by Zhou (2017). First, validation of the Basilisk solver for Taylor bubbles rising in vertical straight pipes is performed. Second, the Taylor bubbles passing through sudden expansions/contractions are studied.

4.1 Taylor bubble rising in a vertical straight pipe

4.1.1 Experimental facility

The experimental setup consists of two main parts: the gas supply apparatus and the test section. The schematic diagram of the experimental setup is shown in Fig. 4.1. The gas in the present experiments is provided by a compressed nitrogen tank and controlled by two valves: the depressor valve (Valve 1) and micro-valve (Valve 2). Valve 1 is *AIR LIQUID HBS 200-3-25*, which can control the outlet pressure from 0.01 to 0.3 MPa and is mounted on the nitrogen bottle; Valve 2 can control the gas flux from the nitrogen tank. The test section contains the bubble generator chamber and the visualization box. The bubble generator chamber comprises a cylindrical chamber and a rotational dumping cup. The gas rises from the injector and is collected in the cup. When it is stable, the dumping cup is rotated manually with the help of the rod, and the bubble releases and rises into the larger pipe. In the present experiments, the bubble volume is less than 6 cm^3. The visualization box is a transparent box that includes the upper pipe, the lower pipe, and the connection plate. The size of the visualization box is $10 \times 10 \times 45$ cm^3. Inside, the lower pipe is connected to the bubble generator chamber using a long straight pipe to stabilize the

Cette thèse est accessible à l'adresse : http://theses.insa-lyon.fr/publication/2020LYSEI095/these.pdf
© [L. Guo], [2020], INSA Lyon, tous droits réservés

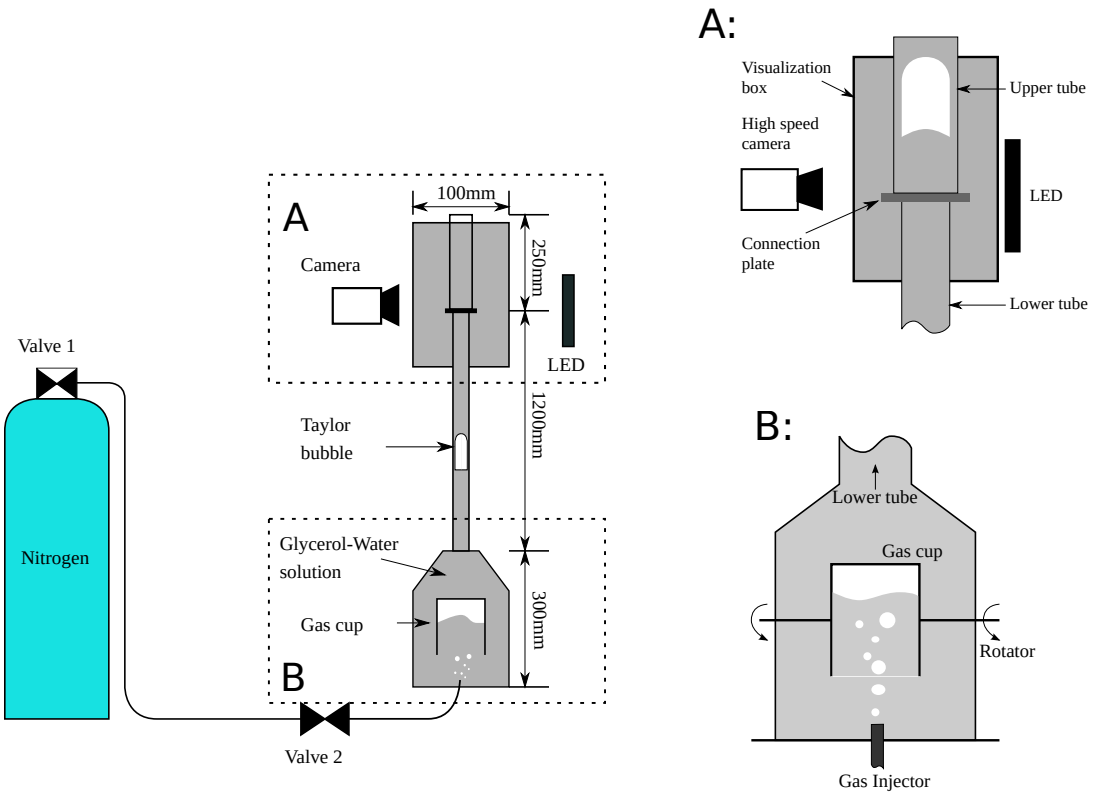

FIGURE 4.1: Experimental apparatus. A: text section, B: gas supply apparatus.

state of the Taylor bubble. A thin plate fixes the expansion section between the upper pipe and the lower pipe. The Taylor bubbles are recorded using a high-speed camera (Photron FASTCAMSA3 model 120K-M2), which is installed at the front of the visualization box. In the present experiments, a resolution of 256×1024 pixels and a frame rate of 1000 fps is used. A light source is installed opposite to the camera.

Fluid properties and geometrical parameters

In the experiments, the gas is nitrogen, and the surrounding liquid is a solution made by a mixture of glycerol and distilled water. The viscosities of these solutions are measured using a rheometer (*Anton Paar MCR 302*) at a controlled temperature of 291K. The liquid density ρ_l is calculated from the mixing model proposed by Volk and Kähler (2018). The surface tension σ is obtained from a mass-weighted averaging of the values for pure water and glycerol, as recommended by Takamura et al. (2012). The properties of these solutions are given in Table 4.1.

A vernier caliper measures the pipe diameters with a resolution of ±0.1 mm. In this study, the inside and outside diameters of the lower pipe are $D_{in}^{lower} = 16.20$ mm and $D_{out}^{lower} = 20.00$ mm, respectively. The diameter of the upper pipes are listed in Table 4.2. ϵ is expansion ratio expressed by inside diameter of the upper pipe over the

Cette thèse est accessible à l'adresse : http://theses.insa-lyon.fr/publication/2020LYSEI095/these.pdf
© [L. Guo], [2020], INSA Lyon, tous droits réservés

TABLE 4.1: Properties of different aqueous solutions of glycerol-water.

% of Glycerol	ρ_0 (kg·m^{-3})	ρ_r	μ_0 (mPa·s)	μ_r	σ (mN·m^{-1})	Mo	Eo	N_f
Pure water	996.56		0.853		71.2	1.44×10^{-11}	36.0	7545.1
60	1169.5	997.0	28.90	1651.4	66.8	1.96×10^{-5}	45.1	261.3
70	1194.6	1018.4	50.76	2900.6	65.9	1.96×10^{-4}	46.7	152.0
80	1218.6	1038.8	93.46	5340.6	65.0	0.00224	48.3	84.2
90	1241.3	1058.2	285.52	16315.4	64.1	0.199	49.8	28.1
95	1252.1	1067.4	520.76	29757.7	63.7	2.23	50.6	15.5
100	1261.34		813.84		62.4	14.1	52.0	10.0
Nitrogen	1.173		0.0175					

TABLE 4.2: Diameter of the upper pipes.

Index	D_{in}^{upper} (mm)	$\epsilon = D_{in}^{\text{upper}}/D_{in}^{\text{lower}}$
Lower tube		
1	16.20	
Upper tube		
1	28.00	1.73
2	23.90	1.47
3	21.95	1.35
4	20.15	1.24
5	18.20	1.12
6	15.20	0.94

lower pipe, i.e., $\epsilon = D_{in}^{upper}/D_{in}^{lower}$. The limited experimental data provide preliminary validation for extending simulations to a wide-range analysis.

4.1.2 Physical model description

Fig. 4.2 shows the computational geometry configuration of the physical model. A cylindrical coordinate is used for 2D simulations, assuming axial symmetry around the centerline of the vertical pipe (dashed line in Fig. 4.2). For the initialization of the Taylor bubble, the frontal radius shown in Fig. 4.2 is r_b, the distance (l_d) between bubble tail and the bottom wall is $4r_b$ to minimize the effect of bottom wall (Kang et al., 2010). The bubble length is l_0. White and Beardmore (1962) concluded the bubble terminal velocity is independent of l_0, and Araújo et al. (2012) conducted the Taylor bubble it should give at least $l_0 = 6r_b$ to obtain a stable liquid film. Unless stated otherwise, we use $l_0 = 7r_b$, but we also have calculated cases with different l_0, especially when comparing with experimental data.

It should be noted that it is difficult to measure the initial volume of the Taylor bubble in the experiments. Therefore, to obtain better consistency with experimental results, we tried several times for each case in simulations. The detailed information will be introduced in the Sec. 4.2.5. The bubble terminal state is independent of the initial film thickness (δ_0). However, choosing an appropriate δ_0 helps make the Taylor bubble obtain a stable terminal state faster. In the present study, the initial

Cette thèse est accessible à l'adresse : http://theses.insa-lyon.fr/publication/2020LYSEI095/these.pdf
© [L. Guo], [2020], INSA Lyon, tous droits réservés

guess of dimensionless liquid film thickness is defined as the ratio of initial liquid film thickness over the diameter of the pipe $\delta' = \delta_0/D_1$, which is estimated from Brown (1965):

$$\delta' = 2\frac{\sqrt{1+2.44N_f^{2/3}}-1}{2.44N_f^{2/3}} \tag{4.1}$$

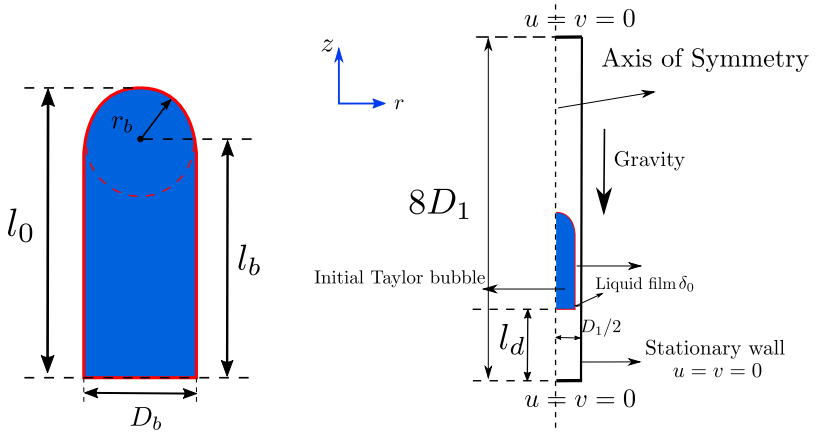

FIGURE 4.2: Schematic diagram of Taylor bubble rising in vertical straight pipe.

The boundary condition on the centerline is axisymmetry, and on the other walls are the Dirichlet conditions ($u = 0, v = 0$). In this chapter, the characteristic length is the pipe diameter of D_1. Therefore, all non-dimensional quantities are normalized to D_1. A general scaling analysis of the Taylor bubble or drop motion is performed by Hayashi et al. (2011). The dimensionless numbers in Sec. 2.2.1 are rewritten here for convenience:

- $Eo = \dfrac{(\rho_l - \rho_g)gD_1^2}{\sigma}$
- $Fr = \dfrac{U}{\sqrt{gD_1}}$
- $N_f = \dfrac{\rho_l\sqrt{gD_1^3}}{\mu_l}$
- $Mo = \dfrac{Eo^3}{N_f^4}$, here the density of gas in Eo is neglected.
- density ratio: $\rho_r = \dfrac{\rho_l}{\rho_g}$
- viscosity ratio: $\mu_r = \dfrac{\mu_l}{\mu_g}$

Cette thèse est accessible à l'adresse : http://theses.insa-lyon.fr/publication/2020LYSEI095/these.pdf
© [L. Guo], [2020], INSA Lyon, tous droits réservés

4.1.3 Comparison of experimental and theoretical results in straight pipe

Mesh independency analysis

In order to test the robustness and accuracy of the Basilisk solver, we choose the experimental case performed by Nogueira et al. (2006a,b). The simulation parameters using here are reported by Araújo et al. (2012), which are $Mo = 4.31 \times 10^{-2}$ and $N_f = 111$. A uniform grid is used with grid resolutions of $h = D_1/[64, 128, 256]$. The bubble nose position Z_h is set as the reference point according to Araújo et al. (2012). The Fig. 4.3 (A) shows there are small differences of the Taylor bubble shapes. A velocity profile comparison is shown in Fig. 4.3 (B). The profiles is at $(Z - Z_h)/D_1 = -2.73$, where Z_h is bubble nose position on the centerline, and Z is z axis in the cylindrical coordinate. Considering the difference between the finest grid and the other two grid sizes, the relative errors are -10.56% for $h = 1/64$ and -1.23% for $h = 1/128$. Therefore, the grid size in the following simulations is either $h = 1/128$ or $h = 1/256$.

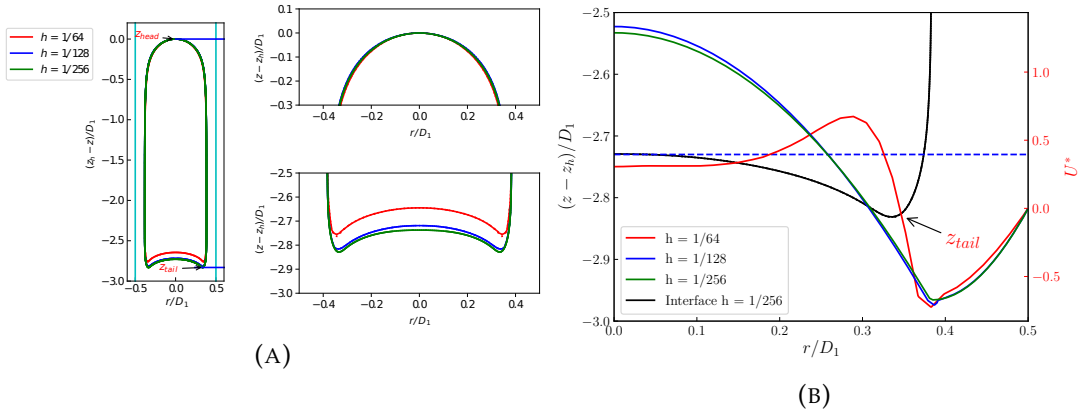

FIGURE 4.3: Mesh sensitivity analysis for the Taylor bubble. (A) Bubble shapes with zoom figures on the bubble nose and bubble tail, (B) Transverse velocity profile at $(Z - Z_h)/D_1 = -2.83$ below the tail ($U^* = U/\sqrt{gD_1}, U = \|\mathbf{u}\|$).

Velocity field

Fig. 4.4 (A) shows the numerical velocity fields and streamlines for the bubble at the steady state. Fig. 4.4 (B) and (C) compare dimensionless axial velocity profiles (u_z/U_{TB}, U_{TB} is Taylor bubble terminal steady velocity) in a fixed frame of reference in the region above the bubble nose and the wake region. We choose the steady-state criteria on the variation of the velocity of the bubble mass center (u_c). When u_c changes less than 1% within 0.1 dimensionless time ($t^* = t\sqrt{g/D_1}$) , we consider the bubble has reached its terminal velocity. The dimensionless time of the bubble in Fig. 4.4 equals 10, which already satisfied the steady-state criteria. Four locations of the velocity profiles are performed in Fig. 4.4 (A). It can be observed that our simulation data is matched well with the experimental data of Nogueira et al. (2006a,b).

Cette thèse est accessible à l'adresse : http://theses.insa-lyon.fr/publication/2020LYSEI095/these.pdf
© [L. Guo], [2020], INSA Lyon, tous droits réservés

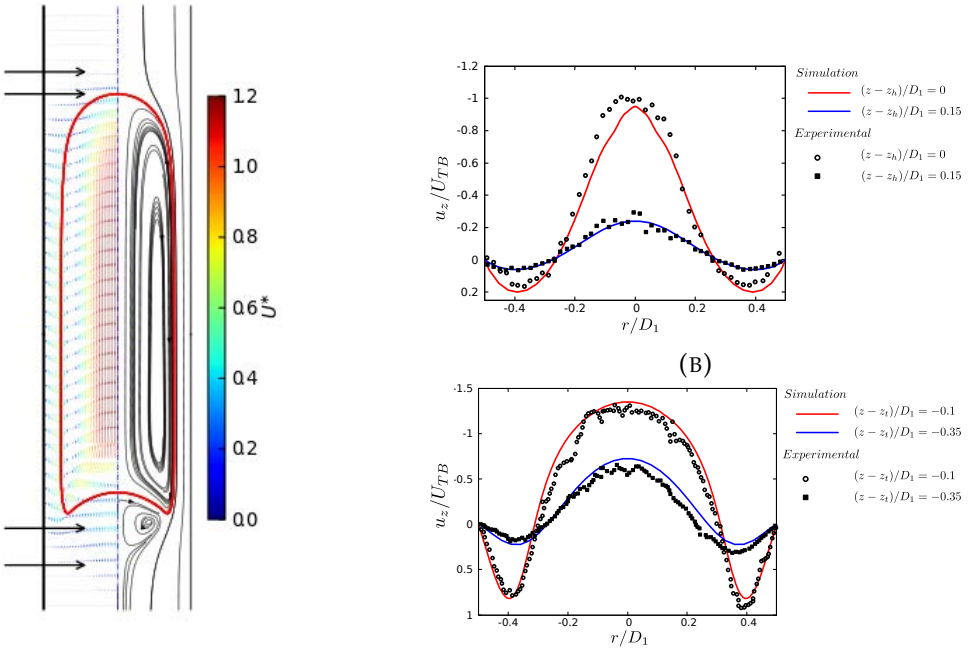

FIGURE 4.4: (A): Numerical velocity field and streamlines for single Taylor bubble rising in stagnant straight pipe ($Mo = 4.31 \times 10^{-2}$ and $N_f = 111$); (B): Comparison of dimensionless velocity profiles (u_z/U_{TB}) at bubble nose region with experimental results from Nogueira et al. (2006a); (C): Comparison of dimensionless velocity profiles (u_z/U_{TB}) at bubble tail region with experimental results from Nogueira et al. (2006b). The colors on the left show the absolute value of the non-dimensional velocity.

Terminal velocity

The Froude number is related to the non-dimensional Taylor bubble terminal velocity ($Fr = U_{TB}/\sqrt{gD_1}$), and is a function of Eo and Mo. We plot the profile of the Froud number and Eo numbers in Fig. 4.5. The lines are the results obtained from three correlations, Wallis (1969), Viana et al. (2003) and Hayashi et al. (2010). The experimental data indicated by open symbols come from White and Beardmore (1962). Our numerical results (closed symbols) show a good agreement with the experimental data. Comparing with the correlations, the present numerical results are closer to the more recent correlations from Viana et al. (2003) and Hayashi et al. (2010), as can be seen in Fig. 4.6, parity plots of U_{TB} comparison between simulation and experimental data are sketched, and the agreement is obvious. Again, the mean relative error (MRE) shows our simulations are closer to the more recent correlation from Viana et al. (2003).

Cette thèse est accessible à l'adresse : http://theses.insa-lyon.fr/publication/2020LYSEI095/these.pdf
© [L. Guo], [2020], INSA Lyon, tous droits réservés

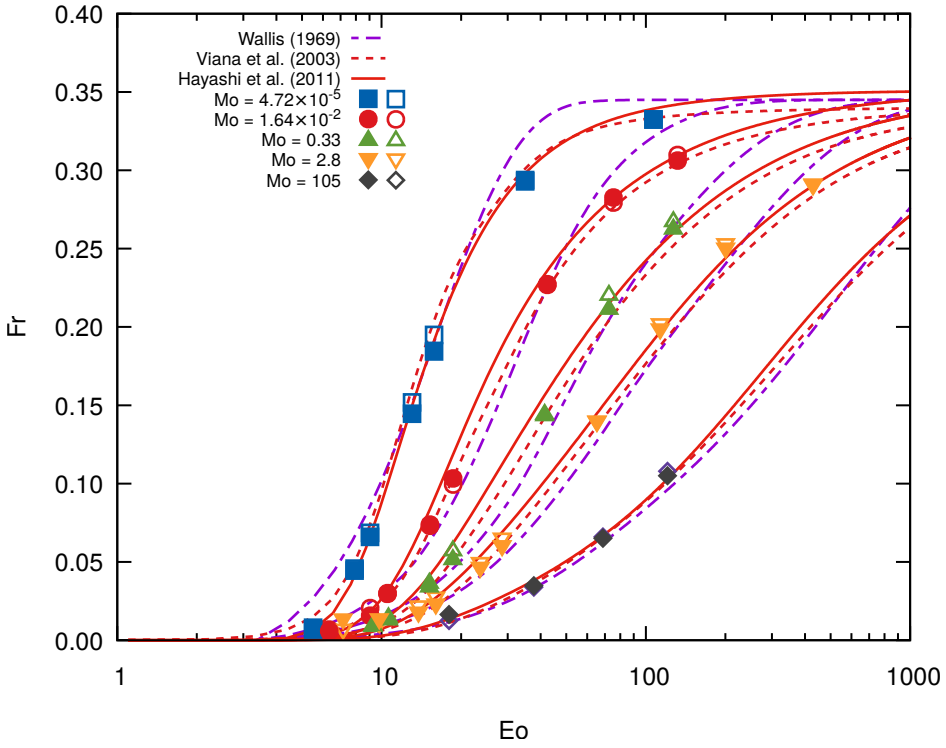

FIGURE 4.5: Numerical results (closed symbols) of a set of Froude numbers. The experimental data(open symbols) from White and Beardmore (1962) and the curve predicted by the correlations of Wallis (1969) (short-long dashed line). Viana et al. (2003) (uniform dashed line), Hayashi et al. (2010) (solid line).

Cette thèse est accessible à l'adresse : http://theses.insa-lyon.fr/publication/2020LYSEI095/these.pdf
© [L. Guo], [2020], INSA Lyon, tous droits réservés

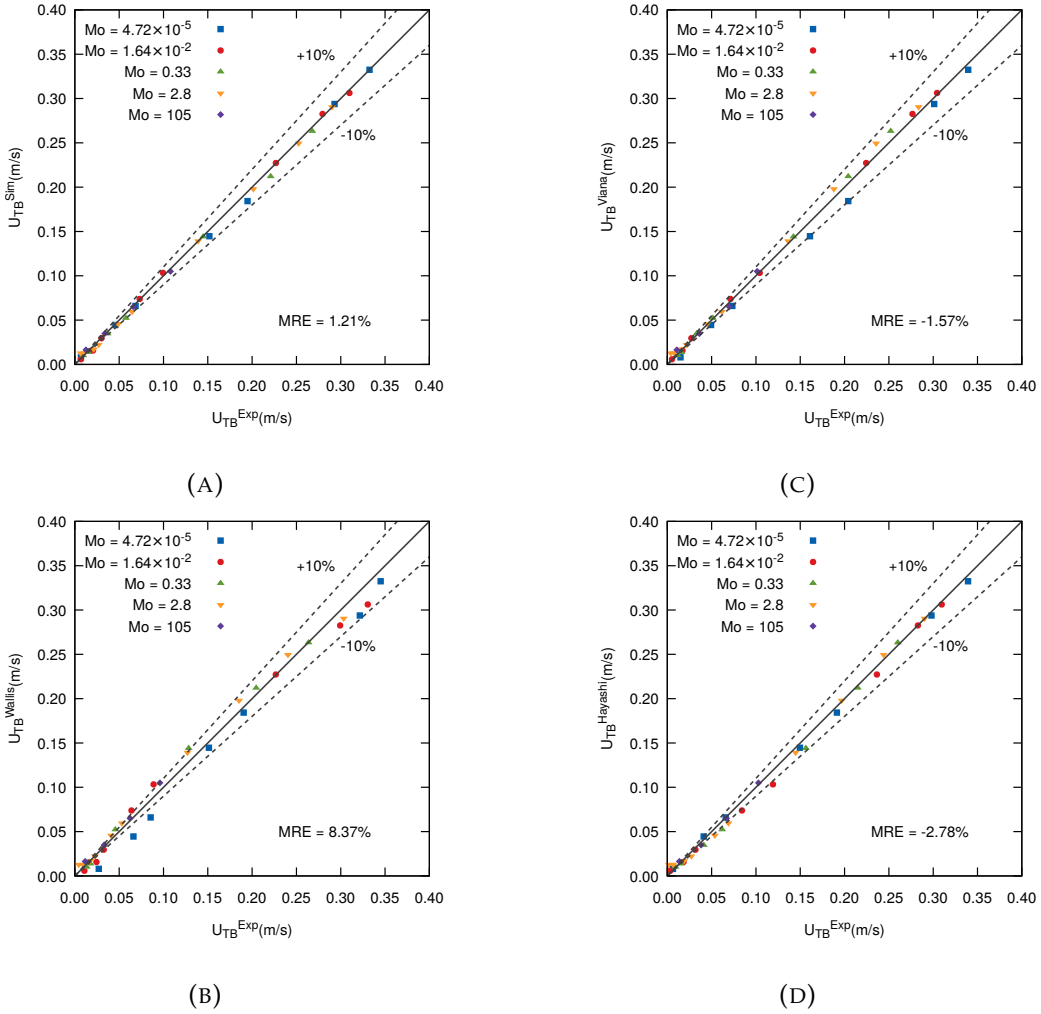

FIGURE 4.6: Parity plots of the Taylor bubble velocities. (A). simulation results with experimental data (White and Beardmore, 1962). (B); Wallis (1969) and experimental data; (C).Viana et al. (2003) and experimental data; (D). Hayashi et al. (2010) and experimental data.

Taylor bubble rises in different mixed glycerol-water solutions

To investigate the Taylor bubble in different solutions, we first give the experiments of Taylor bubble shapes in pure water and pure glycerol, see Fig. 4.7. The Taylor bubble in water is a turbulent flow according to the large N_f (Campos and De Carvalho, 1988). The bubble tail wake is unstable and asymmetrical. Contrary to this, the Taylor bubble in pure glycerol has a stable shape, and the bubble tail is round.

Cette thèse est accessible à l'adresse : http://theses.insa-lyon.fr/publication/2020LYSEI095/these.pdf
© [L. Guo], [2020], INSA Lyon, tous droits réservés

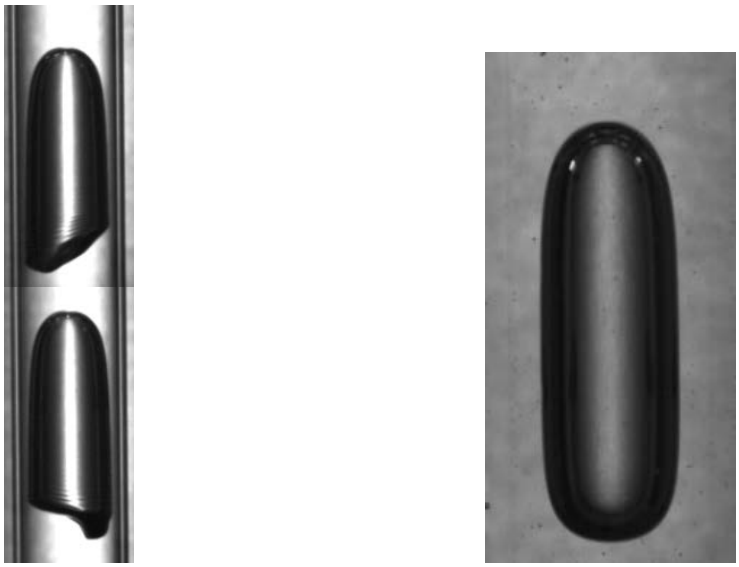

(A) (B)

FIGURE 4.7: Taylor bubble shapes in pure water and glycerol. (A). Pure water; (B). Pure glycerol.

In Fig. 4.8, the Taylor bubbles rising in different mixed glycerol-water solutions have reached a steady state. The first row is the Basilisk simulation results, and the second row is the experimental results. The physical properties are those presented in Table. 4.1. It is observed that the bubble tail shape changes from flat to oblate with increased concentration of the glycerol. The comparison between the simulation results and the experimental results of bubble shapes match well.

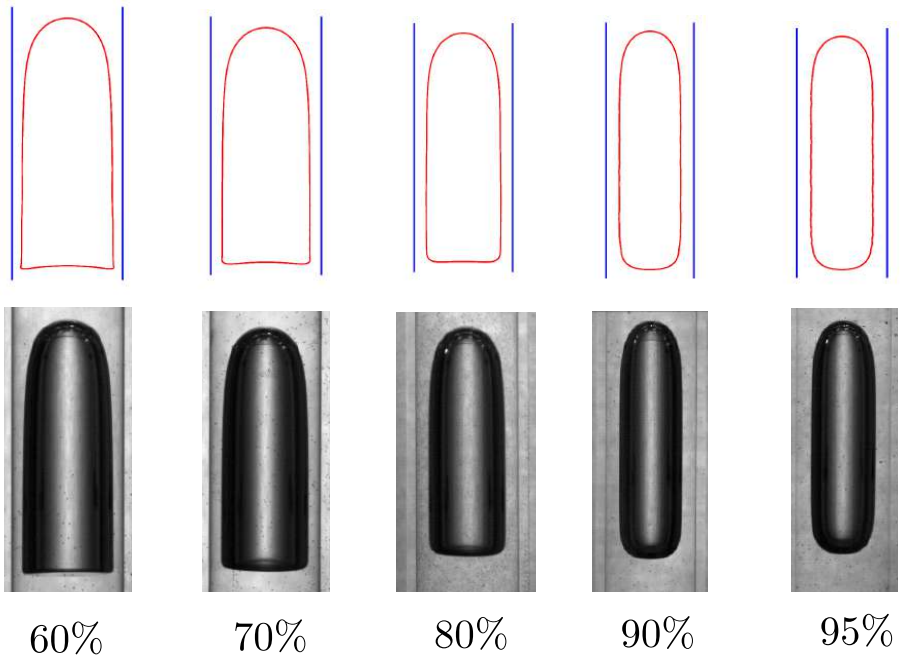

FIGURE 4.8: Comparisons of bubble shapes in different glycerol-water diluted solutions.

Cette thèse est accessible à l'adresse : http://theses.insa-lyon.fr/publication/2020LYSEI095/these.pdf
© [L. Guo], [2020], INSA Lyon, tous droits réservés

4.1.4 Influence of non-dimensional parameters

In order to study which parameter dominates the change of the Taylor bubble shape, we did a sensitivity analysis. The dimensionless numbers in Sec. 4.1.2 demonstrate only four dimensionless numbers are independent, i.e. Eo, N_f, ρ_r and μ_r. The analysis is performed for the Taylor bubble reaches a steady state.

Effect of density ratio

Five density ratio cases are given in this section, which are $\rho_r = [5, 10, 100, 500, 1000]$, the other parameters are $Eo = 50, N_f = 50, \mu_r = 100$. Fig. 4.9 (A) shows the Taylor bubble mass center velocity with different density ratios. It is observed when $\rho_r < 100$, the bubble moves slower than that for higher density ratios due to the reduction of the buoyancy force. When the density ratio is large enough, it has a minor influence on the bubble velocity. The bubble terminal velocity in Fig. 4.9 (B) also demonstrates this conclusion. Fig. 4.10 shows the influence of the density ratios on the shape of the bubble. The result shows that for large density ratios of $\rho_r > 100$, there is a minimal effect on the Taylor bubble shapes. Kang et al. (2010) also obtained a similar conclusion that ρ_r has a negligible effect on Taylor bubble shapes for high density ratios.

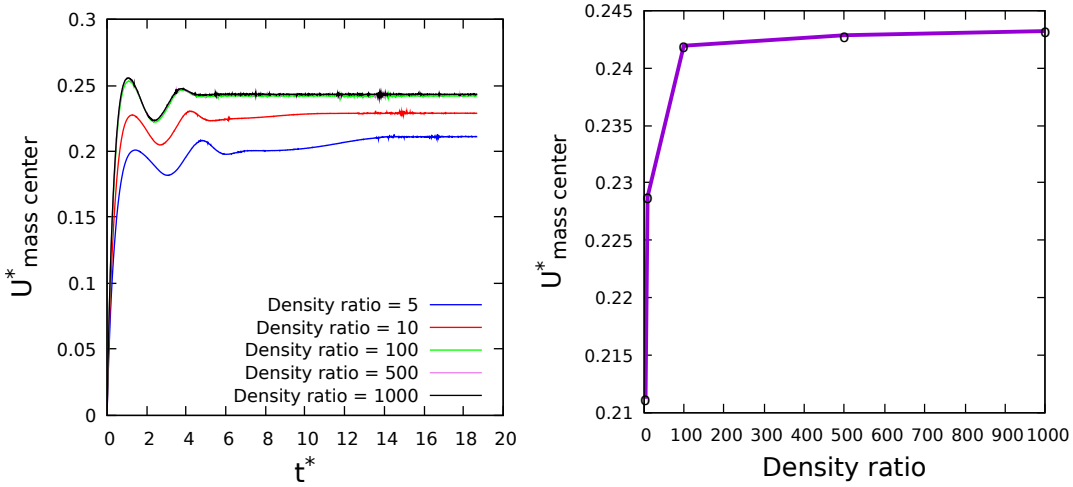

(A) (B)

FIGURE 4.9: (A). Effect of density ratios on bubble velocities. (B). Effect of density ratios on the bubble terminal velocities.

Cette thèse est accessible à l'adresse : http://theses.insa-lyon.fr/publication/2020LYSEI095/these.pdf
© [L. Guo], [2020], INSA Lyon, tous droits réservés

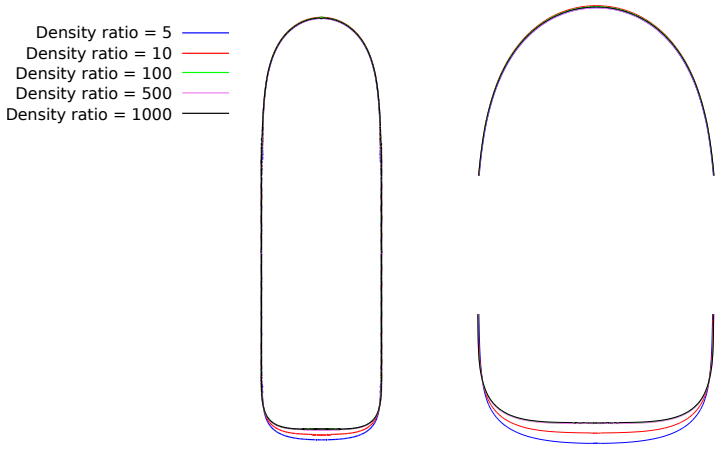

FIGURE 4.10: Effect of density ratios on bubble shapes.

Effect of viscosity ratio

In this test case, the viscosity ratios (μ_r) range from 10 to 100000. Other parameters are $\rho_r = 1000, Eo = 50$, and $N_f = 50$. Fig. 4.11 and Fig. 4.12 show large viscosity ratios have minimal effect on bubble velocities and shapes. Considering the parameters in Table. 4.1, we use large μ_r in experiments. Therefore, μ_r is not the main factor to change the bubble shapes. However, it should be noted with μ_r smaller than 100, the bubble moves slower.

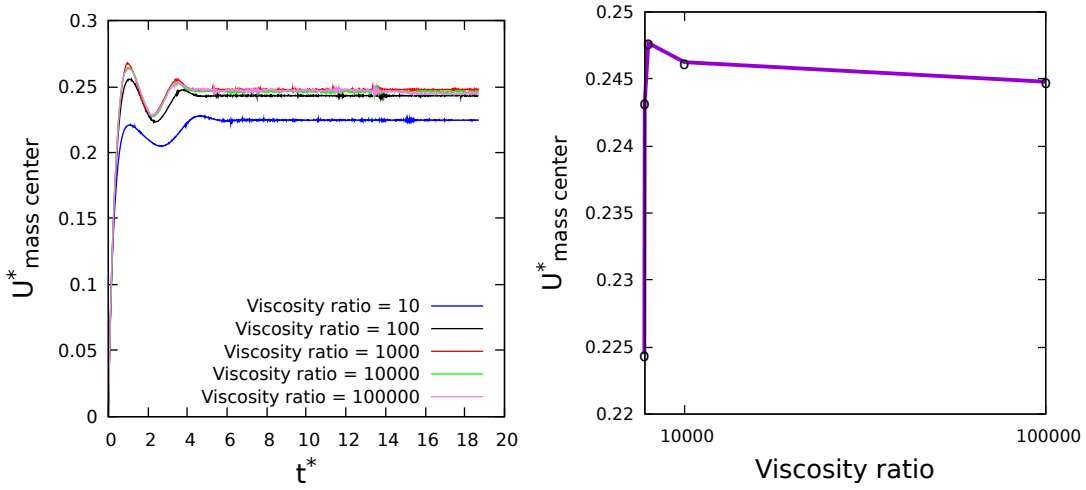

(A) (B)

FIGURE 4.11: (A). Effect of viscosity ratios on bubble velocities. (B). Effect of viscosity ratios on the bubble terminal velocities.

Cette thèse est accessible à l'adresse : http://theses.insa-lyon.fr/publication/2020LYSEI095/these.pdf
© [L. Guo], [2020], INSA Lyon, tous droits réservés

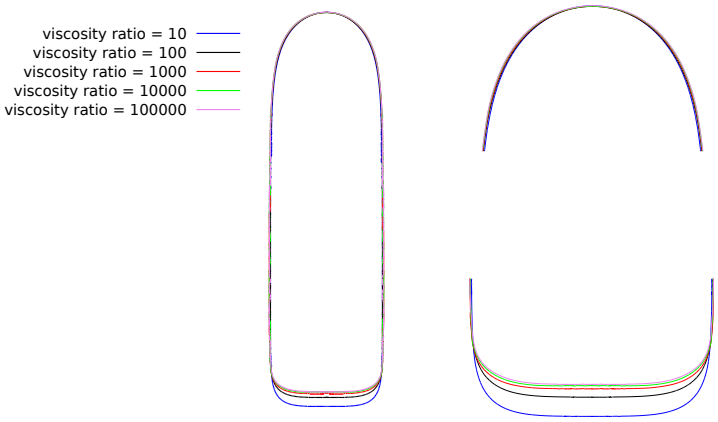

FIGURE 4.12: Effect of viscosity ratios on bubble shapes.

Effect of Eo number

The Eo numbers here range from 20 to 500. Other parameters are $\rho_r = 1000, \mu_r = 100$, and $N_f = 50$. When increasing the Eo numbers, the surface tension force will be reduced. From Fig. 4.13, the bubble velocities are increasing with increase of Eo numbers (see also in Fig. 4.5). Fig. 4.14 shows the Eo numbers have a strong influence on the bubble shapes, especially for the bubble tail shapes. Increasing the Eo numbers from 20 to 500, the bubble tail shape changes from oval to skirt. Kang et al. (2010) obtained a skirted tail shape when increasing the Eo number to 304.

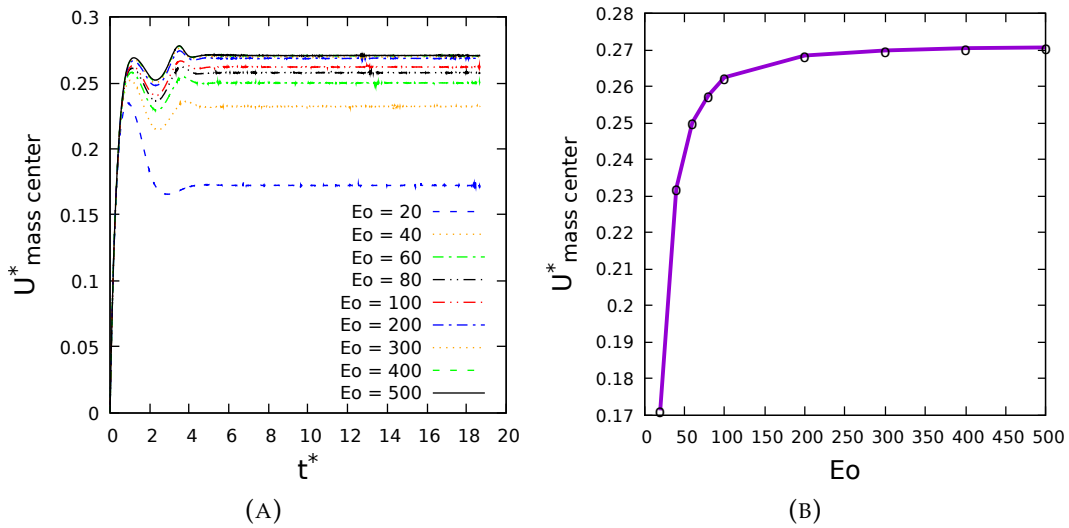

(A) (B)

FIGURE 4.13: (A). Effect of Eo on bubble velocities. (B). Effect of Eo on the bubble terminal velocities.

Cette thèse est accessible à l'adresse : http://theses.insa-lyon.fr/publication/2020LYSEI095/these.pdf
© [L. Guo], [2020], INSA Lyon, tous droits réservés

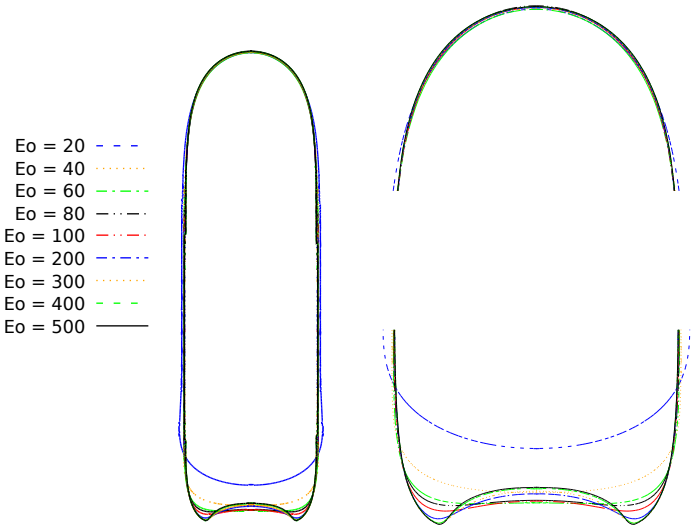

FIGURE 4.14: Effect of Eo numbers on bubble shapes.

Effect of N_f number

The previous work by Campos and De Carvalho (1988) concluded the N_f numbers would affect the bubble wake structure, and when $N_f < 500$, an axisymmetric laminar wake is observed. However, for higher N_f, the flow becomes turbulent. Therefore, in this section, the N_f numbers change from 20 to 300. The other parameters remain the same, i.e. $\rho_r = 1000, \mu_r = 100$, and $Eo = 50$. As see in Fig. 4.15, the bubble velocity will increase with increasing the N_f numbers. Fig. 4.16 shows the N_f number has a great effect on the bubble shapes like Eo numbers.

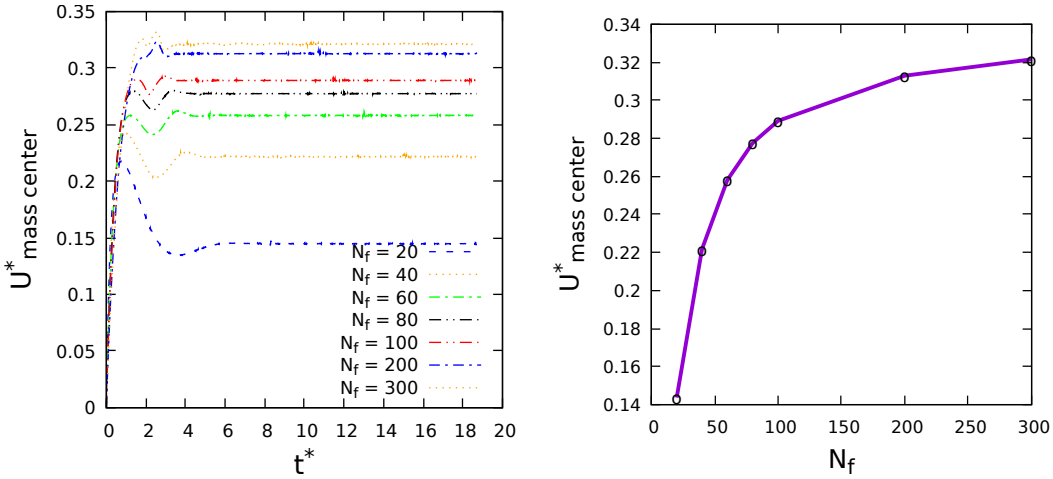

(A) (B)

FIGURE 4.15: (A). Effect of N_f on bubble velocities. (B). Effect of N_f on the bubble terminal velocities.

Cette thèse est accessible à l'adresse : http://theses.insa-lyon.fr/publication/2020LYSEI095/these.pdf
© [L. Guo], [2020], INSA Lyon, tous droits réservés

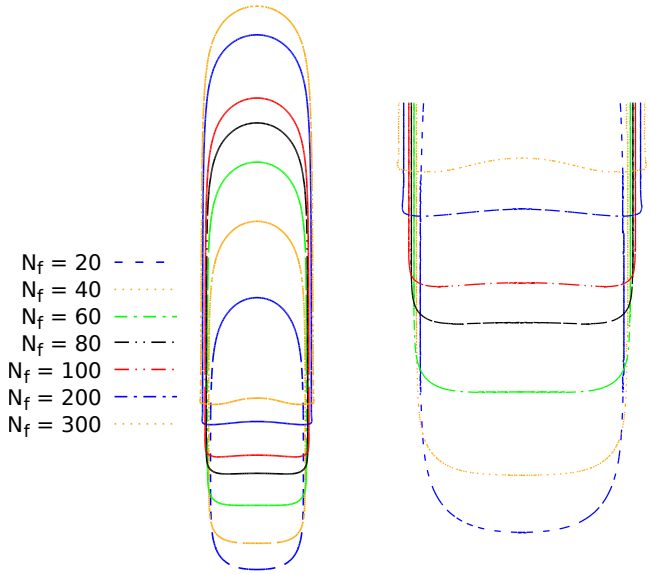

FIGURE 4.16: Effect of N_f numbers on bubble shapes.

4.2 Taylor bubble rising through sudden expansions

In this part, we mainly investigate the Taylor bubble rising in pipes with sudden expansions. Comparisons between experiments (Zhou, 2017) and simulations are also performed.

4.2.1 Physical model description

The numerical model in this section is similar to the model mentioned in the straight pipe. The only difference is the change in pipe diameters. As shown in Fig. 4.17, the geometry contains the upper pipe (D_2) and lower pipe (D_1). The expansion A in Fig. 4.17 represents the sudden expansion of the pipe. The expansion ratio (ϵ) is defined as $\epsilon = \frac{D_2}{D_1}$. The characteristic length is the lower pipe diameter (D_1). All dimensionless parameters are defined with respect to D_1. For simulations of a single Taylor bubble rising in a straight pipe, a moving frame of reference is often adopted (see Taha and Cui (2006); Liu and Wang (2008); Araújo et al. (2012)). A computational domain moving along with the bubble can significantly reduce the computational load and eliminate possible interference of the upper and lower walls. However, our purpose is to study a bubble going through expansions in which the tube diameter is not constant. Therefore, a moving frame of reference would be much more challenging to use, while a fixed frame of reference is relatively straightforward.

Cette thèse est accessible à l'adresse : http://theses.insa-lyon.fr/publication/2020LYSEI095/these.pdf
© [L. Guo], [2020], INSA Lyon, tous droits réservés

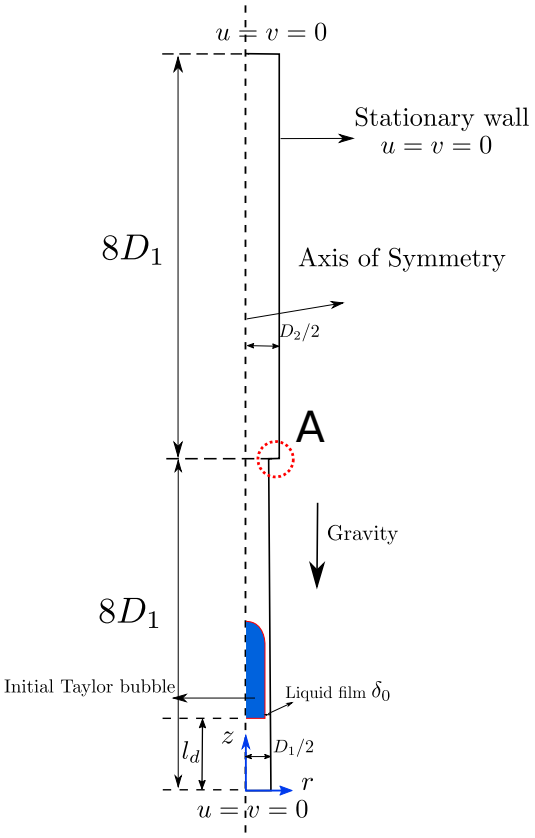

FIGURE 4.17: Schematic diagram of Taylor bubble rising in vertical pipe with sudden expansion.

Illustration of the bubble features

An overview of the hydrodynamic features described in the following sections is illustrated in Fig. 4.18. The center of mass is also the geometric center due to the constant density inside the bubble. The figure shows the locations of the bubble tail center and bubble tail in the z direction. For bubbles with non-concave tail shapes, these two locations coincide. Δ_h is the distance from the expansion to the bubble nose in the z direction, and δ_n is the minimum radius of the bubble body. The reference starting time ($t^* = 0$) is when the bubble head reaches the expansion. In addition, the non-dimensional coordinate is set as $Z^* = (Z - Z_h)/D_1$ and reference position is at expansion ($Z^* = 0$).

Cette thèse est accessible à l'adresse : http://theses.insa-lyon.fr/publication/2020LYSEI095/these.pdf
© [L. Guo], [2020], INSA Lyon, tous droits réservés

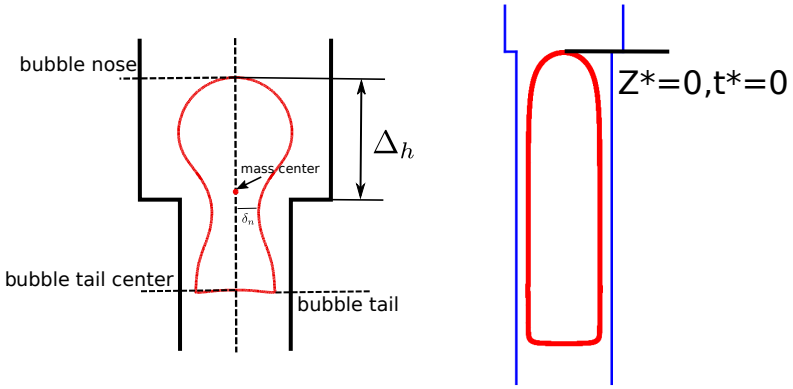

FIGURE 4.18: Illustration of the bubble features described in this study.

4.2.2 Taylor bubble rising in different glycerol-water solutions

Before considering the Taylor bubble rising in mixed glycerol-water liquids through expansion, the Taylor bubble rising in pure water and glycerol through expansion is first studied. Fig. In Fig. 4.19, the liquid is pure, the Taylor bubble rises through the expansion more deformable and the bubble tail oscillates, resulting the bubble motion asymmetrical. In Fig. 4.20, for pure glycerol, the bubble motion is symmetrical, and there is no oscillation in the tail, and the bubble tail shape is more flat after expansion.

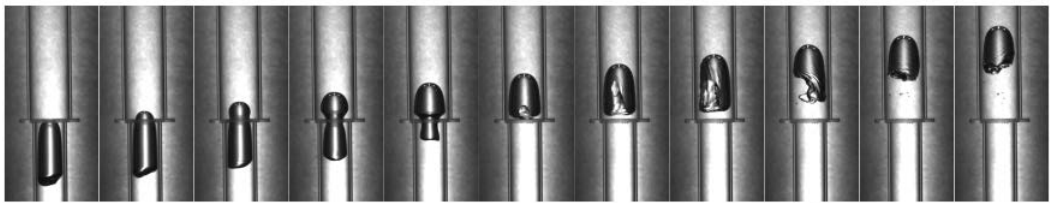

FIGURE 4.19: Experimental Taylor bubble evolution with time rising through the expansion in water ($\epsilon = 1.24$).

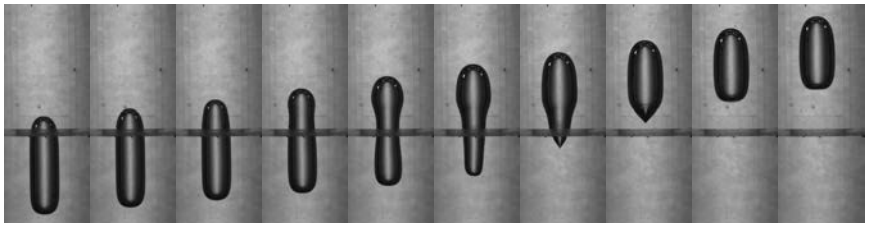

FIGURE 4.20: Experimental Taylor bubble evolution with time rising through the expansion in pure glycerol ($\epsilon = 1.24$).

Five different expansion ratios $\epsilon = [1.73, 1.47, 1.35, 1.24, 1.12]$ are performed according to the experiments. In the experiments, five different glycerol-water solutions are used with properties given in Table. 4.1. In Fig. 4.21, we summarize the

Cette thèse est accessible à l'adresse : http://theses.insa-lyon.fr/publication/2020LYSEI095/these.pdf
© [L. Guo], [2020], INSA Lyon, tous droits réservés

Taylor bubble velocity before and after different expansions at the steady state. It is noted the characteristic length for the upper pipe is the diameter of the upper pipe for the Taylor bubble steady state. The results show that the Taylor bubble velocity increases after expansions. Moreover, in the same liquid (correspond to N_f), the velocity increases with the increase of expansion ratios. With a smaller N_f number, the Taylor bubble velocity is smaller.

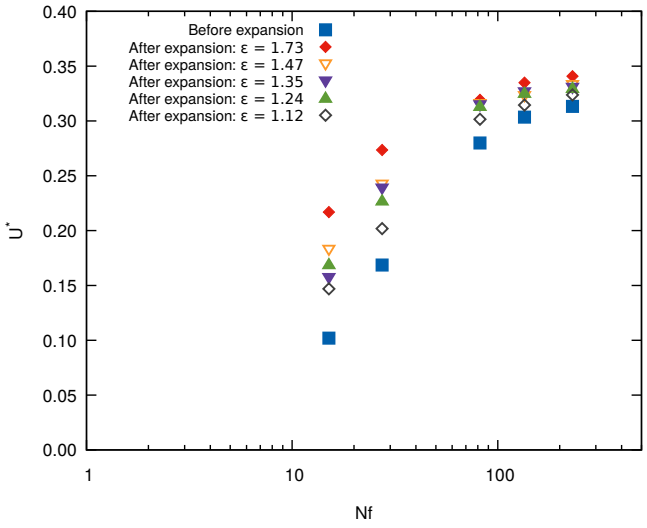

FIGURE 4.21: The Taylor bubble velocity as a function of N_f numbers.

In the following parts, we consider two main problems. First, we fix $\epsilon = 1.24$ to study the Taylor bubble rising in different glycerol-water solutions (Table. 4.1). Second, we consider the effect of the expansion ratio in a fixed solution, more details are provided in the case of $G-W$: 80%, $Mo = 0.00224$, $Eo = 48.3$. It should be noted the initial bubble volume in experiments is not constant for all cases. Therefore, we compare the results of experiments and simulations (see Table. 4.3) with equivalent bubble volumes. Then we keep the initial bubble volume $l_0 = 7r_b$ to investigate the effect of expansion ratio.

TABLE 4.3: The initial equivalent bubble length for simulations.

Expansion ratios	Initial bubble length (l_0)
1.73	$4.5r_b$
1.47	$3.9r_b$
1.35	$7.4r_b$
1.24	$7r_b$
1.12	$4.8r_b$
0.94 (contraction ratio)	$5r_b$

Cette thèse est accessible à l'adresse : http://theses.insa-lyon.fr/publication/2020LYSEI095/these.pdf
© [L. Guo], [2020], INSA Lyon, tous droits réservés

Taylor bubble shapes

Experimental and simulation results with the same expansion ratio ($\epsilon = 1.24$) are demonstrated in Fig. 4.22, corresponding to different glycerol-water solutions. Several basic results could be obtained:

- The bubble frontal diameter becomes larger after expansions.
- The bubble body is shrunk when passing through the expansions, which is named as "necking".
- The bubble tail shape is more flat after expansions.

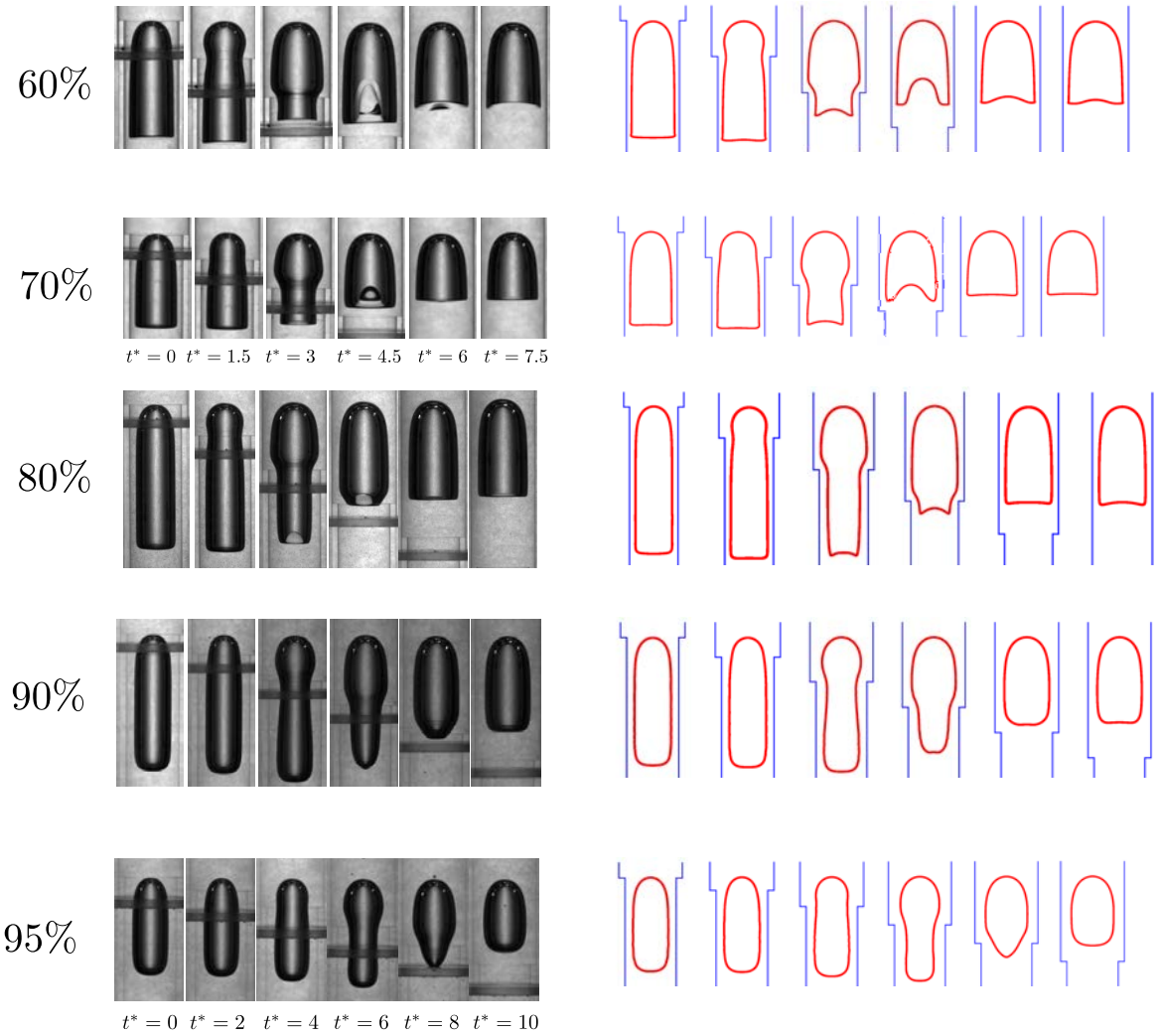

FIGURE 4.22: Experimental and simulation results of Taylor bubble rises through the same expansion in different glycerol-water solutions (% represents percentage of glycerol, expansion ratio $\epsilon = 1.24$).

Taylor bubble velocity

The variation of the bubble velocity through the expansion is investigated and compared with the experimental results in Fig. 4.23. Four typical positions are

Cette thèse est accessible à l'adresse : http://theses.insa-lyon.fr/publication/2020LYSEI095/these.pdf
© [L. Guo], [2020], INSA Lyon, tous droits réservés

adopted for numerical velocity analysis: the bubble nose, the bubble tail, the bubble tail center, and the bubble center of mass (Fig. 4.18). The experimental velocities are computed by measuring the deviation of two consecutive images for bubble nose and tail position. The time series of bubble velocities were obtained by processing more than 2000 images.

In Fig. 4.23, the bubble velocity varies as a function of dimensionless time. The experimental and simulation results match well, especially for the bubble nose. The distinct difference for tail velocity is caused by the oscillation of the tail when passing through the expansion, which is hard to measure in experiments. When the bubble nose begins to accelerate as it passes through the expansion, the tail remains unchanged. Therefore, the bubble length was elongated during this period, and the bubble body is shrunk at the expansion. James et al. (2006) concluded the liquid around the bubble nose is fallen rapidly into the top of the smaller pipe due to the bubble rising motion, and the liquid is accumulated at the expansion forming a thickening annulus in the falling liquid film. Consequently, as the liquid continues to flow into the falling annulus, an increasingly narrow neck is formed when the bubble's nose becomes larger.

When the bubble reaches the minimum neck radius (δ_n), the tail is rapidly accelerated, and the velocity reaches a peak value. The bubble tail center velocity is larger than the bubble tail, which leads to liquid protrusion inside the bubble. Fig. 4.24 shows the fluid motion ahead of the bubble nose. The amount of liquid moves towards the bubble tail and accumulates there. The liquid at the bubble tail affects the bubble tail shape. In Fig. 4.25, we plot the velocity streamlines using the Taylor bubble mass center velocity as a reference frame. It shows two symmetrical vortexes are formed at bubble tail after the expansion, which illustrates the bubble tail shape is more concave corresponds to a higher effective N_f after the expansions, and the amount of liquid is accumulated.

Cette thèse est accessible à l'adresse : http://theses.insa-lyon.fr/publication/2020LYSEI095/these.pdf
© [L. Guo], [2020], INSA Lyon, tous droits réservés

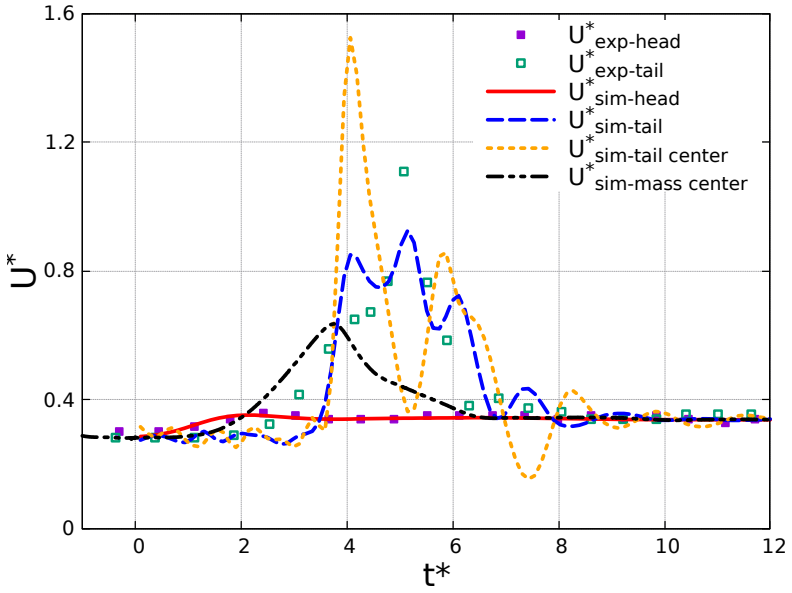

FIGURE 4.23: The comparisons of experimental and simulation Taylor bubble velocities ($G-W:80\%, \epsilon=1.24, Mo=0.00224, Eo=48.3$).

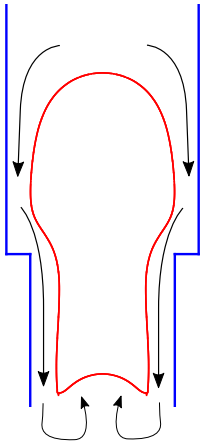

FIGURE 4.24: The schematic diagram of surrounding liquid motion when Taylor bubble passing through expansions.

Cette thèse est accessible à l'adresse : http://theses.insa-lyon.fr/publication/2020LYSEI095/these.pdf
© [L. Guo], [2020], INSA Lyon, tous droits réservés

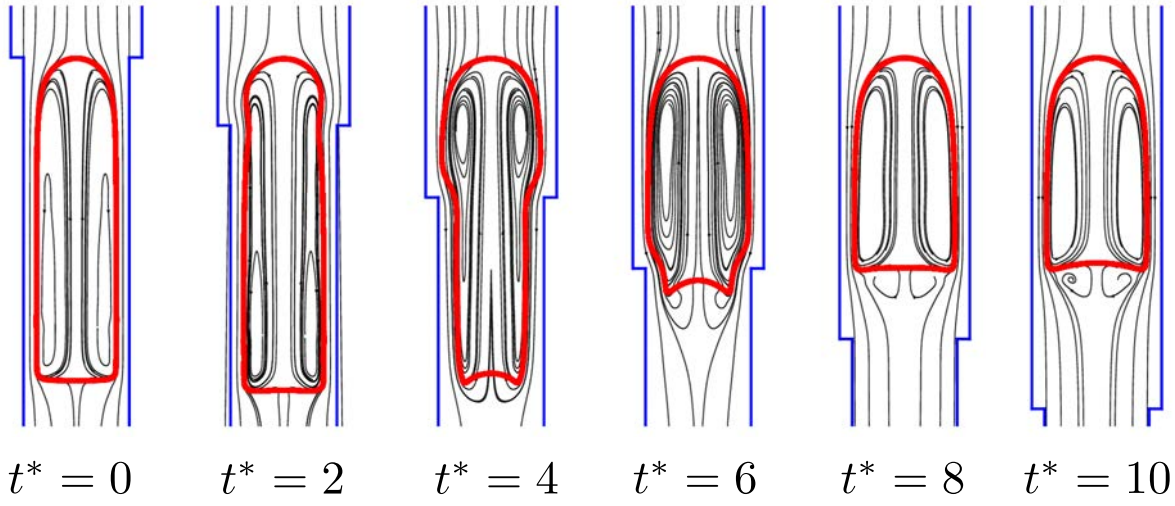

FIGURE 4.25: The streamlines of Taylor bubble rising through the expansion with evolution of time ($G - W : 80\%, \epsilon = 1.24, Mo = 0.00224, Eo = 48.3$).

Wall shear stress

When the Taylor bubble rises in the vertical pipe, the wall shear stress is an important factor to describe the strength of acceleration of the bubble. As depicted in Fig. 4.26 (A), the evolution of the dimensionless wall shear stress ($\tau_w/(\rho_l g D_1)$) is presented for five time instants when bubble is rising. It is observed that the wall shear stress reaches a kind of plateau and maintains constant along with the bubble before the expansion. Near the wall of the expansion, there is a narrow high shear stress region. After the expansion, the wall shear stress first goes down shortly, and then increases sharply to another plateau. This also illustrates that the presence of the expansion changes the flow velocity in the liquid film around the bubble. Fig. 4.26 (B) shows the wall shear stress at steady state becomes bigger after the expansion. The according bubble shapes and velocity vector field are displayed in Fig. 4.27. It shows at expansion, the bubble moves faster, which corresponds to a larger wall shear stress (i.e., position 4). While the bubble nose becomes larger, great variation for wall shear stress near the expansion occurs.

Cette thèse est accessible à l'adresse : http://theses.insa-lyon.fr/publication/2020LYSEI095/these.pdf
© [L. Guo], [2020], INSA Lyon, tous droits réservés

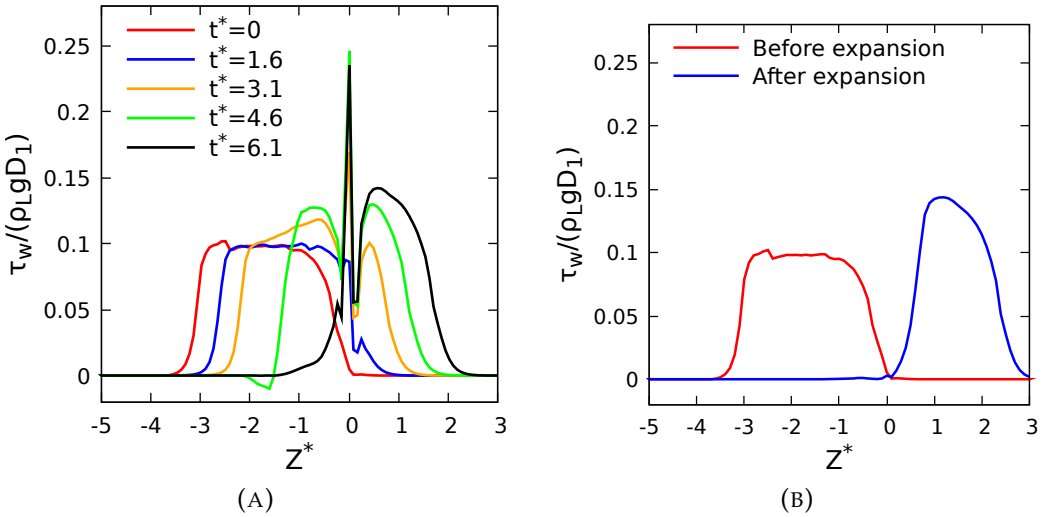

(A) (B)

FIGURE 4.26: (A). Dimensionless wall shear stress for different bubble positions along the axial distance from the bubble nose. (B). Wall shear stress at steady state before and after the expansion ($G-W$: 80%, $\epsilon = 1.24$, $Mo = 0.00224$, $Eo = 48.3$).

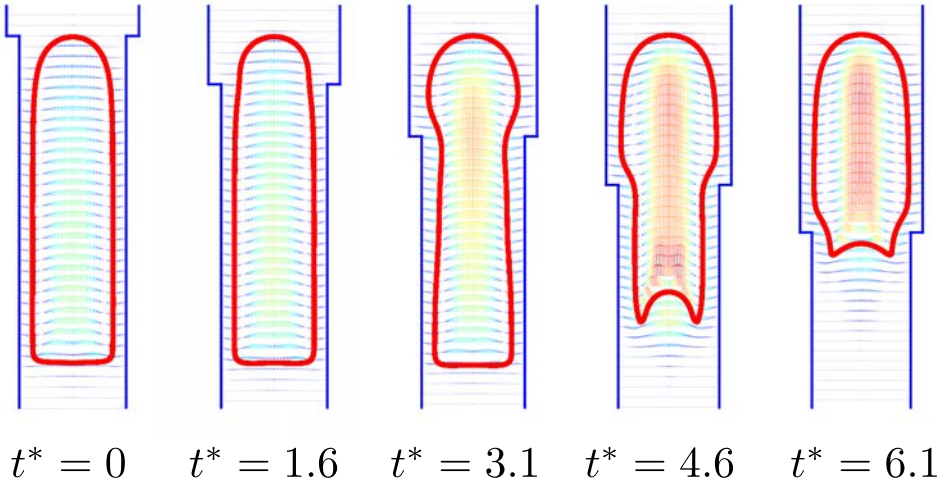

FIGURE 4.27: Bubble velocity vector field corresponds to the position in Fig. 4.26 ($G-W$: 80%, $\epsilon = 1.24$, $Mo = 0.00224$, $Eo = 48.3$).

Pressure distribution around Taylor bubble

Another important parameter is the pressure drop. The pressure distribution around the Taylor bubble at the radial midpoint of the liquid film is shown in Fig. 4.28. The dominant pressure variation in the flow channel is caused by gravity. Therefore, $p' = (p - \rho_l g Z_h)/(\rho_l g D_1)$ is used to eliminate the effect of gravity and purely reveal the pressure variation caused by the flow. Six axial positions are selected to present the pressure distribution when the bubble passes through the expansion. It can be observed that when the bubble nose enters the expansion, the change of pressure is not obvious (see position a, b, c). However, when the bubble body is in the expansion, there is a sharp pressure drop before expansion, and a steep ascent in the

Cette thèse est accessible à l'adresse : http://theses.insa-lyon.fr/publication/2020LYSEI095/these.pdf
© [L. Guo], [2020], INSA Lyon, tous droits réservés

expansion (see position d, e). When the bubble leaving the expansion, the pressure gradually changes to be similar to the situation before expansion (see position f).

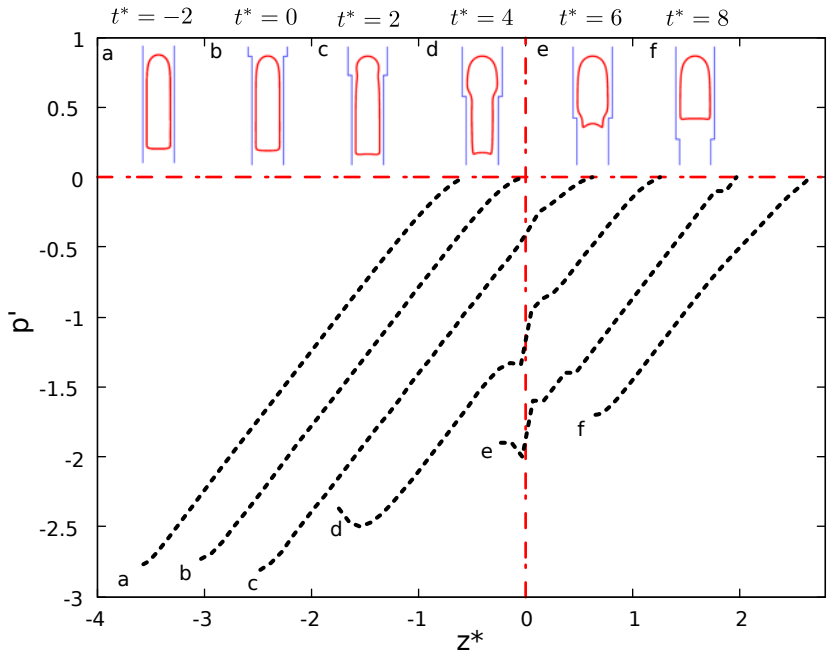

FIGURE 4.28: Pressure distribution in the middle of the liquid film around Taylor bubble and the corresponding snapshots of the bubble shape ($G-W$: $80\%, \epsilon = 1.24, Mo = 0.00224, Eo = 48.3$).

4.2.3 Taylor bubble through sudden expansions with different ratios

In Fig. 4.29, we compare the bubble shapes of experimental results and simulations for different expansion ratios in the same glycerol-water solution (Table. 4.1). It is observed that with an increase of the ϵ, the bubble is more easily deformed, and bubble movement is more intense at the expansion.

The initial bubble volume could not be maintained for all cases in experiments. To investigate the dynamics of Taylor bubbles rising through different expansion ratios, the same initial conditions are adopted for each case using experimental case $G-W$: $80\%, l_0 = 7r_b$ in Table. 4.1. Five different expansion ratios are performed, which are $\epsilon = [1.73, 1.47, 1.35, 1.24, 1.12]$.

Cette thèse est accessible à l'adresse : http://theses.insa-lyon.fr/publication/2020LYSEI095/these.pdf
© [L. Guo], [2020], INSA Lyon, tous droits réservés

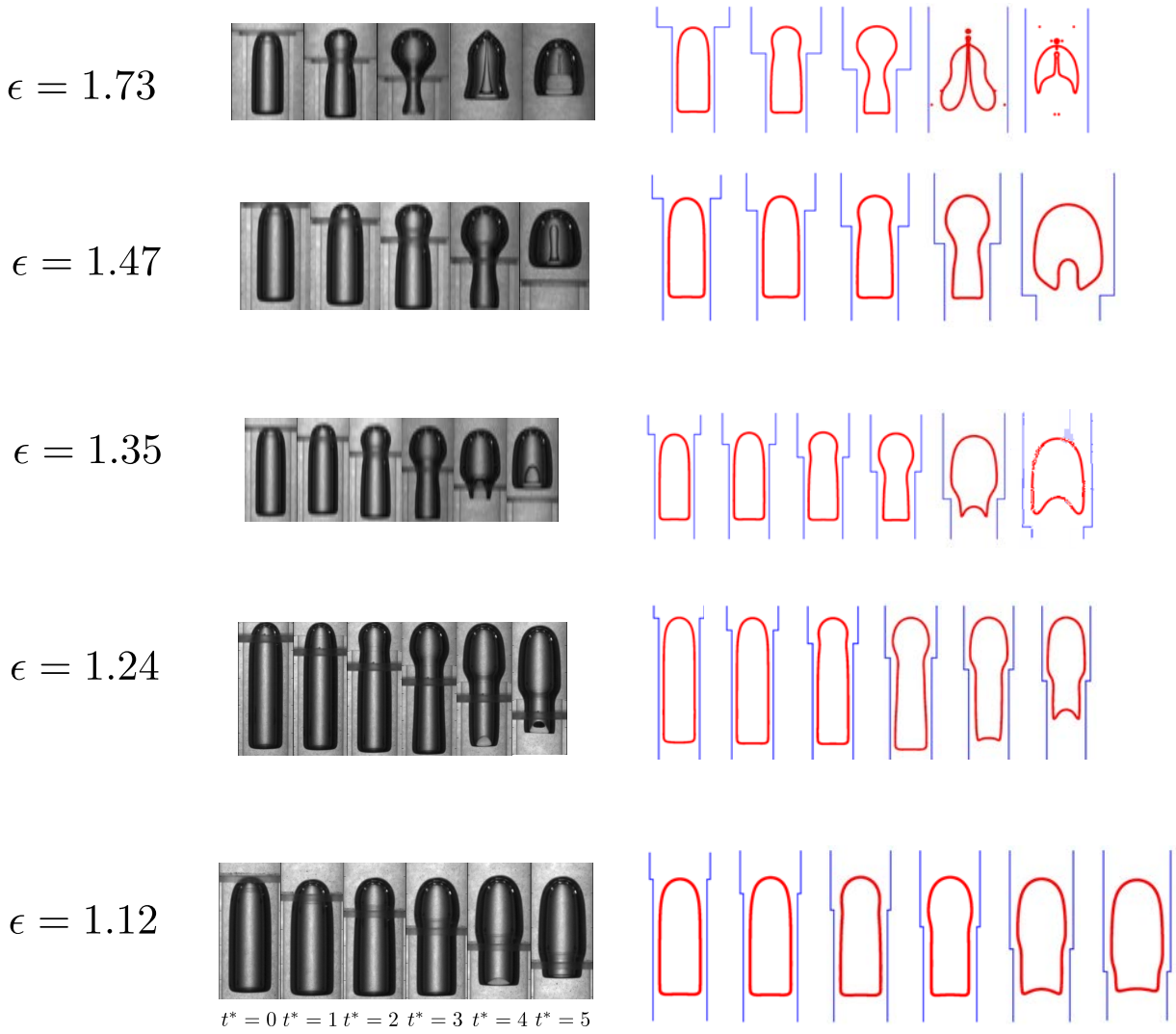

FIGURE 4.29: Experimental and simulation results of Taylor bubble rises through different expansion ratios (ϵ) in the same glycerol-water solution (80%).

Bubble shapes

Fig. 4.30 displays the evolution of the bubble shapes as a function of time. When $\epsilon = 1.73$, there are two particular phenomena noted. One is the bubble pinched off from the necking at the expansion position. The volume of the upper bubble is larger than the lower one. Secondly, two separated bubbles are all penetrated when going through the expansion. With a decrease in the expansion ratios, the bubble moves entirely through the expansion. Fig. 4.31 shows the bubble length varies in different expansion ratios. The large $\epsilon = 1.73$ is not considered here due to large deformation. The bubble rises through expansion, having three stages. First, bubble length does not change early when the bubble entering the expansion. Then the bubble is shrinking, leading to the bubble length elongated. There is a peak length value. After the bubble leaving the expansion, the bubble becomes shorter. We demonstrate the position for bubble tail leaving the expansion. The corresponding time shows smaller ϵ

Cette thèse est accessible à l'adresse : http://theses.insa-lyon.fr/publication/2020LYSEI095/these.pdf
© [L. Guo], [2020], INSA Lyon, tous droits réservés

needs more time for bubble leaving expansions.

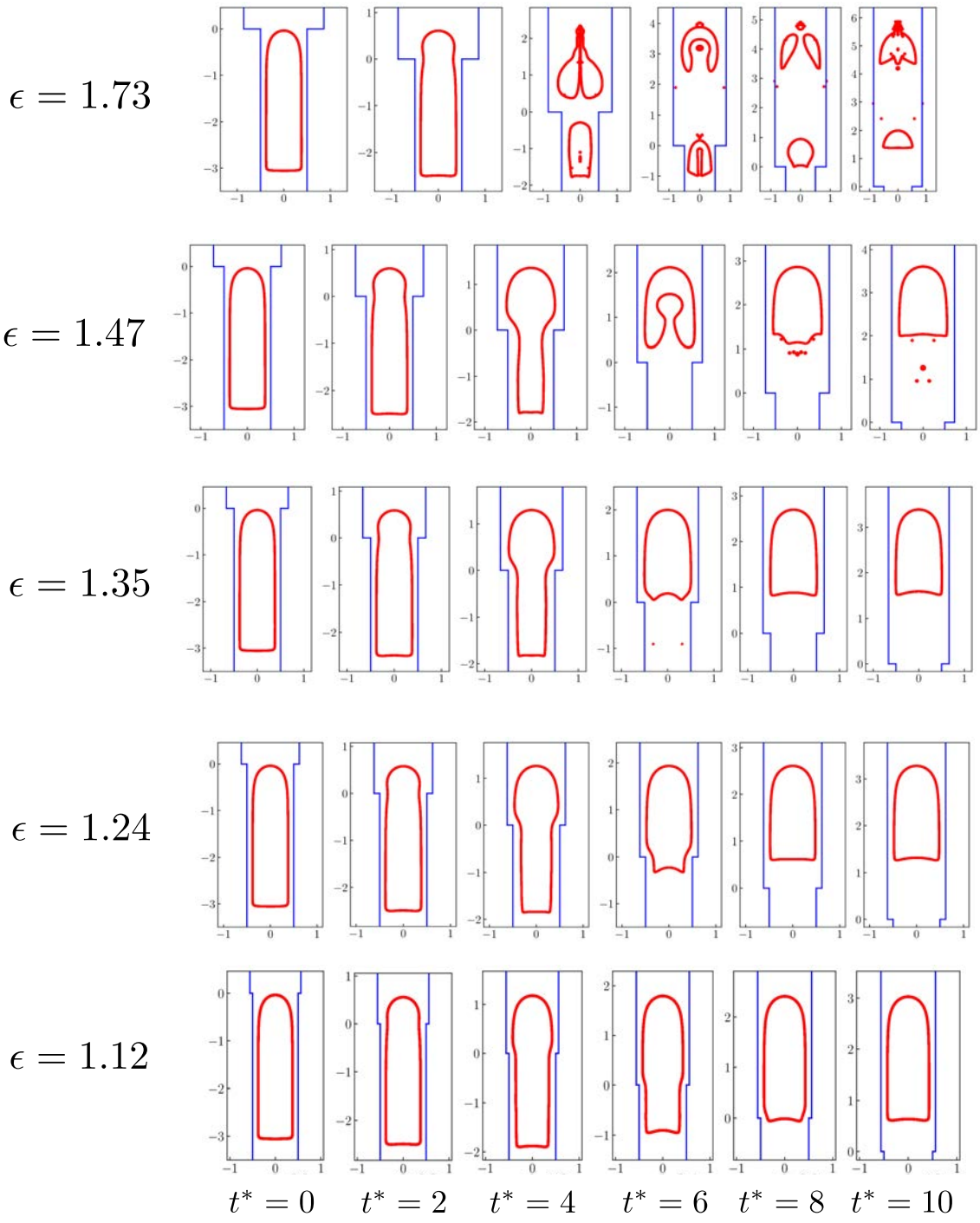

FIGURE 4.30: The simulation results of bubble shapes with different expansion ratios under same bubble length.

Cette thèse est accessible à l'adresse : http://theses.insa-lyon.fr/publication/2020LYSEI095/these.pdf
© [L. Guo], [2020], INSA Lyon, tous droits réservés

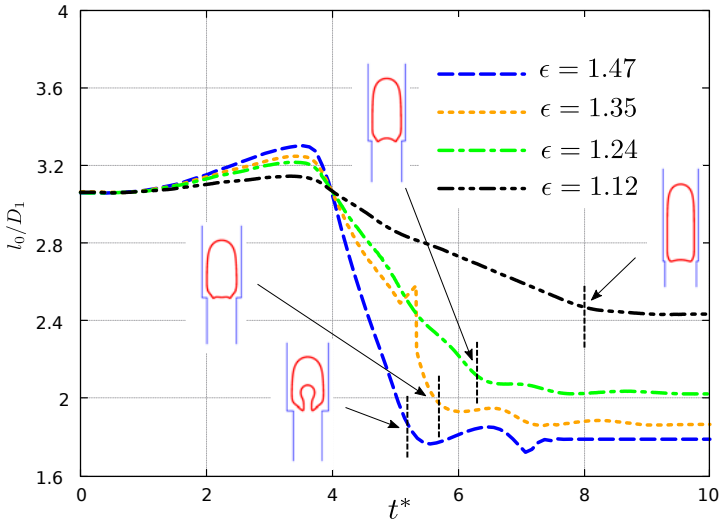

FIGURE 4.31: Evolution of bubble length for different expansion ratios as a function of time.

Frontal radius for Taylor bubble nose

The deformation of the Taylor bubble nose is characterized by the estimation of the mean curvature radius at the bubble head point, defining the frontal radius (R_F, see Fig. 4.32). In Fig. 4.32 (A), two steady bubble shape before the expansion and after the expansion are given. The maximum bubble radius (R_{TB}) is obtained by subtracting the stabilized liquid film thickness (δ_l) to the pipe radius, see A and B, the maximum bubble radius is $R_{TB} = D_2/2 - \delta_l$ and $R_{TB} = D_1/2 - \delta_l$, respectively (Araújo et al., 2012). R_F helps understand the topology evolution in the rising process of the Taylor bubble. As shown in Fig. 4.32 (B), after the expansion, $\frac{R_F}{R_{TB}}$ is more close to 1, which demonstrates the bubble nose tends to be circular, and this phenomenon is more obvious for higher ϵ.

Cette thèse est accessible à l'adresse : http://theses.insa-lyon.fr/publication/2020LYSEI095/these.pdf
© [L. Guo], [2020], INSA Lyon, tous droits réservés

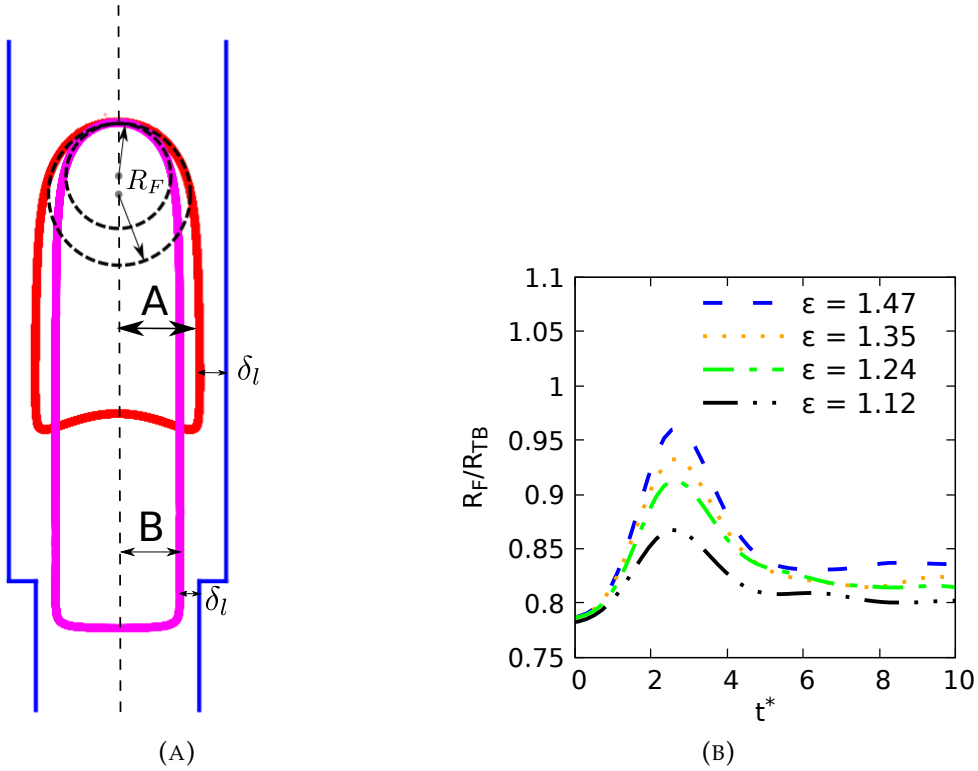

(A) (B)

FIGURE 4.32: (A). Schematic diagram of bubble shape before and after the expansion (B). Frontal radius of the bubble in different expansion ratios ($G - W$: 80%, $Mo = 0.00224$, $Eo = 48.3$).

Wall shear stress and pressure distribution

Fig. 4.33 shows the Taylor bubble rising in the expansion at $t^* = 3$ for different expansion ratios. The wall shear stress is given for the part of the bubble before the expansion. It is observed, the wall shear stress has a sharp increase at the bubble tail, and a peak value is reached. Near the expansion, the peak wall shear stress first decreases, and it shows a larger expansion ratio has a steeper tendency. After the wall shear stress reaching the minimum value, which correspond to the minimum bubble neck radius, the wall shear stress increases sharply at the expansion. The larger expansion ratio has larger wall shear stress at the expansion point ($Z^* = 0$).

Cette thèse est accessible à l'adresse : http://theses.insa-lyon.fr/publication/2020LYSEI095/these.pdf
© [L. Guo], [2020], INSA Lyon, tous droits réservés

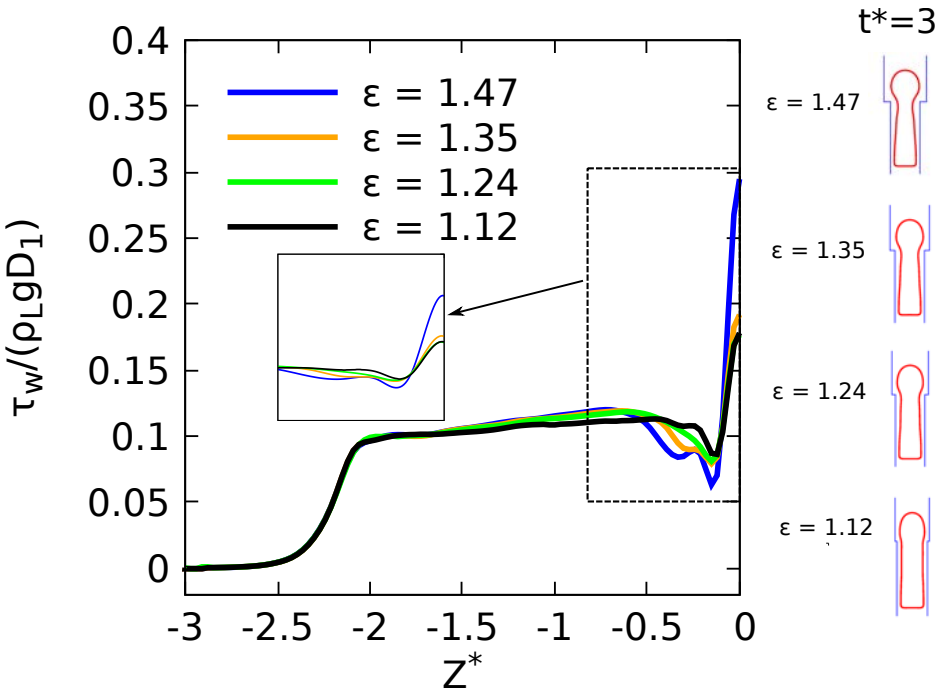

FIGURE 4.33: Dimensionless wall shear stress for different expansion ratios with the same bubble initial length at $t^* = 3$ ($G-W$: 80%, $Mo = 0.00224$, $Eo = 48.3$).

The pressure distribution in Fig. 4.33 shows the pressure drop for the Taylor bubble at $t* = 3$ with different expansion ratios. The pressure drop for all expansion ratios are approximated linear increasing except for the expansion section. In the expansion,the pressure drop has a sharp steep increasing, and this phenomenon is more obvious for larger expansion ratios. The reason is that larger expansion ratios would provide more acceleration for the Taylor bubble.

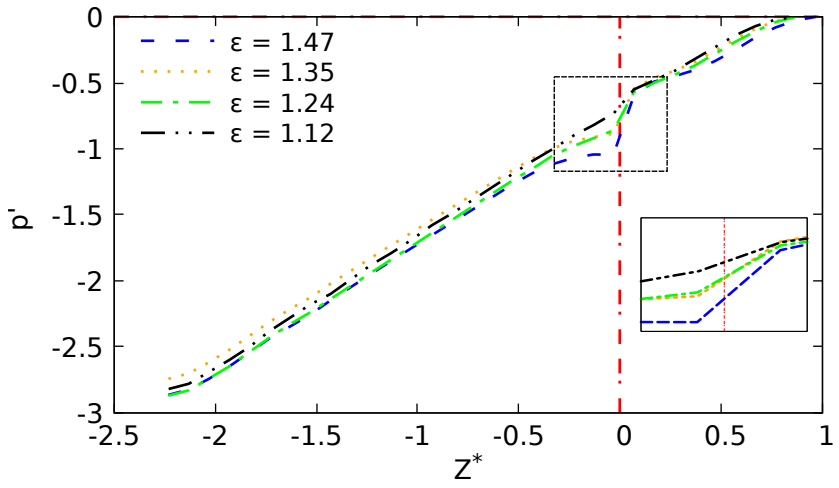

FIGURE 4.34: Pressure drop for different expansion ratios with the same bubble initial length at $t^* = 3$ ($G-W$: 80%, $Mo = 0.00224$, $Eo = 48.3$).

Cette thèse est accessible à l'adresse : http://theses.insa-lyon.fr/publication/2020LYSEI095/these.pdf
© [L. Guo], [2020], INSA Lyon, tous droits réservés

Taylor bubble velocity

Fig. 4.35 shows the Taylor bubble velocity of the center of mass as a function of dimensionless time. The peak of the velocity is at the same time for each ϵ with the same initial bubble length. As expected, the larger expansion ratios change more significantly and have larger velocity than lower expansion ratios. This is consistent with the conclusion that the higher expansion ratio induces stronger perturbation of the liquid inside the bubble at expansion. The bubble tail is more flat and not concave for higher expansion ratios. For lower expansion ratios, the bubble reaches the new terminal state earlier.

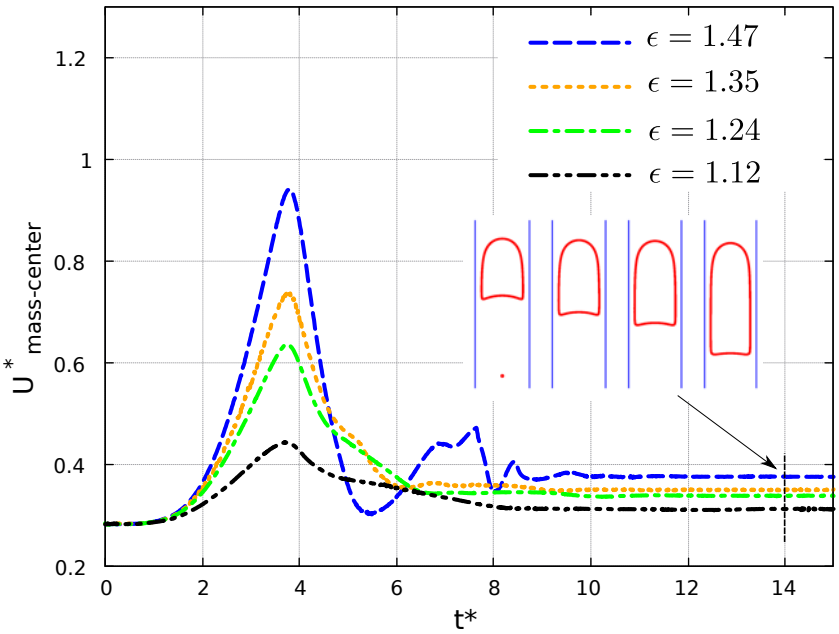

FIGURE 4.35: Evolution of the mass center velocity of Taylor bubbles through different expansion ratios with same surrounding liquid ($G - W$: 80%, $Mo = 0.00224$, $Eo = 48.3$).

Necking

Unlike straight vertical pipe, a particular feature for the Taylor bubble passing through expansions is a neck region. The minimum bubble neck radius δ_n defined in Fig. 4.18 is used to study the evolution of bubble neck. Fig. 4.36 illustrates the evolution of δ_n when the bubble passes through the expansions. The position A is where the bubble reaches the largest δ_n, the corresponding images of the bubble at this position show similar shapes, which means the expansion has a minor effect on the bubble nose entering the expansion. The formation of the bubble neck interprets the flow pattern in the vicinity of the expansion. As similar in a vertical straight pipe, when the bubble rises, the liquid around the bubble nose is pushed away, and a falling liquid film is created that drains the flow in the liquid film to the bubble tail region. In expansion cases, the neck region makes the velocity in liquid film decelerate above. From the observation of the minimum position of neck radius in Fig. 4.36,

Cette thèse est accessible à l'adresse : http://theses.insa-lyon.fr/publication/2020LYSEI095/these.pdf
© [L. Guo], [2020], INSA Lyon, tous droits réservés

the larger expansion has smaller neck radius. For $\epsilon = 1.12$, there is no minimum neck radius, which means the bubble slowly passes through the expansion. The velocity in the liquid film is so small that it can not make the bubble neck deformed.

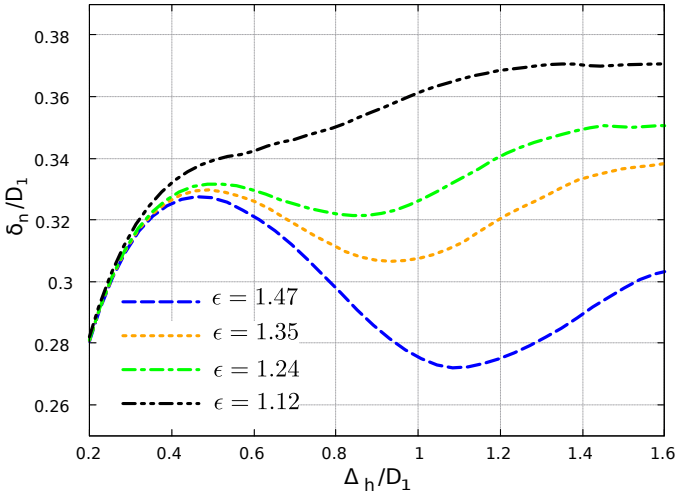

FIGURE 4.36: Evolution of the bubble neck radius for different expansion ratios as a function of the bubble head position ($G - W$: 80%, $Mo = 0.00224$, $Eo = 48.3$).

4.2.4 Special bubble shapes when rising through large expansion ratios

When studying individual Taylor bubble rising through expansions, an interesting phenomenon has been observed in experiments. As seen in Fig. 4.37, the bubble tail will penetrate towards the bubble nose after leaving the expansion. The previous experimental work by Kondo et al. (2002) and Carter et al. (2016) also found this penetration phenomenon after the bubble leaving the expansion. The extent of the penetration depends on the velocity of the rear of the bubble, i.e., the effect of the expansion ratio through the analysis of the previous sections. This phenomenon is not easily captured in 2D simulations. Therefore, we use 3D simulations to describe this phenomenon more precisely. In the work of Ambrose et al. (2017), they performed 3D simulations to study individual Taylor bubble rising through expansions, however, their research more focuses on the bubble breakup phenomenon after the expansion. In this case, we prefer to study the bubble entirely rises through expansion with penetration phenomenon. Fig. 4.38 shows our 3D simulations match well with the experiments, it is available to proceed the following investigations.

Cette thèse est accessible à l'adresse : http://theses.insa-lyon.fr/publication/2020LYSEI095/these.pdf
© [L. Guo], [2020], INSA Lyon, tous droits réservés

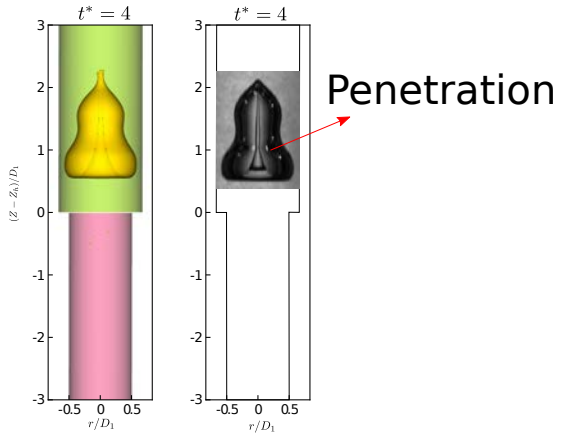

FIGURE 4.37: Bubble shape evolution after expansion ($G - W$: $70\%, Mo = 1.96 \times 10^{-4}, Eo = 46.7, \epsilon = 1.73$).

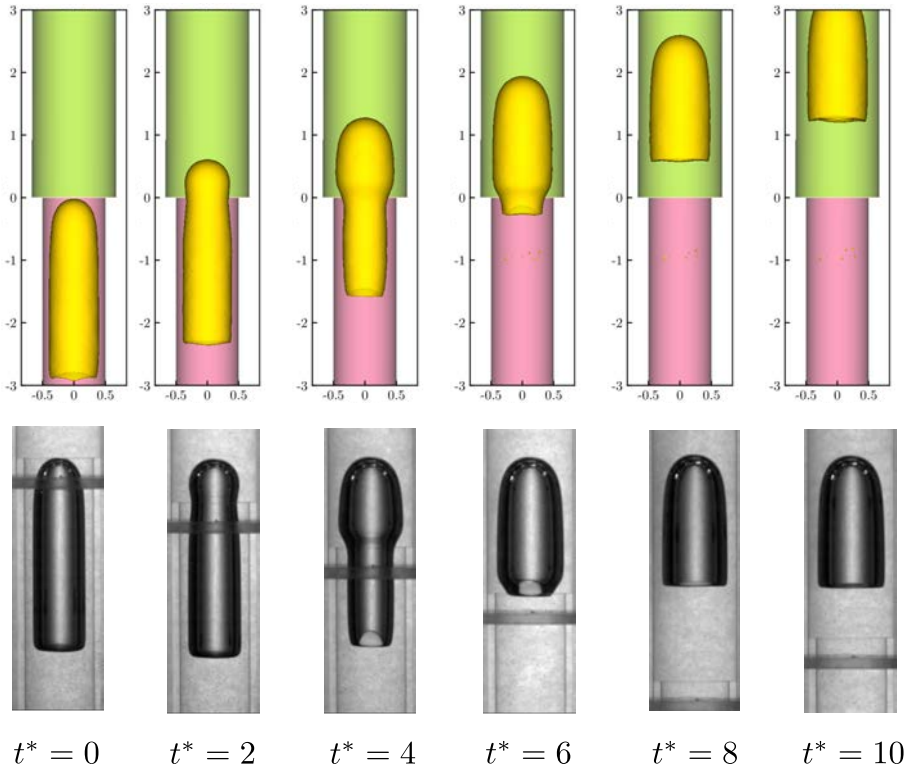

FIGURE 4.38: Bubble shape evolution after expansion ($G - W$: $80\%, \epsilon = 1.24, Mo = 0.00224, Eo = 48.3$).

Fig. 4.39 and Fig. 4.40 show a relatively complete plot of bubble variation with different expansion ratios. The reference time is the bubble head reaches the expansion, see Fig. 4.39. In Fig. 4.39, the tail of the bubble penetrates towards the bubble nose, which creates some small bubbles on the outside of the top of the bubble (see point A), similar results can be found in Ambrose et al. (2017). Then the liquid column inside the bubble begins to drop by gravity and oscillates back and forth near the tail (See point B). This is the reason that the tail velocity cannot be measured accurately in the experiment. In Fig. 4.40, with a relatively smaller expansion ratio, the bubble tail

Cette thèse est accessible à l'adresse : http://theses.insa-lyon.fr/publication/2020LYSEI095/these.pdf
© [L. Guo], [2020], INSA Lyon, tous droits réservés

will not penetrate the bubble nose. It forms a thin liquid column inside the bubble (see point A). Then, as the case $\epsilon = 1.73$ did, the liquid column will fall and oscillate near bubble tail. However, from point B, we can observe a thin gas column.

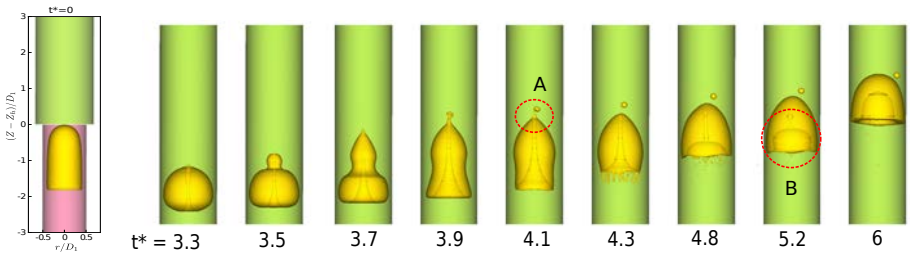

FIGURE 4.39: Penetration of Taylor bubble rising through large expansion ratio ($G-W$: 70%, $Mo = 1.96 \times 10^{-4}$, $Eo = 46.7$, $\epsilon = 1.73$).

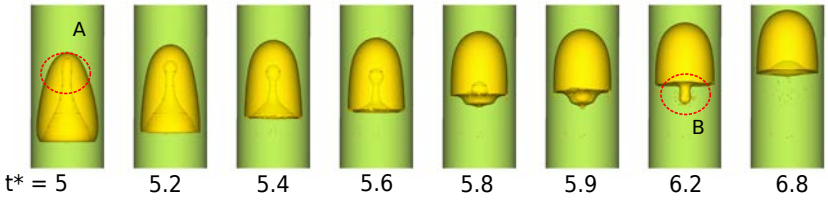

FIGURE 4.40: Bubble shape evolution after expansion ($G-W$: 70%, $Mo = 1.96 \times 10^{-4}$, $Eo = 46.7$, $\epsilon = 1.47$).

4.2.5 Bubble breakup pattern

Fit. 4.41 shows the Taylor bubble is split into two small parts in experiment and simulation. The bubble breakup position is not at the expansion, it is below the expansion structure. After the bubble breaks up, the lower part will move through the expansion. If the bubble length is long enough, the lower part undergoes a similar breakup pattern. As the experiments results shown in Fig. 4.42, four different Taylor bubble volumes are used. The expansion ratio $\epsilon = 1.73$ is the same for all cases. It is observed in Fig. 4.42 (A), the bubble rises through expansion without breakup. However, with the increase of the bubble volume, the Taylor bubble shows breakup at expansion, especially in case D, Where the bubble volume is large enough to split the bubble into three parts.

Cette thèse est accessible à l'adresse : http://theses.insa-lyon.fr/publication/2020LYSEI095/these.pdf
© [L. Guo], [2020], INSA Lyon, tous droits réservés

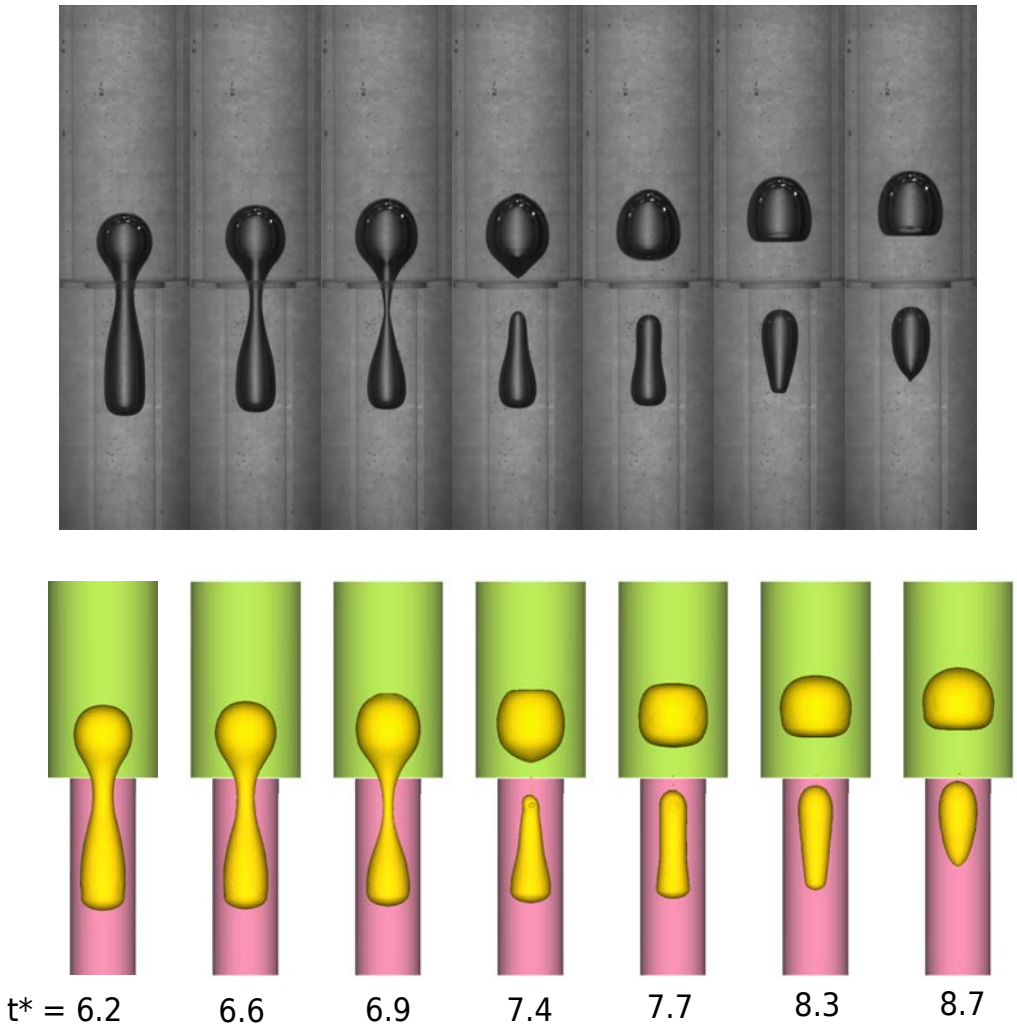

FIGURE 4.41: Experiments and simulations of bubble breakup process when bubble rises through expansion. ($G-W$: $90\%, \epsilon = 1.73, Mo = 0.199, Eo = 49.8$,).

Cette thèse est accessible à l'adresse : http://theses.insa-lyon.fr/publication/2020LYSEI095/these.pdf
© [L. Guo], [2020], INSA Lyon, tous droits réservés

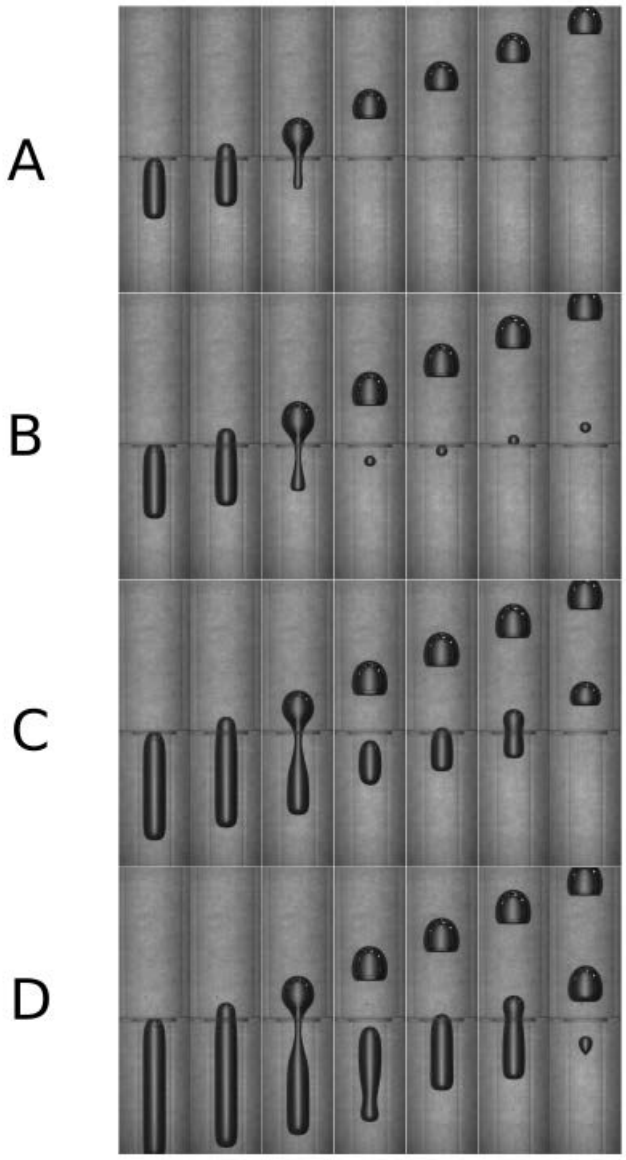

FIGURE 4.42: Taylor bubble with different initial volume rises through expansion in experiments (Zhou, 2017) ($G-W$: $90\%, Mo = 0.199, Eo = 49.8, \epsilon = 1.73$).

Based on the results of the experiments, the Taylor bubble breakup phenomenon is studied in two aspects:

- Fixing the initial Taylor bubble volume, while changing the expansion ratios. The objective of this part is to find the critical expansion ratio at each Eo number.
- Fixing the Eo number, while changing the initial bubble length to find the critical value at a fixed expansion ratio. The objective of this part is to find the critical length of the Taylor bubble rising through expansions.

Cette thèse est accessible à l'adresse : http://theses.insa-lyon.fr/publication/2020LYSEI095/these.pdf
© [L. Guo], [2020], INSA Lyon, tous droits réservés

Breakup pattern – critical expansion ratio

In this section, a wide range of expansion ratios from 1.1 to 3.0 are added to illustrate the dynamics of the Taylor bubble with larger expansion ratios. The Morton number is independent of the pipe diameters. Therefore, a group of the simulations are carried out with a fixed value of Morton number $Mo = 0.00224$, and this value is equal to the $G - W : 80\%$ experimental mixture. In this study, the initial length of the bubble is fixed to $9r_b$.

For a fixed Eo number and in the given range of expansion ratios, the bubble behavior presents three break-up patterns, as shown in Fig. 4.43. The three patterns are interpreted in details as follows:

- Intact: The Taylor bubble rising through expansion entirely.
- Single-breakup: The bubble is divided into two parts when passing through expansions.
- Double-breakup: The bubble is divided into three parts when passing through expansions.

In Fig. 4.43, the solid line separates the intact and single-breakup patterns; the dashed line is for separating the single-breakup and double-breakup. We can conclude in lower Eo numbers and larger expansion ratios, the bubble is easier to break up. The bubble initially $l_0 = 9l_b$ undergoes three stages when gradually increases the expansion ratios for a fixed Eo: bubble entirely passing through, bubble is split into two parts and bubble is split into three parts. If giving a larger initial bubble volume, the bubble may be split into more small parts.

Cette thèse est accessible à l'adresse : http://theses.insa-lyon.fr/publication/2020LYSEI095/these.pdf
© [L. Guo], [2020], INSA Lyon, tous droits réservés

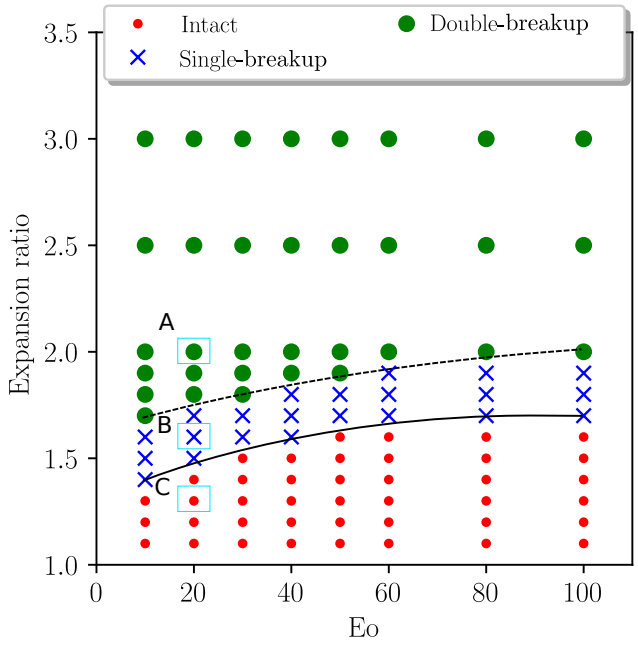

FIGURE 4.43: Bubble break-up map is obtained by simulations ($Mo = 0.00224, l_0 = 9r_b$).

In order to further investigate the break-up patterns, three points in Fig. 4.44 at $G - W : 80\%, Eo = 20, Mo = 0.00224$ with different expansion ratios are analyzed, which are A ($\epsilon = 2$), B ($\epsilon = 1.6$), and C ($\epsilon = 1.3$). We briefly compare the bubble shapes for different expansion ratios in Fig. 4.44. The results show that the expansion accelerates the bubble when bubble passing through expansions, and the Taylor bubble has critical length breaking up into two parts.

Cette thèse est accessible à l'adresse : http://theses.insa-lyon.fr/publication/2020LYSEI095/these.pdf
© [L. Guo], [2020], INSA Lyon, tous droits réservés

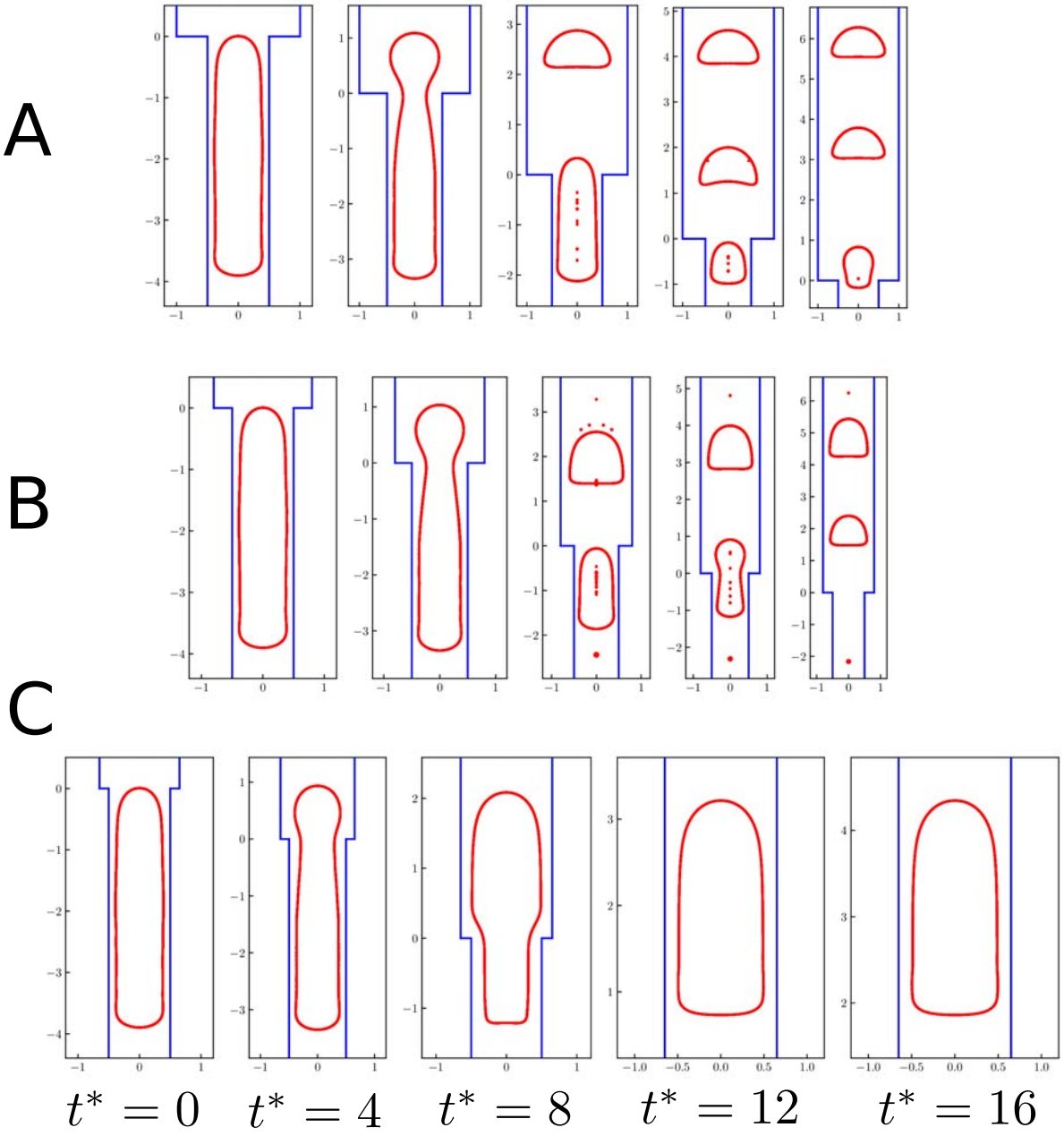

FIGURE 4.44: Bubble break-up map obtained by simulations ($G - W$: $80\%, Eo = 20, Mo = 0.00224, l_0 = 9r_b$).

Cette thèse est accessible à l'adresse : http://theses.insa-lyon.fr/publication/2020LYSEI095/these.pdf
© [L. Guo], [2020], INSA Lyon, tous droits réservés

Breakup pattern – critical bubble length

Through the above analysis, the bubble breaks up when it rises through the expansion of its length large enough. Therefore, it is better to know the critical length for bubble breakup. In this section, the initial bubble volume is changed to find this critical bubble length. The physical parameters are set as $G-W:80\%, Mo=0.00224, Eo=48.3$, while the initial bubble length is changeable. Fig. 4.45 shows the critical bubble length as function of the expansion ratio. As a consequence of the results, the critical bubble length is decreased with increasing the expansion ratios, but this tendency does not appear after $\epsilon > 2.5$. Moreover, for smaller expansion ratio critical length, it should be noted that when the expansion ratio $\epsilon < 1.6$, it is difficult to find the bubble critical length because the Taylor bubble moves through expansion without remains.

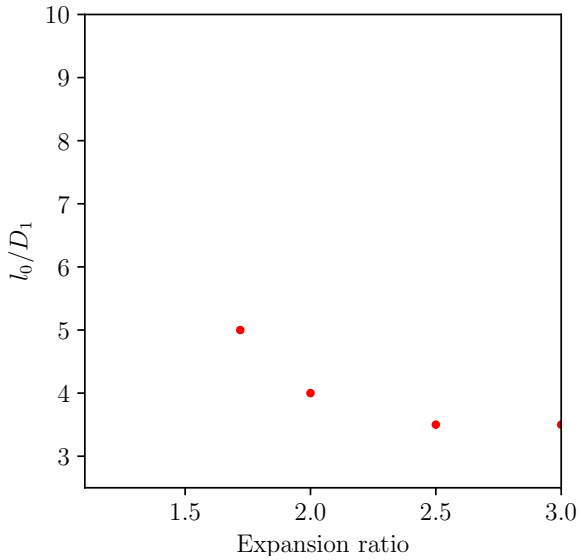

FIGURE 4.45: Bubble break-up map for critical length ($Mo = 0.00224, G-W: 80\%$).

Cette thèse est accessible à l'adresse : http://theses.insa-lyon.fr/publication/2020LYSEI095/these.pdf
© [L. Guo], [2020], INSA Lyon, tous droits réservés

4.3 Taylor bubble rising through sudden contractions

4.3.1 Physical model description

The geometry model for sudden contractions is shown in Fig. 4.46. The expansion A in Fig. 4.46 represents the sudden contraction of the pipe. In this section, several contraction ratios $\epsilon = \frac{D_2}{D_1}$ are compared with experimental data. The Taylor bubble through contractions present a different behavior. In particular, the bubble moves slower than that in the expansion, and the bubble length becomes longer.

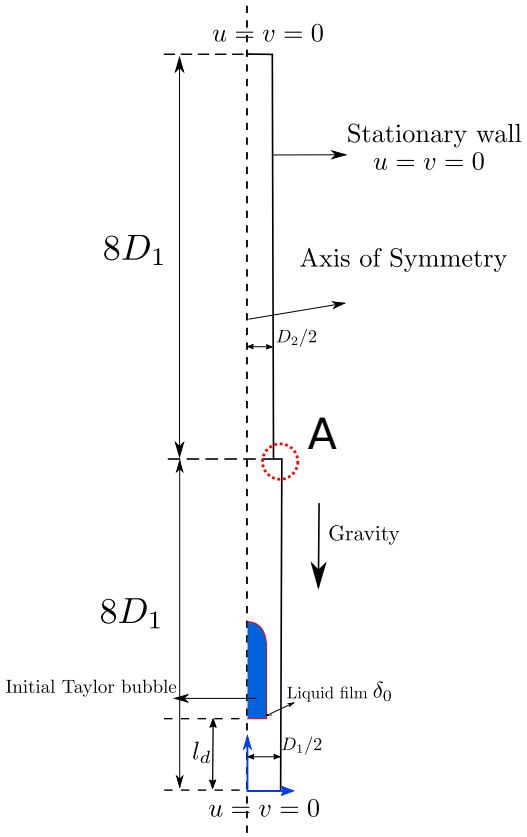

FIGURE 4.46: Schematic diagram of Taylor bubble rising in vertical pipe with sudden contraction.

Comparison between experiments and simulation

Fig. 4.47 shows the Taylor bubble in water through contraction, compared the Taylor bubble in pure glycerol (see Fig. 4.48), the bubble moves faster and the motion is asymmetrical and unstable.

Cette thèse est accessible à l'adresse : http://theses.insa-lyon.fr/publication/2020LYSEI095/these.pdf
© [L. Guo], [2020], INSA Lyon, tous droits réservés

FIGURE 4.47: Experimental Taylor bubble evolution with time rising through the contraction ($\epsilon = 0.94$) in water.

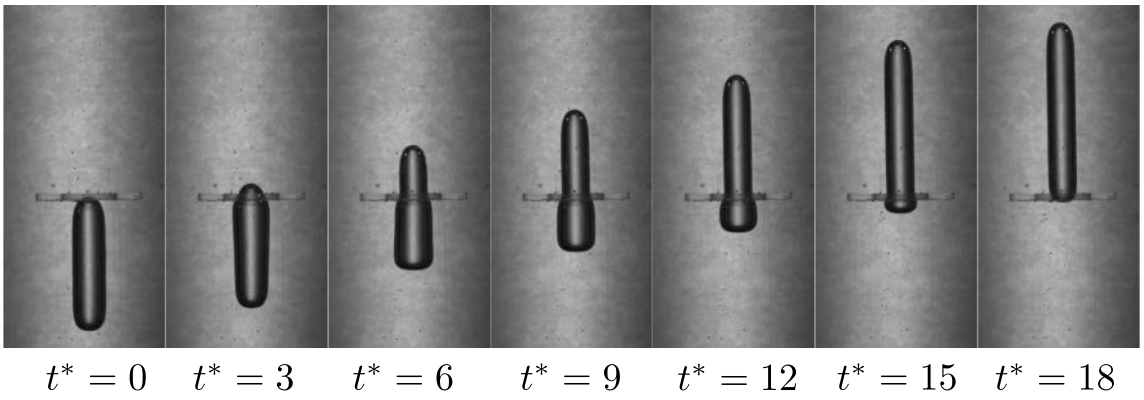

FIGURE 4.48: Experimental Taylor bubble evolution with time rising through the contraction in glycerol ($\epsilon = 0.94$).

We compare the simulation and experimental results under the condition (W-G: 95%,Eo = 50.6, Mo = 2.23, ϵ=0.94). The initial equivalent bubble length is defined in Table. 4.3. In Fig. 4.49, the numerical and experimental figures are rescaled to the same dimension for a better comparison. As mentioned in the expansion section, $t = 0$ is the time when the Taylor bubble head reaches the singularity. We can conclude a good agreement for comparison obtained from Fig. 4.49. Unlike the Taylor bubble through the expansion, several typical features for the bubble passing through contraction can be summarized as follows:

- The Taylor bubble remains intact when passing through the contraction. The tail shape does not change too much before and after the singularity.
- The Taylor bubble spends more time rising through the contraction compared to the expansion, which means the bubble velocity is lower than that in contractions.

Cette thèse est accessible à l'adresse : http://theses.insa-lyon.fr/publication/2020LYSEI095/these.pdf
© [L. Guo], [2020], INSA Lyon, tous droits réservés

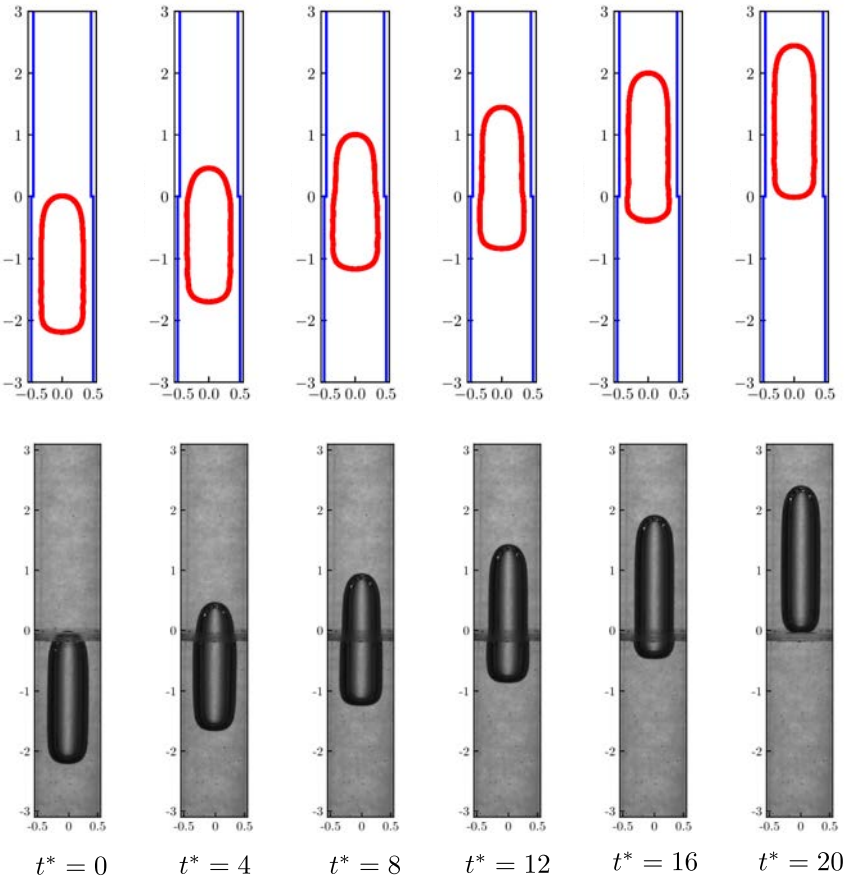

FIGURE 4.49: Numerical and experimental results of Taylor bubble rising through a contraction (W-G: 95%,Eo = 49.8, Mo = 2.35, ϵ=0.94).

4.3.2 Qualitative analysis for Taylor bubble through different contraction ratios

Four different contraction ratios [0.78, 0.8, 0.85, 0.95] are set to study the Taylor bubble rising through contraction structures. The parameters in the following contraction section are W-G: 60%, Eo = 45.1, Mo = 1.96×10^{-5}, $l_0 = 7r_b$. In this condition, as mentioned in Sec. 4.2.5, the bubble moves faster, therefore, it is easier to reach terminal state. We have also simulated smaller contraction ratios. However, the Taylor bubble is blocked and can not get through the contractions. This phenomenon is discussed in the following section. The bubble evolution for different contraction ratios is displayed in Fig. 4.50. Two features for the bubble tails are obtained different from expansions. First, the bubble tail oscillates, and capillary waves can be observed, that are in particular visible for lower contraction ratios. Secondly, the bubble tail shape becomes more flat after contractions.

Cette thèse est accessible à l'adresse : http://theses.insa-lyon.fr/publication/2020LYSEI095/these.pdf
© [L. Guo], [2020], INSA Lyon, tous droits réservés

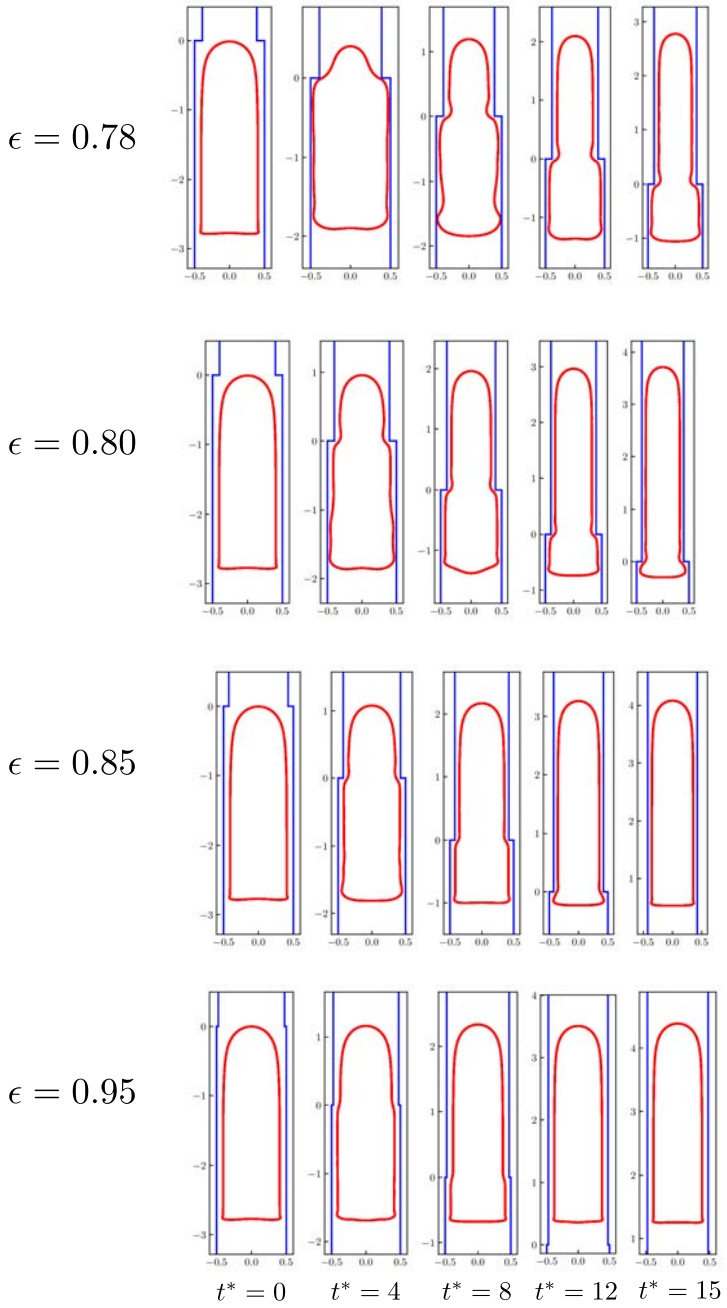

FIGURE 4.50: Taylor bubble shapes evolution with time instants when rising through contractions.

Taylor bubble velocity

The Taylor bubble velocity analysis is similar to the expansion part. We can obtain two terminal velocities in the lower pipe and upper pipe, respectively. Fig. 5.11 shows the mass center velocities for Taylor bubble rising through different contraction ratios. It is observed that the velocity begins to decelerate after reaching the contraction, which is due to the liquid ahead of the bubble blocked by the contraction. In Fig. 4.52, the oscillation at bubble tail is apparent and more intensive for lower ratios. However, this oscillation is not observed at bubble nose. The bubble

Cette thèse est accessible à l'adresse : http://theses.insa-lyon.fr/publication/2020LYSEI095/these.pdf
© [L. Guo], [2020], INSA Lyon, tous droits réservés

nose velocity shows a sudden deceleration when the bubble passing through contractions.

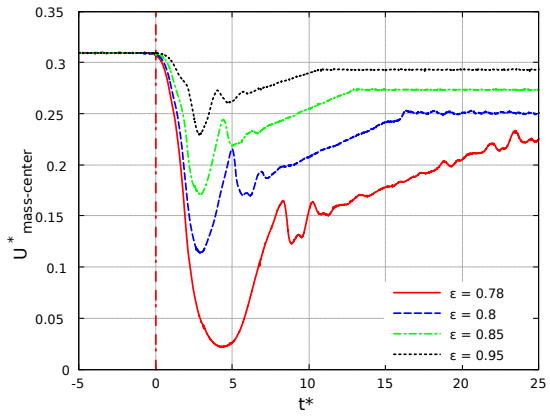

FIGURE 4.51: Mass center velocity of Taylor bubble rising through different contractions.

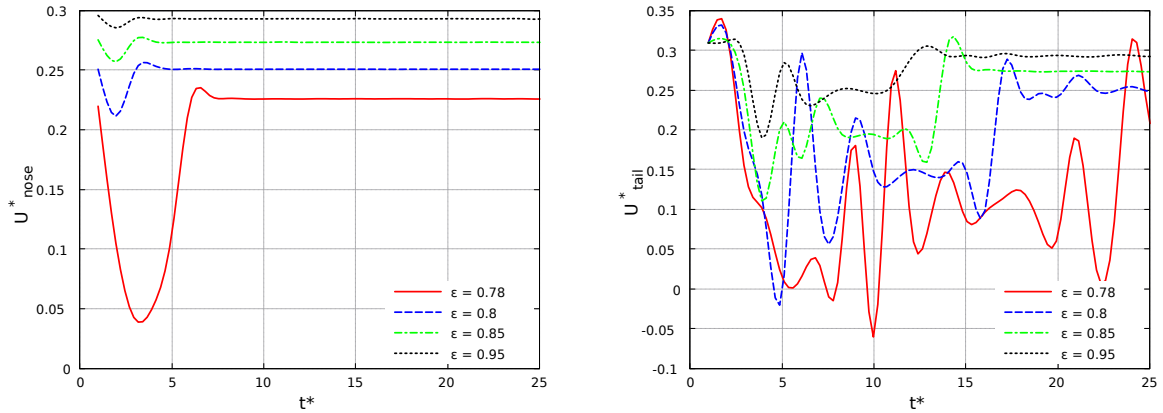

FIGURE 4.52: The Taylor bubble nose and tail velocities after reaching the contractions.

Bubble length variation

Fig. 4.53 shows the bubble length variation for different contraction ratios. For all cases, the bubble length decreases shortly after contractions. This is due to the fact that the bubble is blocked first by the liquid. After the bubble head through the contractions, the bubble is elongated in a smaller pipe. The bubble length slowly increases until the bubble body is entirely passed through the contraction. The contraction affects the bubble velocity passing through the singularity, and the bubble length variation explains this phenomenon.

Cette thèse est accessible à l'adresse : http://theses.insa-lyon.fr/publication/2020LYSEI095/these.pdf
© [L. Guo], [2020], INSA Lyon, tous droits réservés

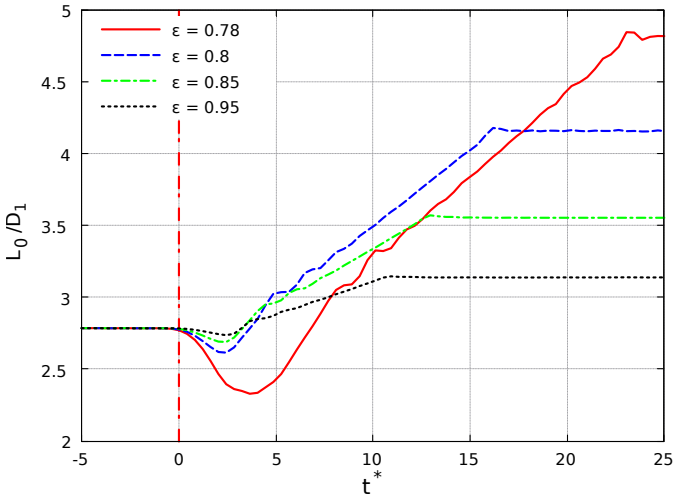

FIGURE 4.53: Taylor bubble length evolution with time for different contractions.

Pressure drop distribution

The pressure drop distribution at the radial midpoint of the liquid film is shown in Fig. 4.54. Unlike the Taylor bubble rising through expansions, for the bubble through contractions, the pressure in the liquid film before a distance from the contraction point has a sharp descent and then rises. The reason for this is that the bubble is blocked by the contraction, and the liquid close to contraction moves upstream. After the contractions, the liquid film flows towards downstream due to the bubble's liquid ahead of the bubble, pushed by the Taylor bubble's movement. Therefore, the pressure suddenly increases.

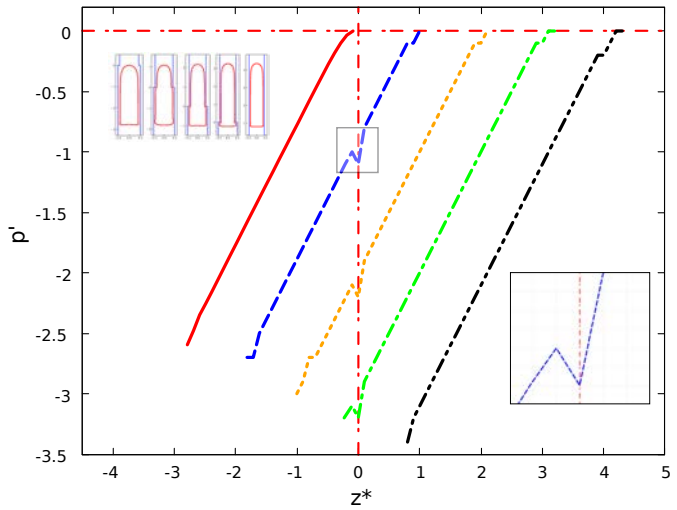

FIGURE 4.54: Pressure drop distribution in the middle of falling liquid film ($G-W$: $60\%, \epsilon = 0.85$).

Cette thèse est accessible à l'adresse : http://theses.insa-lyon.fr/publication/2020LYSEI095/these.pdf
© [L. Guo], [2020], INSA Lyon, tous droits réservés

4.3.3 Bubble blocking pattern

As mentioned in 4.3.2, the bubble will be blocked when passing through contractions. To investigate the critical contraction ratio of bubble blocked contraction ratios, a group of tests has been carried out with the same Morton number. The parameters are fixed to $Mo = 0.00224, l_0 = 9r_b$. Two interesting features are observed in Fig. 4.55. With increasing Eo numbers, the critical blocked ratios are decreased. Another feature is in a small range of Eo numbers, the critical blocked contraction ratio is constant. When fixing the liquid properties and expansion ratios, we found the bubble length has a minor effect on the blocking phenomenon.

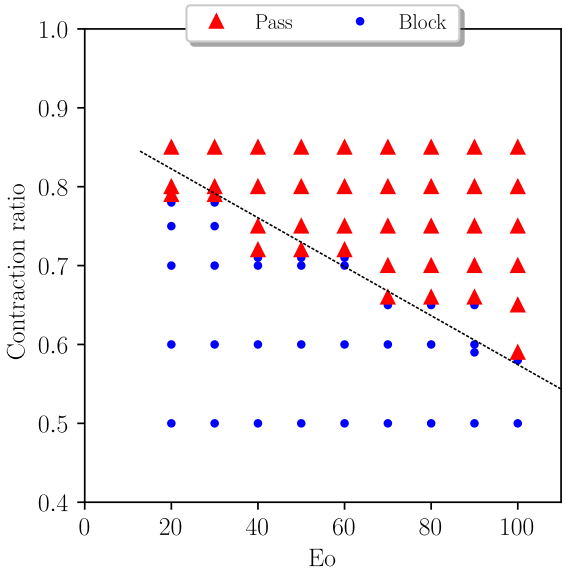

FIGURE 4.55: Bubble blocking regime map.

4.4 Chapter conclusion

A detailed experimental and numerical study on individual Taylor bubbles rising through sudden expansions and contractions in various glycerol-water solutions is reported in this chapter. The numerical method used in this study is first verified by comparing with an experimental database that had been previously published. From analyzing the experimental and numerical results, the following conclusion can be pointed out:

- The evolution of the bubble in expansion can be roughly divided into three stages. First, the bubble nose accelerates and the bubble length increases. Second, the bubble neck shrinks and the bubble reaches a velocity peak, and the bubble tail moves towards the bubble head. In the third stage, the bubble leaves the expansion, and the tail shows an oscillating behavior.

Cette thèse est accessible à l'adresse : http://theses.insa-lyon.fr/publication/2020LYSEI095/these.pdf
© [L. Guo], [2020], INSA Lyon, tous droits réservés

- The expansion ratio of the tubes induces the Taylor bubble neck shrink at the expansion, and a larger ratio corresponds to more intensive deformation of the neck. In addition, the larger expansion ratio accelerates the Taylor bubble passing through the expansion which has higher terminal velocity after the expansion. When the bubble leaves the expansion, the bubble tail becomes more concave than that before expansion.
- The rise of the Taylor bubble through sudden expansion generates sudden pressure variation at the expansion, which drains the liquid flow above the bubble nose towards the bubble tail region. The Taylor bubble nose in the upper tube has more circular property than in the lower tube, and a larger expansion ratio has a more significant value of frontal radius (R_F). Moreover, the bubble tail velocity is higher than the bubble head velocity.
- The bubble break-up pattern is observed in experiments and simulations. The pattern map concludes there is a critical ratio for bubble breaking up with fixed length. In addition, with a fixed liquid solution, the bubble will pinch off when the bubble length reaches a critical length.
- The bubble velocity decreases in the contractions. When the bubble passing through the contractions, the bubble length is stretched and elongated. Moreover, The bubble tail oscillates when bubble through contractions.
- The Taylor bubble will be blocked when the contraction ratios get one critical value. The bubble length has a minor effect on bubble blocking.

Cette thèse est accessible à l'adresse : http://theses.insa-lyon.fr/publication/2020LYSEI095/these.pdf
© [L. Guo], [2020], INSA Lyon, tous droits réservés

Chapter 5

Numerical study of individual Taylor bubbles rising through various singularities

The analysis of the Taylor bubble rising through sudden expansions/contractions in experiments and simulation demonstrates the singularity changes the dynamic behavior of the Taylor bubble. In this chapter, the gradual, parabolic concave, parabolic convex expansions/contractions are numerically studied for an individual Taylor bubble rising in stagnant liquid.

5.1 Physical model description

The geometry of the different singularities studied in this chapter is shown in Fig. 5.1. The expansion ratio is fixed at 1.47 and the contraction ratio is 0.7 unless specified otherwise. The physical properties of the liquid are of 80% glycerol-water solution of the experiments (Tab. 4.1). In the gradual expansions and contractions, α is the angle between the upper pipe and gradual wall. We change the value of α to design different gradual structures. In parabolic structures, we obtain different arc angles (θ) by changing the diameter of the circle (see Fig. 5.1). The initial bubble length $l_0 = 6r_b$ and the other geometry sizes and boundary conditions are kept the same as in Chapter 4.

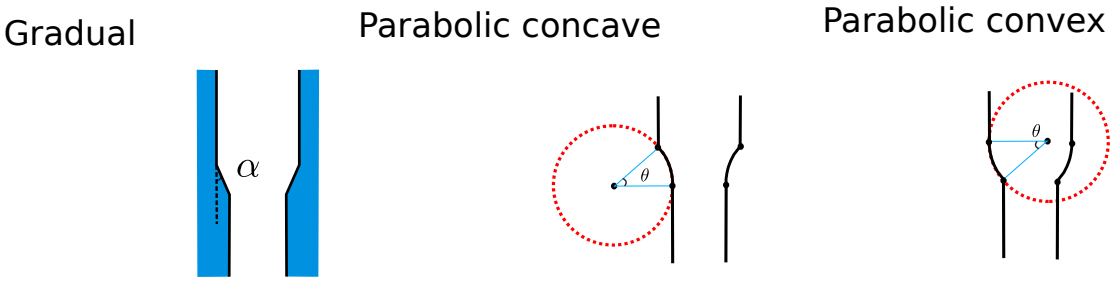

FIGURE 5.1: Different geometrical structure of singularities.

Cette thèse est accessible à l'adresse : http://theses.insa-lyon.fr/publication/2020LYSEI095/these.pdf
© [L. Guo], [2020], INSA Lyon, tous droits réservés

5.2 Taylor bubble rising through gradual expansions/contractions

5.2.1 Gradual expansion

Fig. 5.2 presents the non-dimensional velocity at mass center, bubble tail and bubble nose positions as a function of the dimensionless time. In Fig. 5.2 (a), smaller α leads to smaller peak mass center velocity, while the peak velocity has minor change when $\alpha > 30°$. The Fig. 5.2 (c) has a similar result with the Fig. 5.2 (a). Fig. 5.2 (b) shows the bubble tail velocity in smaller α needs more time to reach peak value and this peak value grows with the increase of the gradual angles. After the expansion, the bubble oscillates. Therefore the tail velocity shows negative peaks, whose values increase when α increases. When α is very small, as $\alpha = 10°$ in Fig. 5.2, the bubble less oscillates after expansions, and the Taylor bubble needs more time to pass through the expansion.

Fig. 5.3 shows at different time instants, the bubble shapes with streamlines and velocity fields for six different gradual expansions. Some features in gradual expansions are similar to sudden expansions, i.e., the bubble is accelerated at gradual expansion and penetration phenomenon is found for large angles. Moreover, the bubble tail shape becomes more concave at expansions with increasing α (see $t^* = 4$ in Fig. 5.3). However, some differences can be remarked. The Taylor bubble moves slower at smaller α. In addition, the penetration phenomenon is less obvious in smaller α. It is worth mentioning before and after expansions, the bubbles have the same terminal states.

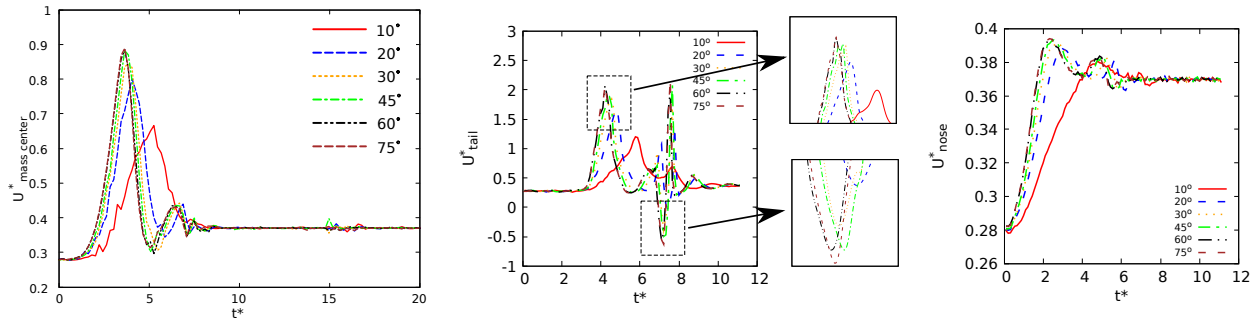

(a) Mass center velocity (b) Tail velocity (c) Nose velocity

FIGURE 5.2: Evolution of the dimensionless bubble velocity as a function dimensionless time.

Cette thèse est accessible à l'adresse : http://theses.insa-lyon.fr/publication/2020LYSEI095/these.pdf
© [L. Guo], [2020], INSA Lyon, tous droits réservés

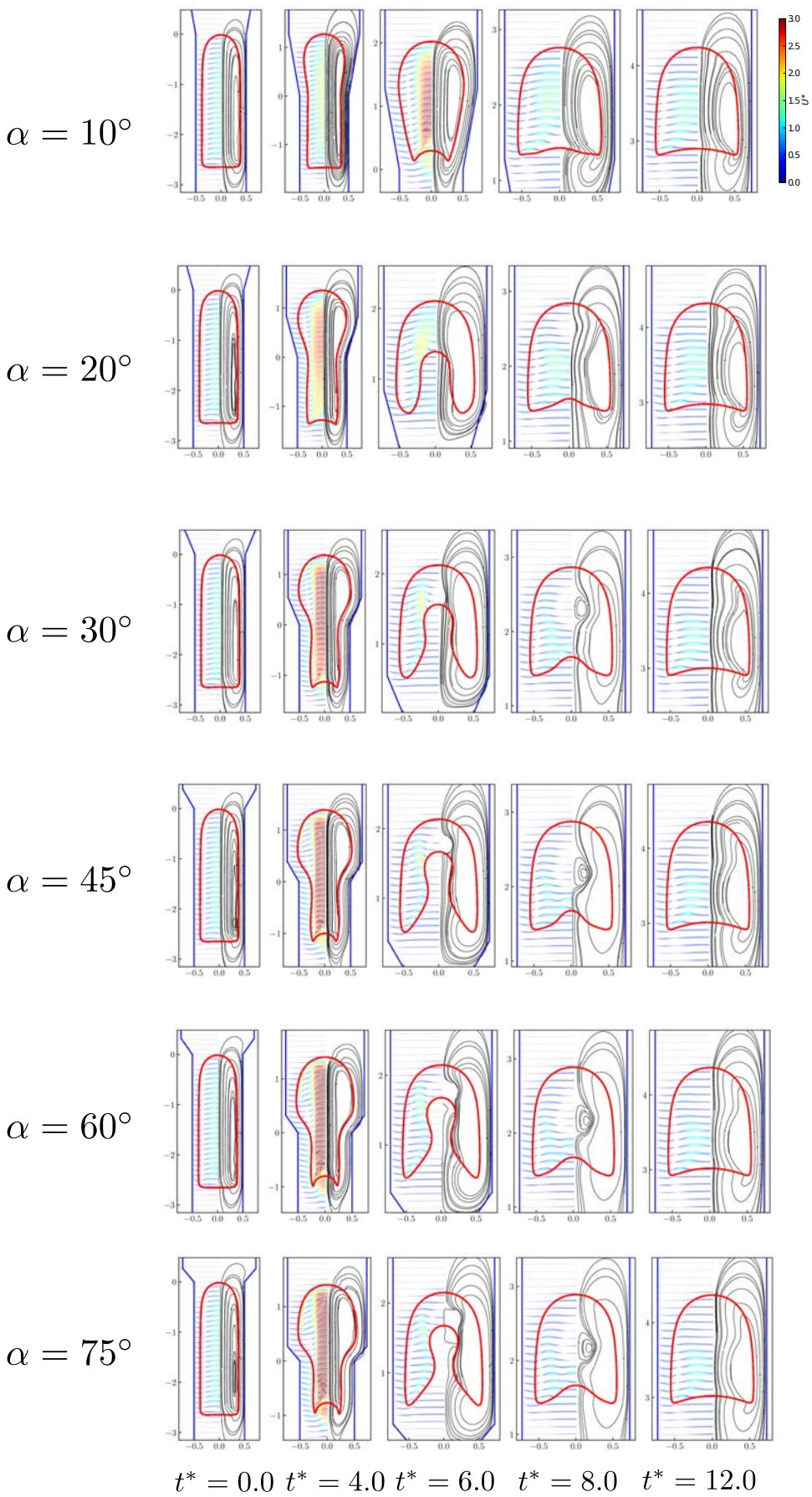

FIGURE 5.3: The streamlines, velocity fields and bubble shapes for different gradual expansion angles and dimensionless time instants.

Cette thèse est accessible à l'adresse : http://theses.insa-lyon.fr/publication/2020LYSEI095/these.pdf
© [L. Guo], [2020], INSA Lyon, tous droits réservés

Fig. 5.4 shows the evolution of bubble length for different α. The bubble length initially is slightly increased due to the bubble nose is shrinking by the expansion. For a larger α, the corresponding maximum length is larger. Moreover, similar to sudden expansions, after gradual expansions, l_0/D_1 becomes shorter. The bubble length in Fig. 5.4 also presents oscillation phenomena after expansions, which tend to disappear after a period of time.

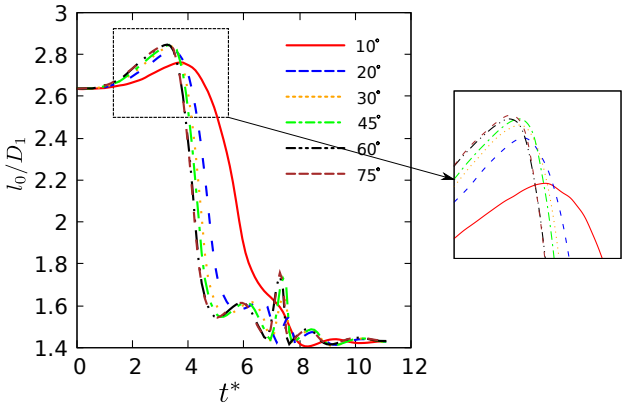

FIGURE 5.4: Evolution of the bubble length as a function dimensionless time.

In order to investigate the bubble time and velocity in gradual expansions. We consider the bubble nose and tail position. The bubble nose undergoes Δt_e in expansion, which indicates a period from bubble nose reaching the expansion to leaving the expansion. The gradual expansion length along z direction can be defined as $l_e = \frac{D_2 - D_1}{2tan(\alpha)}$. Therefore, the mean velocity for bubble nose in expansion is $U_e^* = \frac{l_e}{\Delta t_e}$. Fig. 5.5 shows the bubble rising time in expansions and mean velocity for different gradual expansions. It is observed with an increase of α, bubble needs less time for nose passing through expansions. Moreover, smaller α has a larger value of mean velocity.

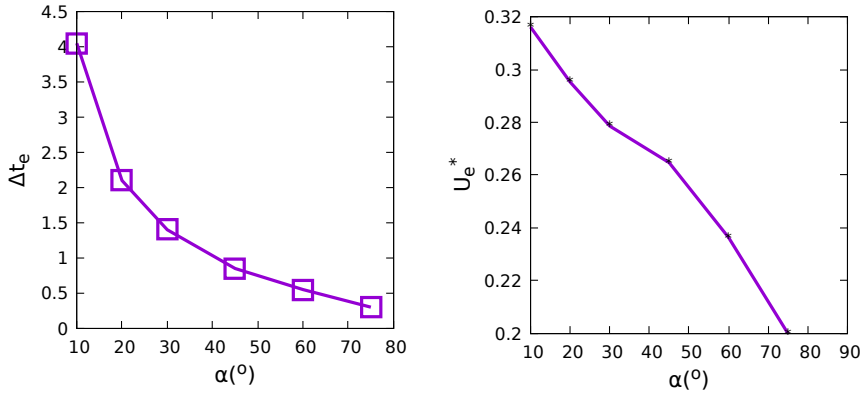

FIGURE 5.5: Time in gradual expansion and mean velocity for different angles.

Cette thèse est accessible à l'adresse : http://theses.insa-lyon.fr/publication/2020LYSEI095/these.pdf
© [L. Guo], [2020], INSA Lyon, tous droits réservés

Lagrangian particle method

The Lagrangian particle method is used to capture the trajectory of liquid particles. Three particles (indicated as A, B, C) at different positions in liquid are investigated (see Fig. 5.6). The coordinates of these particles at $t^* = 0$ are $[0.1, 1.5]$ for A, $[0.1, 0.2]$ for B and $[0.45, -0.5]$ for C.

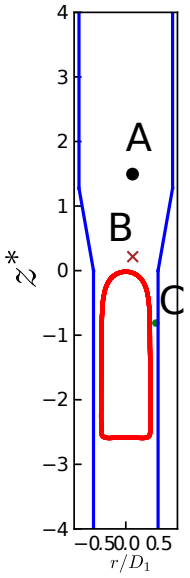

FIGURE 5.6: Position of liquid particles A, B and C at $t^* = 0$.

In Fig. 5.7, the trajectories of the particles are presented for $\alpha = 10°$. The trajectory of Particle-A shows when the bubble reaches A, the particle firstly moves towards the wall. Then the particle is trapped in the wake of the bubble tail and follows the upward bubble motion. The trajectory Particle-B shows the particle is trapped in the bubble wake and has recirculation motion. The Particle-C shows the fluid in the initial liquid film moves downstream but does not enter the wake of the bubble. The corresponding particle trajectories with bubble interface are shown in Fig. 5.8.

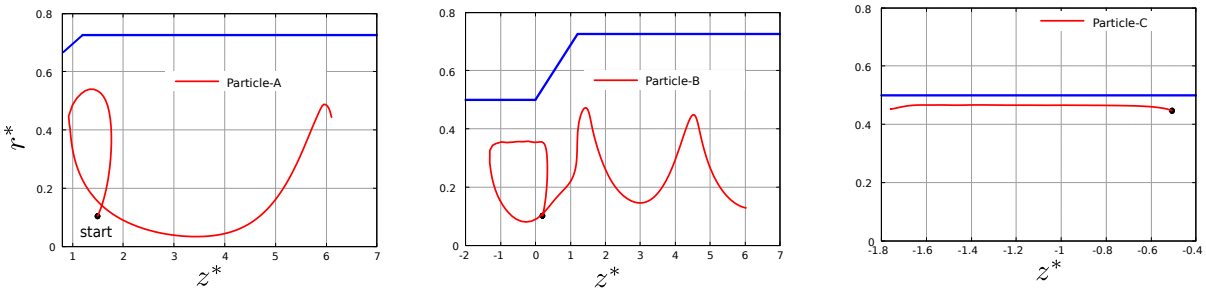

FIGURE 5.7: The liquid particle trajectories of different positions for $\alpha = 10°$.

Cette thèse est accessible à l'adresse : http://theses.insa-lyon.fr/publication/2020LYSEI095/these.pdf
© [L. Guo], [2020], INSA Lyon, tous droits réservés

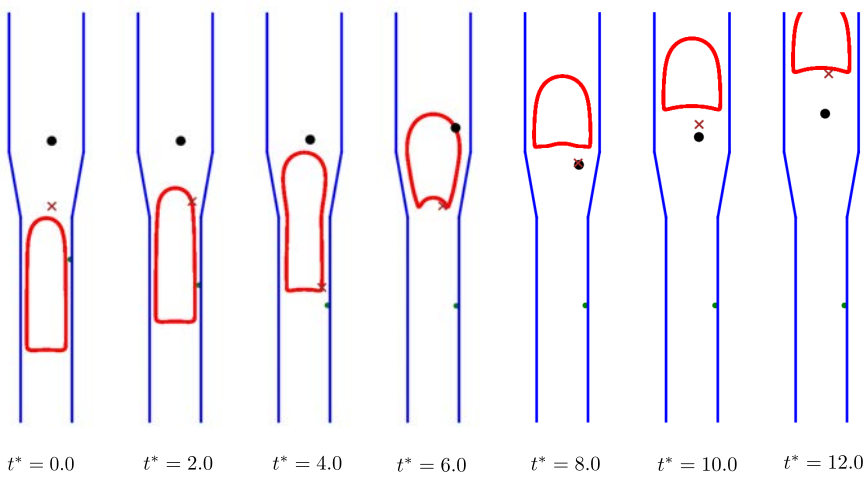

FIGURE 5.8: The liquid particle trajectories of different positions for $\alpha = 10°$ at different time instants.

Fig. 5.9 shows particles trajectories for a small and large value of α. The Particle-C for two cases coincides, which means the gradual angle has little influence on lower pipes. The trajectory of Particle-A shows the bubble motion has a great effect on fluid ahead of bubble nose for small α. The trajectory of Particle-B shows more recirculation motion for small α after expansion.

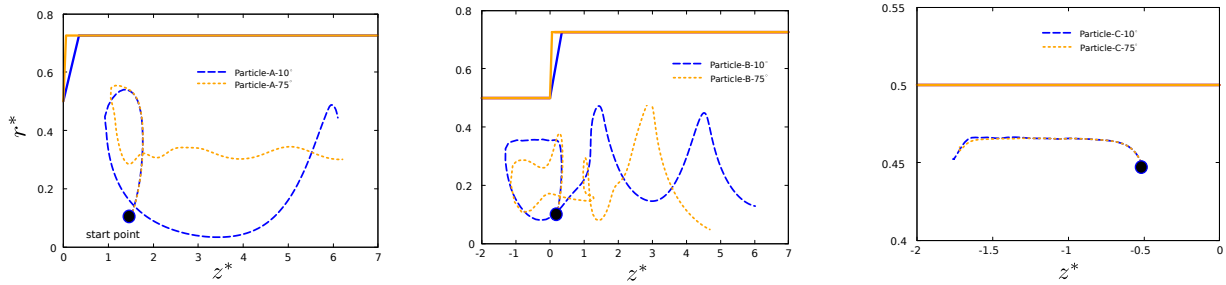

FIGURE 5.9: The particle trajectories for different gradual expansion angles.

5.2.2 Gradual contraction

Fig. 5.10 (next page) shows the bubble shapes and velocity fields for different time instants and angles α. When $\alpha > 45°$, the Taylor bubble is blocked by the contraction. Therefore, the results are not shown here. It is observed bubble moves faster for smaller α, and at $t^* = 10.0$, the bubble interface of $\alpha = 45°$ has more oscillation.

In Fig. 5.11, the velocities in different positions are performed. The results show that the bubble nose immediately decelerates when entering the contraction. The amplitude of deceleration depends on the contraction angle. Oscillation is found at the bubble tail.

Cette thèse est accessible à l'adresse : http://theses.insa-lyon.fr/publication/2020LYSEI095/these.pdf
© [L. Guo], [2020], INSA Lyon, tous droits réservés

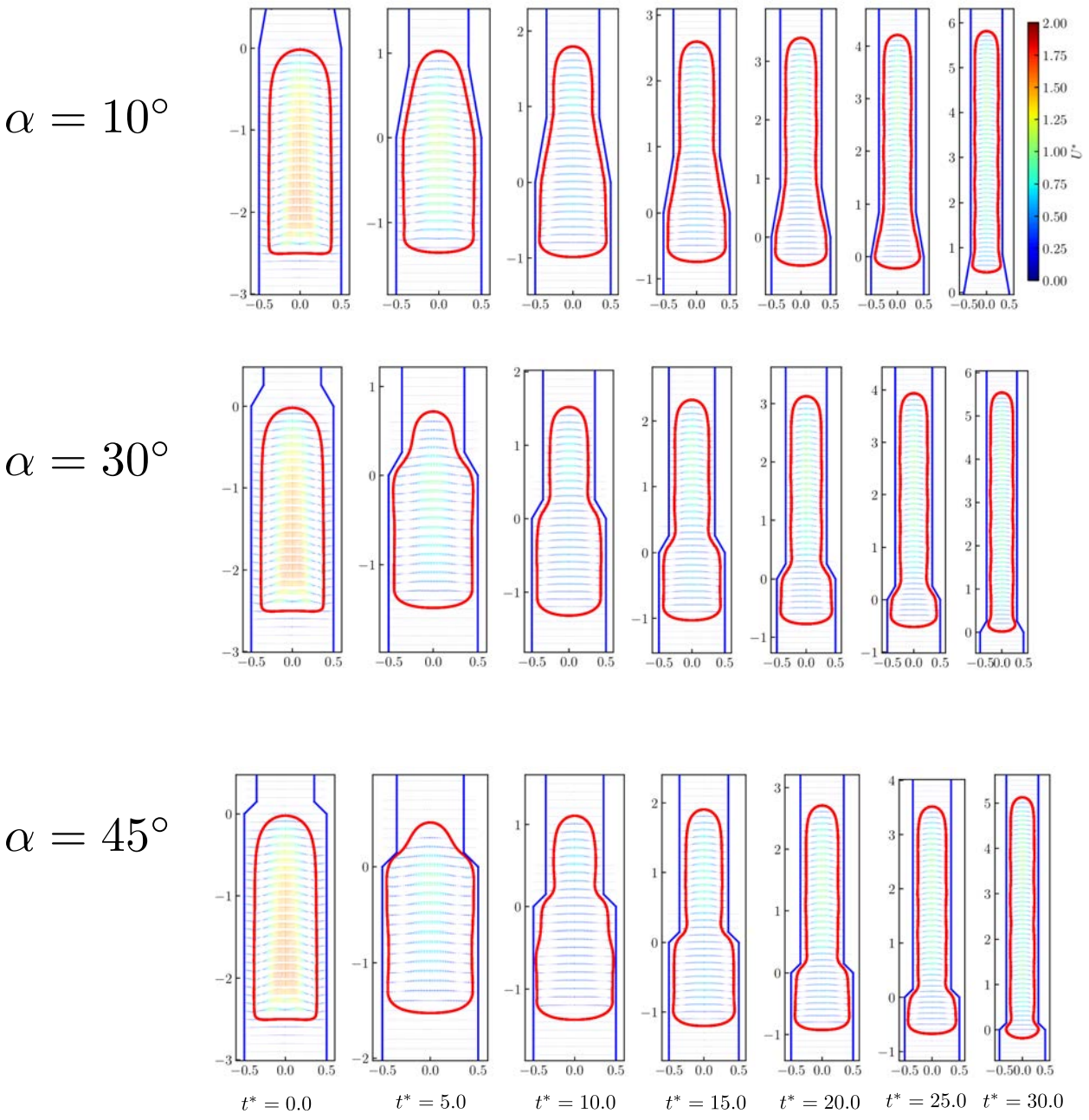

FIGURE 5.10: The bubble evolution with different gradual contraction angles.

Cette thèse est accessible à l'adresse : http://theses.insa-lyon.fr/publication/2020LYSEI095/these.pdf
© [L. Guo], [2020], INSA Lyon, tous droits réservés

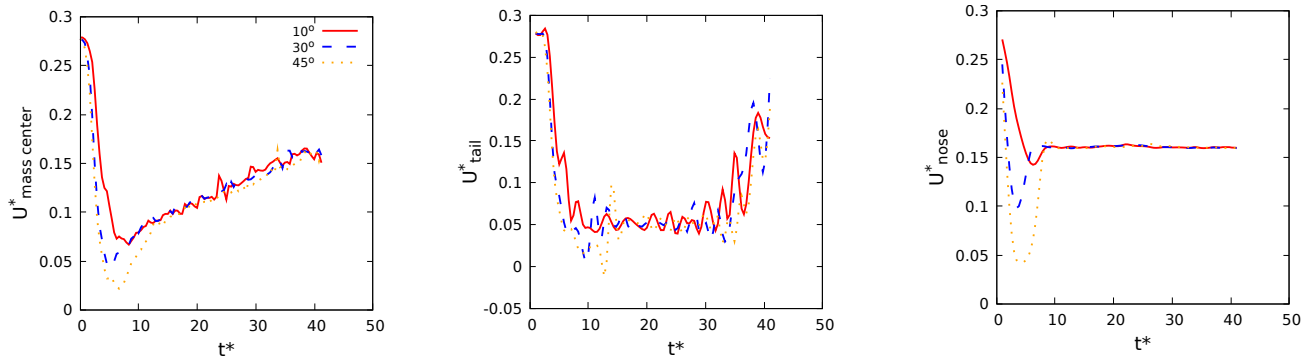

FIGURE 5.11: Evolution of the dimensionless bubble velocity as a function dimensionless time with gradual contractions.

The evolution of the Taylor bubble going through gradual contractions can be divided into three stages. As shown in Fig. 5.12, the first stage is reducing the bubble length in the z-direction due to the reduction of the bubble nose velocity. This phenomenon decreases with a decrease of α. In the second stage, the bubble takes some time to pass through the contraction, and the bubble length increases almost linearly. After contraction, a new bubble is formed in the upper pipe after some oscillatory behavior at the tail.

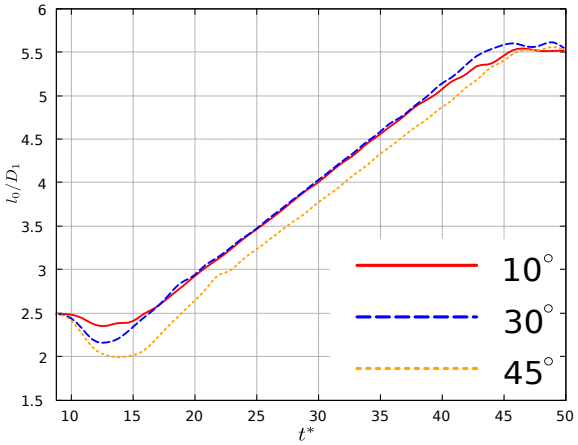

FIGURE 5.12: Evolution of the bubble length as a function of the dimensionless time with gradual contractions.

We define a similar transient time Δt_c to describe the bubble rising through contractions. The gradual contraction length along z direction can be defined as $l_c = \frac{D_1 - D_2}{tan(\theta)}$. The mean velocity for bubble nose in contraction is $U_c^* = \frac{l_c}{\Delta t_c}$. Fig. 5.13 shows Δt_c and mean velocity for different gradual contractions. The value of Δt_e is decreasing with increase of α. However, the mean velocity is larger in larger α.

Cette thèse est accessible à l'adresse : http://theses.insa-lyon.fr/publication/2020LYSEI095/these.pdf
© [L. Guo], [2020], INSA Lyon, tous droits réservés

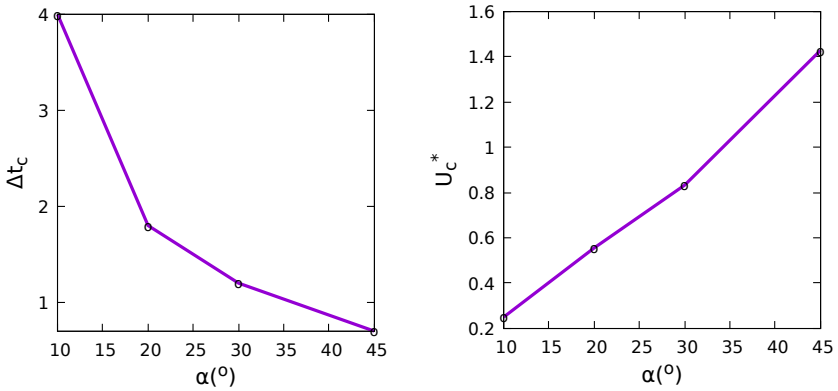

FIGURE 5.13: Time shift with fixed distance and mean velocity for different gradual contractions.

The liquid particle analysis

The liquid particle trajectories motion in gradual contractions are shown in Fig. 5.14. Particle-A trajectory describes the Taylor bubble passing through contractions. The particle moves towards downstream along the interface and reaches the bubble tail. Moreover, the total displacement of the particle A is larger for larger α. Particle-B has more intense motion. The Taylor bubble body appears to oscillate. The behavior of particle-C is similar to that discussed in the gradual expansion section.

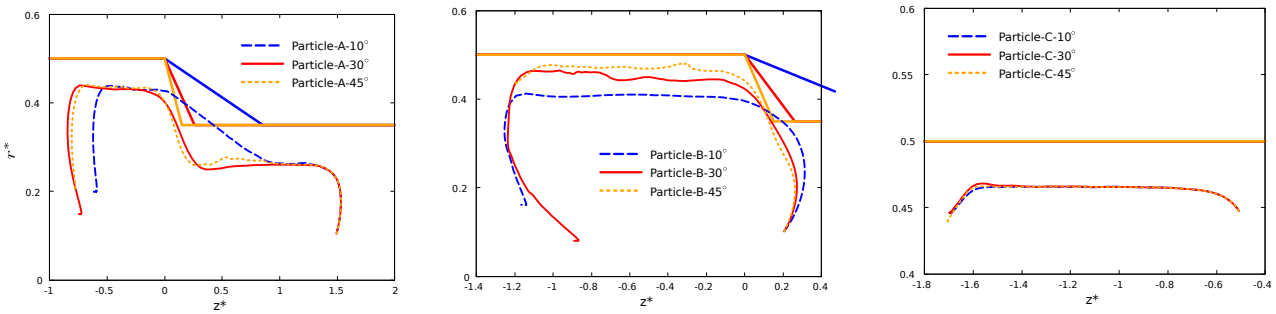

FIGURE 5.14: The particle trajectories for different gradual contraction angles.

5.3 Taylor bubble rising through parabolic expansions/contractions

Two different types of expansions/contractions are carried out in this section. The geometry of the problem has been introduced in Sec. 5.1. In the following part, we first investigate parabolic convex expansions/contractions. Then results for the parabolic concave expansions/contractions are presented.

5.3.1 Parabolic convex expansion

Fig. 5.15 shows the Taylor bubble rises through parabolic convex expansions with different angles (θ) at two time instants. The first row shows the expansions shrink the Taylor bubble and the extent of this effect is slighter when θ is smaller. Moreover,

Cette thèse est accessible à l'adresse : http://theses.insa-lyon.fr/publication/2020LYSEI095/these.pdf
© [L. Guo], [2020], INSA Lyon, tous droits réservés

the bubble necking does not change too much for larger angles. When θ is closer to sudden one, the bubble necking tends to the maximum of necking value. The second figure row in Fig. 5.15 presents the penetration phenomenon at different θ, larger θ strengthens the level of penetration.

Two convex angles, $\theta = 20°$ and $\theta = 45°$, are performed to detail the bubble shape evolutions. In Fig. 5.16, the difference between the two cases is the phenomena in parabolic convex expansions. The larger θ has much thinner bubble necking and longer liquid penetration.

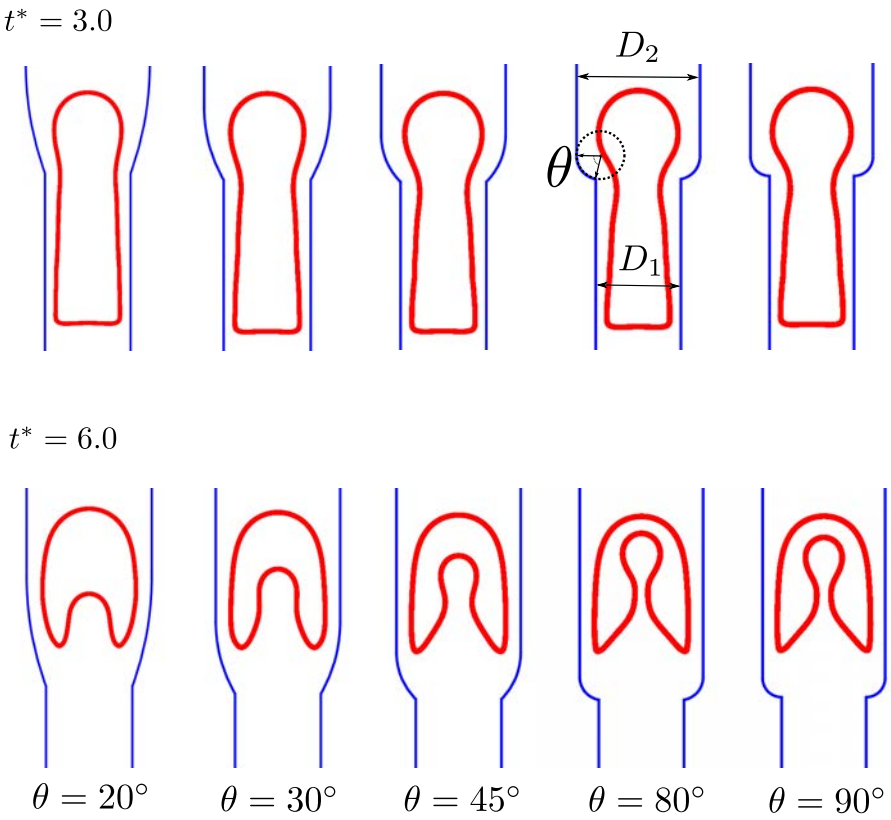

FIGURE 5.15: The Taylor bubble shapes at different dimensionless times for the parabolic convex with different angles.

Cette thèse est accessible à l'adresse : http://theses.insa-lyon.fr/publication/2020LYSEI095/these.pdf
© [L. Guo], [2020], INSA Lyon, tous droits réservés

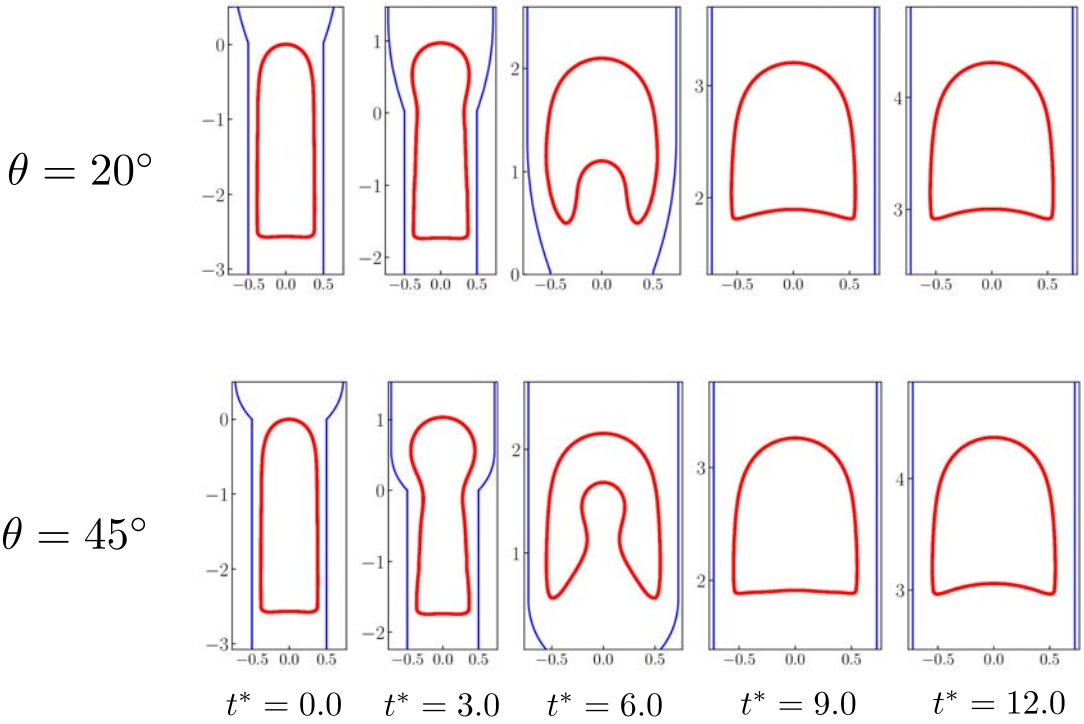

FIGURE 5.16: The Taylor bubble shapes for the parabolic convex expansions.

The bubble velocity variation is shown in Fig. 5.17. It is worth pointing out that with the increase of the parabolic convex angle, the results tend to those obtained for the sudden expansion, while smaller θ reduces the bubble tail oscillation.

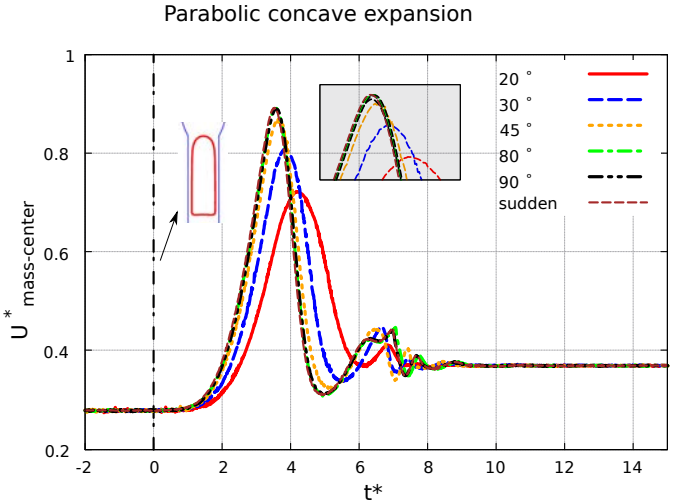

FIGURE 5.17: Bubble mass center velocity evolution with time for the parabolic convex expansions.

5.3.2 Parabolic convex contraction

Bubble shape variation

Fig. 5.18 shows the bubble shape deformations in the parabolic convex contractions with different θ. Bubble blocking phenomenon is observed for $\theta = 80°$. Similar

Cette thèse est accessible à l'adresse : http://theses.insa-lyon.fr/publication/2020LYSEI095/these.pdf
© [L. Guo], [2020], INSA Lyon, tous droits réservés

to the analysis of previous contractions, small values of θ lead to a smoother transition of the bubble through the contraction.

5.3.3 Parabolic concave expansion

Simulation results of bubble shape snapshots are reported in Fig. 5.19. The necking effect if more pronounced for larger θ. The bubble tail oscillates after expansions. After several cycles of oscillation, the bubble reaches the terminal steady state. The oscillation of the bubble tail affects the bubble velocity (see Fig. 5.20). It is worth pointing out, for larger θ, after bubble oscillation, the bubble tail possibly breaks up into smalls bubbles because of the strong motion of falling.

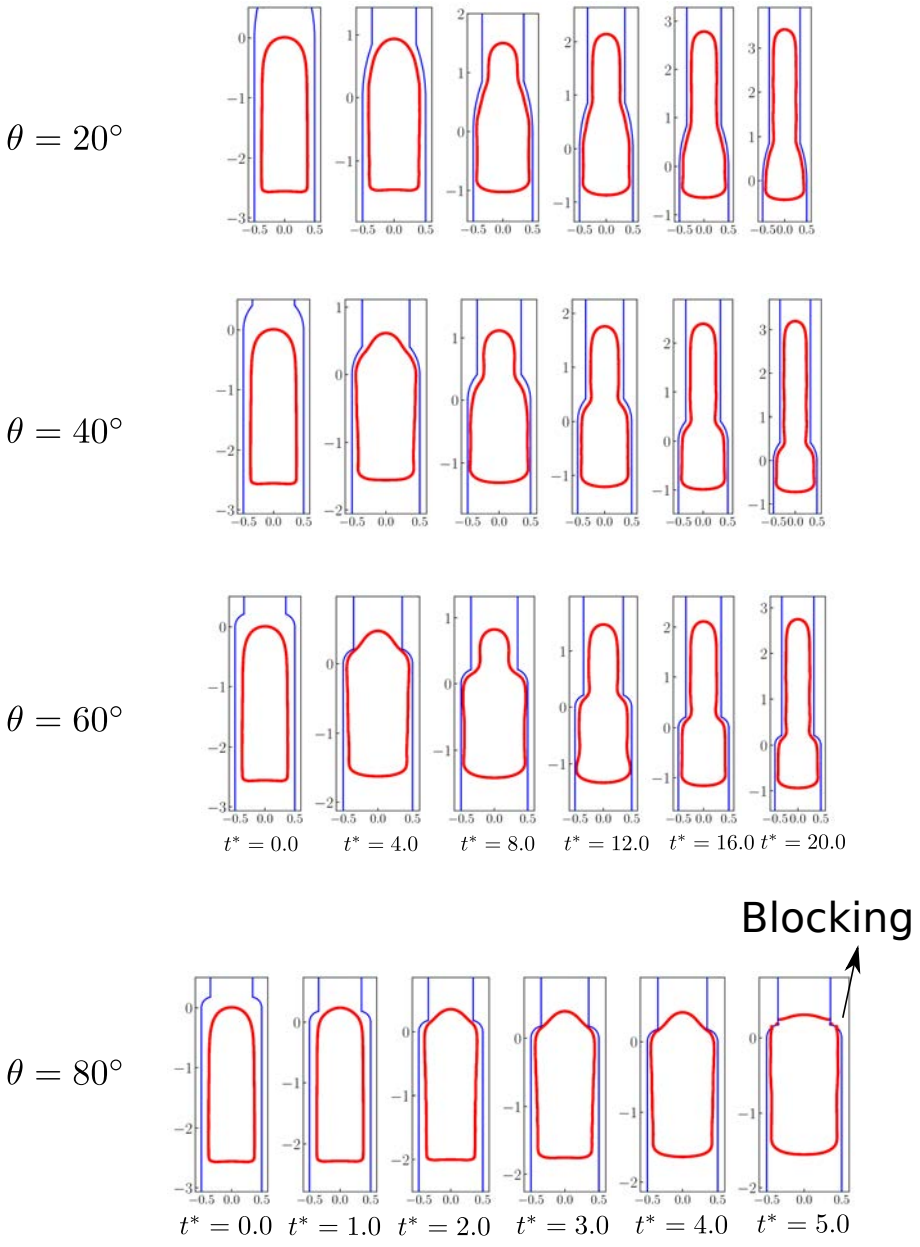

FIGURE 5.18: Taylor bubble shapes with different time instants for parabolic convex contractions.

Cette thèse est accessible à l'adresse : http://theses.insa-lyon.fr/publication/2020LYSEI095/these.pdf
© [L. Guo], [2020], INSA Lyon, tous droits réservés

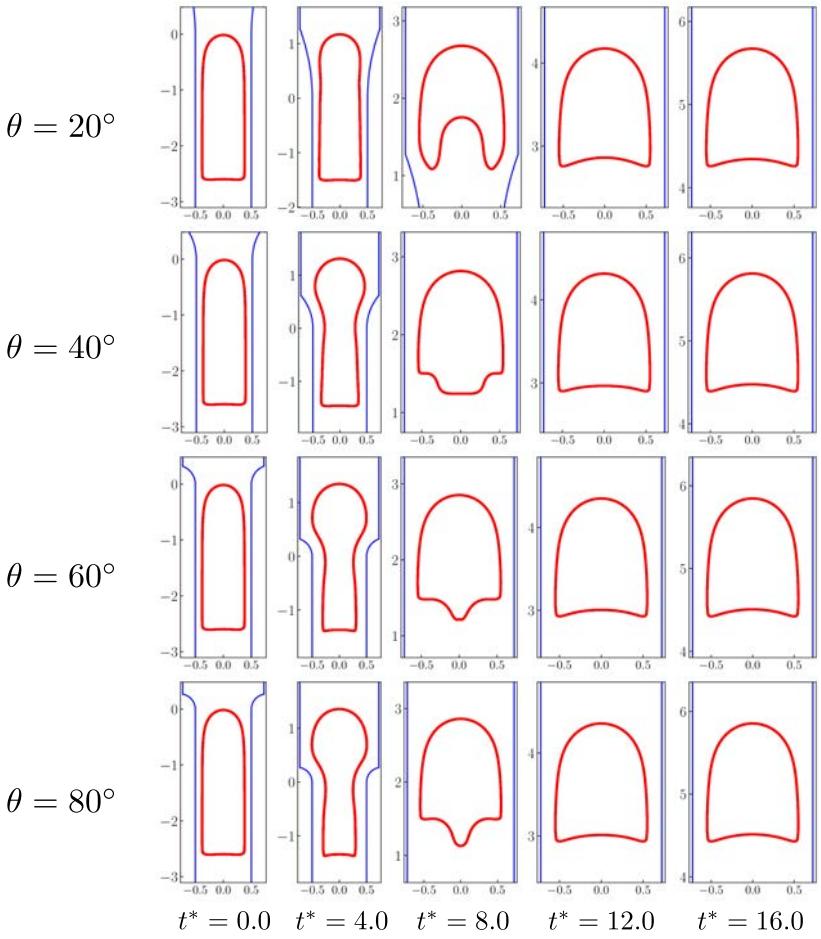

FIGURE 5.19: The Taylor bubble shapes at different dimensionless time for parabolic convex contraction with different angles.

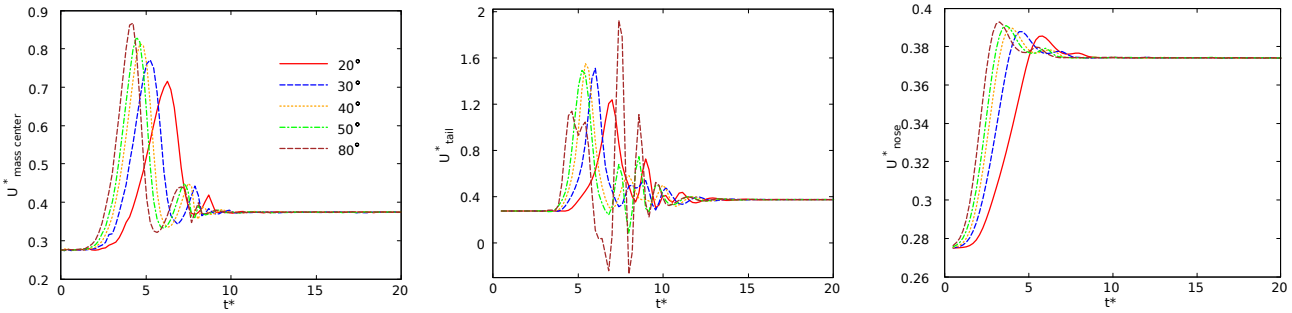

FIGURE 5.20: Evolution of the dimensionless bubble velocity as a function of dimensionless time for different parabolic concave expansions.

The Taylor bubble length variation is presented in Fig. 5.21. Similar to the previous expansions, the bubble has a maximum length when passing through the expansion. After the expansion, the bubble oscillates. We found that the bubble length with $\theta = 80°$ has stronger oscillations than others.

Cette thèse est accessible à l'adresse : http://theses.insa-lyon.fr/publication/2020LYSEI095/these.pdf
© [L. Guo], [2020], INSA Lyon, tous droits réservés

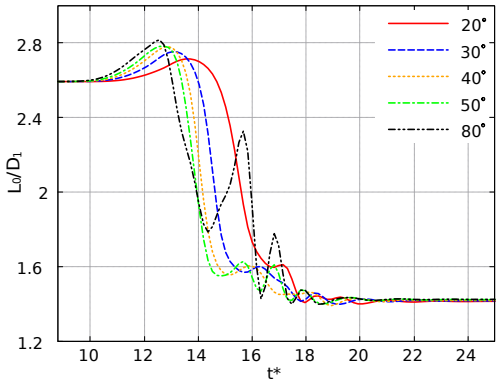

FIGURE 5.21: Bubble length evolution for different parabolic concave expansions.

5.3.4 Parabolic concave contraction

Fig. 5.23 shows the Taylor bubble shapes in parabolic concave contractions for different angles. The bubble is stretched at contractions which is similar to the previous contraction types. However, the difference here is that the bubble is not blocked with an increase of θ. Fig. 5.22 shows bubble length variation for different parabolic concave contractions. Similar to the previous analysis for other types of contractions, the bubble length undergoes the same stages, and the minimum bubble length is decreased with an increase of θ.

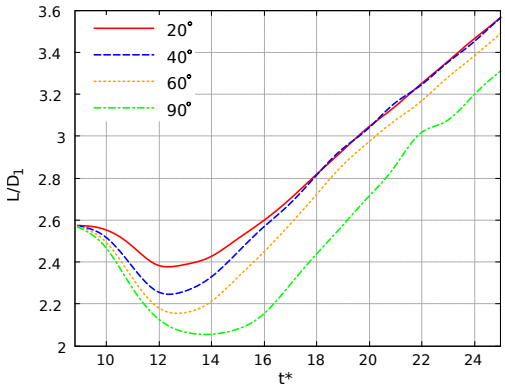

FIGURE 5.22: Bubble length variation for different parabolic concave contractions.

Cette thèse est accessible à l'adresse : http://theses.insa-lyon.fr/publication/2020LYSEI095/these.pdf
© [L. Guo], [2020], INSA Lyon, tous droits réservés

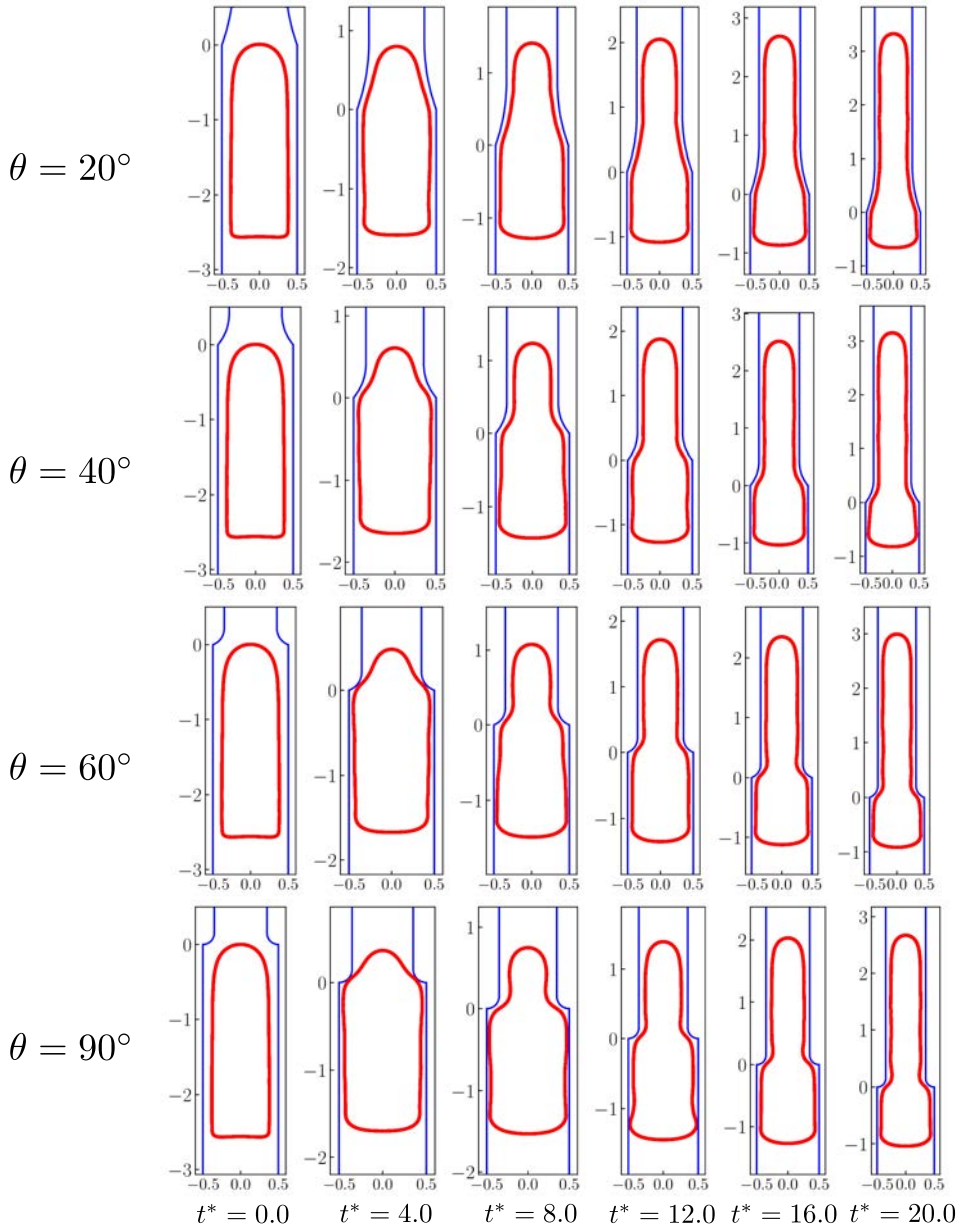

FIGURE 5.23: The Taylor bubble shapes for parabolic concave contraction.

5.4 Comparison of different expansions/contractions

When $\alpha = 90°$, the gradual expansion/contraction becomes the sudden expansions/contractions. Therefore, we compare these singularities with parabolic convex and the parabolic concave geometries under the same condition of $\theta = 90°$.

Cette thèse est accessible à l'adresse : http://theses.insa-lyon.fr/publication/2020LYSEI095/these.pdf
© [L. Guo], [2020], INSA Lyon, tous droits réservés

5.4.1 Expansion comparison

Bubble shapes variation

The bubble shape snapshots at different time instants are shown in Fig. 5.24 for different types of expansions. The dynamics of the Taylor bubble in the sudden expansion and the parabolic convex are similar. The bubble shows slight necking at $t^* = 2$ and the tail becomes concave at $t^* = 4$. However, after the bubble leaves the expansion, they present different behavior, especially for the penetration phenomena (see Fig. 5.25). The Taylor bubble in parabolic concave expansions exhibits different dynamic behavior compared with the other two expansions. The differences are mainly reflected in the process of the bubble passing through expansion and the period that bubble recovers the terminal steady-state in the upper pipe. We can see this difference in Fig. 5.24 at $t^* = 4$ and $t^* = 6$, also in Fig. 5.25.

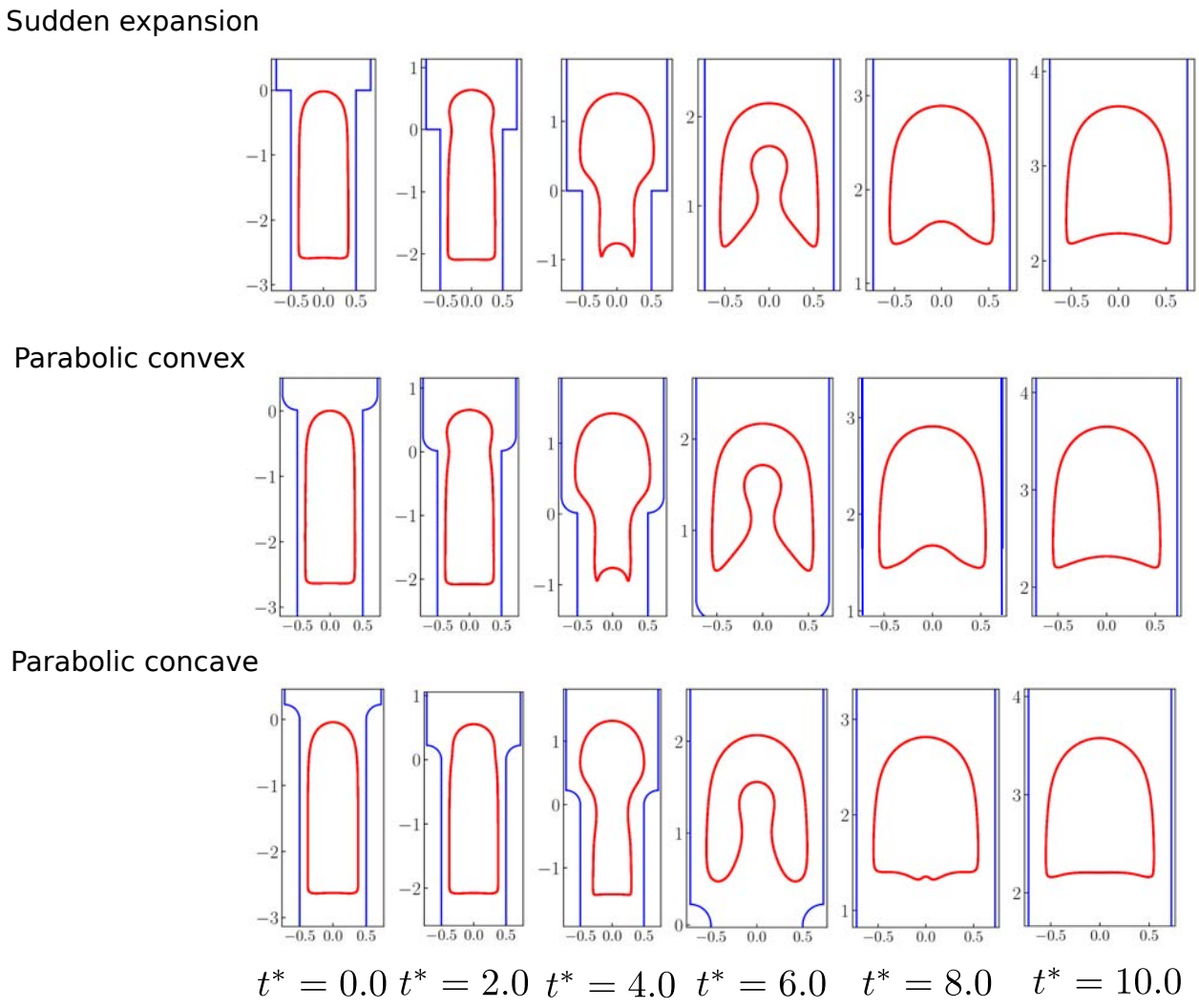

FIGURE 5.24: Taylor bubble evolution for different types of expansions.

Cette thèse est accessible à l'adresse : http://theses.insa-lyon.fr/publication/2020LYSEI095/these.pdf
© [L. Guo], [2020], INSA Lyon, tous droits réservés

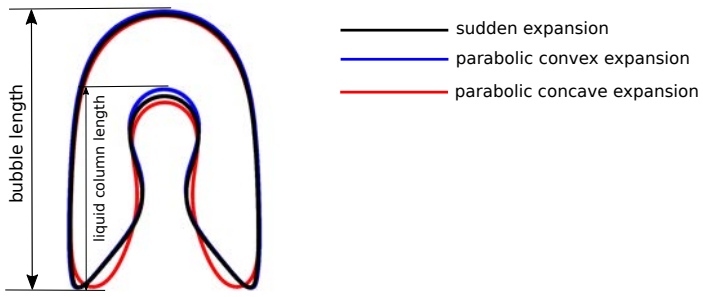

FIGURE 5.25: The liquid column length for different types of expansions.

Bubble length variation

The bubble length variation for the bubble rising through different expansions is shown in Fig. 5.26. First, we can see that concave geometry delays the bubble with respect to the other two expansions. After the expansion, the bubble length fluctuates due to the oscillation of the bubble tail. The amplitude of fluctuation reflects the liquid column length inside the Taylor bubble. Because the bubble volume is constant, when the liquid column is larger inside the bubble, the bubble length is much longer. Therefore, as mentioned in Fig. 5.25, the parabolic convex has the largest liquid column length, the bubble length corresponds to the longest.

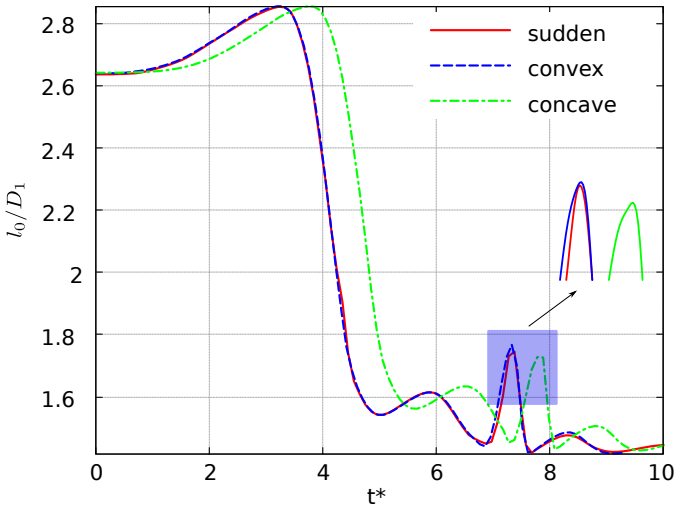

FIGURE 5.26: The bubble length when the bubble rising through expansions.

Inspired by liquid penetration behavior, we tracked the bubble tail center using a Lagrangian particle method for different expansions. The definition of liquid column length is defined in Fig. 5.25. The result in Fig. 5.27 shows that the parabolic convex after expansions has the largest L_{liquid} inside bubble.

Cette thèse est accessible à l'adresse : http://theses.insa-lyon.fr/publication/2020LYSEI095/these.pdf
© [L. Guo], [2020], INSA Lyon, tous droits réservés

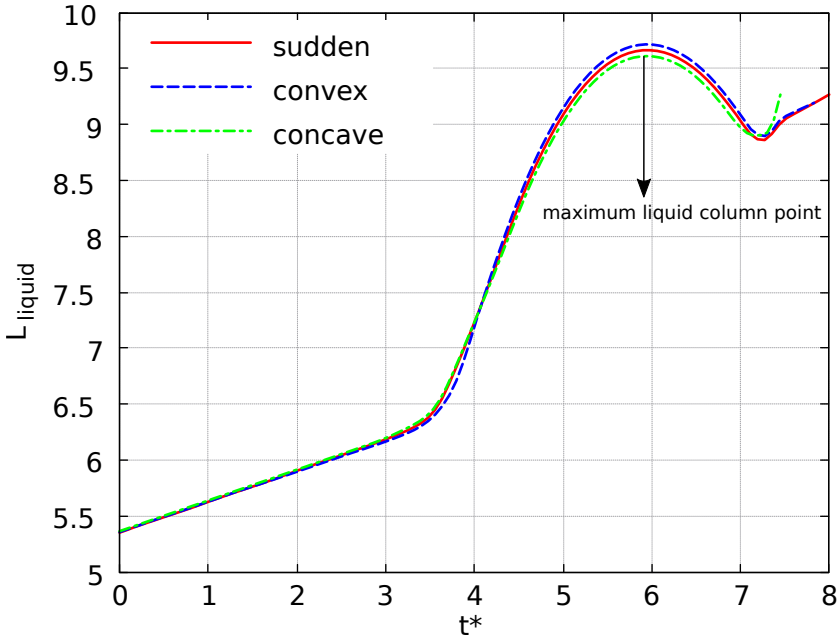

FIGURE 5.27: The bubble tail particle variation.

5.4.2 Contraction comparison

Through the comparison of different contraction singularities in Fig. 5.28, several remarks are obtained:

- The Taylor bubble can rise through parabolic concave contractions even for large θ, while it is blocked in gradual and parabolic convex contractions.
- The Taylor bubble in parabolic concave contraction moves without large oscillation for the bubble body.
- It appears that the sharpness/smoothness of the inner edge has a much more significant impact on the bubble dynamic that the outer corner.

Cette thèse est accessible à l'adresse : http://theses.insa-lyon.fr/publication/2020LYSEI095/these.pdf
© [L. Guo], [2020], INSA Lyon, tous droits réservés

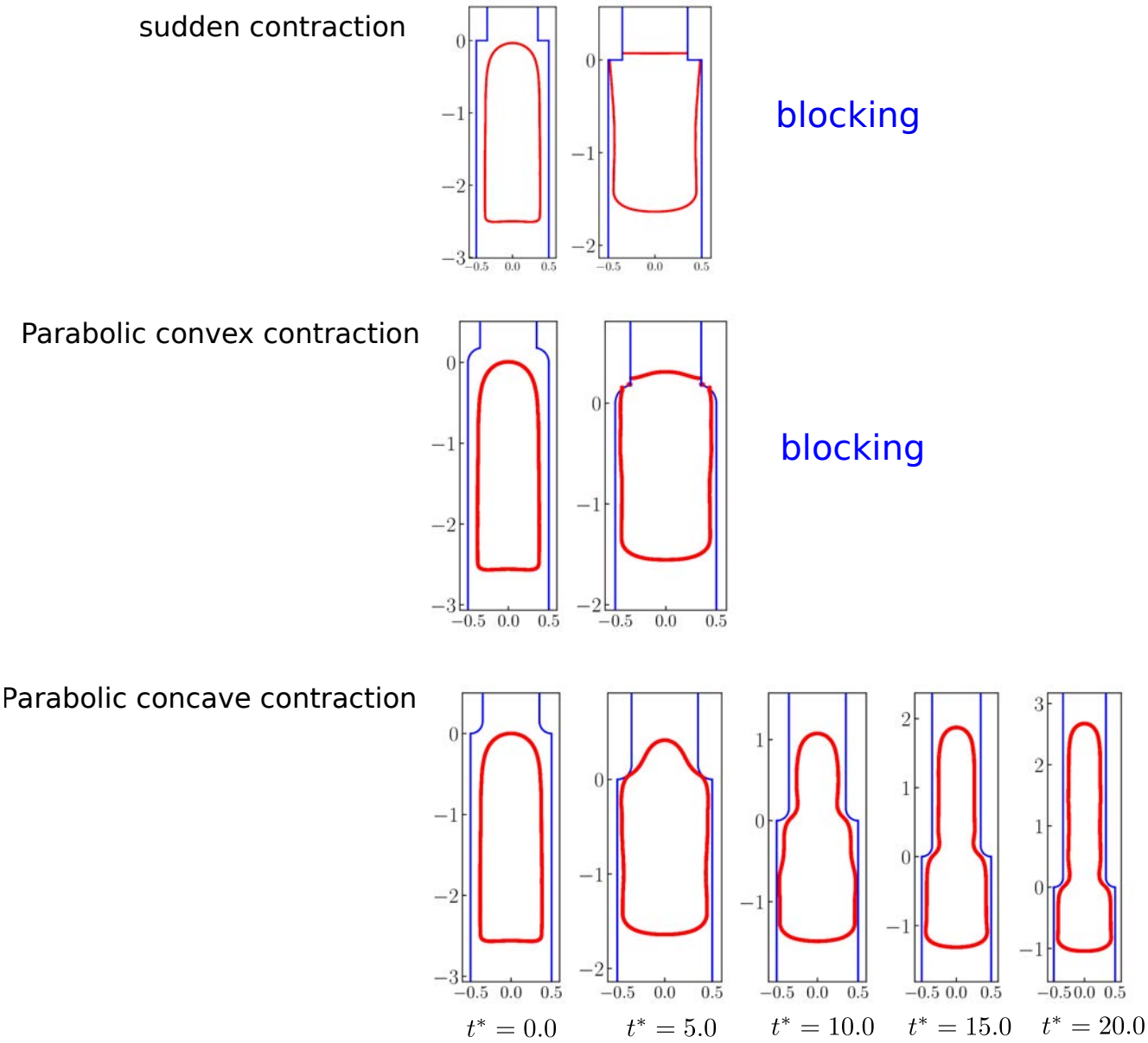

FIGURE 5.28: Bubble shapes with evolution of time instants for different types of contractions.

5.5 Chapter conclusion

In this chapter, we have investigated the simulation of an individual Taylor bubble rising through different types of expansions/contractions. Some conclusions can be obtained through the analysis:

- The gradual expansion reduces the intense motion and deformation of the Taylor bubble. The transient time $\Delta t_e/\Delta t_c$ show with an increase of expansion/contraction angle, the bubble needs less time to pass through expansion/contraction. Maximum bubble length is found in expansions and the maximum value decreases

Cette thèse est accessible à l'adresse : http://theses.insa-lyon.fr/publication/2020LYSEI095/these.pdf
© [L. Guo], [2020], INSA Lyon, tous droits réservés

with a decrease of α. On the contrary, the minimum bubble length in contractions is increased with a decrease of α. The bubble tail oscillation after expansions affects the bubble length.

- The parabolic convex expansion accelerates the bubble motion and the extent of the motion with $\theta = 90^{\circ}$ is stronger than that in sudden expansions. The bubble is blocked for large angles of the convex contractions.
- The Taylor bubbles exhibit different behavior in parabolic concave expansions/contractions. For expansions, the Taylor bubble moves slower than the other expansions and the liquid column length inside the bubble is the smallest. For contractions, the Taylor bubble is easier to pass the contraction geometry, even to larger concave angles.

Cette thèse est accessible à l'adresse : http://theses.insa-lyon.fr/publication/2020LYSEI095/these.pdf
© [L. Guo], [2020], INSA Lyon, tous droits réservés

Chapter 6

Two phase flow with phase change

In this chapter, we introduce a phase change model which is developed in the Basilisk solver. First, the governing equations and interface jump conditions considering phase change are introduced. Secondly, the numerical methods, including mass flux calculation, the geometric VOF method with phase change, the thermal boundary conditions at interface are presented. Finally, the phase change model is validated by several benchmark test cases.

6.1 Governing equations and interface jump conditions

The governing equations with phase change are similar to the previous Eqs. (3.1, 3.2). However, when considering phase change at the interface, it is necessary to add additional interfacial jump conditions to guarantee mass, momentum, and energy conservation.

6.1.1 Mass conservation

The general mass conservation integral formula in a fixed control volume is still valid for two-phase flow with phase change.

$$\int_V \frac{\partial \rho}{\partial t} dV + \oint_S \rho \mathbf{u} \cdot \mathbf{n} dA = 0 \tag{6.1}$$

where V is the volume of grid, S is the cell surface area.

Interface jump conditions

The gas and liquid phases are separated for immiscible two-phase flows by an interface where the phase change occurs (i.e., liquid vaporization or vapor gas condensation processes). The interface velocity ($\mathbf{u}_\Gamma$), which differs from the liquid and gas velocities on either side, was introduced for calculating a jump in the mass, momentum, and energy across the interface. Considering a two-dimension computational cell with interface in Fig. 6.2, the mass conservation equation for each phase can be written as (see in Fig. 6.1):

Cette thèse est accessible à l'adresse : http://theses.insa-lyon.fr/publication/2020LYSEI095/these.pdf
© [L. Guo], [2020], INSA Lyon, tous droits réservés

$$\frac{d}{dt}\left(\int_{V_g(t)} \rho_g dV\right) + \oint_{S_g(t)} \rho_g \mathbf{u}_g \cdot \mathbf{n}_g dA - \int_\Gamma \rho_g(\mathbf{u}_g - \mathbf{u}_\Gamma) \cdot \mathbf{n}_\Gamma dA = 0 \tag{6.2}$$

$$\frac{d}{dt}\left(\int_{V_l(t)} \rho_l dV\right) + \oint_{S_l(t)} \rho_l \mathbf{u}_l \cdot \mathbf{n}_l dA + \int_\Gamma \rho_l(\mathbf{u}_l - \mathbf{u}_\Gamma) \cdot \mathbf{n}_\Gamma dA = 0 \tag{6.3}$$

where $V_g(t)$, $S_g(t)$, $V_l(t)$ and $S_l(t)$ are the cell volumes and surface area for the cell boundaries at the vapor and liquid regions, respectively. The interface Γ moves with interface velocity $\mathbf{u}_\Gamma$.

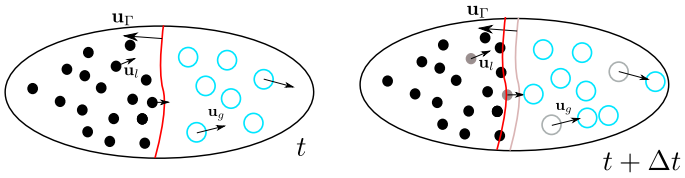

FIGURE 6.1: A schematic diagram of mass transfer across interface from time t to time $t + \Delta t$ under droplet evaporation. On the right side, the previous time liquid points are shown in faded packets.

There is a relative velocity at interface which is different from pure vapor or liquid velocity close to interface. The unit normal vector for one cell with interface points into the liquid phase on Γ is indicted in Fig. 6.2, note that $\mathbf{n}_\Gamma = \mathbf{n}_l = -\mathbf{n}_g$.

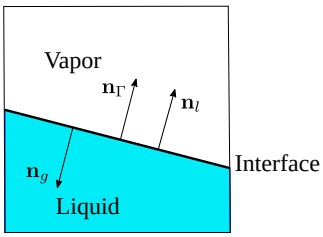

FIGURE 6.2: Definition of unit normal vector in interfacial cell.

By recognizing Eqs. (6.1, 6.2, 6.3), the relative velocity on liquid side equals to the vapor side, which follows mass balance at the interface

$$\int_\Gamma \rho_l(\mathbf{u}_l - \mathbf{u}_\Gamma) \cdot \mathbf{n}_\Gamma dA = \int_\Gamma \rho_g(\mathbf{u}_g - \mathbf{u}_\Gamma) \cdot \mathbf{n}_\Gamma dA \tag{6.4}$$

The mass generated in one phase equals the mass missed in the other one. Therefore, the mass flux ($\dot{m}$) normal to the interface, positive for liquid evaporation and negative for vapor condensation, is given by

$$\dot{m} = \rho_l(\mathbf{u}_l - \mathbf{u}_\Gamma) \cdot \mathbf{n}_\Gamma = \rho_g(\mathbf{u}_g - \mathbf{u}_\Gamma) \cdot \mathbf{n}_\Gamma \tag{6.5}$$

Cette thèse est accessible à l'adresse : http://theses.insa-lyon.fr/publication/2020LYSEI095/these.pdf
© [L. Guo], [2020], INSA Lyon, tous droits réservés

The velocity jump condition due to mass transfer across interface can be obtained from eliminating $\mathbf{u}_\Gamma$ in Eq. (6.5).

$$(\mathbf{u}_g - \mathbf{u}_l) \cdot \mathbf{n}_\Gamma = \dot{m} \left(\frac{1}{\rho_l} - \frac{1}{\rho_g} \right) \tag{6.6}$$

With the incompressibility of fluid on each side of the interface, the integral form of the mass conservation governing equation for fluid is written as:

$$\int_V \nabla \cdot \mathbf{u} dV = \int_\Gamma \dot{m} \left(\frac{1}{\rho_g} - \frac{1}{\rho_l} \right) dA = \int_V \dot{m} \left(\frac{1}{\rho_g} - \frac{1}{\rho_l} \right) \delta_\Gamma dV \tag{6.7}$$

The delta function indicates that the divergence of velocity is zero everywhere, except on the interface due to phase change. In this study, we adopt $\delta_\Gamma = |\nabla C|$ according to Magnini (2012).

6.1.2 Momentum conservation

To integrate the linear momentum over $V(t)$, the forces acting on the interface need to be taken into account in addition to the forces acting on the fluid bodies. With the effect of surface tension as a line force on the interface, the conservation of linear momentum reads

$$\frac{d}{dt} \int_V \rho \mathbf{u} dV = \oint_S \tau \cdot \mathbf{n} dA + \int_V \rho \mathbf{g} dV + \int_V \sigma \kappa \delta_\Gamma \mathbf{n}_\Gamma dV \tag{6.8}$$

where $\tau = -p\mathbf{I} + 2\mu\mathbf{D}$.

Interface jump condition

Considering interface jump condition, a force balance on the interface should be satisfied.

$$\rho_l \mathbf{u}_l \left[(\mathbf{u}_l - \mathbf{u}_\Gamma) \cdot \mathbf{n}_l \right] + \rho_g \mathbf{u}_g \left[(\mathbf{u}_g - \mathbf{u}_\Gamma) \cdot \mathbf{n}_g \right] = \tau_l \cdot \mathbf{n}_l + \tau_g \cdot \mathbf{n}_g + \sigma \kappa \mathbf{n}_\Gamma \tag{6.9}$$

Using $\mathbf{n}_\Gamma = \mathbf{n}_g = -\mathbf{n}_l$ and the mass transfer jump condition in Sec. 6.1.1, the general interface jump condition can be written as

$$\dot{m}(\mathbf{u}_l - \mathbf{u}_g) = (p_g \mathbf{I} - p_l \mathbf{I} + 2\mu_l \mathbf{D}_l - 2\mu_g \mathbf{D}_g) \cdot \mathbf{n}_\Gamma + \sigma \kappa \mathbf{n}_\Gamma \tag{6.10}$$

Projecting the above jump condition along the normal to the interface, and making use of Eq. 6.6, the pressure jump is obtained

$$p_g - p_l = 2(\mathbf{n}_\Gamma \cdot \mu_l \mathbf{D}_l \cdot \mathbf{n}_\Gamma - \mathbf{n}_\Gamma \cdot \mu_v \mathbf{D}_v \cdot \mathbf{n}_\Gamma) + \dot{m}^2 \left(\frac{1}{\rho_l} - \frac{1}{\rho_g} \right) - \sigma \kappa \tag{6.11}$$

Cette thèse est accessible à l'adresse : http://theses.insa-lyon.fr/publication/2020LYSEI095/these.pdf
© [L. Guo], [2020], INSA Lyon, tous droits réservés

6.1.3 Energy conservation

Neglecting kinetic energy, viscous dissipation and with fluid incompressibility property and constant heat capacity, the energy conservation equation can be written as

$$\int_V \frac{\partial(\rho c_p T)}{\partial t} + \oint_S (\rho c_p T \mathbf{u}) \cdot \mathbf{n} dA = \oint_S \lambda \nabla T \cdot \mathbf{n} dA + \int_V \dot{q}_\Gamma \delta_\Gamma dV \tag{6.12}$$

Interface jump condition

In this study, we assume the thermal equilibrium assumption was made at the interface, which means the interface temperature is set to equal the saturated temperature of the fluid. According to Tryggvason et al. (2006), this assumption is accurate when the flow characteristic length is much larger than thermal conditions.

Cells in the computational domain can be divided into two general types. The first type contains interface segment and is called interfacial cells. The second type contains no interface. The mass flux $\dot{m}$ in Eq. (6.16) should be calculated in all interfacial cells using the energy jump condition of

$$\dot{m} h_{lg} = [\dot{q}] \tag{6.13}$$

$$\dot{m} = \frac{\dot{q}_l - \dot{q}_g}{h_{lg}} = \frac{(\lambda \nabla T|_l - \lambda \nabla T|_g) \cdot \mathbf{n}_\Gamma}{h_{lg}} \tag{6.14}$$

where [] is the normal jump for a given variable across the interface. $\dot{q}$ is heat flux indicated by $\dot{q} = \dot{m} h_{lg}$. As aforementioned, the interface is assumed to be at the saturated temperature during phase change, which is expressed by

$$T_\Gamma = T_{sat}(p_\infty) \tag{6.15}$$

where p_∞ is the saturated pressure.

6.1.4 Systems of governing equations

We summarize the integral form of governing equations for two-phase flow with phase change:
Mass conservation:

$$\int_V \nabla \cdot \mathbf{u} dV = \int_V \dot{m} \left(\frac{1}{\rho_g} - \frac{1}{\rho_l} \right) \delta_\Gamma dV \tag{6.16}$$

Momentum conservation:

$$\frac{d}{dt} \int_V \rho \mathbf{u} dV = \oint_S \tau \cdot \mathbf{n} dA + \int_V \rho \mathbf{g} dV + \int_V \sigma \kappa \delta_\Gamma \mathbf{n}_\Gamma dV \tag{6.17}$$

Cette thèse est accessible à l'adresse : http://theses.insa-lyon.fr/publication/2020LYSEI095/these.pdf
© [L. Guo], [2020], INSA Lyon, tous droits réservés

Energy conservation:

$$\int_V \frac{\rho c_p \partial T}{\partial t} + \oint_S \rho c_p (T\mathbf{u}) \cdot \mathbf{n} dA = \oint_S \lambda \nabla T \cdot \mathbf{n} dA + \int_V \dot{q}_\Gamma \delta_\Gamma dV \tag{6.18}$$

6.2 Numerical methods

In this section, a phase change model developed in the Basilisk solver is introduced. The work includes:

- Mass flux ($\dot{m}$) calculation.
- Implementation of the VOF equation considering phase change.
- Thermal boundary condition at the interface.

6.2.1 Mass flux calculation

The calculation of the temperature gradient is not performed directly in interfacial cells but in the neighboring pure liquid cells. Kunkelmann (2011) pointed out that the temperature in interfacial cells is not the liquid temperature but a mean value of the liquid and vapor phase and depends on the weighting procedure of the fluid properties. In this section, we assume the liquid phase is saturated and the vapor phase is unsaturated. Therefore, heat transfer in the liquid phase is negligible. The mass flux in Eq. (6.14) for the vapor side can be calculated using a similar method to Ling et al. (2014). The temperature gradient in cell (i, j) can be computed by using weighted method in cell $(i-1, j)$ and $(i-1, j+1)$. The cell $(i-1, j+1)$ is pure vapor cell and $(i-1, j)$ is pure vapor cell or interfacial cell.

$$\left.\frac{\partial T}{\partial n}\right|_{(i,j)} = \nabla T \cdot \mathbf{n}_\Gamma \approx \nabla T_{i-1,j} |\mathbf{n}_{\Gamma,x}| + \nabla T_{i-1,j+1} |\mathbf{n}_{\Gamma,y}| \tag{6.19}$$

where $\nabla T_{i-1,j} = \frac{T_{i-1,j} - T_{i-2,j}}{\Delta x}$ and $\nabla T_{i-1,j+1} = \frac{T_{i-1,j+1} - T_{i-2,j+1}}{\Delta x}$.

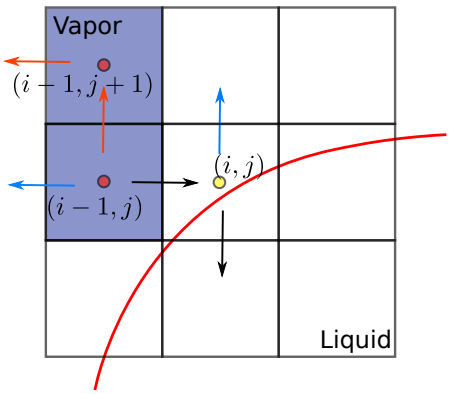

FIGURE 6.3: Illustration of temperature interpolation method.

Cette thèse est accessible à l'adresse : http://theses.insa-lyon.fr/publication/2020LYSEI095/these.pdf
© [L. Guo], [2020], INSA Lyon, tous droits réservés

After solving the temperature gradient at the vapor side in Eq. (6.19), the mass flux $\dot{m}$ can be obtained by Eq. (6.27), adding this term in the approximate projection step to solve the Navier-Stokes equation with phase change. The predicted velocity of $\mathbf{u}^*$ in the momentum equations are calculated using the time-fractional method after solving advection and viscous terms. A pressure Poisson equation is then solved,

$$\nabla \cdot \left[\frac{\Delta t}{\rho^{n+1/2}} \nabla p^{n+1/2} \right] = \nabla \cdot \mathbf{u}^* - \dot{m} \left(\frac{1}{\rho_l} - \frac{1}{\rho_g} \right) \delta_\Gamma^n \tag{6.20}$$

Using the constraint of Eq. (6.8), the one fluid velocity $\mathbf{u}^{n+1}$ can be obtained using $p^{n+1/2}$

$$\mathbf{u}^{n+1} = \mathbf{u}^* - \frac{\Delta t}{\rho^{n+1/2}} \nabla p^{n+1/2} \tag{6.21}$$

6.2.2 Implementation of the VOF equation considering phase change.

As mentioned in Chapter 2, the geometric VOF method is used in the Basilisk solver. For more details on this method, refer to Scardovelli and Zaleski (2003); López-Herrera et al. (2015); Tryggvason et al. (2011); Weymouth and Yue (2010). The existence of the phase change source term results in non divergence-free velocity by solving Navier-Stokes equations. Therefore, the geometric VOF method in the Basilisk solver can not be directly used due to the divergence-free velocity considering in the advection term.

In this work, we use a method similar to Malan et al. (2020); Scapin et al. (2020). Phase change induces a Stefan flow, which causes a jump in the flow velocity. The basic idea of the method is that a divergence-free liquid velocity extension can be obtained by subtracting this jump to the flow velocity, then use the existed geometric VOF method to account for phase change. The method can be divided into two steps. In the first step, a divergence-free liquid velocity is constructed to produce an intermediate VOF field (C^*); in the second step, the mass source term is added to move the interface accounting for phase change.

For the phase change problem, the VOF advection equation is written as

$$\frac{\partial C}{\partial t} + \nabla \cdot (\mathbf{u} C) = -\frac{\dot{m}}{\rho_l} \delta_\Gamma \tag{6.22}$$

Note that the tracked phase here is the liquid by convention. The source term in the right hand side indicates the volume change due to phase change at the interface.

Due to $\delta_\Gamma = |\nabla C|$, Eq. (6.22) can be further written as

$$\frac{\partial C}{\partial t} + \nabla \cdot (\mathbf{u} C) + \frac{\dot{m}}{\rho_l} |\nabla C| = 0 \tag{6.23}$$

Cette thèse est accessible à l'adresse : http://theses.insa-lyon.fr/publication/2020LYSEI095/these.pdf
© [L. Guo], [2020], INSA Lyon, tous droits réservés

Step 1: Constructing divergence-free liquid velocity

In this step, an intermediate VOF value C^* is calculated by constructing a divergence-free liquid velocity.

$$\frac{C^* - C^{n-1/2}}{\Delta t} + \nabla \cdot (\mathbf{u}_l C)^n = 0 \tag{6.24}$$

where $\mathbf{u}_l$ is the divergence-free velocity ($\nabla \cdot \mathbf{u}_l = 0$) which is constructed by Stefan flow velocity ($\widetilde{\mathbf{u}}$) and one-fluid velocity ($\mathbf{u}$) (Scapin et al., 2020).

In order to obtain $\mathbf{u}_l$, we propose a simple but effective method similar to Malan et al. (2020). First, the one-fluid velocity ($\mathbf{u}^{n+1}$) is obtained after solving the Eq. (6.22), which has a discontinuity at the interface. Second, we solve the Stefan flow velocity $\widetilde{\mathbf{u}}$ in the entire domain just consider the effect of phase change, which can be obtained like Eq. (6.22)

$$\nabla \cdot \left[\frac{\Delta t}{\rho^{n+1/2}} \nabla \widetilde{p} \right] = \dot{m} (\frac{1}{\rho_g} - \frac{1}{\rho_l}) \delta_\Gamma \tag{6.25}$$

The above equation is solved using the same method when solving the one-fluid velocity. A Stefan flow velocity is obtained:

$$\widetilde{\mathbf{u}}^{n+1} = -\frac{\Delta t}{\rho^{n+1/2}} \nabla \widetilde{p}^{n+1/2} \tag{6.26}$$

The divergence-free liquid velocity can be obtained as

$$\mathbf{u}_l^{n+1} = \mathbf{u}^{n+1} + \widetilde{\mathbf{u}}^{n+1} \tag{6.27}$$

This velocity field is divergence-free in the liquid, the gas and at the interface since:

$$\nabla \cdot \mathbf{u}_l^{n+1} = \nabla \cdot \mathbf{u}^{n+1} + \nabla \cdot \widetilde{\mathbf{u}}^{n+1} = \dot{m} (\frac{1}{\rho_g} - \frac{1}{\rho_l}) \delta_\Gamma - \dot{m} (\frac{1}{\rho_g} - \frac{1}{\rho_l}) \delta_\Gamma = 0 \tag{6.28}$$

Step 2: Shifting the interface accounting for phase change

The interface movement due to phase change can be expressed by adding a source term in the VOF equation. After step-1, the intermediate VOF value C^* will be used in the following equation

$$\frac{C^{n+1/2} - C^*}{\Delta t} + \frac{S_l}{\rho_l} = 0 \tag{6.29}$$

where S_l is the volumetric source term expressed as $S_l = \dot{m} |\nabla C|$.

There are two general methods to solve Eq. (6.29). The first one uses the PLIC reconstruction in Basilisk solver, and this method is also introduced in Malan et al. (2020). To account for phase change, we need to shift the interface in the normal direction by adding a mass source term. The shift distance (Δd) due to phase change is defined as

Cette thèse est accessible à l'adresse : http://theses.insa-lyon.fr/publication/2020LYSEI095/these.pdf
© [L. Guo], [2020], INSA Lyon, tous droits réservés

$$\Delta d = -\frac{\dot{m}}{\rho_l}\Delta t \tag{6.30}$$

where Δt is the timestep. Using the PLIC method, the distance (α^{n+1}) in 3.2 is defined and the new $C^{n+1/2}$ is obtained.

$$\alpha^{n+1/2} = \alpha^n + \|\mathbf{n_\Gamma}\|\frac{\Delta d}{h} \tag{6.31}$$

$$C^{n+1/2} = f(\alpha^{n+1/2}, \mathbf{n}_\Gamma) \tag{6.32}$$

where h is grid spacing and α^n is the smallest distance from cell origin to interface in initial interface reconstruction at beginning of each timestep. $\mathbf{n}_\Gamma$ is the interface normal vector. $f(\alpha^{n+1}, \mathbf{n_\Gamma})$ is the "forward problem" described in Chapter 3.

The other method directly obtains the $C^{n+1/2}$ from Eq. (6.29) as

$$C^{n+1/2} = C^* - \frac{\Delta t \dot{m}}{\rho_l}|\nabla C| \tag{6.33}$$

$$|\nabla C| \approx \sqrt{\left(\frac{\partial C}{\partial x}\right)^2 + \left(\frac{\partial C}{\partial y}\right)^2} \tag{6.34}$$

The calculation of $|\nabla C|$ in Eq. (6.34) uses a smoothed derivative of the color function across the interface (Magnini, 2012), i.e. the $|\nabla C|$ in x direction is expressed in the following equation and the y direction derivative can use a similar approach:

$$\left(\frac{\partial C}{\partial x}\right)^2 = \frac{C_{i-1,j+1} + 2C_{i,j+1} + C_{i+1,j+1} - C_{i-1,j-1} - 2C_{i,j-1} - C_{i+1,j-1}}{8\Delta x} \tag{6.35}$$

Combining the Eqs. (6.33,6.34), the new $C^{n+1/2}$ is obtained. Subsequently, the physical properties such as ρ, μ are updated.

6.2.3 Thermal boundary condition at interface

In order to maintain the interface at the saturated temperature, we use a ghost cell method proposed by Zhang and Ni (2018) to impose such a boundary condition on the interface. We assume the liquid phase is saturated and the vapor phase is unsaturated, as described in Zhang and Ni (2018), we only introduce the numerical method in the vapor phase. For the liquid phase, it is an analogous manner to apply the method. First, we need to define the ghost cells outside the vapor phase, which can be divided into two types: one is the cell contains interface, while the cell center is outside the interface. Using the PLIC interface reconstruction definition in Chapter 3, this means the distance vector from the cell center to the interface is positive, as labeled by the yellow circle in Fig. 6.4. The other type of ghost cell is the pure liquid

Cette thèse est accessible à l'adresse : http://theses.insa-lyon.fr/publication/2020LYSEI095/these.pdf
© [L. Guo], [2020], INSA Lyon, tous droits réservés

cell, which has a corner neighbor belonging to the interfacial cells but not belonging to the ghost cells, as labeled by the red circle.

After defining the ghost cells, the temperature in ghost cells is calculated to satisfy the thermal boundary condition accounting for phase change. The treatment for interfacial ghost cell is different from the pure liquid ghost cell. Taking the ghost cell (i, j) in interfacial cell as example (see Fig. 6.4 point A), the temperature at vapor barycenter (T_b) is calculated by averaging the cell center temperature around the barycenter point. The ghost cell temperature is calculated as an artificial temperature expressed as $T_{i,j} = 2T_{sat} - T_b$. It should be noted $T_{i,j}$ and T_b are dependent on each other because of the northeast corner of the cell $(i-1, j-1)$ in point A. An iterative method is applied to get a convergent solution until the error between two adjacent iterative steps is smaller than 10^{-6}; this method is also used in Zhang and Ni (2018). The calculation of temperature in pure ghost cell is different. The schematic is shown in Fig. 6.4 point B. We consider a mirror point (p) in $(i-1, j-1)$. Temperature of point p is first calculated, then $T_{i,j} = 2T_{sat} - T_p$ is calculated as an artificial temperature at pure ghost cell.

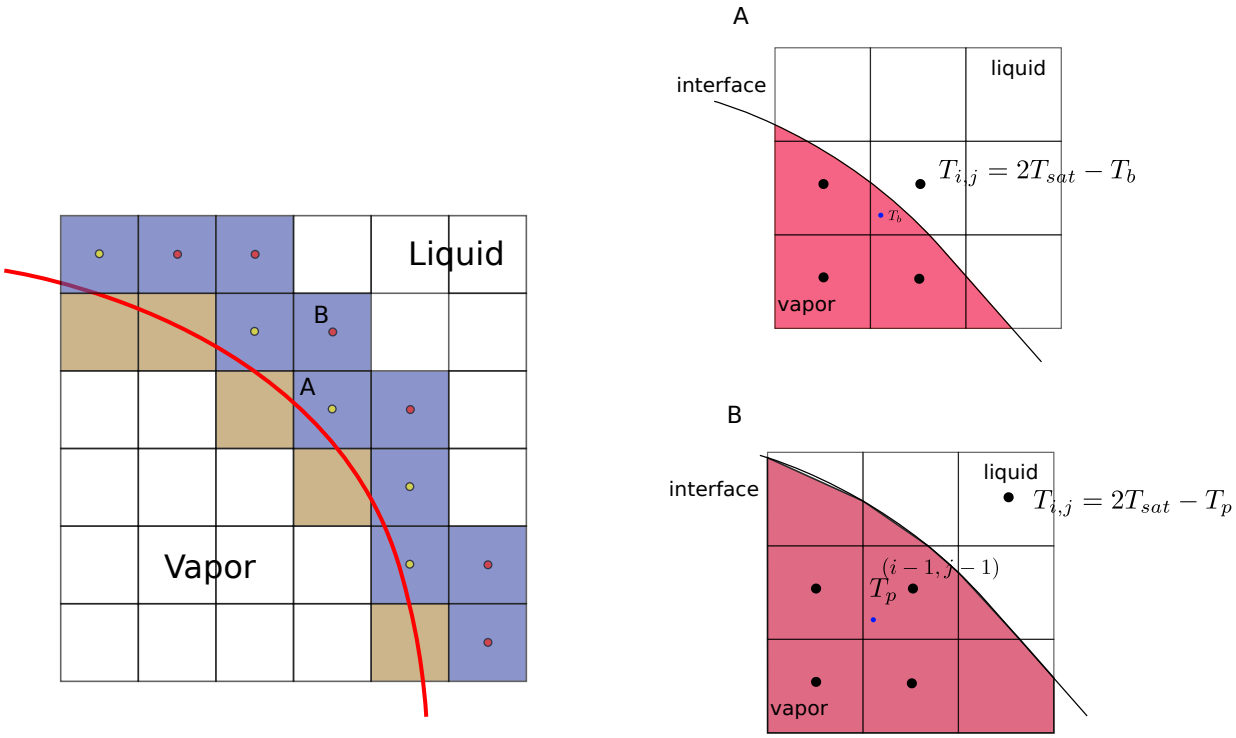

FIGURE 6.4: The calculation of the temperature field in the ghost cells lying outside the vapor phase (Zhang and Ni, 2018).

Cette thèse est accessible à l'adresse : http://theses.insa-lyon.fr/publication/2020LYSEI095/these.pdf
© [L. Guo], [2020], INSA Lyon, tous droits réservés

6.2.4 Overview of phase change procedure

1). Timestep is calculated by the CFL condition and the constraint of surface tension stability.

$$\Delta t = \min\left(\left(\frac{|u_{i,j}|}{\Delta x}+\frac{|v_{i,j}|}{\Delta y}\right)^{-1}, \sqrt{\frac{(\rho_l+\rho_g)\min(\Delta x^3,\Delta y^3)}{4\pi\sigma}}\right) \tag{6.36}$$

2). The mass flux is calculated using Eqs. (6.14) and (6.19).

3). The VOF equation is integrated in time as

$$\frac{C^{n+1/2}-C^{n-1/2}}{\Delta t}+\nabla\cdot(\mathbf{u}C)^n+\frac{\dot{m}}{\rho_l}\delta_\Gamma|^n=0 \tag{6.37}$$

The procedure of VOF equation is detailed in Sec. 6.2.2. The fluid properties can be updated using the $C^{n+1/2}$ ($\rho^{n+1/2}, \mu^{n+1/2}, \delta^{n+1/2}, \mathbf{n}_\Gamma^{n+1/2}, \kappa^{n+1/2}, \lambda^{n+1/2}, c_p^{n+1/2}$).

4). The thermal boundary condition is imposed at the interface. Then the backward implicit Euler time integration of temperature field is applied to each cell and reads

$$\frac{T^{n+1/2}-T^{n-1/2}}{\Delta t}+(\mathbf{u}\cdot\nabla T)^n=\nabla\cdot\left(\frac{\lambda}{\rho c_p}\nabla T\right)^{n+1/2}+\dot{m}h_{lg}\delta_\Gamma \tag{6.38}$$

5). The provisional face velocity ($\mathbf{u}_f^{n+1,*}$) at t^{n+1} is obtained by interpolating the centered intermediate velocity ($\mathbf{u}_c^*$) in Eq. (3.58). Then use approximate projection to compute $p^{n+1/2}$ and face velocity ($\mathbf{u}_f^{n+1}$).

$$\begin{aligned}\nabla\cdot\mathbf{u}_f^{n+1}&=\dot{m}\left(\frac{1}{\rho_g}-\frac{1}{\rho_l}\right)\delta_\Gamma\\ \rho_c^{n+1/2}\frac{\mathbf{u}_f^{n+1}-\mathbf{u}_f^{n+1,*}}{\Delta t}&=-\nabla p_c^{n+1/2}\end{aligned} \tag{6.39}$$

6). Use interpolation method to obtain $\mathbf{u}_c^{n+1,*}$ from $\mathbf{u}_f^{n+1}$. Then correct $\mathbf{u}_c^{n+1,*}$ using new pressure gradient and acceleration terms at $t+1/2$.

$$\mathbf{u}_c^{n+1}=\mathbf{u}_c^{n+1,*}+\Delta t\left(\mathbf{a}-\frac{1}{\rho}\nabla p\right)_{f\to c}^{n+1/2} \tag{6.40}$$

6.3 Validation of phase change models

6.3.1 Droplet evaporation with constant mass flux

A two-dimensional circular droplet is considered, where evaporation is driven by a dimensionless constant mass flux $\dot{m}_0 = 0.1$. This case specifically evaluates the

Cette thèse est accessible à l'adresse : http://theses.insa-lyon.fr/publication/2020LYSEI095/these.pdf
© [L. Guo], [2020], INSA Lyon, tous droits réservés

two-step VOF-advection procedure without calculating mass flux and considering solving the thermal energy equation. The dimensionless analysis is used, and the parameters come from Scapin et al. (2020). The liquid droplet with an initial diameter $d_0 = 1$ is initialized at the center of a square domain with dimensions $[-4, 4]$, and zero-pressure outflow boundaries. The Reynolds number ($Re = 25$) and Weber number ($We = 0.1$) are used to determining viscosity and surface tension, which are defined as:

$$Re = \frac{\rho_l U_{ref} d_0}{\mu_l} \tag{6.41}$$

$$We = \frac{\rho_l U_{ref}^2 d_0}{\sigma} \tag{6.42}$$

where U_{ref} in Scapin et al. (2020) is indicated by $\dot{m}_0/\rho_g$.

According to the work of Tanguy et al. (2007), the droplet diameter evolves in time with the expression:

$$\frac{d(t)}{d_0} = 1 - (\frac{2\dot{m}_0}{d_0 \rho_l})t \tag{6.43}$$

The ability of the method to handle interface-normal velocity jumps across the interface (see Eq. (6.5)) is analyzed here. Four different grid spacings $1/h = [32, 64, 128, 256]$ are used to test the magnitudes of this jump. Fig. 6.5 (A) is the droplet diameter temporal evolution with different density ratios. The results show a good agreement with the analytical solution (see Eq. (6.43)). Fig. 6.5 (B) shows an accurate solution is achieved for $1/h > 32$. Fig. 6.6 gives two time instants of the droplet evolution for the finest resolution. The velocity magnitude reveals resulting radial flow patterns (Malan et al., 2020) and the droplet shape is maintained throughout, the velocity field around the droplet seems to be symmetric.

Cette thèse est accessible à l'adresse : http://theses.insa-lyon.fr/publication/2020LYSEI095/these.pdf
© [L. Guo], [2020], INSA Lyon, tous droits réservés

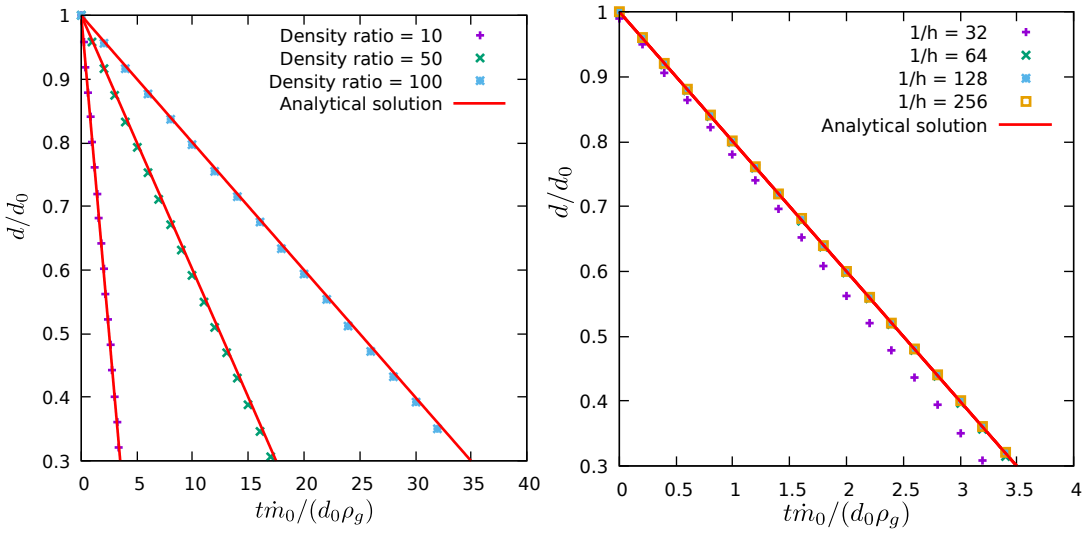

(A) (B)

FIGURE 6.5: (A) Temporal evolution of the droplet diameter for $\rho_r = 10, 50, 100$ on a 128×128 grid. (B) Grid convergence test for an evaporating droplet with $\rho_r = 10$.

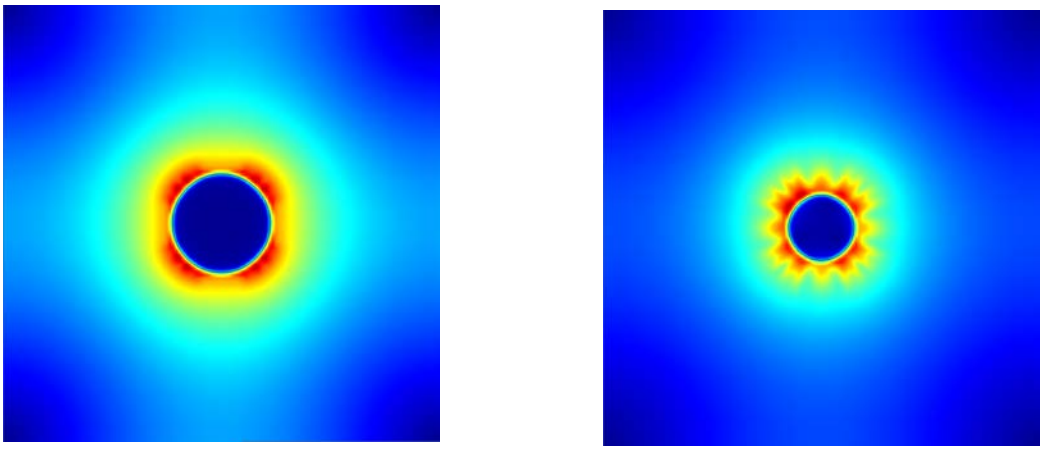

FIGURE 6.6: Velocity magnitude on a 256×256 grid.

Finally, in this test, we give the velocity vector field at $d/d_0 = 0.6$ for different velocity vectors used in the method. The one-fluid velocity $\mathbf{u}$ is calculated from the Navier-Stokes equations, which shows velocity jump at the interface. The liquid divergence-free velocity $\mathbf{u}_l$ is used in the geometric VOF advection step. For an evaporating static droplet, the $\mathbf{u}_l$ should be zero. The results in Fig. 6.7 are expected and show proper velocity distribution. Besides, the velocity jump condition is shown in Fig. 6.7, it is observed at interface there is a sharp increase of velocity.

Cette thèse est accessible à l'adresse : http://theses.insa-lyon.fr/publication/2020LYSEI095/these.pdf
© [L. Guo], [2020], INSA Lyon, tous droits réservés

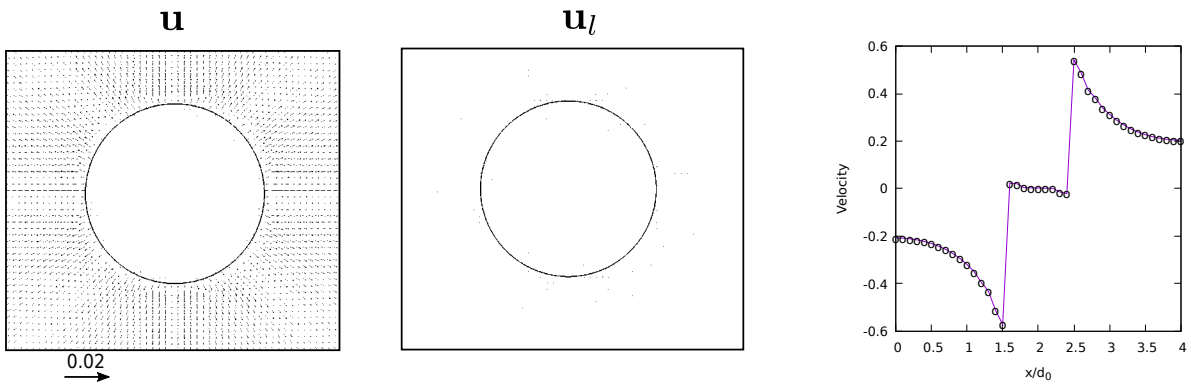

FIGURE 6.7: Velocity vector filed of one-fluid velocity $\mathbf{u}$, divergence-free liquid velocity $\mathbf{u}_l$ and velocity jump in normal direction at $d/d_0 = 0.6$.

6.3.2 One dimensional Stefan problem

To validate the phase change models, we consider the one dimensional Stefan problem widely used by many authors (Hardt and Wondra, 2008; Sato and Ničeno, 2013; Tsui and Lin, 2016; Zhang and Ni, 2018; Rajkotwala et al., 2019). The geometry of the Stefan problem is illustrated in Fig. 6.8. In the test case, the vapor and liquid are assumed as incompressible. The water properties at 1atm are considered in Tab. 6.1. The liquid-vapor interface is initially near the left wall of the domain, which is viewed as a constant temperature of T_{wall} higher than saturated temperature T_{sat}. We can write $T_{wall} = T_{sat} + \Delta T$, where ΔT is the degrees above the saturation temperature. The interface keeps saturated conditions during its motion. Initially, the liquid fills the computational domain at saturation temperature, while the vapor temperature linearly decreases from the left wall to the interface position.

TABLE 6.1: Water properties at saturation pressure of 1 atm ($T_{sat} = 373.15K$).

Property	Unit	Vapor	Liquid
Density ρ	kg/m^3	0.6	958
Viscosity μ	$kg/(m\ s)$	1.23×10^{-5}	2.82×10^{-4}
Heat capacity c_p	$J/(kg\ K)$	2080	4216
Thermal conductivity λ	$W/(m\ K)$	0.025	0.68
Surface tension σ	N/m	0.059	-

An analytical solution available for the evolution of the interface thickness and temperature profile is given in Welch and Wilson (2000). The evolution of the interface position follows

$$\delta(t) = 2\beta\sqrt{\alpha_v t} \tag{6.44}$$

Cette thèse est accessible à l'adresse : http://theses.insa-lyon.fr/publication/2020LYSEI095/these.pdf
© [L. Guo], [2020], INSA Lyon, tous droits réservés

with δ is the interface position, $\alpha_v = \lambda_v/(\rho_v c_{p,v})$ is the thermal diffusivity of the vapor phase and β is the solution of the transcendental equation

$$\beta e^{\beta^2} \text{erf}(\beta) = \frac{c_{p,v}(T_{wall} - T_{sat})}{h_{lg}\sqrt{\pi}} \tag{6.45}$$

where erf(β) is the error function for β and $h_{lg} = 2256$ kJ/kg is the latent heat of vaporization.

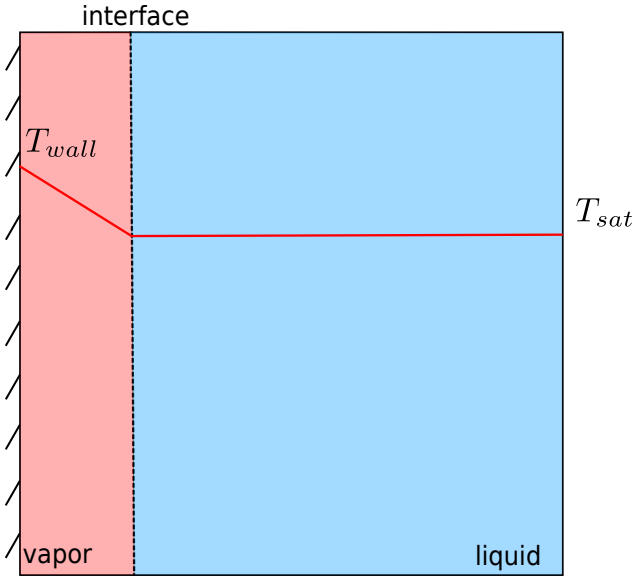

FIGURE 6.8: The schematic diagram of the one dimensional Stefan problem.

The analytical solution of temperature at any point x in the gas phase is given by

$$T_g(x,t) = T_{wall} + (\frac{T_{sat} - T_{wall}}{\text{erf}(\beta)})\text{erf}(\frac{x}{2\sqrt{\alpha_g t}}) \tag{6.46}$$

According to Irfan and Muradoglu (2017), the analytical velocity in the liquid phase uses the following relation

$$u_l = (1 - \frac{\rho_g}{\rho_l})u_n \tag{6.47}$$

where $u_n = \beta\sqrt{\alpha_g/t}$.

We perform numerical simulation on a domain size of 10 $mm\times$ 10 mm (Malan et al., 2020), and ΔT = 10 K is initially given. Three grid numbers in x direction is: $N_x = [64, 128, 256]$. The initial interface position is set as 32.25 μm, corresponding to an initial time $t = 0.28$ s. The simulation is running until the time $t = 10$ s is reached. The corresponding analytical solution is $\delta(10) = 191.9$ μm and a linear temperature profile from the left wall to the interface is initialized. The Basilisk results in Fig. 6.9 shows an excellent agreement with analytical solution. Tab. 6.2 shows the relative

Cette thèse est accessible à l'adresse : http://theses.insa-lyon.fr/publication/2020LYSEI095/these.pdf
© [L. Guo], [2020], INSA Lyon, tous droits réservés

errors of the interface position at final time $t = 10\ s$ for grid resolutions. The results show the relative error is less than 1% even for the coarsest grid.

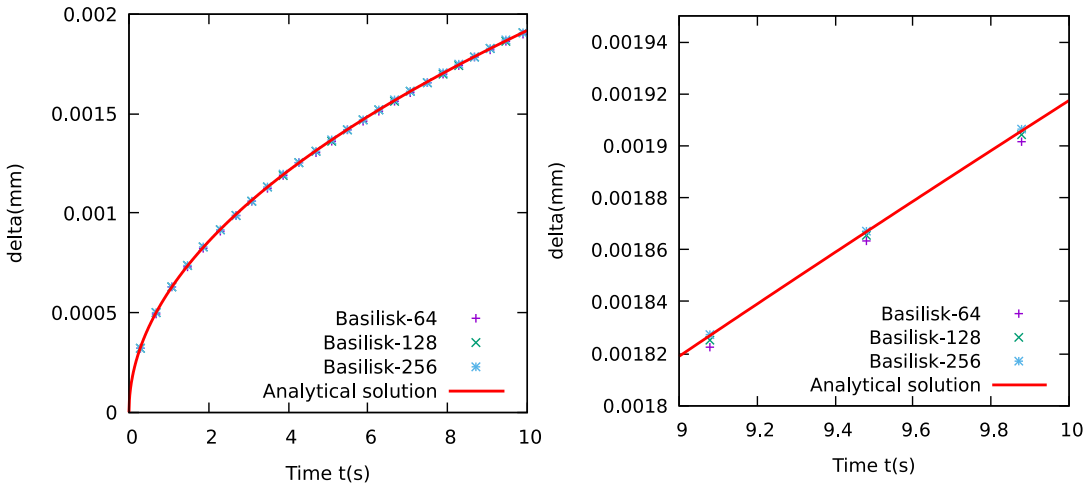

(A) (B)

FIGURE 6.9: Different mesh analysis on one dimensional Stefan problem. (A) The interface evolution with time, (B) Zoom view.

TABLE 6.2: Absolute relative errors of interface location at $t = 10s$ for different grid resolutions.

Grid points	δ	Absolute relative error $\%$
N_x = 64	191.398 μm	0.26$\%$
N_x = 128	191.476 μm	0.22$\%$
N_x = 256	191.672 μm	0.12$\%$

Fig. 6.10 shows the evolution of the simulation of u_l with time and temperature variation along the domain length on the finest grid. The results agree well with the analytical solutions.

Cette thèse est accessible à l'adresse : http://theses.insa-lyon.fr/publication/2020LYSEI095/these.pdf
© [L. Guo], [2020], INSA Lyon, tous droits réservés

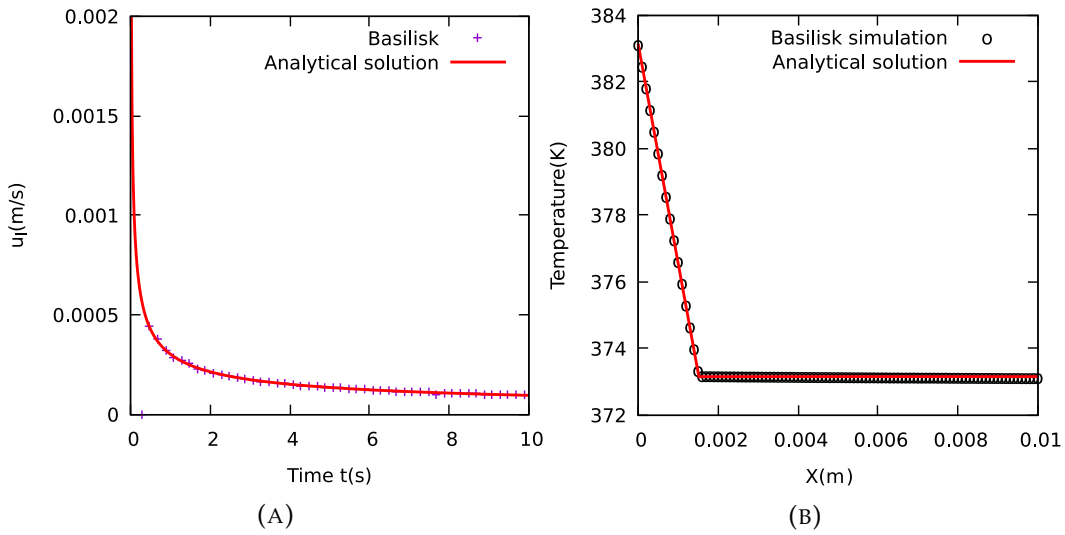

FIGURE 6.10: Results on the finest grid. (A) Evolution of liquid velocity with time, (B) Temperature profile along the domain length at $t = 6s$.

6.3.3 One dimensional sucking interface problem

Another interesting one-dimensional test case is the sucking interface problem, which is also a benchmark case used to validate phase change models and has previously studied by some investigators (Welch and Wilson, 2000; Kunkelmann, 2011; GUEDON, 2013; Irfan and Muradoglu, 2017; Rajkotwala et al., 2019). The schematic diagram of this test case is shown in Fig. 6.11. Like the Stefan problem, a vapor layer is initially attached to the left wall of the domain, while the rest is filled with a liquid. The initial temperature in the vapor side is saturated, and the liquid temperature is higher than the vapor side; thus, the heat absorbed through evaporation comes from the liquid. The left wall temperature is set as $T_{wall} = T_{sat}$, and outflow boundary condition is imposed on right wall with temperature $T_{\infty} = T_{sat} + \Delta T$. In this problem, $\Delta T = 5K$.

Cette thèse est accessible à l'adresse : http://theses.insa-lyon.fr/publication/2020LYSEI095/these.pdf
© [L. Guo], [2020], INSA Lyon, tous droits réservés

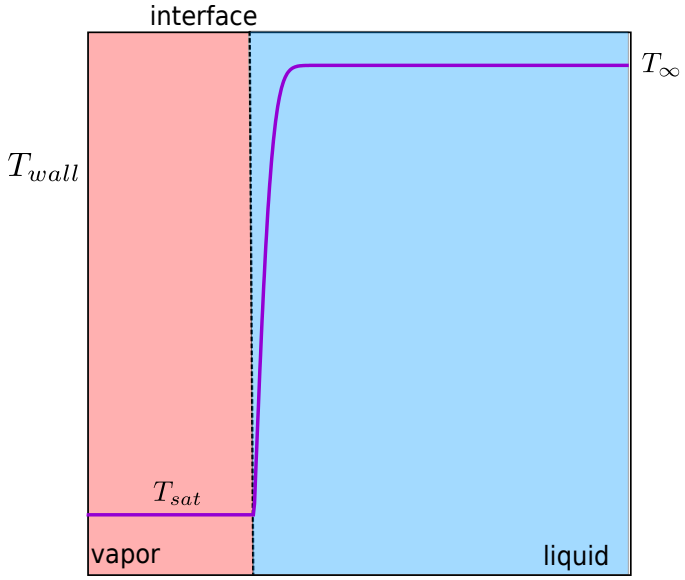

FIGURE 6.11: The schematic diagram of the one dimensional Sucking problem.

An analytical solution available for the evolution of the interface thickness same with the Stefan problem is given in Welch and Wilson (2000). The evolution of the interface position follows

$$\delta(t) = 2\beta\sqrt{\alpha_v t} \tag{6.48}$$

where β is the solution of the following transcendental equation

$$e^{\beta^2}\text{erf}(\beta)\left[\beta - \frac{(T_\infty - T_{sat})c_{p,g}\lambda_l\sqrt{\alpha_g}e^{-\beta^2\frac{\rho_g^2\alpha_g}{\rho_l^2\alpha_l}}}{h_{lg}\lambda_l\sqrt{\pi\alpha_l}\text{erfc}(\beta\frac{\rho_g\sqrt{\alpha_g}}{\rho_l\sqrt{\alpha_l}})}\right] = \frac{c_{p,g}(T_{wall} - Tsat)}{h_{lg}\sqrt{\pi}} \tag{6.49}$$

The analytical solution for the temperature profile in the liquid phase is given as following equation, and this is also the initial solution in simulation (see Fig. 6.11).

$$T_l(x,t) = T_\infty - \left(\frac{T_\infty - T_{wall}}{\text{erfc}(\beta\frac{\rho_g\sqrt{\alpha_g}}{\rho_l\sqrt{\alpha_l}})}\right)\text{erfc}\left(\frac{x}{2\sqrt{\alpha_l t}} + \frac{\beta(\rho_g - \rho_l)}{\rho_l}\sqrt{\frac{\rho_g}{\rho_l}}\right) \tag{6.50}$$

The horizontal velocity used in the test using the same expression in the Stefan problem, Eq. (6.47). The fluid properties come from Tab. 6.1. The initial vapor thickness is set as 30.85 μm, which corresponds to the initial time $t = 0.2$ s and the simulation is run until the time $t = 1.1$ s is reached. The corresponding analytical solution for the position of the interface is $\delta(1.1) = 7.288$ mm.

Fig. 6.12 shows the sucking interface evolution with time on different grid resolutions. Fig. 6.12 (A) is the interface position evolution with time, and the instantaneous profiles of temperature at $t = 1.1$ s is shown in Fig. 6.12 (B). Compared with the Stefan problem, the sucking interface problem is more dependent on the mesh resolutions.

Cette thèse est accessible à l'adresse : http://theses.insa-lyon.fr/publication/2020LYSEI095/these.pdf
© [L. Guo], [2020], INSA Lyon, tous droits réservés

This phenomenon is also observed in the work of GUEDON (2013); Irfan and Muradoglu (2017). Nevertheless, with a decrease of the grid sizes, the simulation results can be improved. The absolute relative errors are shown in Tab. 6.3. The error below 10% is acceptable for the fine mesh resolution.

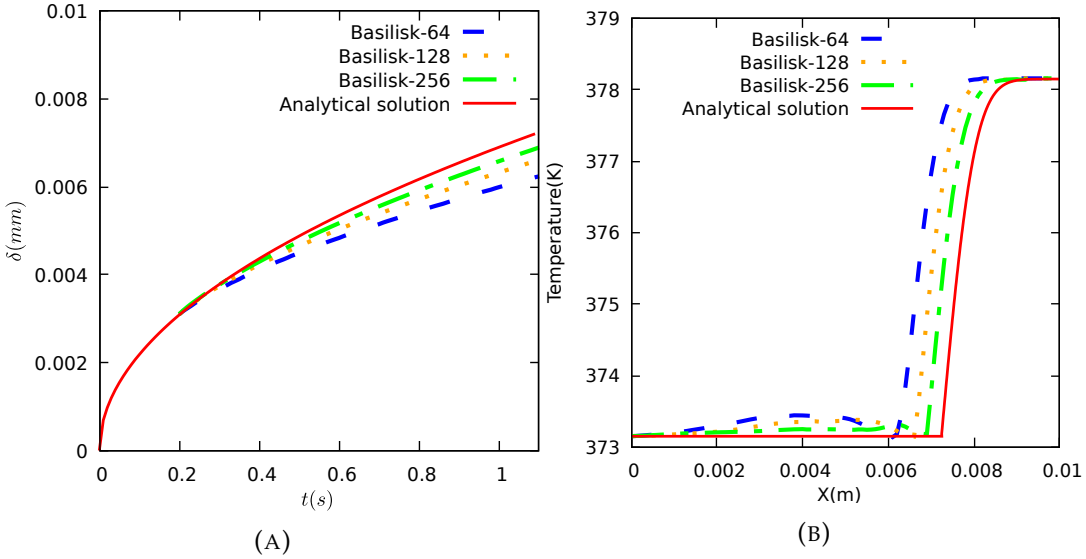

(A) (B)

FIGURE 6.12: Different mesh analysis on one dimensional Stefan problem. (A) Evolution of interface with time, (B) Temperature profile along the domain length at $t = 1.1s$.

TABLE 6.3: Absolute relative errors of interface location at $t = 1.1s$ for different grid resolutions.

Grid points	δ	Absolute relative error %
N_x = 64	6.2355 mm	14.4%
N_x = 128	6.6082 mm	9.33%
N_x = 256	6.8915 mm	5.44%

6.3.4 Film boiling

In this test case, we turn to the two-dimensional film boiling flows. In the film boiling problem, the initial state of the vapor phase completely covers the superheated wall, which separates saturated liquid from the heated bottom plate (consider saturated liquid here). With the evolution of time, the denser liquid above the vapor film will fall, while lighter vapor rises due to the Rayleigh-Taylor instability. The film boiling test case has been studied by many investigators (Welch and Wilson, 2000; Gibou et al., 2007; Guo et al., 2011).

A two-dimension computational domain of film boiling is shown in Fig. 6.13. The domain size is $0.5\lambda_0 \times 3\lambda_0$, where λ_0 is the most unstable Taylor wave length. In this

Cette thèse est accessible à l'adresse : http://theses.insa-lyon.fr/publication/2020LYSEI095/these.pdf
© [L. Guo], [2020], INSA Lyon, tous droits réservés

case, we set λ_0 according to the work of Berenson (1961) by

$$\lambda_0 = 2\pi \left(\frac{3\sigma}{(\rho_l - \rho_g)g} \right)^{\frac{1}{2}} \tag{6.51}$$

The initial thickness of vapor film in y direction is defined by a function of cosine wave as follows

$$y = \frac{\lambda_0}{128}(4 + \cos(\frac{2\pi x}{\lambda_0})) \tag{6.52}$$

We consider the left and right walls are symmetry boundary conditions. The liquid and interface are at saturated temperature (T_{sat}). The bottom wall is superheated at a higher temperature ($T_{wall} - T_{sat} = 5K$). The temperature from the wall to the interface is assumed to be linear. Incompressible two-phase flow is considered with surface tension coefficient $\sigma = 0.1N/m$, latent heat $h_{lg} = 10^5 J/kg$ and the gravity acceleration $g = 9.81m/s^2$. The physical parameters of the two phases considered in the present study are shown in Tab. 6.4. The grid size in this test case is $\frac{3\lambda_0}{2^9}$, because we have validated grid analysis in previous cases; therefore, we will not perform this anymore in this test case.

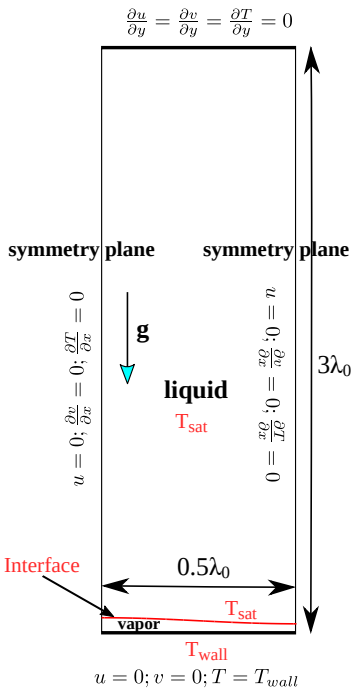

FIGURE 6.13: Schematic diagram of film boiling geometry.

TABLE 6.4: 2D film boiling physical parameters

	ρ kg/m^3	c_p $J/(kg \cdot K)$	T K	μ $Pa \cdot s$	λ $W/(m \cdot K)$
liquid	200	400	373.15	0.1	40
vapor	5	200	linear	5×10^{-3}	1

Cette thèse est accessible à l'adresse : http://theses.insa-lyon.fr/publication/2020LYSEI095/these.pdf
© [L. Guo], [2020], INSA Lyon, tous droits réservés

Fig. 6.14 depicts the vapor volume relative to the initial vapor volume over time. It shows a good agreement of our simulation with the results of Zhang and Ni (2018). Moreover, the vapor shapes at different time instants are presented in Fig. 6.15, respectively at $t = 0\ s$, $t = 0.3\ s$, $t = 0.5\ s$, $t = 0.7\ s$ and $t = 0.9\ s$. It is observed the vapor bubble is generated due to vaporization at the interface, while the detachment of the vapor bubble is not seen from the thin vapor film. This phenomenon is also observed that by many studies (Takahashi et al., 1994; Gibou et al., 2007; Akhtar and Kleis, 2013; Zhang and Ni, 2018). Gibou et al. (2007) thinks this to be qualitatively correct for a two-dimensional simulation because "the curvature for the stem is close to zero and therefore the effects of surface tension are negligible". The fragile surface tension near to the neck cannot make the bubble breakup from the thin film. In addition, this phenomenon is also reported by other authors (Hardt and Wondra, 2008; Welch and Wilson, 2000; Samkhaniani and Ansari, 2017). According to Samkhaniani and Ansari (2017), the components of the interface force are only in the computational plane, whereas neglecting the out-of-plane components. In addition, Gibou et al. (2007) observed the vapor bubble detachment from vapor film in 3D cases.

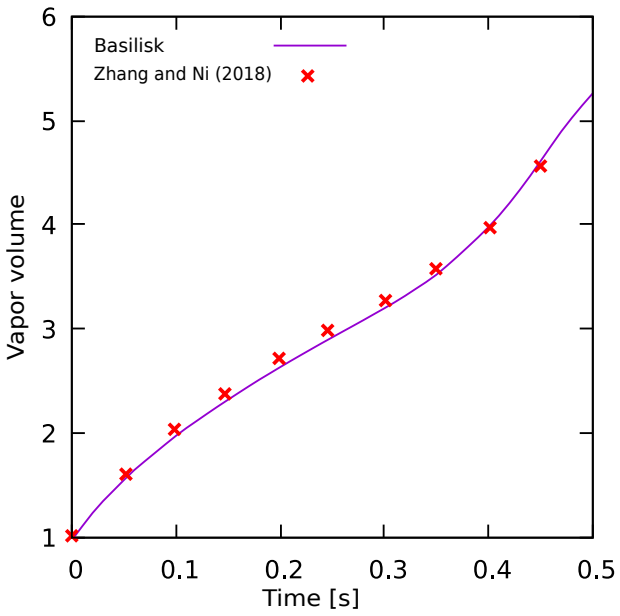

FIGURE 6.14: The ratio of void fraction evolution with time is compared with Zhang and Ni (2018).

Cette thèse est accessible à l'adresse : http://theses.insa-lyon.fr/publication/2020LYSEI095/these.pdf
© [L. Guo], [2020], INSA Lyon, tous droits réservés

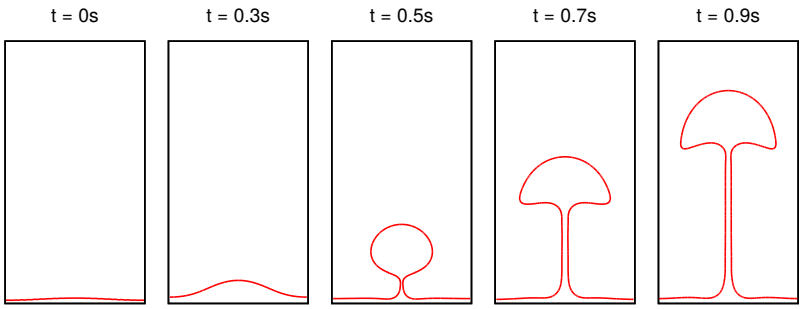

FIGURE 6.15: The film boiling interface evolution with time.

Regarding the heat transfer characteristic in film boiling, Klimenko (1981) proposed a semi-empirical model to obtain the Nusselt number correlation at the bottom wall:

$$Nu = \begin{cases} 0.19 Gr^{1/3} Pr^{1/3} s_1 & \text{for } Gr \leq 4.03 \times 10^5 \\ 0.0216 Gr^{1/2} Pr^{1/3} s_2 & \text{for } Gr > 4.03 \times 10^5 \end{cases} \tag{6.53}$$

where

$$s_1 = \begin{cases} 1 & \text{for } \beta \geq 0.71 \\ 0.089 \beta^{-1/3} & \text{for } \beta < 0.71 \end{cases} \tag{6.54}$$

$$s_2 = \begin{cases} 1 & \text{for } \beta \geq 0.5 \\ 0.089 \beta^{-1/2} & \text{for } \beta < 0.5 \end{cases} \tag{6.55}$$

Klimenko's correlation is believed to agree with most experimental data within an accuracy of $\pm 25\%$ Klimenko (1981). In Eqs (6.56, 6.57, 6.58), the parameters Gr, Pr and β are expressed as,

$$Gr = \frac{\rho_g^2 g \lambda'^3}{\mu_g^2} \left(\frac{\rho_l}{\rho_g} - 1 \right) \tag{6.56}$$

$$Pr = \frac{C_{p,g} \mu_g}{\lambda_g} \tag{6.57}$$

$$\beta = \frac{C_{p,g} (T_{wall} - T_{sat})}{h_{lg}} \tag{6.58}$$

where λ' is the characteristic length.

$$\lambda' = \sqrt{\frac{\sigma}{(\rho_l - \rho_g) g}} \tag{6.59}$$

In our cases, $Gr = 145$ and $\beta = 0.1$, the Klimenko correlation equals to 1.914. In the present study, the Nusselt number is defined by the dimensionless heat flux through the bottom wall

$$Nu = \int_0^{\lambda_0/2} \left(\frac{\lambda'}{T_{wall} - T_{sat}} \frac{\partial T}{\partial y} \bigg|_{y=0} \right) dx / \frac{\lambda_0}{2} \tag{6.60}$$

Cette thèse est accessible à l'adresse : http://theses.insa-lyon.fr/publication/2020LYSEI095/these.pdf
© [L. Guo], [2020], INSA Lyon, tous droits réservés

where $\frac{\partial T}{\partial y}\Big|_{y=0}$ is the temperature gradient at the bottom wall.

Fig. 6.16 shows the comparison of simulation Nusselt number (see Eq. (6.60)) with the Klimenko analytical solution (see Eq. (6.53)). The result shows good agreement with each other. As explained above, we do not observe the Nusselt number changing periodically with time but converge to the correlation solution.

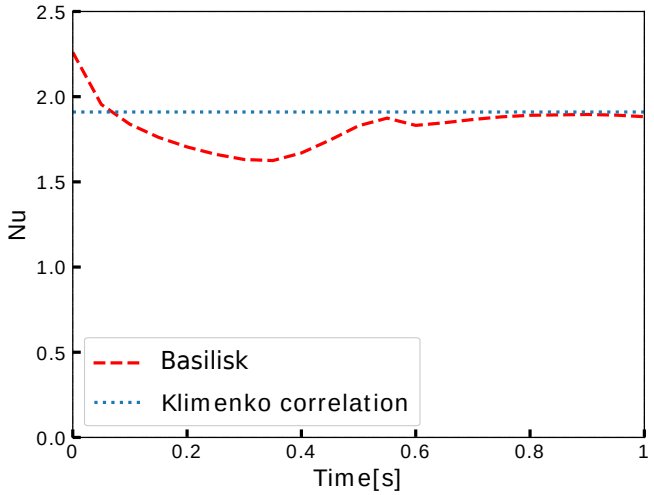

FIGURE 6.16: Comparison of Nusselt number with Klimenko correlation.

6.4 Chapter conclusion

In this chapter, we developed a phase change model in the Basilisk solver. A two-step VOF advection method was proposed to account for phase change. In the first step, a divergence-free liquid velocity is constructed from the one-fluid velocity and a Stefan flow velocity. In the second step, the mass source term was added into the VOF equation to shift the interface due to phase change.

The mass flux was not calculated directly in the interfacial cells but in the neighboring cells that contain pure unsaturated fluid. The weighted average method was used to consider two neighboring cells around the interface. The boundary condition at the interface is imposed saturated temperature using a ghost cell method.

The phase change model was tested by several benchmark test cases. First, a two-dimensional droplet evaporation with constant mass flux was used to purely test the two-step geometric VOF method. The magnitude of the velocity jump was investigated through different density ratios, and the results matched well with the analytical solution. Then one-dimensional Stefan and Sucking interface problems were solved. The Stefan problem showed excellent accuracy, while the Sucking interface problems have a strong dependency on grid sizes. Subsequently, the planar film boiling case was studied. It was observed that the predicted space-averaged Nusselt number is in good agreement with the Klimenko correlation. A "vapor stem"

Cette thèse est accessible à l'adresse : http://theses.insa-lyon.fr/publication/2020LYSEI095/these.pdf
© [L. Guo], [2020], INSA Lyon, tous droits réservés

phenomenon was observed in planar simulation, which prevented the vapor bubble pinch-off from vapor film.

Cette thèse est accessible à l'adresse : http://theses.insa-lyon.fr/publication/2020LYSEI095/these.pdf
© [L. Guo], [2020], INSA Lyon, tous droits réservés

Cette thèse est accessible à l'adresse : http://theses.insa-lyon.fr/publication/2020LYSEI095/these.pdf
© [L. Guo], [2020], INSA Lyon, tous droits réservés

Chapter 7

Conclusions and perspectives

The objective of this thesis included two main parts. The first one is to numerically study the Taylor bubble rising through singularities and compare previous experiments with simulations. The second part is to develop a phase change model in the Basilisk solver and validate the accuracy of the phase change model.

In the first part, we studied the Taylor bubble rising in straight pipes by comparing numerical and experimental results to validate the accuracy of the Basilisk solver. Individual Taylor bubbles rising through expansions and contractions were investigated. In Chapter 4, the Taylor bubble rising in different glycerol-water solutions were studied when passing through a fixed expansion ratio. Afterwards, Taylor bubble rising through different expansion ratios were studied in the same glycerol-water solution. In addition, the break-up pattern and blocking pattern has been observed for expansion and contractions, respectively. In Chapter 5, several types of expansions/contractions are studied in particular the Taylor bubble rising through gradual, parabolic convex and parabolic concave singularities.

In the second part, a phase change model was developed in the Basilisk solver in Chapter 6. The accuracy of the phase change model was validated by several benchmark test cases.

7.1 Conclusions

The conclusions are composed of the Taylor bubble parts and the phase change parts.

Taylor bubble

As we mentioned in Chapter 4 and Chapter 5, the numerical simulation of the Taylor bubble rising through singularities include expansions and contractions. For each type of singularity, the Taylor bubble presents unique characteristics. The conclusions in this part are summarized according to expansions and contractions.

- The bubble velocity increases in the sudden expansion. After the expansion, the bubble tail oscillates until the steady state. The wall shear stress and the pressure drop have sharp increases at the expansion. For a larger expansion ratio,

Cette thèse est accessible à l'adresse : http://theses.insa-lyon.fr/publication/2020LYSEI095/these.pdf
© [L. Guo], [2020], INSA Lyon, tous droits réservés

the bubble moves faster with intensive deformation. The bubble shows a more circular bubble nose after the expansion. Besides, The bubble breakup pattern is observed at expansions in both experiments and simulations. The bubble breakup pattern depends on the bubble volume and the sudden expansion ratio. The bubble is split into two parts at the expansion when its initial length increases beyond a critical value. On the contrary, the bubble velocity decreases in the sudden contraction. When the contraction ratio increases over a critical value, the bubble is blocked and cannot pass through the contraction.

- Compared with bubble motion in the sudden expansion, the gradual expansion mitigates the bubble motion. It is more apparent for smaller gradual angles. The liquid particle analysis shows the liquid ahead of bubble nose presenting recirculation motion at the bubble tail. The transient time shows the bubble spends more time passing through the gradual expansion with smaller gradual angles. For the gradual contraction, the bubble velocity is decreased at the contraction. The bubble motion also shows a blocking phenomenon for larger gradual angles.

- The parabolic convex expansion accelerates the bubble motion and the bubble deformation at 90° expansion angle is stronger than sudden expansions. The bubble shows longer liquid column length compared with sudden expansions. A smaller angle leads to a smoother transition of the bubble through the contraction. The bubble is blocked at a larger angle for parabolic convex contractions.

- For parabolic concave expansions, the Taylor bubble moves slower than convex and sudden expansions. The liquid column inside the bubble is the shortest. For parabolic concave contractions, the bubble is easier to pass through the singularity, even for a larger concave angle.

phase change

A two-step VOF advection method was implemented to account for phase change. The mass flux was not calculated directly in the interfacial cells but in the neighboring cells that contain pure unsaturated fluid. The weighted average method was used to consider two neighboring cells around the interface. The boundary condition at the interface is imposed with saturated temperature using a ghost cell method. In summary, the present phase change model could be used to study two-phase flow with evaporation or condensation. The constraint of this model is one fluid is saturated and the other one is unsaturated, but a better accuracy of calculation of mass flux could be developed based on the existed two-step geometric VOF method.

Cette thèse est accessible à l'adresse : http://theses.insa-lyon.fr/publication/2020LYSEI095/these.pdf
© [L. Guo], [2020], INSA Lyon, tous droits réservés

7.2 Perspectives

Based on the current work, there are some aspects that need to be further investigated.

Taylor bubble

- To compare the simulations and experiments in a wide range of analysis, more experiments on the Taylor bubble rising through sudden expansions/contractions could be performed. This work includes using different liquid solutions (not only limit to glycerol-water) and changing the expansion/contraction ratios into more values.
- A better experimental method to measure the initial Taylor bubble volume should be developed. This is important to compare the experiments and simulations results.
- More experiments need to be carried out based on the present simulation results of various types of expansions/contractions. Moreover, three-dimensional test cases can be carried out to study the region of expansions/contractions.
- The Taylor bubble rising in non-Newtonian liquid could be investigated based on the work of Amani et al. (2019). It is necessary to do experiments to compare the Taylor bubble in non-Newtonian liquid through expansions/contractions.
- A pair of Taylor bubble through expansions/contractions can be investigated based on the work of Araújo et al. (2013a).

Phase change

- An accurate method to calculate mass flux could be implemented based on the present two-step geometric VOF method, such as the embedded boundary method.
- Based on the present phase change model or more accurate phase change model, several specific phase change problems, such as bubble condensation, the film boiling could be further investigated. In addition, three-dimensional cases could be considered to model more complex problems. It is straightforward to extend two-dimensional cases to three-dimensional cases.
- Further investigation on nucleate boiling could be considered based on the work of Guion (2017). They performed some related work in the Gerris solver (Popinet, 2013b).

Cette thèse est accessible à l'adresse : http://theses.insa-lyon.fr/publication/2020LYSEI095/these.pdf
© [L. Guo], [2020], INSA Lyon, tous droits réservés

Cette thèse est accessible à l'adresse : http://theses.insa-lyon.fr/publication/2020LYSEI095/these.pdf
© [L. Guo], [2020], INSA Lyon, tous droits réservés

Appendix A

VOF: distance and volume fraction calculation

A.1 Forward problem

The Basilisk solver adopts the PLIC method to represent interface in each computational cell, as mentioned in Chapter 3, The interface line can be defined by the Hesse normal form:

$$\mathbf{m} \cdot \mathbf{x} = \alpha \tag{A.1}$$

In a two-dimension domain, the "forward" problem can be demonstrated as follows. Given a rectangular (or square) grid in Cartesian coordinate with Δx and Δy, as depicted in Fig. A.1. The grid is divided into two parts by a straight line (EH), which forms the interface segment (GF) with normal vector $\mathbf{m}$ in the grid cell. The "forward" problem's objective is to determine the area of the region below the interface segment, which corresponds to the area ABFGD. The direction of interface normal vector $\mathbf{m}$ is defined by convention as the opposite direction of inside of ABFGD. The expression for the area of ABFGD depends on the positive normal direction which is below GF within ABCD is given by:

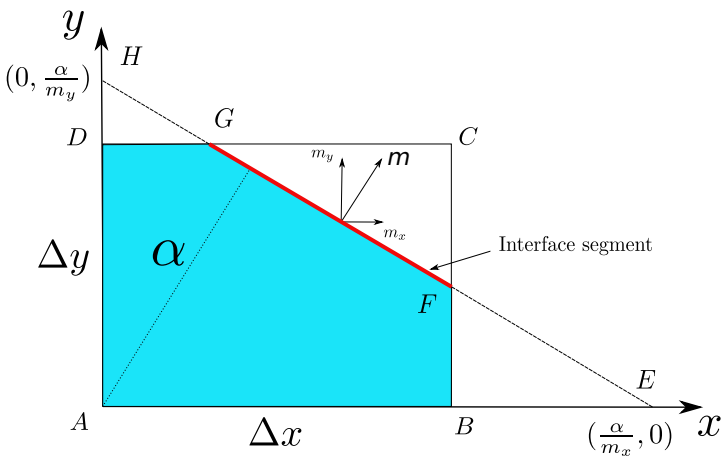

FIGURE A.1: The schematic diagram of the computational domain.

Cette thèse est accessible à l'adresse : http://theses.insa-lyon.fr/publication/2020LYSEI095/these.pdf
© [L. Guo], [2020], INSA Lyon, tous droits réservés

$$A = \frac{\alpha^2}{2m_x m_y}\left[1 - H(\alpha - m_x\Delta x)\left(\frac{\alpha - m_x\Delta x}{\alpha}\right)^2 - H(\alpha - m_y\Delta y)\left(\frac{\alpha - m_y\Delta y}{\alpha}\right)^2\right] \tag{A.2}$$

where $H(\cdot)$ is the Heaviside step function which is defined such that

$$H(x) = \begin{cases} 0 & \text{for } x < 0 \\ 1 & \text{for } x > 0 \end{cases} \tag{A.3}$$

The line EH intersects with the coordinates at $(\frac{\alpha}{m_x}, 0)$ and $(0, \frac{\alpha}{m_y})$, respectively. For the sake of simplification, we assume the direction of normal is positive, as shown in Fig. A.2, all possible cases are displayed for $m_x \geq 0$ and $m_y \geq 0$. The "forward" problem for $m_x > m_y > 0$ is in details for making brief, which can be divided into three types showing in Fig. A.3. For the other cases in Fig. A.2, we use the similar method to calculate the volume fraction.

Cette thèse est accessible à l'adresse : http://theses.insa-lyon.fr/publication/2020LYSEI095/these.pdf
© [L. Guo], [2020], INSA Lyon, tous droits réservés

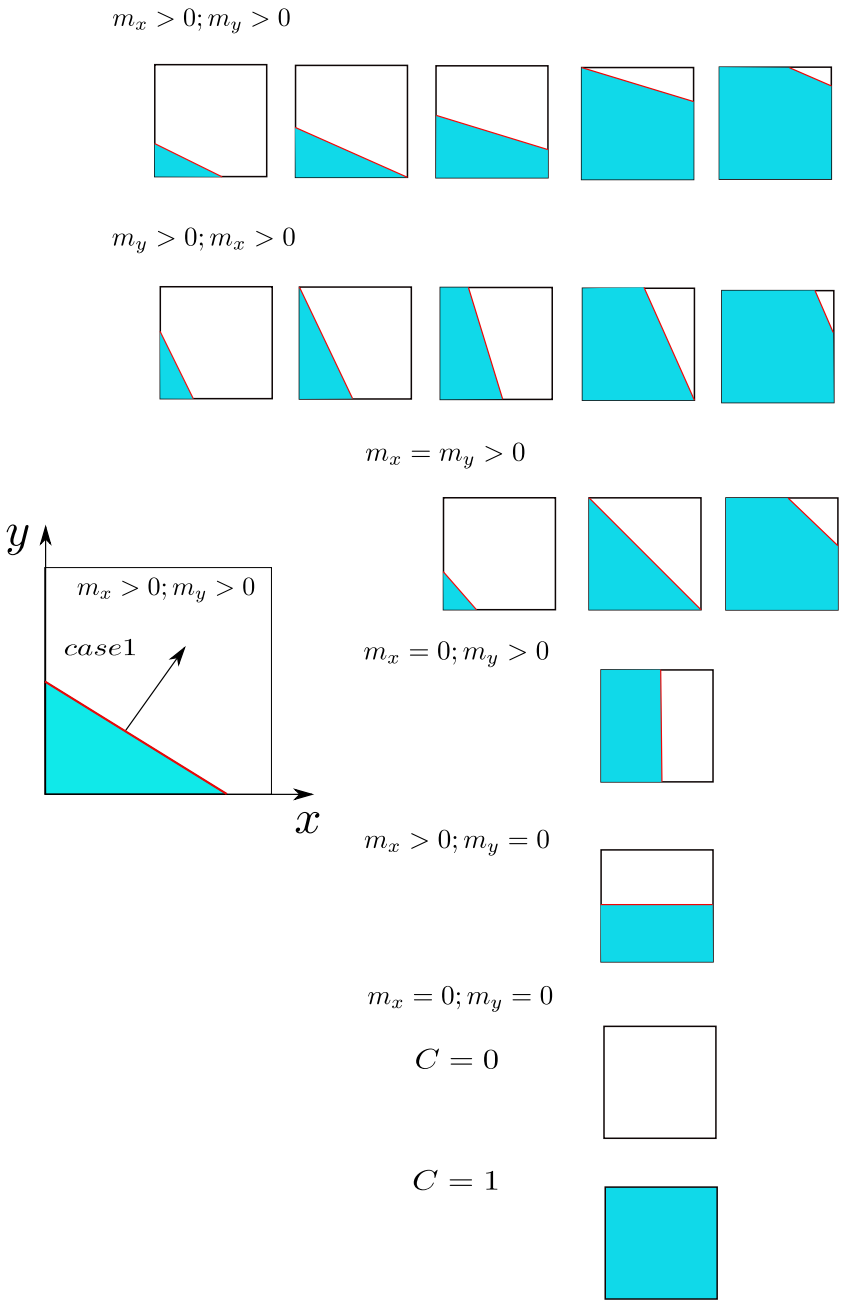

FIGURE A.2: Possible cases with positive normal values for the linear interface in 2D Cartesian grid.

If the points E and H lie within AB and AD (including B and D points, see Fig. A.3 (a)), $\frac{\alpha^2}{2m_x m_y}$ on the right-hand side of the Eq. (A.2) is the desired area. While if point E is to the right of point B, i.e., $\alpha > m_x \Delta x$ (see Fig. A.3 (b)), the proper area for calculating volume fraction is to subtract triangle BEF from the desired area. The triangle area BEF is geometrically similar to triangle AEH, the ratio of these two areas can be expressed by the square of the ratio of the side BE to AE, which is given as follows:

$$\frac{A_{BEF}}{A_{AEH}} = \left(\frac{\alpha/m_x - \Delta x}{\alpha/m_x}\right)^2 = \left(\frac{\alpha - m_x \Delta x}{\alpha}\right)^2 \tag{A.4}$$

Cette thèse est accessible à l'adresse : http://theses.insa-lyon.fr/publication/2020LYSEI095/these.pdf
© [L. Guo], [2020], INSA Lyon, tous droits réservés

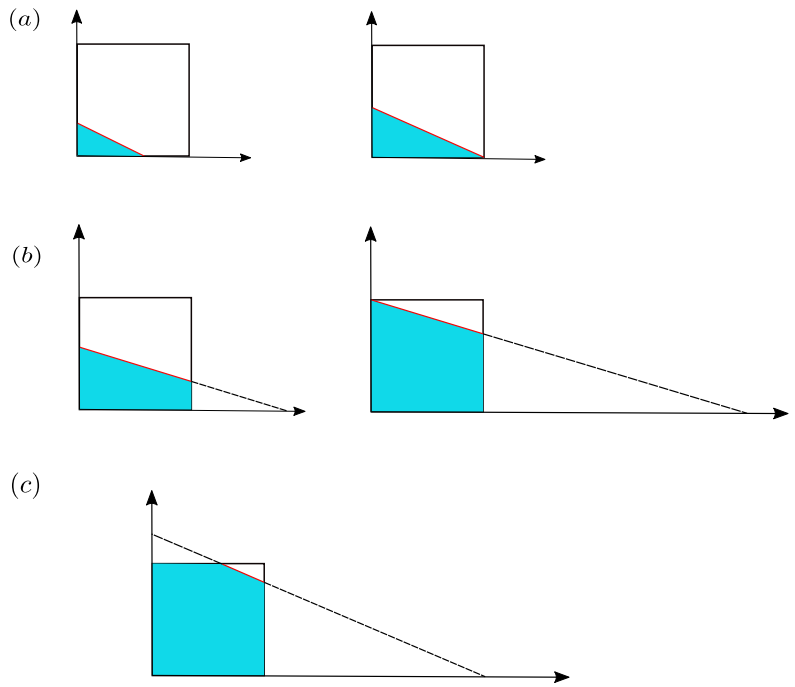

FIGURE A.3: Possible cases with $m_x > m_y > 0$ for the calculation of volume fraction.

Eq. (A.4) corresponds to the second term on the right-hand side of the Eq. (A.2). Similarly, as point H coincides with the point D, this is the third term on the right-hand side of the Eq. (A.2). The expected proper area ABFGD is calculated by subtracting the triangle BEF and triangle DGH.

The expected area below the interface fragment is a function of α with the continuous, monotonically increasing properties. It ranges from zero to $\Delta x \Delta y$. According to this, there exist two critical values of α, corresponding to the Heaviside step functions. The geometries are as shown in Fig. A.2, when $\alpha = 0$ with $C = 0$ and $\alpha = m_x \Delta x + m_y \Delta y$ with $C = 1$. After obtaining the expected area, the volume fraction C in each computational cell can be described by the relations below:

$$C = \frac{\int_{A_i} A(\mathbf{x}, t) d\mathbf{x}}{A_i} \tag{A.5}$$

where i indicates random computational cell, $A(\mathbf{x}, t)$ is the desired area and A is the computational cell area. The procedure of determining the volume fraction C in 2D Cartesian grid systems is detailed in Algorithm. 1.

A.2 Inverse problem

When considering the "inverse" problem, α is a function of given C and $\mathbf{m}$ in each computational cell. The volume fraction is monotonically increasing when m_x and m_y are both positive in one cell (Gueyffier et al., 1999; Scardovelli and Zaleski, 2000). In a 2D Cartesian grid, the interface's position can be compiled into four cases, as

Cette thèse est accessible à l'adresse : http://theses.insa-lyon.fr/publication/2020LYSEI095/these.pdf
© [L. Guo], [2020], INSA Lyon, tous droits réservés

Algorithm 1: Volume fraction computation with known α and $\boldsymbol{m}$ in 2D Cartesian grid system

Input: $\boldsymbol{m} = (m_x, m_y)$, α
Output: C
if $(\alpha \leq 0)$ **then**
  return 0
end
if $(\alpha \geq (m_x + m_y))$ **then**
  return 1
end
if $(m_x < 0)$ **then**
  $C \leftarrow \frac{\alpha}{m_y}$
end
else if $(m_y < 0)$ **then**
  $C \leftarrow \frac{\alpha}{m_x}$
end
else
  $v^* = \alpha^2$
  $a = \alpha - m_x$
  if $(a > 0)$ **then**
    $v = v^* - a^2$
    $a = \alpha - m_y$
  end
  $C = \frac{v}{2m_x m_y}$
end
$C \leftarrow \max(0, \min(C, 1))$
return C

Cette thèse est accessible à l'adresse : http://theses.insa-lyon.fr/publication/2020LYSEI095/these.pdf
© [L. Guo], [2020], INSA Lyon, tous droits réservés

shown in Fig. A.4. The interface satisfies the Hessian Form (Eq. (A.3)) and is mapped onto case-1 condition (Wu and Young, 2013). To illustrate the mapping method in detail, one can see four cases in Fig. A.5. By the simple transformation, we can get four linear equations of the interface, i.e., the distance in case-2 is transformed into $\alpha - m_x \Delta x$. The algorithm's pseudo-code to determine the distance of α in 2D Cartesian grid systems is demonstrated in the Algorithm. 2.

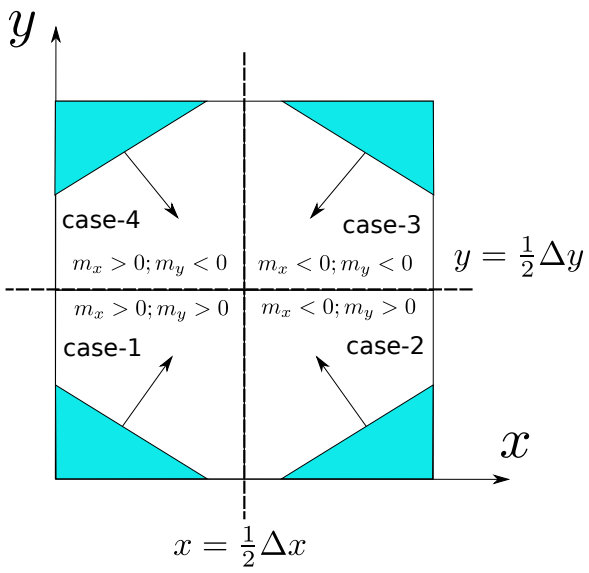

FIGURE A.4: The schematic diagram of the computational domain.

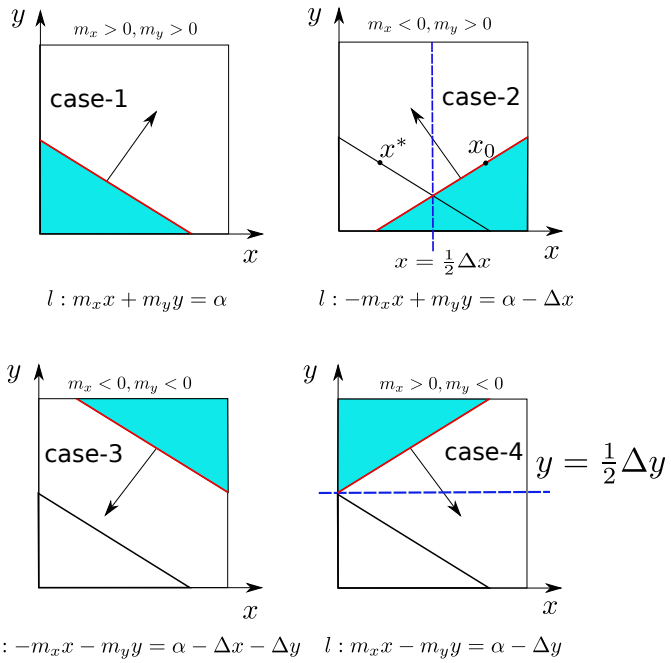

FIGURE A.5: Four different cases correspond to map onto the same case (case-1), l: the interface line equation in the computational cell.

The case-1 in Fig. A.5 is the benchmark case for other circumstances. In order to investigate the details of distance computation and reduce the situations of the

Cette thèse est accessible à l'adresse : http://theses.insa-lyon.fr/publication/2020LYSEI095/these.pdf
© [L. Guo], [2020], INSA Lyon, tous droits réservés

possible cases, we explain the mapping procedure of the case of $(m_x < 0, m_y > 0)$ onto case-1. The linear equation of the interface can be reflected to case-1 by the line function $x = \frac{1}{2}\Delta x$. With the simple linear transformation, The symmetry relation between point on present interface (x^*) and the original interface (x_0) can be expressed as $x^* = \Delta x - x_0$, then substitute the formula into the Eq. (A.1). The linear equation for the case-2 can be described as $m_x\Delta x - m_x x + m_y y = \alpha$, and the distance can be written after rearranging the interface equation $\alpha^* = \alpha - m_x\Delta x$. Similarly, the interface linear equations of case-3 and case-4 can be determined by the same approach. α^* in case-3 and case-4 are computed by $\alpha^* = \alpha - m_y\Delta y$ and $\alpha^* = \alpha - m_x\Delta x - m_y\Delta y$, respectively.

Algorithm 2: Distance computation with known C and $\boldsymbol{m}$ in 2D Cartesian grid system

Input: $\boldsymbol{m} = (m_x, m_y)$, $C \leftarrow \max(0, \min(C, 1))$
Output: α Cell center to the interface
if $(|m_x| < 10^{-10}$ || $|m_y| < 10^{-10})$ **then**
  $\alpha^* \leftarrow C$
  else if $(|m_x| > |m_y|)$ **then**
    swap$(|m_x|, |m_y|)$;
    if $(C \leq \frac{|m_x|}{2|m_y|})$ **then**
      $\alpha^* \leftarrow \sqrt{2|m_x||m_y|C}$
      else if $(C \leq (1 - \frac{|m_x|}{2|m_y|}))$ **then**
        $\alpha^* \leftarrow C|m_y| + \frac{|m_x|}{2}$
        else
          $\alpha^* \leftarrow |m_x| + |m_y| - \sqrt{2|m_x||m_y|(1-C)}$
        end
      end
    end
  end
  else if $(m_x < 0)$ **then**
    $\alpha = \alpha^* + m_x$
    else if $(m_y < 0)$ **then**
      $\alpha = \alpha^* + m_y$
    end
  end
end
return α

Cette thèse est accessible à l'adresse : http://theses.insa-lyon.fr/publication/2020LYSEI095/these.pdf
© [L. Guo], [2020], INSA Lyon, tous droits réservés

Cette thèse est accessible à l'adresse : http://theses.insa-lyon.fr/publication/2020LYSEI095/these.pdf
© [L. Guo], [2020], INSA Lyon, tous droits réservés

Bibliography

Abdelall, F., Hahn, G., Ghiaasiaan, S., Abdel-Khalik, S., Jeter, S., Yoda, M., and Sadowski, D. (2005). Pressure drop caused by abrupt flow area changes in small channels. *Experimental Thermal and Fluid Science*, 29(4):425–434.

Ahmed, W. H., Ching, C. Y., and Shoukri, M. (2008). Development of two-phase flow downstream of a horizontal sudden expansion. *International Journal of Heat and Fluid Flow*, 29(1):194–206.

Akhtar, M. W. and Kleis, S. J. (2013). Boiling flow simulations on adaptive octree grids. *International journal of multiphase flow*, 53:88–99.

Alizadehdakhel, A., Rahimi, M., and Alsairafi, A. A. (2010). Cfd modeling of flow and heat transfer in a thermosyphon. *International Communications in Heat and Mass Transfer*, 37(3):312–318.

Amani, E., Ahmadpour, A., and Tohidi, M. (2019). A numerical study of the rise of a taylor bubble through a sudden/gradual expansion in newtonian and shear-thinning liquids. *International Journal of Mechanical Sciences*, 152:236–246.

Ambrose, S., Lowndes, I. S., Hargreaves, D. M., and Azzopardi, B. (2017). Numerical modelling of the rise of taylor bubbles through a change in pipe diameter. *Computers & Fluids*, 148:10–25.

Aniszewski, W., Arrufat, T., Crialesi-Esposito, M., Dabiri, S., Fuster, D., Ling, Y., Lu, J., Malan, L., Pal, S., Scardovelli, R., et al. (2019). Parallel, robust, interface simulator (paris).

Ansari, M. R., Azadi, R., and Salimi, E. (2016). Capturing of interface topological changes in two-phase gas–liquid flows using a coupled volume-of-fluid and level-set method (voset). *Computers & Fluids*, 125:82–100.

Aoyama, S., Hayashi, K., Hosokawa, S., and Tomiyama, A. (2016). Shapes of ellipsoidal bubbles in infinite stagnant liquids. *International Journal of Multiphase Flow*, 79:23–30.

Araújo, J., Miranda, J., and Campos, J. (2013a). Flow of two consecutive taylor bubbles through a vertical column of stagnant liquid—a cfd study about the influence of the leading bubble on the hydrodynamics of the trailing one. *Chemical Engineering Science*, 97:16–33.

Cette thèse est accessible à l'adresse : http://theses.insa-lyon.fr/publication/2020LYSEI095/these.pdf
© [L. Guo], [2020], INSA Lyon, tous droits réservés

Araújo, J., Miranda, J., and Campos, J. (2013b). Simulation of slug flow systems under laminar regime: Hydrodynamics with individual and a pair of consecutive taylor bubbles. *Journal of Petroleum science and engineering*, 111:1–14.

Araújo, J., Miranda, J., and Campos, J. (2015). Cfd study of the hydrodynamics of slug flow systems: interaction between consecutive taylor bubbles. *International Journal of Chemical Reactor Engineering*, 13(4):541–549.

Araújo, J., Miranda, J., Pinto, A., and Campos, J. (2012). Wide-ranging survey on the laminar flow of individual taylor bubbles rising through stagnant newtonian liquids. *International Journal of Multiphase Flow*, 43:131–148.

Aulisa, E., Manservisi, S., Scardovelli, R., and Zaleski, S. (2007). Interface reconstruction with least-squares fit and split advection in three-dimensional cartesian geometry. *Journal of Computational Physics*, 225(2):2301–2319.

Balakhrisna, T., Ghosh, S., Das, G., and Das, P. (2010). Oil–water flows through sudden contraction and expansion in a horizontal pipe–phase distribution and pressure drop. *International Journal of Multiphase Flow*, 36(1):13–24.

Barnea, D. (1987). A unified model for predicting flow-pattern transitions for the whole range of pipe inclinations. *International Journal of Multiphase Flow*, 13(1):1–12.

Bell, J. B., Colella, P., and Glaz, H. M. (1989). A second-order projection method for the incompressible navier-stokes equations. *Journal of Computational Physics*, 85(2):257–283.

Bendiksen, K. H. (1984). An experimental investigation of the motion of long bubbles in inclined tubes. *International journal of multiphase flow*, 10(4):467–483.

Berenson, P. J. (1961). Film-boiling heat transfer from a horizontal surface.

Bhaga, D. and Weber, M. (1981). Bubbles in viscous liquids: shapes, wakes and velocities. *Journal of fluid Mechanics*, 105:61–85.

Bhusan, S., Ghosh, S., Das, G., and Das, P. (2009). Rise of taylor bubbles through narrow rectangular channels. *Chemical Engineering Journal*, 155(1-2):326–332.

Bouche, E., Vergniolle, S., Staudacher, T., Nercessian, A., Delmont, J.-C., Frogneux, M., Cartault, F., and Le Pichon, A. (2010). The role of large bubbles detected from acoustic measurements on the dynamics of erta'ale lava lake (ethiopia). *Earth and Planetary Science Letters*, 295(1-2):37–48.

Brackbill, J. U., Kothe, D. B., and Zemach, C. (1992). A continuum method for modeling surface tension. *Journal of computational physics*, 100(2):335–354.

Cette thèse est accessible à l'adresse : http://theses.insa-lyon.fr/publication/2020LYSEI095/these.pdf
© [L. Guo], [2020], INSA Lyon, tous droits réservés

Brown, R. (1965). The mechanics of large gas bubbles in tubes: I. bubble velocities in stagnant liquids. *The Canadian Journal of Chemical Engineering*, 43(5):217–223.

Bugg, J., Mack, K., and Rezkallah, K. (1998). A numerical model of taylor bubbles rising through stagnant liquids in vertical tubes. *International Journal of Multiphase Flow*, 24(2):271–281.

Bugg, J. and Saad, G. (2002). The velocity field around a taylor bubble rising in a stagnant viscous fluid: numerical and experimental results. *International Journal of Multiphase Flow*, 28(5):791–803.

Bunner, B. and Tryggvason, G. (1999). Direct numerical simulations of three-dimensional bubbly flows. *Physics of Fluids*, 11(8):1967–1969.

Campos, J. and De Carvalho, J. G. (1988). An experimental study of the wake of gas slugs rising in liquids. *Journal of Fluid Mechanics*, 196:27–37.

Carter, W., Azzopardi, B., and Agunlejika, E. (2016). Taylor bubble destruction at sudden expansions. In *9th International Conference on Multiphase Flow*.

Chen, E., Li, Y., and Cheng, X. (2009a). Cfd simulation of upward subcooled boiling flow of refrigerant-113 using the two-fluid model. *Applied Thermal Engineering*, 29(11-12):2508–2517.

Chen, G., Nie, T., and Yan, X. (2020). An explicit expression of the empirical factor in a widely used phase change model. *International Journal of Heat and Mass Transfer*, 150:119279.

Chen, S., Yang, Z., Duan, Y., Chen, Y., and Wu, D. (2014). Simulation of condensation flow in a rectangular microchannel. *Chemical Engineering and Processing: Process Intensification*, 76:60–69.

Chen, Y., Tseng, C.-Y., Lin, Y.-T., and Wang, C.-C. (2009b). Two-phase flow pressure change subject to sudden contraction in small rectangular channels. *International Journal of Multiphase Flow*, 35(3):297–306.

Chorin, A. J. (1968). Numerical solution of the navier-stokes equations. *Mathematics of computation*, 22(104):745–762.

Chorin, A. J. (1969). On the convergence of discrete approximations to the navier-stokes equations. *Mathematics of computation*, 23(106):341–353.

Clarke, A. and Issa, R. (1997). A numerical model of slug flow in vertical tubes. *Computers & fluids*, 26(4):395–415.

Clift, R., Grace, J., and Weber, M. (1978). Bubbles, drops, and particles.

Cette thèse est accessible à l'adresse : http://theses.insa-lyon.fr/publication/2020LYSEI095/these.pdf
© [L. Guo], [2020], INSA Lyon, tous droits réservés

Colella, P. (1990). A multidimensional second order godunov scheme for conservation laws. *J. Comput. Phys*, 87:171–200.

Da Riva, E., Del Col, D., Garimella, S. V., and Cavallini, A. (2012). The importance of turbulence during condensation in a horizontal circular minichannel. *International Journal of Heat and Mass Transfer*, 55(13-14):3470–3481.

Danabalan, D. (2012). New insights into bubble-driven convection in lava lakes. *University of Bristol Master Thesis*.

Davies, R. and Taylor, G. I. (1950). The mechanics of large bubbles rising through extended liquids and through liquids in tubes. *Proceedings of the Royal Society of London. Series A. Mathematical and Physical Sciences*, 200(1062):375–390.

De Schepper, S. C., Heynderickx, G. J., and Marin, G. B. (2009). Modeling the evaporation of a hydrocarbon feedstock in the convection section of a steam cracker. *Computers & Chemical Engineering*, 33(1):122–132.

Dong, L., Gong, S., and Cheng, P. (2018). Direct numerical simulations of film boiling heat transfer by a phase-change lattice boltzmann method. *International Communications in Heat and Mass Transfer*, 91:109–116.

Dukler, A. (1952). Characteristics of flow in falling liquid film. In *Proc. of Chem. Eng. Progress Symp. Series, 1952*, volume 48, pages 557–563.

Dumitrescu, D. T. (1943). Strömung an einer luftblase im senkrechten rohr. *ZAMM-Journal of Applied Mathematics and Mechanics/Zeitschrift für Angewandte Mathematik und Mechanik*, 23(3):139–149.

Esmaeeli, A. and Tryggvason, G. (2004a). Computations of film boiling. part i: numerical method. *International journal of heat and mass transfer*, 47(25):5451–5461.

Esmaeeli, A. and Tryggvason, G. (2004b). Computations of film boiling. part ii: multimode film boiling. *International journal of heat and mass transfer*, 47(25):5463–5476.

Fleckenstein, S. and Bothe, D. (2015). A volume-of-fluid-based numerical method for multi-component mass transfer with local volume changes. *Journal of Computational Physics*, 301:35–58.

Fulford, G. D. (1964). The flow of liquids in thin films. In *Advances in Chemical Engineering*, volume 5, pages 151–236. Elsevier.

Fuster, D., Arrufat, T., Crialesi-Esposito, M., Ling, Y., Malan, L., Pal, S., Scardovelli, R., Tryggvason, G., and Zaleski, S. (2018). A momentum-conserving, consistent, volume-of-fluid method for incompressible flow on staggered grids. *arXiv preprint arXiv:1811.12327*.

Cette thèse est accessible à l'adresse : http://theses.insa-lyon.fr/publication/2020LYSEI095/these.pdf
© [L. Guo], [2020], INSA Lyon, tous droits réservés

Ganapathy, H., Shooshtari, A., Choo, K., Dessiatoun, S., Alshehhi, M., and Ohadi, M. (2013). Volume of fluid-based numerical modeling of condensation heat transfer and fluid flow characteristics in microchannels. *International Journal of Heat and Mass Transfer*, 65:62–72.

Georgoulas, A., Andredaki, M., and Marengo, M. (2017). An enhanced vof method coupled with heat transfer and phase change to characterise bubble detachment in saturated pool boiling. *Energies*, 10(3):272.

Ghajar, A. J. (2005). Non-boiling heat transfer in gas-liquid flow in pipes: a tutorial. *Journal of the Brazilian Society of Mechanical Sciences and Engineering*, 27(1):46–73.

Gibou, F., Chen, L., Nguyen, D., and Banerjee, S. (2007). A level set based sharp interface method for the multiphase incompressible navier–stokes equations with phase change. *Journal of Computational Physics*, 222(2):536–555.

Goldsmith, H. and Mason, S. (1962). The movement of single large bubbles in closed vertical tubes. *Journal of Fluid Mechanics*, 14(1):42–58.

Goodson, K., Rogacs, A., David, M., and Fang, C. (2010). Volume of fluid simulation of boiling two-phase flow in a vapor-venting microchannel. *Frontiers in Heat and Mass Transfer (FHMT)*, 1(1).

Gorlé, C., Lee, H., Houshmand, F., Asheghi, M., Goodson, K., and Parida, P. R. (2015). Validation study for vof simulations of boiling in a microchannel. In *International Electronic Packaging Technical Conference and Exhibition*, volume 56901, page V003T10A022. American Society of Mechanical Engineers.

GUEDON, G. R. (2013). Two-phase heat and mass transfer modeling: flexible numerical methods for energy engineering analyses.

Gueyffier, D., Li, J., Nadim, A., Scardovelli, R., and Zaleski, S. (1999). Volume-of-fluid interface tracking with smoothed surface stress methods for three-dimensional flows. *Journal of Computational physics*, 152(2):423–456.

Guion, A. N. (2017). *Modeling and simulation of liquid microlayer formation and evaporation in nucleate boiling using computational fluid dynamics*. PhD thesis, Massachusetts Institute of Technology.

Guo, D., Sun, D., Li, Z., and Tao, W. (2011). Phase change heat transfer simulation for boiling bubbles arising from a vapor film by the voset method. *Numerical Heat Transfer, Part A: Applications*, 59(11):857–881.

Gutiérrez, E., Balcázar, N., Bartrons, E., and Rigola, J. (2017). Numerical study of taylor bubbles rising in a stagnant liquid using a level-set/moving-mesh method. *Chemical Engineering Science*, 164:158–177.

Cette thèse est accessible à l'adresse : http://theses.insa-lyon.fr/publication/2020LYSEI095/these.pdf
© [L. Guo], [2020], INSA Lyon, tous droits réservés

Haberman, W. L. and Morton, R. (1953). An experimental investigation of the drag and shape of air bubbles rising in various liquids. Technical report, David Taylor Model Basin Washington DC.

Hardt, S. and Wondra, F. (2008). Evaporation model for interfacial flows based on a continuum-field representation of the source terms. *Journal of Computational Physics*, 227(11):5871–5895.

Harris, A. and Ripepe, M. (2007). Synergy of multiple geophysical approaches to unravel explosive eruption conduit and source dynamics–a case study from stromboli. *Geochemistry*, 67(1):1–35.

Hartunian, R. A. and Sears, W. (1957). On the instability of small gas bubbles moving uniformly in various liquids. *Journal of Fluid Mechanics*, 3(1):27–47.

Hasan, A. R., Kabir, C. S., et al. (1988). Predicting multiphase flow behavior in a deviated well. *SPE Production Engineering*, 3(04):474–482.

Hayashi, K., Kurimoto, R., and Tomiyama, A. (2010). Dimensional analysis of terminal velocity of a taylor bubble in a vertical pipe. *Multiphase Science and Technology*, 22(3).

Hayashi, K., Kurimoto, R., and Tomiyama, A. (2011). Terminal velocity of a taylor drop in a vertical pipe. *International Journal of Multiphase Flow*, 37(3):241–251.

Hewitt, G. F. and Roberts, D. (1969). Studies of two-phase flow patterns by simultaneous x-ray and flast photography. Technical report, Atomic Energy Research Establishment, Harwell, England (United Kingdom).

Hirt, C. W. and Nichols, B. D. (1981). Volume of fluid (vof) method for the dynamics of free boundaries. *Journal of computational physics*, 39(1):201–225.

Hua, J. and Lou, J. (2007). Numerical simulation of bubble rising in viscous liquid. *Journal of Computational Physics*, 222(2):769–795.

Hua, J., Stene, J. F., and Lin, P. (2008). Numerical simulation of 3d bubbles rising in viscous liquids using a front tracking method. *Journal of Computational Physics*, 227(6):3358–3382.

Irfan, M. and Muradoglu, M. (2017). A front tracking method for direct numerical simulation of evaporation process in a multiphase system. *Journal of Computational Physics*, 337:132–153.

James, M., Lane, S. J., and Chouet, B. (2006). Gas slug ascent through changes in conduit diameter: Laboratory insights into a volcano-seismic source process in low-viscosity magmas. *Journal of Geophysical Research: Solid Earth*, 111(B5).

Cette thèse est accessible à l'adresse : http://theses.insa-lyon.fr/publication/2020LYSEI095/these.pdf
© [L. Guo], [2020], INSA Lyon, tous droits réservés

Janssen, E. and Kervinen, J. (1964). Two-phase pressure drop across contractions and expansions water-steam mixtures at 600 to 1400 psia. Technical report, General Electric Co. Atomic Power Equipment Dept., San Jose, Calif.

Jeon, S.-S., Kim, S.-J., and Park, G.-C. (2011). Numerical study of condensing bubble in subcooled boiling flow using volume of fluid model. *Chemical engineering science*, 66(23):5899–5909.

Juric, D. and Tryggvason, G. (1998). Computations of boiling flows. *International journal of multiphase flow*, 24(3):387–410.

Kang, C.-W., Quan, S., and Lou, J. (2010). Numerical study of a taylor bubble rising in stagnant liquids. *Physical Review E*, 81(6):066308.

Kang, M., Fedkiw, R. P., and Liu, X.-D. (2000). A boundary condition capturing method for multiphase incompressible flow. *Journal of Scientific Computing*, 15(3):323–360.

Karapantsios, T., Paras, S. t., and Karabelas, A. (1989). Statistical characteristics of free falling films at high reynolds numbers. *International Journal of Multiphase Flow*, 15(1):1–21.

Kartuzova, O. and Kassemi, M. (2011). Modeling interfacial turbulent heat transfer during ventless pressurization of a large scale cryogenic storage tank in microgravity. In *47th AIAA/ASME/SAE/ASEE Joint Propulsion Conference & Exhibit*, page 6037.

Kaushik, V., Ghosh, S., Das, G., and Das, P. K. (2012). Cfd simulation of core annular flow through sudden contraction and expansion. *Journal of Petroleum Science and Engineering*, 86:153–164.

Kawahara, A., Mansour, M. H., Sadatomi, M., Law, W. Z., Kurihara, H., and Kusumaningsih, H. (2015). Characteristics of gas–liquid two-phase flows through a sudden contraction in rectangular microchannels. *Experimental Thermal and Fluid Science*, 66:243–253.

Kharangate, C. R., Lee, H., and Mudawar, I. (2015). Computational modeling of turbulent evaporating falling films. *International Journal of Heat and Mass Transfer*, 81:52–62.

Kharangate, C. R. and Mudawar, I. (2017). Review of computational studies on boiling and condensation. *International Journal of Heat and Mass Transfer*, 108:1164–1196.

Khokhlov, A. M. (1998). Fully threaded tree algorithms for adaptive refinement fluid dynamics simulations. *Journal of Computational Physics*, 143(2):519–543.

Kim, D. G., Jeon, C. H., and Park, I. S. (2017). Comparison of numerical phase-change models through stefan vaporizing problem. *International Communications in Heat and Mass Transfer*, 87:228–236.

Cette thèse est accessible à l'adresse : http://theses.insa-lyon.fr/publication/2020LYSEI095/these.pdf
© [L. Guo], [2020], INSA Lyon, tous droits réservés

Klimenko, V. (1981). Film boiling on a horizontal plate—new correlation. *International Journal of Heat and Mass Transfer*, 24(1):69–79.

Knudsen, M. and Partington, J. (1935). The kinetic. theoryof gases. some modern aspects. *The Journal of Physical Chemistry*, 39(2):307–307.

Kondo, K., Yoshida, K., Matsumoto, T., Okawa, T., and Kataoka, I. (2002). Flow patterns of gas-liquid two-phase flow in round tube with sudden expansion. In *International Conference on Nuclear Engineering*, volume 35979, pages 179–186.

Kothe, D., Rider, W., Mosso, S., Brock, J., and Hochstein, J. (1996). Volume tracking of interfaces having surface tension in two and three dimensions. In *34th Aerospace Sciences Meeting and Exhibit*, page 859.

Kourakos, V., Rambaud, P., Chabane, S., Pierrat, D., and Buchlin, J. (2009). Two-phase flow modelling within expansion and contraction singularities. *Computational Methods in Multiphase Flow V*, 63:27.

Krepper, E., Končar, B., and Egorov, Y. (2007). Cfd modelling of subcooled boiling—concept, validation and application to fuel assembly design. *Nuclear engineering and design*, 237(7):716–731.

Kunkelmann, C. (2011). *Numerical modeling and investigation of boiling phenomena*. PhD thesis, Technische Universität.

Kunkelmann, C. and Stephan, P. (2009). Cfd simulation of boiling flows using the volume-of-fluid method within openfoam. *Numerical Heat Transfer, Part A: Applications*, 56(8):631–646.

Kunkelmann, C. and Stephan, P. (2010). Numerical simulation of the transient heat transfer during nucleate boiling of refrigerant hfe-7100. *International Journal of Refrigeration*, 33(7):1221–1228.

Kurimoto, R., Hayashi, K., and Tomiyama, A. (2013). Terminal velocities of clean and fully-contaminated drops in vertical pipes. *International journal of multiphase flow*, 49:8–23.

Lee, R. and Nydahl, J. (1989). Numerical calculation of bubble growth in nucleate boiling from inception through departure. *Journal of Heat Transfer*, 111(2):474–479.

Lee, W. H. (1980). Pressure iteration scheme for two-phase flow modeling. *IN" MULTIPHASE TRANSPORT: FUNDAMENTALS, REACTOR SAFETY, APPLICATIONS"*., pages 407–432.

Lel, V., Al-Sibai, F., Leefken, A., and Renz, U. (2005). Local thickness and wave velocity measurement of wavy films with a chromatic confocal imaging method and a fluorescence intensity technique. *Experiments in fluids*, 39(5):856–864.

Cette thèse est accessible à l'adresse : http://theses.insa-lyon.fr/publication/2020LYSEI095/these.pdf
© [L. Guo], [2020], INSA Lyon, tous droits réservés

Liao, Q. and Zhao, T. (2003). Modeling of taylor bubble rising in a vertical mini noncircular channel filled with a stagnant liquid. *International Journal of Multiphase Flow*, 29(3):411–434.

Ling, K., Li, Z.-Y., and Tao, W.-Q. (2014). A direct numerical simulation for nucleate boiling by the voset method. *Numerical Heat Transfer, Part A: Applications*, 65(10):949–971.

Liu, D. and Wang, S. (2008). Hydrodynamics of taylor flow in noncircular capillaries. *Chemical Engineering and Processing: Process Intensification*, 47(12):2098–2106.

Llewellin, E., Del Bello, E., Taddeucci, J., Scarlato, P., and Lane, S. (2011). The thickness of the falling film of liquid around a taylor bubble. *Proceedings of the Royal Society A: Mathematical, Physical and Engineering Sciences*, 468(2140):1041–1064.

López-Herrera, J., Ganan-Calvo, A., Popinet, S., and Herrada, M. (2015). Electrokinetic effects in the breakup of electrified jets: A volume-of-fluid numerical study. *International Journal of Multiphase Flow*, 71:14–22.

Lörstad, D., Francois, M., Shyy, W., and Fuchs, L. (2004). Assessment of volume of fluid and immersed boundary methods for droplet computations. *International journal for numerical methods in fluids*, 46(2):109–125.

Lu, J. and Tryggvason, G. (2008). Effect of bubble deformability in turbulent bubbly upflow in a vertical channel. *Physics of Fluids*, 20(4):040701.

Lu, X. and Prosperetti, A. (2008). A numerical study of taylor bubbles. *Industrial & Engineering Chemistry Research*, 48(1):242–252.

Luo, X.-Y., Ni, M.-J., Ying, A., and Abdou, M. (2005). Numerical modeling for multiphase incompressible flow with phase change. *Numerical Heat Transfer, Part B: Fundamentals*, 48(5):425–444.

Luo, Y., Li, W., Zhou, K., Sheng, K., Shao, S., Zhang, Z., Du, J., and Minkowycz, W. (2020). Three-dimensional numerical simulation of saturated annular flow boiling in a narrow rectangular microchannel. *International Journal of Heat and Mass Transfer*, 149:119246.

Magnini, M. (2012). *CFD modeling of two-phase boiling flows in the slug flow regime with an interface capturing technique*. PhD thesis, alma.

Magnini, M. and Pulvirenti, B. (2011). Height function interface reconstruction algorithm for the simulation of boiling flows. *WIT Transactions on Engineering Sciences; WIT Press: Southampton, UK*, 70:69–80.

Malan, L., Malan, A., Zaleski, S., and Rousseau, P. (2020). A geometric vof method for interface resolved phase change and conservative thermal energy advection. *arXiv preprint arXiv:2001.03477*.

Cette thèse est accessible à l'adresse : http://theses.insa-lyon.fr/publication/2020LYSEI095/these.pdf
© [L. Guo], [2020], INSA Lyon, tous droits réservés

Mao, Z.-S. and Dukler, A. (1991). The motion of taylor bubbles in vertical tubes—ii. experimental data and simulations for laminar and turbulent flow. *Chemical Engineering Science*, 46(8):2055–2064.

Marek, R. and Straub, J. (2001). Analysis of the evaporation coefficient and the condensation coefficient of water. *International Journal of Heat and Mass Transfer*, 44(1):39–53.

Massoud, E., Xiao, Q., El-Gamal, H., and Teamah, M. (2018). Numerical study of an individual taylor bubble rising through stagnant liquids under laminar flow regime. *Ocean Engineering*, 162:117–137.

Moreiras, J., Pereyra, E., Sarica, C., and Torres, C. F. (2014). Unified drift velocity closure relationship for large bubbles rising in stagnant viscous fluids in pipes. *Journal of Petroleum Science and Engineering*, 124:359–366.

Morgado, A., Miranda, J., Araújo, J., and Campos, J. (2016). Review on vertical gas–liquid slug flow. *International Journal of Multiphase Flow*, 85:348–368.

Ndinisa, N., Wiley, D., and Fletcher, D. (2005). Computational fluid dynamics simulations of taylor bubbles in tubular membranes: model validation and application to laminar flow systems. *Chemical Engineering Research and Design*, 83(1):40–49.

Nichita, B. A. and Thome, J. R. (2010). A level set method and a heat transfer model implemented into fluent for modeling of microscale two phase flows. In *AVT-178 Specialists' Meeting on System Level Thermal Management for Enhanced Platform Efficiency*, number CONF.

Ningegowda, B. and Premachandran, B. (2014). A coupled level set and volume of fluid method with multi-directional advection algorithms for two-phase flows with and without phase change. *International Journal of Heat and Mass Transfer*, 79:532–550.

Nogueira, S., Riethmuler, M., Campos, J., and Pinto, A. (2006a). Flow in the nose region and annular film around a taylor bubble rising through vertical columns of stagnant and flowing newtonian liquids. *Chemical Engineering Science*, 61(2):845–857.

Nogueira, S., Riethmuller, M., Campos, J., and Pinto, A. (2006b). Flow patterns in the wake of a taylor bubble rising through vertical columns of stagnant and flowing newtonian liquids: An experimental study. *Chemical engineering science*, 61(22):7199–7212.

Nogueira, S., Sousa, R., Pinto, A., Riethmuller, M., and Campos, J. (2003). Simultaneous piv and pulsed shadow technique in slug flow: a solution for optical problems. *Experiments in Fluids*, 35(6):598–609.

Cette thèse est accessible à l'adresse : http://theses.insa-lyon.fr/publication/2020LYSEI095/these.pdf
© [L. Guo], [2020], INSA Lyon, tous droits réservés

Nusselt, W. (1916). Die oberflächenkondensation des wasserdampfes zeitschrift.

Ohta, M., Imura, T., Yoshida, Y., and Sussman, M. (2005). A computational study of the effect of initial bubble conditions on the motion of a gas bubble rising in viscous liquids. *International journal of multiphase flow*, 31(2):223–237.

Osher, S. and Sethian, J. A. (1988). Fronts propagating with curvature-dependent speed: algorithms based on hamilton-jacobi formulations. *Journal of computational physics*, 79(1):12–49.

Padilla, M., Revellin, R., and Bonjour, J. (2013). Two-phase flow of hfo-1234yf, r-134a and r-410a in sudden contractions: Visualization, pressure drop measurements and new prediction method. *Experimental Thermal and Fluid Science*, 47:186–205.

Pan, Z., Weibel, J. A., and Garimella, S. V. (2016). A saturated-interface-volume phase change model for simulating flow boiling. *International Journal of Heat and Mass Transfer*, 93:945–956.

Pilliod Jr, J. E. and Puckett, E. G. (2004). Second-order accurate volume-of-fluid algorithms for tracking material interfaces. *Journal of Computational Physics*, 199(2):465–502.

Pinto, A., Pinheiro, M. C., and Campos, J. (1998). Coalescence of two gas slugs rising in a co-current flowing liquid in vertical tubes. *Chemical engineering science*, 53(16):2973–2983.

Pivello, M. R., Villar, M. M., Serfaty, R., Roma, A. M., and Silveira-Neto, A. d. (2014). A fully adaptive front tracking method for the simulation of two phase flows. *International Journal of Multiphase Flow*, 58:72–82.

Popinet, S. (2003). Gerris: a tree-based adaptive solver for the incompressible euler equations in complex geometries. *Journal of Computational Physics*, 190(2):572–600.

Popinet, S. (2009). An accurate adaptive solver for surface-tension-driven interfacial flows. *Journal of Computational Physics*, 228(16):5838–5866.

Popinet, S. (2013a). The basilisk flow solver. *a Free-Software program for the solution of partialdifferential equations on adaptive Cartesian meshes*.

Popinet, S. (2013b). The gerris flow solver. *A free, open source, general-purpose fluid mechanics code (2001-2014)*.

Popinet, S. (2015). A quadtree-adaptive multigrid solver for the serre–green–naghdi equations. *Journal of Computational Physics*, 302:336–358.

Popinet, S. and Rickard, G. (2007). A tree-based solver for adaptive ocean modelling. *Ocean Modelling*, 16(3-4):224–249.

Cette thèse est accessible à l'adresse : http://theses.insa-lyon.fr/publication/2020LYSEI095/these.pdf
© [L. Guo], [2020], INSA Lyon, tous droits réservés

Prothero, J. and Burton, A. (1961). The physics of blood flow in capillaries: I. the nature of the motion. *Biophysical journal*, 1(7):565–579.

Puckett, E. G., Almgren, A. S., Bell, J. B., Marcus, D. L., and Rider, W. J. (1997). A high-order projection method for tracking fluid interfaces in variable density incompressible flows. *Journal of computational physics*, 130(2):269–282.

Qin, Z., Soldati, A., Velazquez Santana, L. C., Rust, A. C., Suckale, J., and Cashman, K. V. (2018). Slug stability in flaring geometries and ramifications for lava lake degassing. *Journal of Geophysical Research: Solid Earth*, 123(12):10–431.

Rajkotwala, A., Panda, A., Peters, E., Baltussen, M., van der Geld, C., Kuerten, J., and Kuipers, J. (2019). A critical comparison of smooth and sharp interface methods for phase transition. *International Journal of Multiphase Flow*, 120:103093.

Ranz, W., Marshall, W. R., et al. (1952). Evaporation from drops. *Chem. eng. prog*, 48(3):141–146.

Rattner, A. S. and Garimella, S. (2014). Simple mechanistically consistent formulation for volume-of-fluid based computations of condensing flows. *Journal of heat transfer*, 136(7).

Renardy, Y. and Renardy, M. (2002). Prost: a parabolic reconstruction of surface tension for the volume-of-fluid method. *Journal of computational physics*, 183(2):400–421.

Reutzsch, J., Kieffer-Roth, C., and Weigand, B. (2020). A consistent method for direct numerical simulation of droplet evaporation. *Journal of Computational Physics*, page 109455.

Rider, W. and Kothe, D. (1995). Stretching and tearing interface tracking methods. In *12th Computational Fluid Dynamics Conference*, page 1717.

Rider, W. J. and Kothe, D. B. (1998). Reconstructing volume tracking. *Journal of computational physics*, 141(2):112–152.

Rinne, A. and Loth, R. (1996). Development of local two-phase flow parameters for vertical bubbly flow in a pipe with sudden expansion. *Experimental thermal and fluid science*, 13(2):152–166.

Roghair, I., Lau, Y., Deen, N., Slagter, H., Baltussen, M., Annaland, M. V. S., and Kuipers, J. (2011). On the drag force of bubbles in bubble swarms at intermediate and high reynolds numbers. *Chemical engineering science*, 66(14):3204–3211.

Sadatomil, M., Miyagawal, S., Santoso, B., and Kawahara, A. (2013). Air-water two-phase flow through u-bend, sudden expansion and sudden contraction in rectangular mini-channels. *Computational Methods in Multiphase Flow VII*, 79:63.

Cette thèse est accessible à l'adresse : http://theses.insa-lyon.fr/publication/2020LYSEI095/these.pdf
© [L. Guo], [2020], INSA Lyon, tous droits réservés

Samet, H. (1990). Applications of spatial data structures.

Samkhaniani, N. and Ansari, M. R. (2017). The evaluation of the diffuse interface method for phase change simulations using openfoam. *Heat Transfer—Asian Research*, 46(8):1173–1203.

Sato, Y. and Ničeno, B. (2013). A sharp-interface phase change model for a mass-conservative interface tracking method. *Journal of Computational Physics*, 249:127–161.

Scapin, N., Costa, P., and Brandt, L. (2020). A volume-of-fluid method for interface-resolved simulations of phase-changing two-fluid flows. *Journal of Computational Physics*, 407:109251.

Scardovelli, R. and Zaleski, S. (2000). Analytical relations connecting linear interfaces and volume fractions in rectangular grids. *Journal of Computational Physics*, 164(1):228–237.

Scardovelli, R. and Zaleski, S. (2003). Interface reconstruction with least-square fit and split eulerian–lagrangian advection. *International Journal for Numerical Methods in Fluids*, 41(3):251–274.

Schrage, R. W. (1953). *A theoretical study of interphase mass transfer*. Columbia University Press.

Sharaf, D., Premlata, A., Tripathi, M. K., Karri, B., and Sahu, K. C. (2017). Shapes and paths of an air bubble rising in quiescent liquids. *Physics of Fluids*, 29(12):122104.

Shin, S. and Juric, D. (2002). Modeling three-dimensional multiphase flow using a level contour reconstruction method for front tracking without connectivity. *Journal of Computational Physics*, 180(2):427–470.

Shosho, C. E. and Ryan, M. E. (2001). An experimental study of the motion of long bubbles in inclined tubes. *Chemical engineering science*, 56(6):2191–2204.

Silvi, L. D., Saha, A., Chandraker, D. K., Ghosh, S., and Das, A. K. (2020). Numerical analysis of pre-dryout sequences through the route of interfacial evolution in annular gas-liquid two-phase flow with phase change. *Chemical Engineering Science*, 212:115356.

Singh, R. and Sharma, S. (2012). Development of suitable photobioreactor for algae production–a review. *Renewable and Sustainable Energy Reviews*, 16(4):2347–2353.

Soldati, A., Cashman, K., Rust, A., and Rosi, M. (2013). Bubble rise and break-up in volcanic conduits. *AGUFM*, 2013:V13H–06.

Son, G. and Dhir, V. (1997). Numerical simulation of saturated film boiling on a horizontal surface. *Journal of heat transfer*, 119(3):525–533.

Cette thèse est accessible à l'adresse : http://theses.insa-lyon.fr/publication/2020LYSEI095/these.pdf
© [L. Guo], [2020], INSA Lyon, tous droits réservés

Son, G. and Dhir, V. K. (1998). Numerical simulation of film boiling near critical pressures with a level set method.

Son, G., Dhir, V. K., and Ramanujapu, N. (1999). Dynamics and heat transfer associated with a single bubble during nucleate boiling on a horizontal surface.

Spedding, P. and Nguyen, V. T. (1978). Bubble rise and liquid content in horizontal and inclined tubes. *Chemical Engineering Science*, 33(8):987–994.

Strotos, G., Malgarinos, I., Nikolopoulos, N., and Gavaises, M. (2016). Predicting the evaporation rate of stationary droplets with the vof methodology for a wide range of ambient temperature conditions. *International Journal of Thermal Sciences*, 109:253–262.

Sudhakar, T. and Das, A. K. (2018). Interface evolution of a liquid taylor droplet during passage through a sudden contraction in a rectangular channel. *Chemical Engineering Science*, 192:993–1010.

Sun, D. and Tao, W. (2010). A coupled volume-of-fluid and level set (voset) method for computing incompressible two-phase flows. *International Journal of Heat and Mass Transfer*, 53(4):645–655.

Sun, D., Xu, J., and Chen, Q. (2014). Modeling of the evaporation and condensation phase-change problems with fluent. *Numerical Heat Transfer, Part B: Fundamentals*, 66(4):326–342.

Sun, D.-L., Xu, J.-L., and Wang, L. (2012). Development of a vapor–liquid phase change model for volume-of-fluid method in fluent. *International Communications in Heat and Mass Transfer*, 39(8):1101–1106.

Sussman, M. (2003). A second order coupled level set and volume-of-fluid method for computing growth and collapse of vapor bubbles. *Journal of Computational Physics*, 187(1):110–136.

Sussman, M., Fatemi, E., Smereka, P., and Osher, S. (1998). An improved level set method for incompressible two-phase flows. *Computers & Fluids*, 27(5-6):663–680.

Sussman, M. and Ohta, M. (2007). Improvements for calculating two-phase bubble and drop motion using an adaptive sharp interface method. *Fluid Dyn. Mater. Process*, 3(1):21–36.

Sussman, M. and Puckett, E. G. (2000). A coupled level set and volume-of-fluid method for computing 3d and axisymmetric incompressible two-phase flows. *Journal of computational physics*, 162(2):301–337.

Tagawa, Y., Takagi, S., and Matsumoto, Y. (2014). Surfactant effect on path instability of a rising bubble. *Journal of Fluid Mechanics*, 738:124–142.

Cette thèse est accessible à l'adresse : http://theses.insa-lyon.fr/publication/2020LYSEI095/these.pdf
© [L. Guo], [2020], INSA Lyon, tous droits réservés

Taha, T. and Cui, Z. (2004). Hydrodynamics of slug flow inside capillaries. *Chemical Engineering Science*, 59(6):1181–1190.

Taha, T. and Cui, Z. (2006). Cfd modelling of slug flow in vertical tubes. *Chemical Engineering Science*, 61(2):676–687.

Takahashi, M., Inoue, A., and Kaneko, T. (1994). Pool boiling heat transfer of mercury in the presence of a strong magnetic field. *Experimental thermal and fluid science*, 8(1):67–78.

Takamura, K., Fischer, H., and Morrow, N. R. (2012). Physical properties of aqueous glycerol solutions. *Journal of Petroleum Science and Engineering*, 98:50–60.

Tanasawa, I. (1991). Advances in condensation heat transfer. In *Advances in heat transfer*, volume 21, pages 55–139. Elsevier.

Tanguy, S., Ménard, T., and Berlemont, A. (2007). A level set method for vaporizing two-phase flows. *Journal of Computational Physics*, 221(2):837–853.

Tomar, G., Biswas, G., Sharma, A., and Agrawal, A. (2005). Numerical simulation of bubble growth in film boiling using a coupled level-set and volume-of-fluid method. *Physics of Fluids*, 17(11):112103.

Tomiyama, A., Celata, G., Hosokawa, S., and Yoshida, S. (2002). Terminal velocity of single bubbles in surface tension force dominant regime. *International Journal of Multiphase Flow*, 28(9):1497–1519.

Tomiyama, A., Sou, A., Minagawa, H., and Sakaguchi, T. (1993). Numerical analysis of a single bubble by vof method. *JSME International Journal Series B Fluids and Thermal Engineering*, 36(1):51–56.

Tripathi, M. K., Sahu, K. C., and Govindarajan, R. (2015). Dynamics of an initially spherical bubble rising in quiescent liquid. *Nature communications*, 6:6268.

Tryggvason, G., Bunner, B., Esmaeeli, A., Juric, D., Al-Rawahi, N., Tauber, W., Han, J., Nas, S., and Jan, Y.-J. (2001). A front-tracking method for the computations of multiphase flow. *Journal of computational physics*, 169(2):708–759.

Tryggvason, G., Esmaeeli, A., Lu, J., and Biswas, S. (2006). Direct numerical simulations of gas/liquid multiphase flows. *Fluid dynamics research*, 38(9):660.

Tryggvason, G., Scardovelli, R., and Zaleski, S. (2011). *Direct numerical simulations of gas–liquid multiphase flows*. Cambridge University Press.

Tsui, Y.-Y. and Lin, S.-W. (2013). A vof-based conservative interpolation scheme for interface tracking (cisit) of two-fluid flows. *Numerical Heat Transfer, Part B: Fundamentals*, 63(4):263–283.

Cette thèse est accessible à l'adresse : http://theses.insa-lyon.fr/publication/2020LYSEI095/these.pdf
© [L. Guo], [2020], INSA Lyon, tous droits réservés

Tsui, Y.-Y. and Lin, S.-W. (2016). Three-dimensional modeling of fluid dynamics and heat transfer for two-fluid or phase change flows. *International Journal of Heat and Mass Transfer*, 93:337–348.

Tsui, Y.-Y., Lin, S.-W., Lai, Y.-N., and Wu, F.-C. (2014). Phase change calculations for film boiling flows. *International Journal of Heat and Mass Transfer*, 70:745–757.

Tung, K. W. and Parlange, J.-Y. (1976). Note on the motion of long bubbles in closed tubes-influence of surface tension. *Acta Mechanica*, 24(3):313–317.

Udaykumar, H., Shyy, W., and Rao, M. (1996). Elafint: a mixed eulerian–lagrangian method for fluid flows with complex and moving boundaries. *International journal for numerical methods in fluids*, 22(8):691–712.

Unverdi, S. O. and Tryggvason, G. (1992). A front-tracking method for viscous, incompressible, multi-fluid flows. *Journal of computational physics*, 100(1):25–37.

Van Hout, R., Barnea, D., and Shemer, L. (2002). Translational velocities of elongated bubbles in continuous slug flow. *International Journal of Multiphase Flow*, 28(8):1333–1350.

van Sint Annaland, M., Deen, N., and Kuipers, J. (2005). Numerical simulation of gas bubbles behaviour using a three-dimensional volume of fluid method. *Chemical Engineering Science*, 60(11):2999–3011.

van Sint Annaland, M., Dijkhuizen, W., Deen, N., and Kuipers, J. (2006). Numerical simulation of behavior of gas bubbles using a 3-d front-tracking method. *AIChE Journal*, 52(1):99–110.

Vanleer, B. (1983). Multidimensional explicit difference schemes for hyperbolic conservation laws.

Veldhuis, C., Biesheuvel, A., and Van Wijngaarden, L. (2008). Shape oscillations on bubbles rising in clean and in tap water. *Physics of fluids*, 20(4):040705.

Viana, F., Pardo, R., Yánez, R., Trallero, J. L., and Joseph, D. D. (2003). Universal correlation for the rise velocity of long gas bubbles in round pipes. *Journal of Fluid Mechanics*, 494:379–398.

Villarreal, J., Laverde, D., and Fuentes, C. (2006). Carbon-steel corrosion in multiphase slug flow and co2. *Corrosion Science*, 48(9):2363–2379.

Volk, A. and Kähler, C. J. (2018). Density model for aqueous glycerol solutions. *Experiments in Fluids*, 59(5):75.

Wallis, G. B. (1969). One-dimensional two-phase flow.

Cette thèse est accessible à l'adresse : http://theses.insa-lyon.fr/publication/2020LYSEI095/these.pdf
© [L. Guo], [2020], INSA Lyon, tous droits réservés

Walters, J. and Davidson, J. (1962). The initial motion of a gas bubble formed in an inviscid liquid part 1. the two-dimensional bubble. *Journal of Fluid Mechanics*, 12(3):408–416.

Walters, J. and Davidson, J. (1963). The initial motion of a gas bubble formed in an inviscid liquid. *Journal of Fluid Mechanics*, 17(3):321–336.

Welch, J. E. (1968). The mac method-a computing technique for solving viscous, incompressible, transient fluid-flow problems involving free surfaces. *Los Alamos scientific laboratory report LA-3425*.

Welch, S. W. and Wilson, J. (2000). A volume of fluid based method for fluid flows with phase change. *Journal of computational physics*, 160(2):662–682.

Weymouth, G. D. and Yue, D. K.-P. (2010). Conservative volume-of-fluid method for free-surface simulations on cartesian-grids. *Journal of Computational Physics*, 229(8):2853–2865.

White, E. and Beardmore, R. (1962). The velocity of rise of single cylindrical air bubbles through liquids contained in vertical tubes. *Chemical Engineering Science*, 17(5):351–361.

Wu, C. and Young, D. (2013). Interface reconstruction with split lagrangian advection for two-dimensional interfacial flows. *Journal of Mechanics*, 29(2):253.

Wu, H., Peng, X., Ye, P., and Gong, Y. E. (2007). Simulation of refrigerant flow boiling in serpentine tubes. *International Journal of Heat and Mass Transfer*, 50(5-6):1186–1195.

Wu, J. and Dhir, V. K. (2010). Numerical simulations of the dynamics and heat transfer associated with a single bubble in subcooled pool boiling. *Journal of heat transfer*, 132(11).

Wu, M. and Gharib, M. (2002). Experimental studies on the shape and path of small air bubbles rising in clean water. *Physics of fluids*, 14(7):L49–L52.

Yang, X., James, A. J., Lowengrub, J., Zheng, X., and Cristini, V. (2006). An adaptive coupled level-set/volume-of-fluid interface capturing method for unstructured triangular grids. *Journal of Computational Physics*, 217(2):364–394.

Yang, Z., Peng, X., and Ye, P. (2008). Numerical and experimental investigation of two phase flow during boiling in a coiled tube. *International Journal of Heat and Mass Transfer*, 51(5-6):1003–1016.

Youngs, D. L. (1982). Time-dependent multi-material flow with large fluid distortion. *Numerical methods for fluid dynamics*.

Cette thèse est accessible à l'adresse : http://theses.insa-lyon.fr/publication/2020LYSEI095/these.pdf
© [L. Guo], [2020], INSA Lyon, tous droits réservés

Yuan, M., Yang, Y., Li, T., and Hu, Z. (2008). Numerical simulation of film boiling on a sphere with a volume of fluid interface tracking method. *International Journal of Heat and Mass Transfer*, 51(7-8):1646–1657.

Zeng, Q., Cai, J., Yin, H., Yang, X., and Watanabe, T. (2015). Numerical simulation of single bubble condensation in subcooled flow using openfoam. *Progress in Nuclear Energy*, 83:336–346.

Zhang, J. and Ni, M.-J. (2018). Direct numerical simulations of incompressible multiphase magnetohydrodynamics with phase change. *Journal of Computational Physics*, 375:717–746.

Zhang, Y., Faghri, A., and Shafii, M. B. (2001). Capillary blocking in forced convective condensation in horizontal miniature channels. *J. Heat Transfer*, 123(3):501–511.

Zhou, C. (2017). *Numerical simulation and experimental investigations of two-phase flow in singularities*. PhD thesis, Lyon.

Zhou, D., Gambaryan-Roisman, T., and Stephan, P. (2009). Measurement of water falling film thickness to flat plate using confocal chromatic sensoring technique. *Experimental Thermal and Fluid Science*, 33(2):273–283.

Zukoski, E. (1966). Influence of viscosity, surface tension, and inclination angle on motion of long bubbles in closed tubes. *Journal of Fluid Mechanics*, 25(4):821–837.

Cette thèse est accessible à l'adresse : http://theses.insa-lyon.fr/publication/2020LYSEI095/these.pdf
© [L. Guo], [2020], INSA Lyon, tous droits réservés

FOLIO ADMINISTRATIF

THESE DE L'UNIVERSITE DE LYON OPEREE AU SEIN DE L'INSA LYON

NOM : GUO
(avec précision du nom de jeune fille, le cas échéant)

DATE de SOUTENANCE : 28/10/2020

Prénoms : Longkai

TITRE : Numerical investigation of Taylor bubble and development of a phase change model

NATURE : Doctorat

Numéro d'ordre : 2020LYSEI095

Ecole doctorale : MEGA de Lyon (Mécanique, Energétique, Génie Civil, Acoustique)

Spécialité : Mécanique des Fluides

RESUME : The motion of a nitrogen Taylor bubble in glycerol-water mixed solutions rising through different types of expansions and contractions is investigated by a numerical approach. The CFD procedure is based on an open-source solver Basilisk, which adopts the volume-of-fluid (VOF) method to capture the gas-liquid interface. The results of sudden expansions/contractions are compared with experimental results. The results show that the simulations are in good agreement with experiments. The bubble velocity increases in sudden expansions and decreases in sudden contractions. The bubble break-up pattern is observed in sudden expansions with large expansion ratios, and a bubble blocking pattern is found in sudden contractions with small contraction ratios. In addition, the wall shear stress, the liquid film thickness, and pressure in the simulations are studied to understand the hydrodynamics of the Taylor bubble rising through expansions/contractions. The transient process of the Taylor bubble passing through sudden expansion/contraction is further analyzed for three different singularities: gradual, parabolic convex and parabolic concave. A unique feature in parabolic concave contraction is that the Taylor bubble passes through the contraction even for small contraction ratios. Moreover, a phase change model is developed in the Basilisk solver. In order to use the existed geometric VOF method in Basilisk, a general two-step geometric VOF method is implemented. Mass flux is calculated not in the interfacial cells but transferred to the neighboring cells around the interface. The saturated temperature boundary condition is imposed at the interface by a ghost cell method. The phase change model is validated by droplet evaporation with a constant mass transfer rate, the one-dimensional Stefan problem, the sucking interface problem, and a planar film boiling case. The results show good agreement with analytical solutions or correlations.

MOTS-CLÉS : Two-phase flow, Taylor bubble, expansion, contraction, VOF, phase change

Laboratoire (s) de recherche : Centre d'Energétique et Thermique de Lyon - CETHIL

Directeur de thèse: XIN, Shihe

Composition du jury :

DARU, Virginie	Maître de conférences	Arts et Métiers ParisTech - ENSAM	Rapporteur
JOSSERAND, Christophe	Directeur de Recherche	École Polytechnique	Rapporteur
NASO, Aurore	Chargée de Recherche	École Centrale de Lyon	Examinatrice
RUYER-QUIL, Christian	Professeur	Université Savoie Mont Blanc	Examinateur
KNIKKER, Ronnie	Maître de conférences	INSA-LYON	Co-directeur de thèse
ALBIN, Eric	Maître de conférences	INSA-LYON	Invité

Cette thèse est accessible à l'adresse : http://theses.insa-lyon.fr/publication/2020LYSEI095/these.pdf
© [L. Guo], [2020], INSA Lyon, tous droits réservés